



**HAL**  
open science

# Superconducting qubit in a resonator: test of the Legget-Garg inequality and single-shot readout

Agustin Palacios-Laloy

► **To cite this version:**

Agustin Palacios-Laloy. Superconducting qubit in a resonator: test of the Legget-Garg inequality and single-shot readout. Quantum Physics [quant-ph]. Université Pierre et Marie Curie - Paris VI, 2010. English. NNT: 2010PA066321 . tel-00815078

**HAL Id: tel-00815078**

**<https://theses.hal.science/tel-00815078v1>**

Submitted on 18 Apr 2013

**HAL** is a multi-disciplinary open access archive for the deposit and dissemination of scientific research documents, whether they are published or not. The documents may come from teaching and research institutions in France or abroad, or from public or private research centers.

L'archive ouverte pluridisciplinaire **HAL**, est destinée au dépôt et à la diffusion de documents scientifiques de niveau recherche, publiés ou non, émanant des établissements d'enseignement et de recherche français ou étrangers, des laboratoires publics ou privés.

**THESE DE DOCTORAT DE  
L'UNIVERSITE PARIS 6 - PIERRE ET MARIE CURIE**

Spécialité :  
Physique quantique

Présentée par  
Agustin Palacios-Laloy

Pour obtenir le grade de

**DOCTEUR de L'UNIVERSITÉ PIERRE ET MARIE CURIE**

Sujet de la thèse :

BITS QUANTIQUES SUPRACONDUCTEURS ET RESONATEURS :  
TEST DE L'ÉGALITÉ DE LEGGETT-GARG ET LECTURE EN UN COUP

soutenue le 23 septembre 2010

devant le jury composé de :

Alain ASPECT  
Benoît DOUÇOT  
Daniel ESTÈVE (directeur de thèse)  
Hans MOOIJ (rapporteur)  
Jean-Michel RAIMOND  
Andreas WALLRAFF (rapporteur)

Thèse préparée au Service de Physique de l'État Condensé  
CEA-Saclay 91191 Gif-sur-Yvette



RESUMÉ EN FRANÇAIS : Cette thèse présente un ensemble d'expériences de QED en circuit (cQED), dans lesquelles des atomes artificiels basés sur des circuits supraconducteurs sont couplés au champ électromagnétique d'un résonateur micro-ondes. Ce résonateur agit comme appareil de mesure pour l'atome, permettant d'illustrer des aspects fondamentaux de la physique quantique et de développer des briques de base pour un processeur quantique.

Dans une première expérience nous suivons continuellement l'évolution de l'atome tout en variant l'intensité de la mesure. Nous observons la transition du régime de mesure faible à celui de mesure forte, puis le gel de la dynamique du a l'effet Zénon quantique. Dans le régime de mesure faible nous testons si l'atome artificiel est en accord avec les hypothèses du réalisme macroscopique, à partir desquelles Leggett et Garg ont déduit une inégalité de Bell en temps. La violation de cette inégalité confirme que l'atome artificiel, bien que macroscopique, est un objet quantique.

En ce qui concerne l'information quantique, nous avons enrichi l'architecture cQED en démontrant un système de lecture haute fidélité en un coup pour le qubit, un élément crucial pour un processeur quantique. Notre circuit utilise la transition dynamique d'un résonateur non-linéaire. Le système couplé formé par le qubit et le résonateur non linéaire permet en plus d'étudier l'interaction entre couplage fort et effets non linéaires –amplification paramétrique, squeezing...– ouvrant un nouveau sujet : le cQED non linéaire.

Finalement, nous avons mis au point un circuit qui servirait d'intermédiaire pour que deux qubits arbitraires interagissent : un résonateur micro-ondes a fréquence accordable.

TITRE EN ANGLAIS : Superconducting qubit in a resonator: test of the Leggett-Garg inequality and single-shot readout

RESUMÉ EN ANGLAIS : This thesis presents a series of circuit QED (cQED) experiments, in which artificial atoms consisting of superconducting circuits are strongly coupled to the electromagnetic field stored in a microwave resonator. This resonator can be used as a measurement apparatus for the atom, allowing both to address fundamental issues in quantum mechanics, and to develop building blocks for a quantum processor.

In a first experiment we continuously monitored the evolution of a quantum system while varying the measurement strength. We observed the crossover from weak to strong measurement regimes, and, ultimately, the freezing of the dynamics by the Quantum Zeno Effect. In the weak measurement regime, we probed if the artificial atom complies with the macroscopic realism hypotheses, from which Leggett and Garg have derived a Bell's inequality in time. The violation of this inequality confirms that although macroscopic, the artificial atom is a truly quantum object.

On the quantum information side, we have enriched the proposed cQED quantum processor architecture by demonstrating a high fidelity single-shot qubit readout, a crucial element for quantum processors. This new circuit relies on a dynamical transition of a non-linear resonator. The coupled system formed by



the qubit and the non-linear resonator allows in addition to investigate the interplay between strong coupling and non-linear effects –parametric amplification, squeezing...– opening the new field of *non-linear cQED*.

Finally we have operated a circuit which would potentially be able to mediate operations between two arbitrary qubits: a superconducting resonator which is tunable in frequency.

**MOTS CLÉS EN FRANÇAIS :** information quantique, électrodynamique quantique, circuit quantique, jonction Josephson, théorie de la mesure, réalisme macroscopique, cohérence quantique, lecture d'un bit quantique

**MOTS CLÉS EN ANGLAIS :** quantum information, quantum electrodynamics, quantum circuit, Josephson junction, measurement theory, macroscopic realism, quantum coherence, qubit readout

# CONTENTS

---

o	Résumé en français	9
0.1	Des circuits électriques pour réaliser des expériences de physique quantique fondamentale et d'information quantique	9
0.2	CQED avec des atomes artificiels macroscopiques	10
0.3	Mesure et dynamique en cQED	12
0.4	Une architecture cQED pour le processeur quantique	17
0.4.1	Mesure cQED avec un détecteur d'échantillonnage et retenue	18
0.4.2	Un élément de couplage accordable entre qubits	21
I	BACKGROUND	25
1	Introduction	27
1.1	Quantum physics and quantum information experiments with circuits	27
1.2	Cavity QED with macroscopic artificial atoms	28
1.3	Measurement and dynamics in circuit QED	30
1.4	Circuit QED architecture for quantum computing	34
1.4.1	Sample-and-hold measurement in cQED	36
1.4.2	A tunable qubit coupler	38
2	Circuit QED: the building blocks	41
2.1	Superconducting resonators	41
2.1.1	Harmonic oscillators	41
2.1.2	Transmission-line resonators	44
2.1.3	Probing the dynamics of the resonator from the outside : input-output theory	47
2.1.4	Implementation	54
2.1.5	Characterization of the resonators	57
2.2	The transmon artificial atom	65
2.2.1	The Cooper-pair box: an anharmonic artificial atom	66
2.2.2	Coherent manipulation of the CPB	69
2.2.3	Decoherence	70
2.2.4	The transmon: perturbative approximation of the anharmonicity	76
2.3	Transmon-resonator coupling	78
2.3.1	Relaxation through the resonator: the Purcell effect	79
2.3.2	Resonant regime: vacuum Rabi splitting	80
2.3.3	Dispersive regime: cavity pull and AC-Stark shift	81
2.4	Measuring the TLS with a resonator	85
2.4.1	Microwave techniques for measuring the TLS-resonator coupled system	85
2.4.2	An example: TLS spectroscopy	88
2.4.3	Limits of the standard dispersive measurement technique	88

II	THE MEASUREMENT IN cQED	91
3	Measurement and dynamics in circuit QED	93
3.1	Predictions on the continuous weak measurement of a driven TLS	94
3.2	Experimental implementation	95
3.2.1	The sample	96
3.2.2	Measurement setup	96
3.2.3	Calibration of the resonator parameters	98
3.2.4	Choice of the working point	99
3.3	Measurement-induced dephasing	100
3.3.1	Theory of the measurement-induced dephasing	101
3.3.2	Spectroscopic observation of the AC-Stark shift and measurement-induced dephasing	109
3.3.3	Characterization in frequency of the measurement-induced dephasing	112
3.4	Continuous measurements	115
3.4.1	Theoretical predictions for the power spectrum of the detector	116
3.4.2	Implementing a continuous measurement	119
3.4.3	Comparison with theoretical predictions	124
3.4.4	Numerical simulations	126
3.4.5	From weak to strong measurement crossover: quantum trajectories	128
3.5	Non-classicality of the circuit: violation of a Bell's inequality in time	130
3.5.1	The CHSH Bell's inequality	131
3.5.2	The Leggett-Garg inequality	132
3.5.3	A Leggett-Garg inequality adapted for weak continuous measurement	133
3.5.4	Experimental test	135
3.5.5	Interpretation of the violation of the Leggett-Garg inequality	138
3.6	Characterizing the thermal fluctuations with a continuous measurement	142
3.6.1	Measuring the thermal fluctuations	143
3.6.2	Spectrum of a TLS coupled to a thermal bath	144
3.6.3	Experimental characterization of the thermal fluctuations	145
3.6.4	Analysis of the populations and the relaxation rates	146
4	High-fidelity qubit readout and non-linear circuit QED	149
4.1	Fidelity of the dispersive readout method in cQED	149
4.1.1	The standard dispersive readout method	149
4.1.2	A sample-and-hold detector for improving the readout fidelity	151
4.2	Josephson Bifurcation Amplifiers: theoretical description	152
4.2.1	The Duffing oscillator and the Josephson bifurcation amplifier	152
4.2.2	The Cavity Bifurcation Amplifier	155
4.3	Experimental implementation	159
4.3.1	The sample	159

4.3.2	Measurement setup	160
4.4	Experimental characterization of the CBA	161
4.4.1	Frequency response	161
4.4.2	Bistability and hysteresis: the $(\Omega, \beta)$ diagram	162
4.4.3	Transitions between $\bar{B}$ and $B$ : the S-curves	164
4.5	Operating the CBA for qubit readout	168
4.5.1	Mapping the qubit state to the resonator	168
4.5.2	Characterization of the qubit parameters	169
4.5.3	High fidelity readout	170
4.5.4	Is the CBA a Quantum Non Destructive (QND) detector?	175
4.5.5	Conclusions about the CBA qubit readout	178
4.6	Optimization of the CBA parameters	178
4.6.1	Study with fixed qubit frequency (sample B)	179
4.6.2	Study with variable qubit frequency (sample C)	179
4.7	Non-linear Jaynes-Cummings physics : strong coupling of a non-linear resonator and a qubit	181
4.7.1	AC-Stark shift with a non-linear resonator	182
4.7.2	Blue and red sidebands	186
4.7.3	Other features linked to the specific dynamics of non-linear oscillations	192
III	TOWARDS A MULTI-QUBIT ARCHITECTURE	195
5	Tunable resonators for coupling qubits	197
5.1	Qubit interactions mediated by a tunable resonator	197
5.2	Tuning a resonator with a SQUID	199
5.2.1	The SQUID: a tunable inductor	199
5.2.2	Resonance frequency of a $\lambda/2$ resonator containing a SQUID	200
5.2.3	Full analysis of the SQUID inductance	200
5.2.4	The linear regime	202
5.3	Implementation	202
5.3.1	Fabrication of tunable resonators	202
5.3.2	Measurement setup	203
5.4	A first tunable resonator (Sample A)	204
5.4.1	Explaining the drop of $Q$ around $\Phi_0/2$	205
5.5	A high- $Q$ tunable resonator (Sample B)	208
5.5.1	Resonance parameters versus flux	209
5.5.2	Periodicity in flux	210
5.5.3	Maximum quality factor and temperature dependence	211
6	Future directions	213
APPENDIX 219		
A	Adiabatic escape theory for CBA	221
A.1	Noise and CBA dynamics	221
A.2	The effect of noise on a driven CBA: parametric effects	221
A.3	1D equivalent: the cubic meta-potential	223

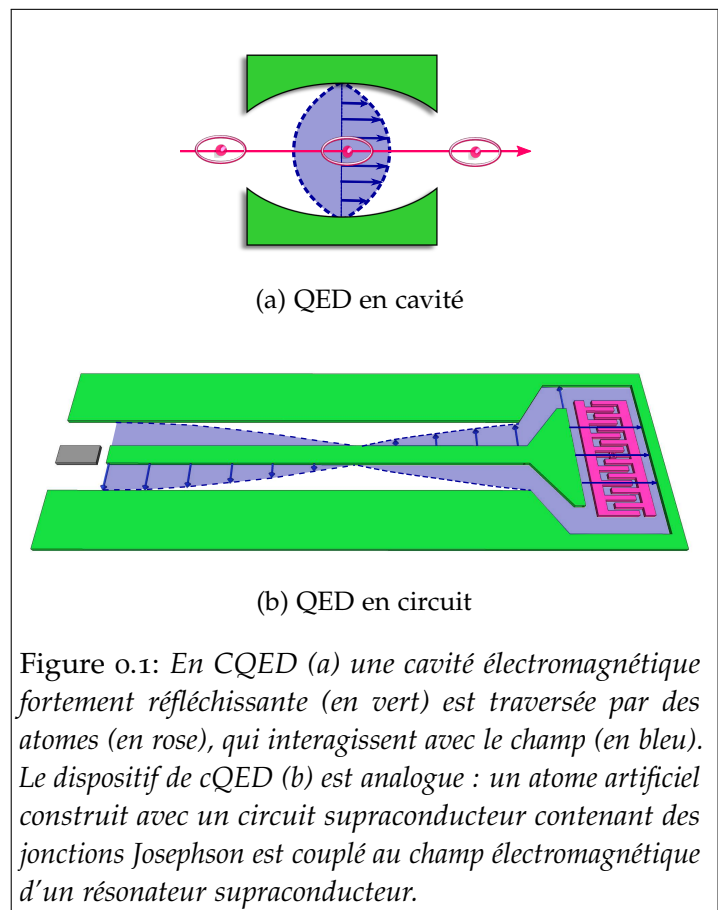
B	Table of symbols	225
B.1	Mathematical symbols	225
B.2	Quantum formalism	225
B.3	Circuit QED	226
B.4	Non-linear cQED	228
B.5	Other physical quantities	228
	Bibliography	229

## RÉSUMÉ EN FRANÇAIS

### 0.1 DES CIRCUITS ÉLECTRIQUES POUR RÉALISER DES EXPÉRIENCES DE PHYSIQUE QUANTIQUE FONDAMENTALE ET D'INFORMATION QUANTIQUE

Cette thèse présente une série d'expériences réalisées avec des atomes artificiels constitués de circuits électriques. Ces expériences ont le double but d'illustrer des questions fondamentales de la mécanique quantique et développer des composants pour un futur processeur quantique. Les expériences réalisées avec de tels systèmes quantiques artificiels ont été amorcées dans les années 1980 dans le but d'éclaircir si les variables électriques collectives avaient ou non une nature véritablement quantique. Une fois ceci établi<sup>1</sup> le domaine bénéficie de l'invention de l'ordinateur quantique<sup>2,3</sup> et de la recherche de systèmes à deux niveaux (TLS) avec des longs temps de cohérence pour former de éléments de mémoire quantiques ou Qubits. A partir de la première observation d'une dynamique cohérente dans un circuit supraconducteur simple, la boîte à paires de Cooper (CPB)<sup>4</sup>, des progrès spectaculaires ont été réalisés sur les différents types de qubits supraconducteurs<sup>5,6,7</sup> dans des groupes de recherche partout dans le monde<sup>6,8,9</sup>.

Une étape importante de ce développement à eu lieu en 2004 dans le groupe de R. Schoelkopf à Yale, qui a réussi à reproduire avec des circuit supraconducteurs<sup>10,11</sup> des expériences d'électrodynamique quantique en cavité (CQED)<sup>12,13</sup>, un champ de la physique atomique lequel étudie l'interaction d'atomes individuels avec un nombre réduit de photons stockés dans une cavité résonante (Fig. 0.1a). Par analogie, dans cette nouvelle discipline appelée électrodynamique quantique en circuit (cQED, Fig. 0.1b), l'atome est remplacé par une CPB et la cavité par un résonateur micro-ondes planaire. Ces deux disciplines permettent d'explorer l'interaction de la matière et du rayonnement à son niveau le plus fondamental. Dans le régime de couplage fort, où l'interaction entre l'atome et le champ domine tous les pro-



cessus dissipatifs, des phénomènes intéressants apparaissent : par exemple quand la résonance de la cavité est accordée à la ligne d'émission des atomes, tout photon émis par l'atome est stocké dans la cavité et réabsorbé par l'atome successivement ; l'émission spontanée devient ainsi réversible<sup>14</sup>. L'étude d'une telle dynamique cohérente entre un atome à deux niveaux et un mode du champ de la cavité (un oscillateur harmonique), permet d'explorer les aspects les plus fondamentaux de la physique quantique : comment une mesure projette-t-elle la superposition de plusieurs états sur un d'entre eux ? Comment l'état d'un système évolue tandis qu'il est observé ? Pouvons nous prouver la nature véritablement quantique d'un système à partir des mesures réalisées sur celui-ci ? Nous avons abordé ces questions dans les expériences présentées dans la Section 0.3 et décrites dans le Chapitre 3.

En ce qui concerne le traitement quantique de l'information, nous avons enrichi l'architecture cQED (Section 0.4) en opérant un circuit de lecture haute fidélité de l'état du qubit, un élément critique pour construire un ordinateur quantique efficace. Cette expérience, discutée dans la Section 0.4.1, est basée sur l'utilisation d'un résonateur non-linéaire, qui n'était pas présent en cQED standard. En plus de permettre une amélioration du système de lecture, ce nouveau circuit constitue un système idéal pour étudier l'interaction entre couplage fort et les effets non linéaires –amplification paramétrique, squeezing...– ouvrant un nouveau domaine de recherche qui pourrait être nommé cQED non-linéaire. Tous ces aspects sont décrits dans le Chapitre 4.

Finalement pour aller vers des architectures multi-qubit en cQED, nous avons opéré un circuit qui pourrait potentiellement médier les opérations entre deux qubits arbitraires : un résonateur supraconducteur accordable en fréquence. Ce dispositif est présenté dans la Section 0.4.2 et décrit dans le Chapitre 5.

## 0.2 CQED AVEC DES ATOMES ARTIFICIELS MACROSCOPIQUES

Pour la plupart des objets macroscopiques on n'observe pas de propriétés purement quantiques, telles que les superpositions d'états, Ceci est dû à l'inévitable couplage entre les différents degrés de liberté des grands objets, qui entraînent la disparition des cohérences dans des temps extrêmement courts. Cependant, dans un supraconducteur, les degrés de liberté des différents électrons ne décohèrent pas individuellement mais sont liés entre eux formant des variables collectives, telles que les tensions et les courants, qui restent cohérentes pendant des temps atteignant plusieurs  $\mu\text{s}$  s'ils sont bien isolés de l'environnement électromagnétique. Le circuit supraconducteur le plus simple, un résonateur LC, a ainsi déjà un spectre d'énergie avec des niveaux discrets équi-espacés. Pour obtenir un spectre anharmonique semblable à celui d'un atome, il est nécessaire d'introduire un élément non-linéaire et sans pertes : la jonction Josephson. Celle-ci consiste en deux électrodes supraconductrices couplées le par une fine couche d'isolant (Fig. 0.2a).

Le type particulier d'atome artificiel utilisé dans cette thèse dérive de la Boîte à paires de Cooper (CPB, voir la Fig. 0.2b), un circuit développé dans le groupe Quantronique<sup>15</sup> et qui est composé d'une jonction Josephson raccordant une électrode isolée (l'île) à un réservoir.

La CPB est caractérisée par deux échelles d'énergie : l'énergie Josephson  $E_J$  et l'énergie de charge  $E_C$ . Il a d'abord été opéré dans la limite  $E_C \gg E_J$  où l'énergie des états propres correspondent à la présence ou l'absence d'une paire de Cooper supplémentaire sur l'île. À la fin des années 1990, Nakamura et ses collègues ont réussi à observer les oscillations Rabi entre ses deux états de plus basse énergie<sup>4</sup>. Peu de temps après, le Quantronium (une CPB avec  $E_J \sim E_C$ )<sup>6,16</sup> fournissait une méthode de lecture en un coup, et permettait une nette amélioration des temps de cohérence grâce à une stratégie appelée de points de travail optimaux. Le Quantronium permet d'effectuer toutes les manipulations quantiques de base sur un TLS ainsi que de réaliser une étude approfondie de la décohérence<sup>17</sup>. Cependant à cause de son processus de fabrication complexe et sa sensibilité au bruit de charge, les circuits contenant plus d'un Quantronium se sont avérés très difficiles à opérer<sup>18</sup>. Par conséquent nous utilisons dans cette thèse, une CPB dans la la limite  $E_J \gg E_C$ , où elle devient insensible au bruit de charge. Le circuit que nous avons utilisé, le transmon<sup>9,19</sup>, mis au point à l'Université de Yale, atteint ce régime grâce à un condensateur externe qui abaisse son énergie de charge  $E_C$  et qui en même temps permet un fort couplage capacitif à l'extérieur. Ces caractéristiques se traduisent par une amélioration de la robustesse et la reproductibilité.

En cQED le transmon est couplé à un résonateur micro-ondes. L'avantage de cette configuration par rapport à la QED est que tous les éléments sont fabriqués sur la même puce : les expériences peuvent donc être effectuées sans avoir à piéger des atomes et les manipuler individuellement. En plus en cQED, le résonateur auquel le transmon est couplé est un résonateur planaire, ce qui permet d'atteindre des couplages plus fort qu'en QED en raison du confinement unidimensionnel des champs et la grande taille du circuit qui constitue l'atome artificiel<sup>20</sup>. Ceci permet d'atteindre aisément le régime de couplage fort et d'accéder à des constantes de couplage non atteignables en optique quantique. Un autre avantage important est la plus grande flexibilité dans la conception car les paramètres du circuit peuvent être déterminés au cours du processus de fabrication, contrairement à ceux d'un atome naturel où ceux-ci sont fixes.

En plus de stocker le champ qui interagit avec le TLS,

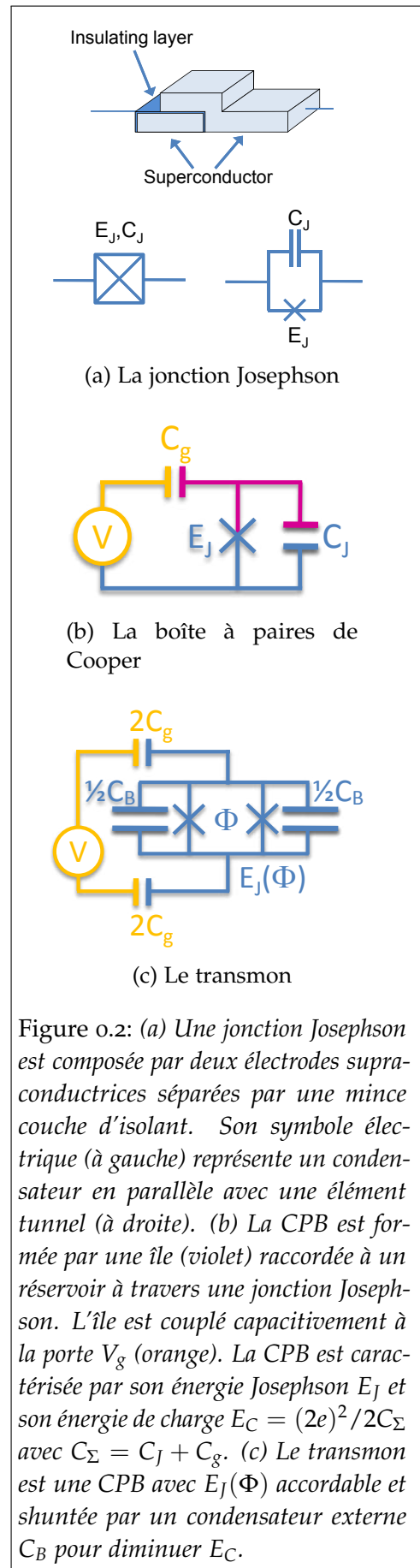


Figure 0.2: (a) Une jonction Josephson est composée par deux électrodes supraconductrices séparées par une mince couche d'isolant. Son symbole électrique (à gauche) représente un condensateur en parallèle avec une élément tunnel (à droite). (b) La CPB est formée par une île (violet) raccordée à un réservoir à travers une jonction Josephson. L'île est couplé capacitivement à la porte  $V_g$  (orange). La CPB est caractérisée par son énergie Josephson  $E_J$  et son énergie de charge  $E_C = (2e)^2 / 2C_\Sigma$  avec  $C_\Sigma = C_J + C_g$ . (c) Le transmon est une CPB avec  $E_J(\Phi)$  accordable et shuntée par un condensateur externe  $C_B$  pour diminuer  $E_C$ .



le résonateur agit également comme un filtre étroit qui isole le TLS de bruit électromagnétique de l'environnement. Selon le rapport entre la constante de couplage  $g$  et le désaccord de fréquence  $\Delta$  entre atome et résonateur, on peut distinguer deux régimes:

- Régime résonant  $g \gg \Delta$ , où le résonateur et le TLS peuvent échanger de l'énergie de façon cohérente et doivent être traités comme un système unique, une sorte de *molécule artificielle*.
- Régime dispersif  $g \ll \Delta$ , où le TLS et le résonateur ne peuvent pas échanger d'énergie, mais s'affectent l'un l'autre par des décalages de fréquence.

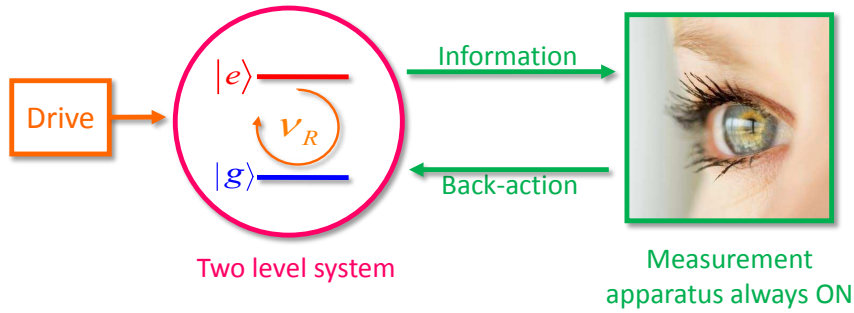
Dans le régime dispersif, le résonateur peut être utilisé comme un appareil de mesure de l'état du TLS. En effet, en fonction de l'état TLS, la fréquence du résonateur est déplacée d'une quantité  $\chi$  (appelée *cavity pull*) vers le haut ou vers le bas. Ce changement peut être détecté en envoyant une impulsion micro-ondes à l'entrée du résonateur et en mesurant la phase du signal réfléchi. La quantité d'information obtenue par cette procédure est proportionnelle au champ que cette impulsion crée à l'intérieur du résonateur. Toutes les mesures de l'état du transmon effectuées dans cette thèse sont basées sur ce principe.

D'autre part, la fréquence de transition du TLS diminue de  $2\chi n$  lorsque le résonateur contient  $n$  photons. Cet effet, appelé décalage de Stark alternatif, est utilisé dans cette thèse pour calibrer le champ à l'intérieur du résonateur. Il explique également la perturbation du TLS qu'entraîne la mesure : l'impulsion micro-ondes utilisée pour sonder le *cavity pull*, crée un champ de  $\bar{n}$  photons dans la cavité. Les fluctuations quantiques  $\delta n$  de ce champ –le bruit de grenaille– se traduisent par des fluctuations  $2\chi\delta n$  de la fréquence de transition du TLS, et ces fluctuations sont responsables d'un déphasage aléatoire dans l'état du TLS<sup>21,22</sup>. Comme le bruit de grenaille obéit à une statistique de Poisson  $\delta n \propto \bar{n}$  et donc la quantité d'information extraite et la perturbation croissent proportionnellement toutes deux à l'énergie stockée dans le résonateur.

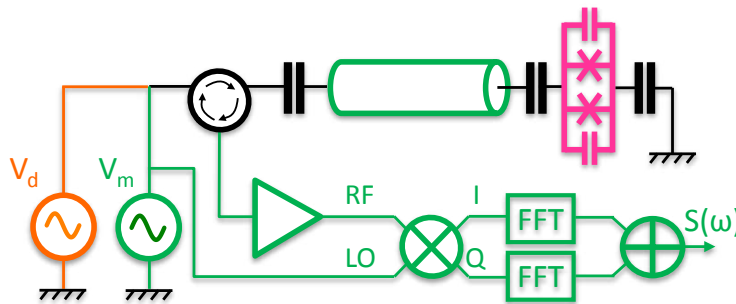
Le chapitre 2 de cette thèse contient une description en profondeur de ces concepts fondamentaux et de la mise en œuvre expérimentale du cQED.

### 0.3 MESURE ET DYNAMIQUE EN cQED

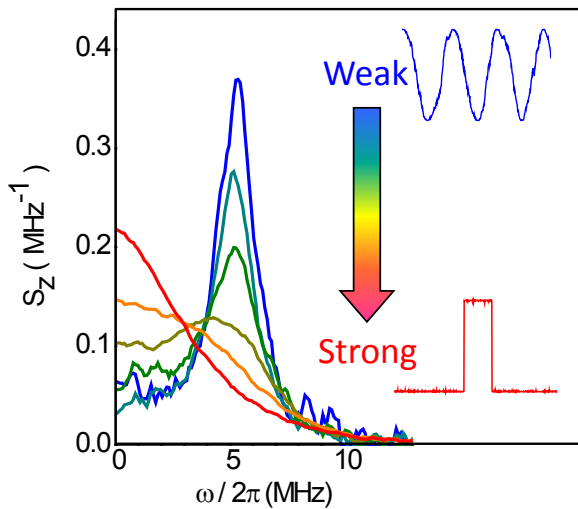
Une situation idéale pour étudier l'effet de la mesure sur la dynamique d'un système quantique est schématisée en Fig. 0.3a: un TLS piloté à sa fréquence de transition réalise des oscillations de Rabi et, en même temps, son état d'énergie est continuellement mesuré par un détecteur. Dans une telle situation le TLS est soumis à deux phénomènes concurrents: le pilotage tend à créer des superpositions des deux états propres, tandis que la mesure tend à projeter l'état du TLS sur l'un de ces deux états propres. Lorsque la mesure est comparativement faible, la dynamique du TLS n'est que légèrement perturbée et conserve son comportement oscillatoire (en bleu dans l'encart de la Fig. 0.3c). Inversement, dans le régime de mesure forte, l'information est rapidement extraite du système et ceci résulte en une projection rapide sur l'état



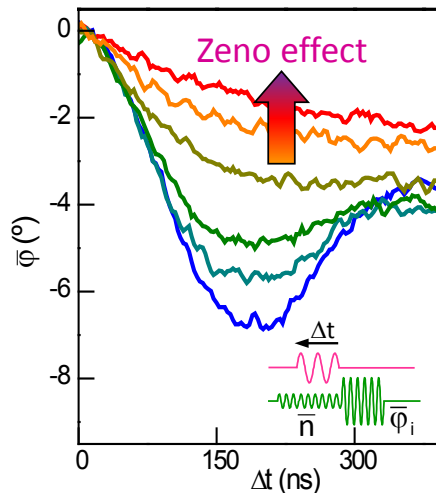
(a) Principe de l'expérience



(b) Dispositif expérimental



(c) Transition mesure faible–mesure forte



(d) Effet Zénon quantique

Figure 0.3: L'expérience de mesure continue. (a) Principe: un TLS effectue des oscillations de Rabi, tout en étant mesuré continûment par un appareil de mesure. (b) Mise en œuvre en cQED: un transmon (rose) est piloté par une source micro-ondes (orange) et couplé à un résonateur (vert). La mesure continue est effectuée en envoyant un ton micro-ondes au résonateur et en effectuant une détection homodyne du signal réfléchi. Le spectre de bruit de ce signal réfléchi permet d'accéder à la dynamique du TLS. (c) Spectres de bruit lorsque le TLS réalise des oscillations de Rabi à 5 MHz. Les courbes correspondent à une mesure faible ( $\bar{n} = 0.23$ , bleu) jusqu'à une mesure forte ( $\bar{n} = 15.6$ , rouge). Les courbes bleue et rouge esquissent les trajectoires quantiques pour les mesures faibles et fortes. (d) Oscillations de Rabi moyennées à 2.5 MHz pour différentes forces de mesure. Le ralentissement de la décroissance exponentielle qui est observé pour les plus fortes mesures est une signature de QZE.

propre du résultat mesuré, comme prévu par le postulat de la mesure. La dynamique n'est alors plus du tout cohérente, et consiste au contraire en un ensemble de sauts quantiques stochastiques entre les états propres<sup>23</sup> (en rouge dans l'encart de la Fig. 0.3c).

La transition entre ces deux régimes a été largement discutée du point de vue théorique<sup>24,25,26</sup>, mais aucun test expérimental a été réalisé avec une mésoscopique système couplé à un détecteur de mesure continue. La configuration est idéale pour cQED effectuer une telle étude parce que l'atome est fixé, permettant de réaliser en continu expériences, et parce que la force de mesure peuvent facilement être modifiées.

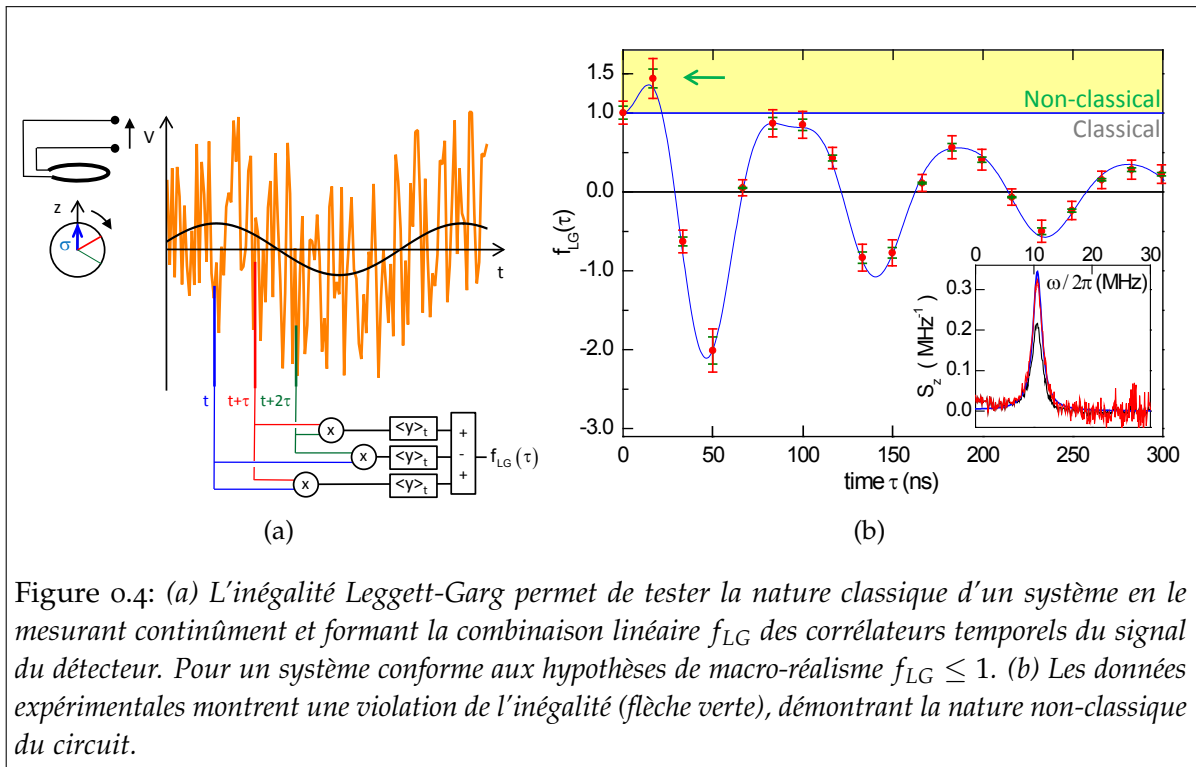
Dans le Chapitre 3 nous expliquons comment nous avons mis en œuvre une telle expérience de mesure continue en cQED (voir Fig. 0.3b) avec un transmon couplé à un résonateur qui sert de détecteur classique pour son état. Par le biais du *cavity pull*, la fréquence du résonateur suit en permanence l'état du qubit : il est toutefois impossible de suivre en permanence cette fréquence en moyennant les périodes successives de l'oscillation de Rabi, car le déphasage induit par la mesure entre celles-ci donne lieu à une moyenne nulle. Cependant, toutes l'information sur la dynamique du système reste accessible dans le spectre de bruit mesuré à la sortie du résonateur, spectre que nous acquérons en utilisant une configuration expérimentale originale.

La Fig. 0.3c montre les spectres de bruit mesurés pour différentes intensités de mesure. Lorsque la mesure est faible (courbe bleue), le spectre consiste en un pic lorentzien à la fréquence de Rabi, qui correspond à la dynamique oscillatoire du système. En augmentant la force de mesure, ce pic perd de sa hauteur et s'élargit progressivement à cause du déphasage induit par la mesure. En même temps, un pic lorentzien croît à fréquence nulle ; pic qui est une signature des sauts quantiques stochastiques qui se produisent dans le régime de mesure forte. Ces spectres de bruit constituent les premières observations quantitatives de la transition entre la mesure faible et forte dans un circuit mesuré de façon continue. Ils sont en très bon accord avec les prédictions théoriques<sup>24</sup>.

#### UN EFFET INTRINSÈQUEMENT QUANTIQUE : L'EFFET ZÉNON QUANTIQUE

Dans le régime des sauts quantiques la dynamique est progressivement gelée par la mesure : ceci constitue un effet intrinsèquement quantique connu sous le nom d'effet Zénon quantique (QZE)<sup>27,28</sup>. Nous avons observé pour la première fois une signature de cet effet dans un circuit quantique. Dans la Fig. 0.3d nous voyons comment les oscillations de Rabi effectuées sous des intensités de mesure croissantes commencent par perdre leur comportement oscillatoire (courbe bleue) pour devenir exponentielles (courbe dorée). En augmentant encore plus l'intensité de la mesure (courbes orange et rouge) le temps caractéristique de ces exponentielles augmente. Il s'agit là d'une signature de l'inhibition de la transition vers l'état excitée  $|g\rangle \rightarrow |e\rangle$  causée par des mesures fortes et continues : le QZE.

## VIOLATION DE L'INÉGALITÉ DE LEGGETT-GARG: UNE PREUVE DU CARACTÈRE NON-CLASSIQUE DU CIRCUIT



Le QZE est une première preuve du caractère quantique du TLS, mais une preuve plus forte peut être obtenue dans le régime de mesure faible en testant si les résultats des mesures sont conformes ou violent une inégalité introduite par Leggett et Garg<sup>29</sup>. Cette inégalité est dérivée de deux hypothèses qui semblent naturelles pour les objets macroscopiques:

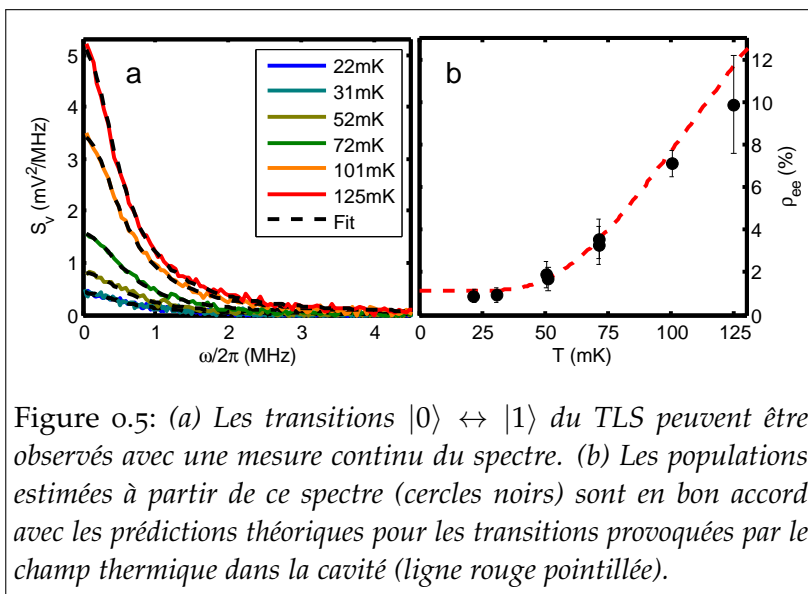
1. *Le macro-réalisme en soi*: «Un objet macroscopique qui peut être dans deux (ou plus) états macroscopiquement distincts, est à chaque moment de façon bien définie dans un de ces états.» (citation littérale de Leggett<sup>30</sup>)
2. *Mesure non invasive*: «Il est possible en principe de déterminer dans lequel de ces états se trouve le système sans affecter l'état lui-même, ni la dynamique future du système.»

A partir de ces deux hypothèses, appelés hypothèse du macro-réalisme, Leggett et Garg ont dérivé en 1985 une inégalité sur les corrélateurs temporels de mesures projectives successives effectuées sur le système. Depuis plus de 20 ans, l'inégalité a été largement discutée du point de vue théorique<sup>31,30,32,33</sup> mais n'a jamais été testée expérimentalement car les mesures projectives instantanées qu'il faudrait réaliser sont difficiles à mettre en œuvre. L'inégalité Leggett-Garg est souvent décrite comme une *inégalité de Bell en temps*, car elle implique des corrélations du signal du détecteur pris à des *moments différents*, tandis que l'inégalité de Bell CHSH<sup>34</sup> implique des corrélations entre les mesures effectuées avec une séparation spatiale.

Dans cette thèse nous décrivons l'une des premières violations expérimentales<sup>35,36</sup> de l'inégalité de Leggett-Garg dans une forme dérivée par Korotkov et ses collègues<sup>32</sup> et qui est adaptée à une mesure continue et faible de l'état du système. Dans le régime de mesure faible et pendant que le TLS est piloté, nous acquerrons un spectre de bruit du détecteur moyenné longuement (Fig. 0.4b encadré). Une unique expérience de calibration permet de redimensionner ce spectre dans ses unités naturelles, et d'en extraire les corrélateurs impliqués dans l'inégalité (Fig. 0.4b). Cette fonction de corrélation temporelle est très bon accord avec les prédictions quantiques, et dépasse la limite prévue par Leggett et Garg pour les systèmes compatibles avec le macro-réalisme. Ceci fournit une preuve forte du caractère véritablement quantique du système.

Notre violation de l'inégalité de Leggett-Garg ouvre des perspectives intéressantes. Premièrement la même inégalité peut être déduite à partir d'hypothèses très différentes liées au déterminisme<sup>37,38</sup>. Nous expliquerons dans cette thèse comment la violation de l'inégalité Leggett-Garg pourra ainsi fournir un critère fort pour exclure tout modèle de variables cachés déterministe. Nous discutons aussi comment la violation de l'inégalité peut être l'indice de l'existence d'une nouvelle ressource quantique, de la même façon que la violation de la inégalité originelle Bell démontrait l'intrication qui est utilisé aujourd'hui pour la cryptographie quantique. Plus précisément, l'excès des corrélations qui est révélé par la violation de l'inégalité de Leggett-Garg suggère que des systèmes de rétroaction quantique, consistant en l'analyse des données acquises de manière continue et à la génération d'une certaine l'action en retour sur le système pourrait être plus puissant que son analogue classique. Il permettrait ainsi par exemple, de corriger le déphasage du TLS et maintenir une oscillation de Rabi aussi longtemps que souhaité<sup>39</sup>. Toutefois, la mise en œuvre pratique de tels systèmes nécessiterait des amplificateurs travaillant à la limite quantique<sup>40,41</sup>.

## CARACTÉRISATION DES EXCITATIONS THERMIQUES DE L'ATOME ARTIFICIEL



Les mesures continues constituent également un outil utile pour caractériser les fluctuations d'état du TLS dûs au champ thermique. En effet, même aux très faibles températures d'un cryostat à dilution l'atome artificiel est souvent excité par le champ thermique présent dans son environnement. En conséquence, même en absence d'excitation extérieure, la population  $\rho_{ee}$  de l'état excité  $|e\rangle$  n'est pas nulle. Les fluctuations thermiques n'étant pas reproductibles d'une séquence expérimentale à la suivante, elles

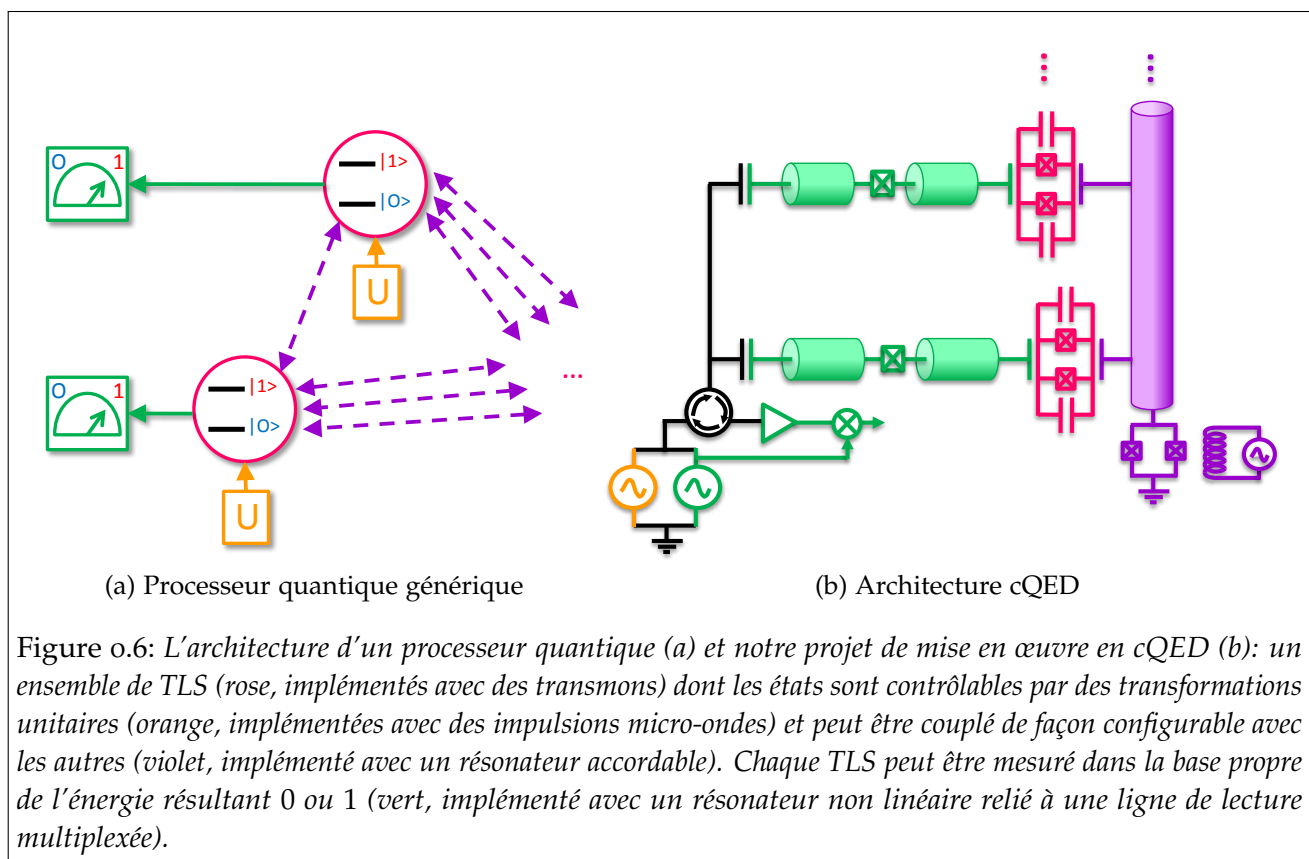
ont pour seul effet de réduire légèrement l'amplitude du signal

mesuré, réduction difficile à calibrer.

Dans le Chapitre 3, nous montrons qu'une mesure de la densité spectrale de bruit à la sortie du résonateur telle que celle réalisée pour la expériences décrites ci-dessus permet une évaluation directe de la population résiduelle due aux fluctuations thermiques (voir Fig. 0.5) et de leur taux de décroissance<sup>42</sup>.

#### 0.4 UNE ARCHITECTURE cQED POUR LE PROCESSEUR QUANTIQUE

En plus de permettre de réaliser des expériences fondamentales de physique quantique telles que celles décrites ci-dessus, la cQED fournit aussi des blocs de base pour construire des dispositifs quantiques avec une application pratique. En effet, à partir des années 1980, les caractéristiques particulières de la mécanique quantique sont exploitées pour construire des dispositifs quantiques dont les capacités vont au delà de celles de leurs homologues classiques. Un exemple est la cryptographie quantique, qui fait usage du théorème de non-clonage pour empêcher l'espionnage des communications<sup>43</sup>.



Le cQED offre une architecture prometteuse pour mettre en œuvre un autre concept, l'ordinateur quantique, qui consisterait à traiter de l'information codée dans des états quantiques<sup>3</sup>. On pourrait ainsi tirer profit du principe de superposition pour parvenir à un parallélisme massif : si une opération est effectuée sur une superposition de



tous les possibles entrées, toutes les sorties correspondantes sont obtenues en une seule étape de calcul. En 1985, Deutsch a montré que, même si la mesure finale sélectionne l'un seul des résultats, il est possible d'appliquer d'ingénieux schémas d'interférence pour obtenir la solution de certains problèmes spécifiques beaucoup plus rapidement qu'avec un ordinateur classique à la von Neumann<sup>2,44</sup>. En cQED les qubits sont fabriqués par des techniques lithographiques : il semble donc facile de construire un grand nombre d'entre eux. Cependant pour cela les systèmes de lecture et couplage entre différents qubits devraient être capables de lire et coupler un nombre croissant de qubits. Pour atteindre cette *capacité de croissance* nous avons l'intention de coupler un résonateur à chaque qubit et l'utiliser pour lire son état avec une impulsion à micro-ondes, comme expliqué ci-dessus. Ces résonateurs sont conçus avec des fréquences différentes, de sorte qu'ils puissent être adressés en utilisant une seule ligne d'entrée multiplexée en fréquence, en analogie avec ce qui est déjà fait dans des matrices de détecteurs micro-ondes à inductance cinétique (MKIDs)<sup>45</sup>. Toutefois, dans les expériences où le résonateur cQED est utilisé comme système de lecture le taux d'erreurs de lecture est considérablement plus élevée que celui nécessaire pour exécuter efficacement des algorithmes quantiques, ce qui compromet le gain de vitesse de ceux-ci. Dans cette thèse, nous montrons comment un résonateur non linéaire opéré comme amplificateur à bifurcation (JBA) peut sensiblement réduire ce taux d'erreurs.

Avec ce système de lecture faible, l'architecture que nous envisageons pour un processeur cQED est indiquée en Fig. 0.6. Elle consiste en une série de qubits, implémentés avec transmons. Chaque qubit peut être individuellement contrôlé pour réaliser des opérations unitaires, implémentées sous la forme de séquences d'impulsions résonantes similaire à celles utilisées en RMN. Chaque qubit peut également être lu individuellement grâce à un résonateur non linéaire dédié, qui est couplé à une ligne d'entrée unique multiplexée en fréquence comme celles utilisées déjà dans les expériences du Yale Qlab<sup>46</sup>. Finalement, les opérations à deux qubits peuvent être effectuées entre toute paire de qubits grâce à un résonateur accordable servant de bus de couplage<sup>47</sup>: pour médier l'interaction entre deux qubits, ce résonateur est d'abord accordé avec le premier qubit, puis, une fois que l'état de ce qubit a été transférée vers le résonateur, celui-ci est accordé avec le deuxième qubit pour effectuer l'opération.

#### 0.4.1 MESURE cQED AVEC UN DÉTECTEUR D'ÉCHANTILLONAGE ET RETENUE

Comme expliqué ci-dessus la mise en oeuvre d'un processeur quantique exige des qubits avec des temps de cohérence longs ainsi qu'un circuit de lecture permettant de caractériser l'état du qubit avec une faible probabilité d'erreur<sup>48</sup>. Un circuit de lecture idéal effectuerait une mesure projective de l'état du qubit sur demande, et lorsqu'il n'est pas sollicité sa présence ne devrait pas affecter la cohérence du qubit. Quand une mesure est effectuée sur un état  $\alpha |0\rangle + \beta |1\rangle$  elle devrait rendre 0 avec une probabilité  $|\alpha|^2$  et 1 avec une probabilité  $|\beta|^2$ . L'état du qubit à la fin de la mesure devrait, quand à lui, être  $|0\rangle$  si 0 est lu et vice versa. Deux types d'erreurs sont susceptibles d'affecter ce processus de lecture:

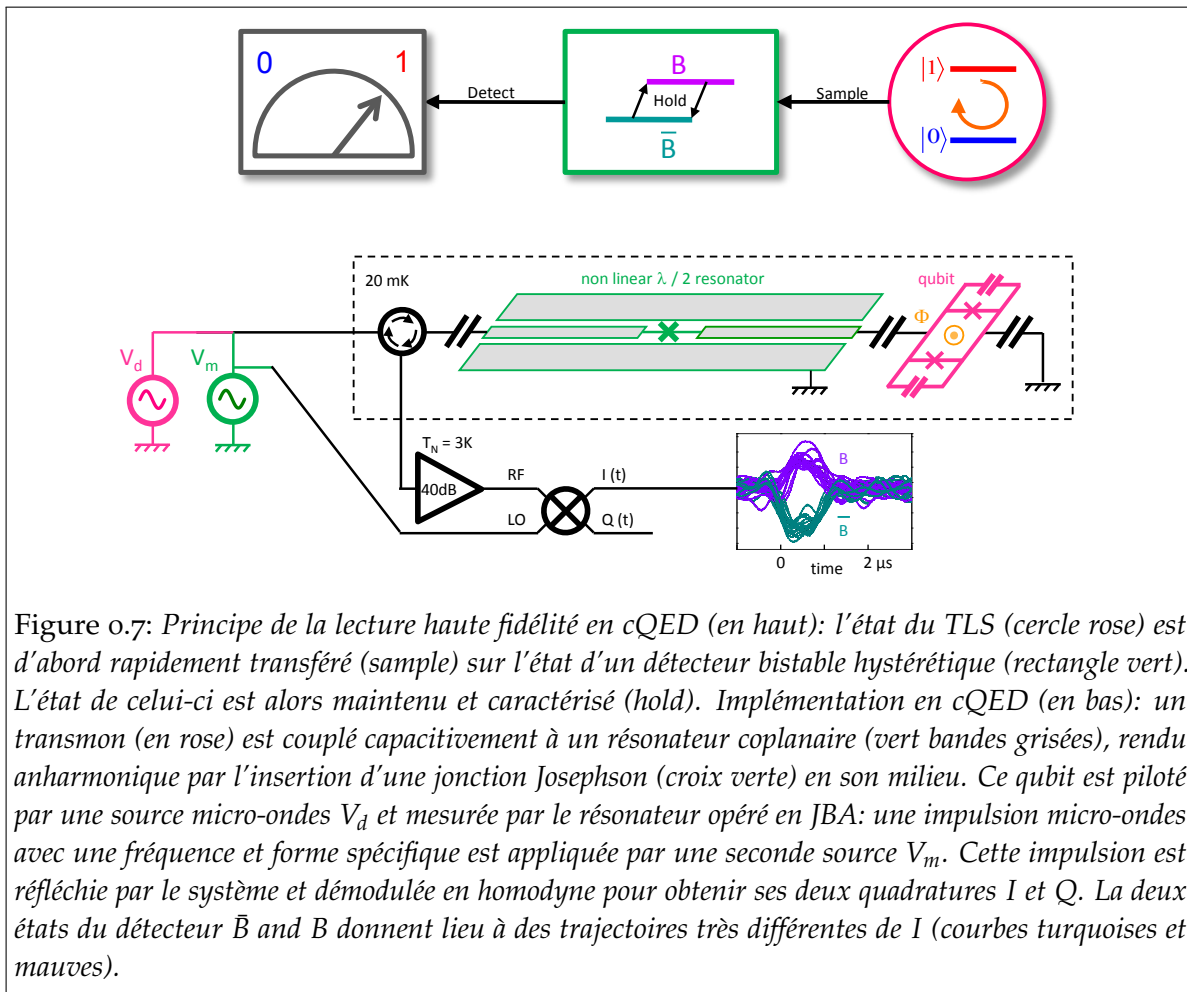


Figure 0.7: Principe de la lecture haute fidélité en cQED (en haut): l'état du TLS (cercle rose) est d'abord rapidement transféré (sample) sur l'état d'un détecteur bistable hystérétique (rectangle vert). L'état de celui-ci est alors maintenu et caractérisé (hold). Implémentation en cQED (en bas): un transmon (en rose) est couplé capacitivement à un résonateur coplanaire (vert bandes grisées), rendu anharmonique par l'insertion d'une jonction Josephson (croix verte) en son milieu. Ce qubit est piloté par une source micro-ondes  $V_d$  et mesurée par le résonateur opéré en JBA: une impulsion micro-ondes avec une fréquence et forme spécifique est appliquée par une seconde source  $V_m$ . Cette impulsion est réfléchiée par le système et démodulée en homodyne pour obtenir ses deux quadratures  $I$  et  $Q$ . La deux états du détecteur  $\bar{B}$  and  $B$  donnent lieu à des trajectoires très différentes de  $I$  (courbes turquoises et mauves).

**ERREURS DE LECTURE** Elles consistent à détecter 0 lorsque  $|1\rangle$  a été préparé avant la lecture, ou vice versa. Si la probabilité de telles erreurs est suffisamment faible, l'état du système peut être mesuré avec une séquence de lecture unique, sans avoir à moyennner sur un ensemble d'expériences avec une préparation identique. Un tel caractère de la lecture *en un coup* est hautement souhaitable pour pouvoir exécuter efficacement des algorithmes quantiques et aussi pour caractériser avec précision l'état du système, par exemple dans un test des inégalités de Bell.

**ACTION EN RETOUR SUR LE QUBIT** En l'absence d'erreur, la lecture perturbe inévitablement le qubit par la compactification de son état  $\alpha|0\rangle + \beta|1\rangle$  sur  $|0\rangle$  si 0 est lu et vice versa. Une caractéristique souhaitable est qu'aucune autre perturbation en plus de cette projection affecte l'état du qubit. Plus précisément, le processus de mesure ne devrait pas induire de relaxation supplémentaire du qubit, ou d'excitations parasites<sup>49</sup>. Un critère fort pour vérifier ceci consiste à réaliser un ensemble de lectures successives et voir si elles donnent les mêmes résultats : si c'est le cas la lecture est dite non-destructive (QND).

Dans cette thèse, nous démontrons pour la première fois la lecture haute fidélité d'un transmon en cQED architecture avec seulement 6% d'erreurs consistant à lire 0 au lieu de 1 et 2% d'erreurs dans le sens inverse. Cette lecture maintient les bonnes



propriétés de cohérence du transmon, et n'induit aucune relaxation supplémentaire du qubit au cours du processus de mesure.

### Améliorer la fidélité sans perdre les bonnes propriétés de cohérence

Dans le régime dispersif du cQED le qubit est lu en utilisant le *cavity pull*, c'est à dire, le décalage de fréquence du résonateur qui est différent selon que le qubit soit dans  $|0\rangle$  ou dans  $|1\rangle$ . La méthode de lecture dispersive standard consiste à détecter ce changement de fréquence en mesurant la phase d'une pulse réfléchi par le résonateur. A ce jour, cette méthode n'a pas permis d'atteindre une haute fidélité, car elle est confrontée deux difficultés liées: la lecture doit être réalisée dans un laps de temps beaucoup plus court que le temps  $T_1$  dans lequel le qubit relaxe de  $|1\rangle$  à  $|0\rangle$ , et ceci avec une puissance suffisamment basse pour éviter les excitations parasites. Ces deux contraintes conduisent à un rapport signal-sur-bruit (SNR) trop faible pour discriminer l'état d'un qubit avec une haute fidélité. Toutefois des progrès dans cette directions ont été réalisés très récemment<sup>50</sup>.

Dans le Chapitre 4, nous décrivons un système de lecture qui est en mesure de surmonter cette limitation en utilisant le principe d'échantillonnage et retenue (Fig. 0.7 en haut). La stratégie de ce détecteur est de séparer le processus de mesure en deux périodes : une première au cours de laquelle l'état qubit est rapidement mappé sur l'état détecteur avant de relaxer (*échantillonnage*), et une seconde au cours de laquelle l'état du détecteur est maintenu aussi longtemps que nécessaire pour pouvoir caractériser l'état dans lequel était le qubit (*retenue*). Cette stratégie nécessite un système bistable hystérétique : la bistabilité permet de faire correspondre de façon univoque les état du qubit avec les états du dispositif de mesure. L'hystérésis permet de maintenir l'état de l'appareil de mesure aussi longtemps que néces-

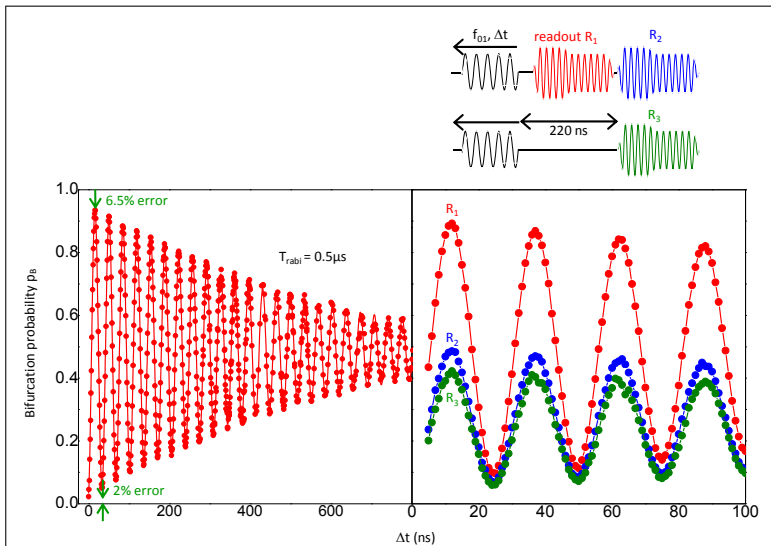


Figure 0.8: (a) Des oscillations de Rabi mesurées avec le JBA atteignent 94% de visibilité. (b) Pour tester la perturbation introduite par la lecture nous comparons le résultat de deux opérations de lecture successives (rouge et bleu) à celui de l'exécution de la seconde seule (vert). La visibilité d'une seconde lecture (en bleu) réalisée après une première lecture (en rouge) n'est pas pire que la lecture seule (en vert), ce qui montre que la lecture est potentiellement QND.

saire afin le caractériser aussi finement que voulu.

Dans notre expérience ce système bistable est implémenté en insérant une jonction Josephson au milieu du résonateur (Fig. 0.7 en bas), ce qui rend non-linéaire. En effet, quand un résonateur non linéaire est forcé à une fréquence légèrement en dessous de sa fréquence de résonance, il apparaît un phénomène de bifurcation entre deux solutions stables, caractérisées par des amplitudes différentes du champ à l'intérieur

du résonateur. Un tel résonateur non-linéaire, nommé amplificateur Josephson à bifurcation (JBA)<sup>51,52</sup>, peut être opéré comme un détecteur d'échantillonnage et retenue pour l'état du qubit pourvu que ses deux solutions soient mises en correspondance avec les états du qubit par l'exécution d'une séquence approprié d'impulsions.

De cette façon, nous avons pu observer des oscillations de Rabi avec une visibilité de 94%<sup>53</sup> (Fig. 0.8a). Cette visibilité est limitée principalement par la relaxation du qubit, qui n'est pas intrinsèque au processus de lecture. Cette haute visibilité est obtenue tout en gardant les bon temps de cohérence des qubits. En plus, aucune relaxation supplémentaire n'a été observée au cours du processus de lecture (Fig. 0.8b), ce qui suggère que ce système de lecture est potentiellement QND.

### *cQED non linéaire*

L'introduction d'un élément non-linéaire dans le résonateur de lecture modifie son comportement de façon très remarquable. Cette modification, qui nous a permis d'améliorer la fidélité de la lecture, ouvre aussi le chemin à une grande variété d'expériences qui visent à aller au delà de la portée du modèle d'interaction dispersif du cQED. Ces expériences de cQED non-linéaire pourraient devenir un nouveau terrain où sonder l'interaction entre couplage fort et phénomènes non-linéaires.

Nous avons réalisé une première série d'expériences où le TLS est utilisé comme sonde pour le champ stockée dans le résonateur. Etant donné que l'effet Stark alternatif déplace la fréquence du TLS proportionnellement à l'amplitude du champ dans résonateur, nous pouvons caractériser le champ établi dans le résonateur par une micro-onde pompe en mesurant le spectre TLS. Avec une telle technique, nous avons pu observer (Fig. 0.9) le saut de l'amplitude du champ à la bifurcation. Plusieurs autres caractéristiques intéressantes révèlent la richesse de la physique de ce système : la plus frappante est sans doute la présence de bandes latérales asymétriques autour de la fréquence de transition du transmon. Nous avons interprété ces spectres par un modèle simple lié à l'amplification paramétrique et le squeezing champ à l'intérieur du résonateur.

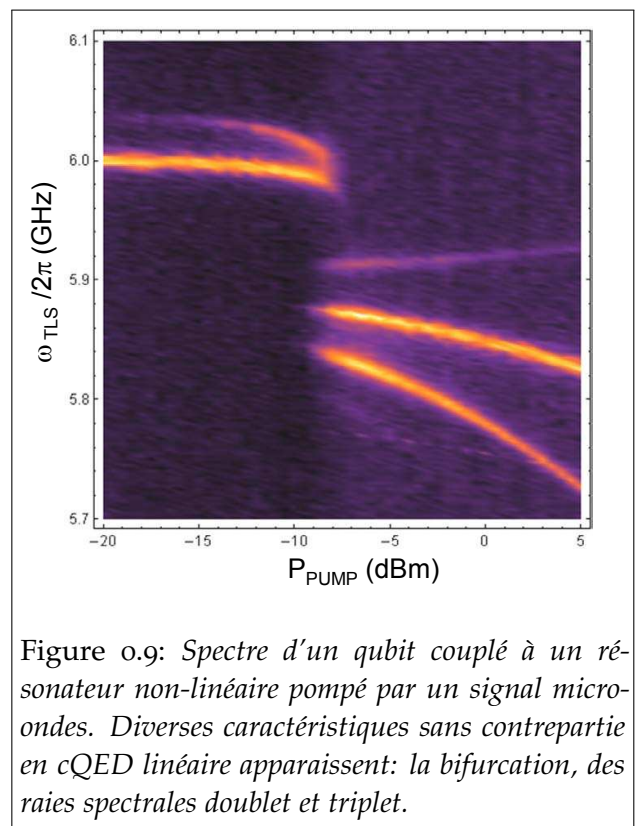
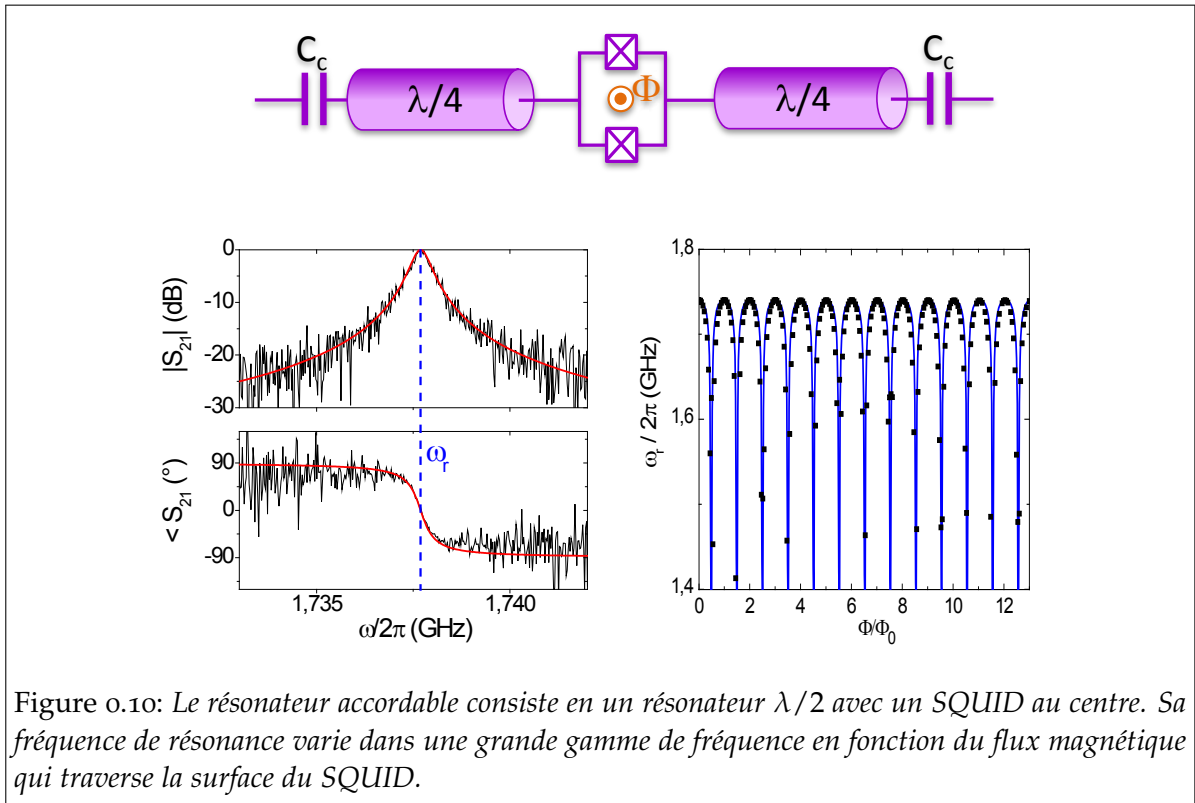


Figure 0.9: Spectre d'un qubit couplé à un résonateur non-linéaire pompé par un signal micro-ondes. Diverses caractéristiques sans contrepartie en cQED linéaire apparaissent: la bifurcation, des raies spectrales doublet et triplet.

#### 0.4.2 UN ÉLÉMENT DE COUPLAGE ACCORDABLE ENTRE QUBITS

En plus d'un circuit de lecture haute fidélité, dans notre architecture cQED nous voulons que n'importe quelle paire de qubits soit capable d'interagir pour implé-



menter une porte quantique. Idéalement cette interaction doit être configurable pour pouvoir implémenter une succession de portes quantiques. Une bonne façon de mettre en œuvre ce couplage en cQED est de coupler les différents qubits à un résonateur commun qui agit comme *bus de couplage*. Les couplages peuvent alors être activés et désactivés en réglant la fréquence de transition des qubits en résonance ou hors résonance avec le résonateur : un tel schéma a été testé expérimentalement avec succès par Silanpaa *et al.*<sup>54</sup>. L'architecture nous prévoyons, quant à nous, d'utiliser est légèrement différente<sup>47</sup>: pour garder les qubits à des points de travail fixes, nous préférons avoir un résonateur accordable qui est mis en résonance et hors résonance avec les différents qubits pour rendre les couplages effectifs. Un tel résonateur accordable devrait:

- être accordable dans la plus large gamme possible de fréquences pour être en mesure de coupler un grand nombre de qubits
- avoir aussi peu de pertes que possible pour éviter des erreurs dans les opérations à deux qubits
- être rapidement accordables pour effectuer des opérations avant que les qubits relaxent

Dans le Chapitre 5, nous décrivons comment nous avons conçu et mesuré un résonateur accordable supraconducteur contenant un SQUID en son milieu. Ce SQUID se comporte comme une inductance dont la valeur est contrôlée par le flux magnétique qui le traverse. De cette manière (Fig. 0.10), nous avons accordé la fréquence de résonance dans une gamme de 300 MHz au dessous de 1,8 GHz et nous avons mesuré

un facteur de qualité intrinsèque de  $3 \times 10^4$  sur notre meilleur échantillon<sup>55</sup>, une valeur suffisamment grande pour le faire fonctionner comme un élément de couplage, mais un ordre de grandeur plus faible que pour un résonateur supraconducteur sans SQUID.

Nous avons aussi observé une dégradation du facteur de qualité du résonateur lorsqu'il est très désaccordé par rapport à sa fréquence de résonance nue. Nous n'avons pas pu expliquer celle-ci comme un effet des valeurs typiques de bruit en flux sur le SQUID, et nous l'interprétons comme un effet de la grande non-linéarité du SQUID pour les grands désaccords, qui peut conduire à un élargissement inhomogène de la résonance en raison des fluctuations thermiques dans le résonateur. Cette dégradation semble fixer un compromis entre la plage d'accordabilité et le facteur de qualité qui pourrait être un problème pour utiliser ces résonateurs comme éléments de couplage. Le réglage rapide de la fréquence de résonance a été réalisé à l'Université de Chalmers sur un échantillon très similaire<sup>56</sup> en utilisant une ligne de flux lithographiée sur la puce afin de modifier rapidement le flux magnétique qui traverse le SQUID.

En conclusion les résonateurs supraconducteurs contenant un SQUID sont des candidats prometteurs comme bus de couplage configurable pour l'architecture cQED.



Part I

BACKGROUND

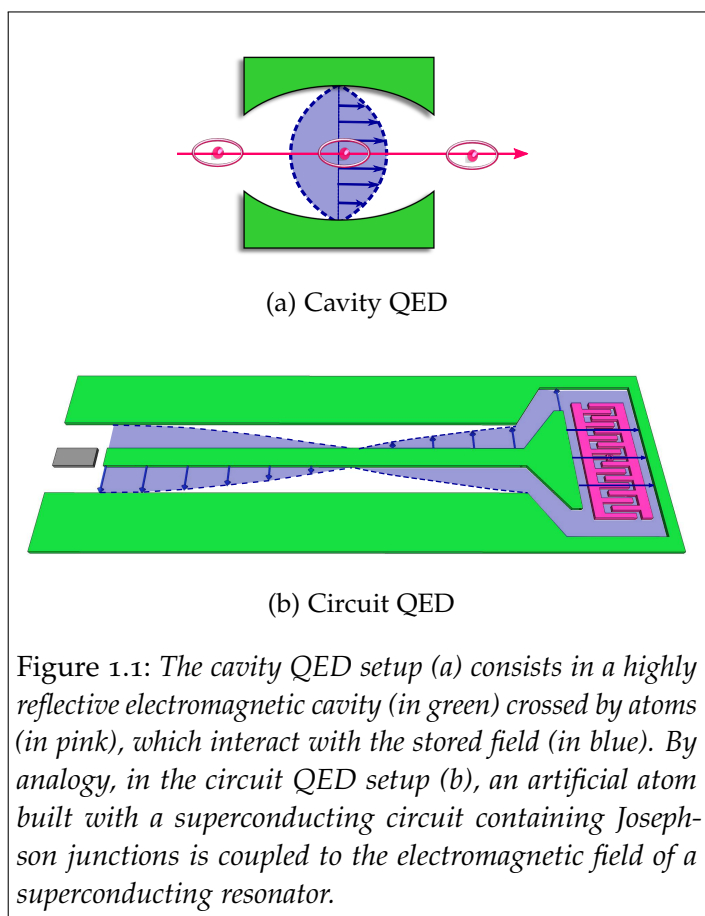


## INTRODUCTION

### 1.1 QUANTUM PHYSICS AND QUANTUM INFORMATION EXPERIMENTS WITH CIRCUITS

This thesis presents a series of experiments performed with artificial atoms consisting of superconducting electrical circuits, with the dual goal of addressing fundamental issues in quantum mechanics, and of developing building blocks for a quantum processor. Experiments using such artificial quantum systems were initiated in the 1980s in the purpose of testing the quantum nature of collective electrical variables, which was at that time under debate. This being established<sup>1</sup>, the field was then boosted by the invention of quantum computing<sup>2,3</sup> and the subsequent need of two-level systems (TLS) with long coherence times to form the quantum bits or qubits. Since the first observation of coherent dynamics in a simple superconducting circuit, the Cooper Pair Box (CPB)<sup>4</sup>, various superconducting qubit designs<sup>5,6,7</sup> were developed worldwide with spectacular progress<sup>6,8,9</sup>

An important landmark was passed in 2004 when Schoelkopf's group at Yale reproduced with superconducting circuits<sup>10,11</sup> the experiments performed in Cavity Quantum Electrodynamics (CQED)<sup>12,13</sup>, a field of atomic physics in which individual atoms interact with one or a few photons stored in a resonant cavity (Fig. 1.1a). In the superconducting circuit analog to CQED, the so-called circuit QED setup (Fig. 1.1b), the atom is replaced by a CPB and the cavity is an on-chip planar microwave resonator. Cavity and circuit QED allow to explore the light-matter interaction at its most fundamental level. In the strong coupling regime, where the atom-field interaction overwhelms dissipative processes, interesting phenomena occur: for instance, when the cavity resonance is tuned to the emission line of the atoms, any photon emitted by the atom is stored in the cavity and reabsorbed many times, so that spontaneous emission becomes





reversible<sup>14</sup>. The study of such coherent dynamics between a two-level atom and the cavity mode (a harmonic oscillator), allows to investigate fundamental aspects of quantum physics: how does a measurement project the superposition of several states on one of them? How does the state of a system evolve while being continuously observed? Can we prove the quantum nature of the system from the measurements performed on it? We have addressed those questions in the experiments introduced in Section 1.3 and described in Chapter 3.

On the quantum information side, we have enriched the proposed cQED quantum processor architecture (Section 1.4) by demonstrating a high fidelity qubit readout, a critical element for building an efficient quantum computer, as discussed in Section 1.4.1. This new circuit relies on the bistability of a non-linear resonator, which was not present in the standard cQED setup. This new circuit constitutes an ideal system to study the interplay between strong coupling and non-linear effects –parametric amplification, squeezing...– opening a new field of research that could be nicknamed *non-linear cQED*. All these aspects are described in Chapter 4.

Finally to make profit of the scalability of the number of qubits in cQED, we have operated a circuit which would potentially be able to mediate operations between two arbitrary qubits: a superconducting resonator which is tunable in frequency. Such a *tunable coupling bus* is introduced in Section 1.4.2 and described in Chapter 5.

## 1.2 CAVITY QED WITH MACROSCOPIC ARTIFICIAL ATOMS

Most of the macroscopic objects lack from purely quantum features, like state superposition, because of the unavoidable coupling between the different degrees of freedom of large bodies, which make the coherences vanish in extremely short times. In a superconductor however, the numerous degrees of freedom of single electrons do not decohere individually but are tied together forming collective variables, like voltages or currents, which remain coherent for times reaching several  $\mu\text{s}$  if they are well isolated from the electromagnetic environment. The simplest superconducting circuit, a LC resonator, already provides an energy spectrum with equally-spaced discrete levels. To obtain an atom-like anharmonic energy spectrum, a non-linear and lossless element is needed: the Josephson junction, which consists of two superconducting electrodes coupled through a thin layer of insulating material (Fig. 1.2a).

The particular artificial-atom used in this thesis is derived from the Cooper Pair Box (CPB, see Fig. 1.2b), a circuit developed in the Quantronics group<sup>15</sup> which consists of a capacitively biased Josephson junction connecting an isolated electrode (island) to a reservoir. It is characterized by two energy scales: the tunneling Josephson energy  $E_J$  and the charging energy  $E_C$ . It was initially operated in the limit  $E_C \gg E_J$  where the energy eigenstates correspond to the presence or absence of an additional Cooper Pair on the island. At the end of the 1990s Nakamura and coworkers were able to observe Rabi oscillations between its two lowest energy eigenstates<sup>4</sup>. Soon after, the Quantronium<sup>6,16</sup> (CPB with  $E_J \sim E_C$ ) provided a single-shot readout method and allowed, thanks to the so-called *optimal working point* strategy, a substantial improvement in the coherence times.

This allowed to perform all basic quantum manipulations on a TLS as well as an in depth study of its decoherence<sup>17</sup>. However the complex fabrication process and the sensitivity to charge noise hindered the operation of circuits containing more than one Quantronium<sup>18</sup>.

As a result, in this thesis we use the Cooper Pair Box in the limit  $E_J \gg E_C$ , where it becomes insensitive to charge noise. The particular circuit we used, called transmon<sup>9,19</sup> and pioneered at Yale, reaches this regime thanks to an external capacitor which is added to lower the charging energy  $E_C$ , and which at the same time provides a good capacitive coupling to the outside. All these features result in an improved robustness and reproducibility.

In cQED the transmon is coupled to an on-chip microwave resonator. The advantage of this setup compared to cavity QED is that all the elements are fabricated on chip; experiments can thus be performed without the challenging task of trapping and manipulating individual atoms. Moreover, in cQED, the resonator to which the transmon is coupled is planar, yielding stronger coupling than in CQED because of the 1D confinement of the fields and the large size of the artificial atom circuit<sup>20</sup>. This allows to easily reach the strong coupling regime and to access coupling constants unattainable in quantum optics. Another substantial advantage is the increased flexibility in the design because the circuit parameters, unlike atom ones, can be engineered during the fabrication process.

Besides storing the field which interacts with the TLS, this resonator also acts as a sharp filter, isolating the TLS from electromagnetic noise from the measuring leads. Depending on the ratio between the atom-resonator coupling constant  $g$  and their frequency detuning  $\Delta$ , two regimes can be distinguished:

- Resonant regime  $g \gg \Delta$ : the resonator and TLS are able to coherently exchange their energy and have to be treated as a single system, a kind of *artificial molecule*.
- Dispersive regime  $g \ll \Delta$ : the TLS and resonator cannot exchange energy, but affect each other via frequency shifts.

In the dispersive regime the resonator can be used as a measurement apparatus for the TLS state. Indeed, depending on the TLS state, the resonator frequency

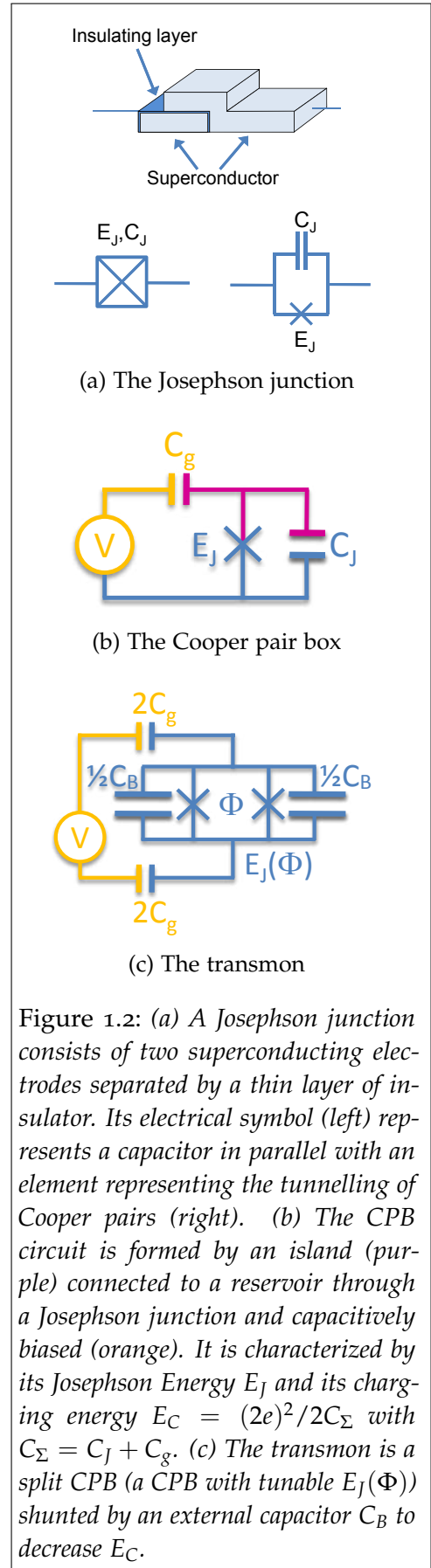


Figure 1.2: (a) A Josephson junction consists of two superconducting electrodes separated by a thin layer of insulator. Its electrical symbol (left) represents a capacitor in parallel with an element representing the tunnelling of Cooper pairs (right). (b) The CPB circuit is formed by an island (purple) connected to a reservoir through a Josephson junction and capacitively biased (orange). It is characterized by its Josephson Energy  $E_J$  and its charging energy  $E_C = (2e)^2/2C_\Sigma$  with  $C_\Sigma = C_J + C_g$ . (c) The transmon is a split CPB (a CPB with tunable  $E_J(\Phi)$ ) shunted by an external capacitor  $C_B$  to decrease  $E_C$ .

shifts up or down by an amount  $\chi$ , the *cavity pull*. This shift can be detected by sending a microwave pulse to the resonator and by measuring the phase of the reflected signal. The amount of information obtained with this procedure is proportional to the intra-resonator field created by this pulse. All the measurements of the transmon state performed in this thesis are based on detecting such cavity pull.

On the other hand, the TLS transition frequency shifts by  $2\chi n$  when the resonator contains  $n$  photons. This effect, called *AC-Stark shift*, is used in this thesis to calibrate in-situ the intra-resonator field. It also explains the perturbation of the TLS during the measurement: the microwave pulse used to probe the cavity pull, builds up a field of  $\bar{n}$  photons in the cavity. The quantum fluctuations  $\delta n$  of this field –its shot-noise– translate to a fluctuating TLS transition frequency  $2\chi\delta n$ , and results in a dephasing of the TLS state<sup>21,22</sup>. Moreover, since the shot noise is Poissonian,  $\delta n \propto \bar{n}$ , and thus the amount of extracted information and the resulting perturbation grow together with the energy stored in the resonator.

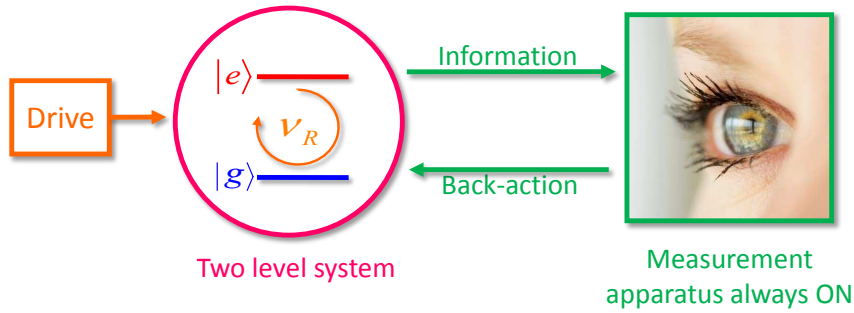
The Chapter 2 of this thesis contains an in-depth description of fundamental concepts and experimental implementation of circuit QED.

### 1.3 MEASUREMENT AND DYNAMICS IN CIRCUIT QED

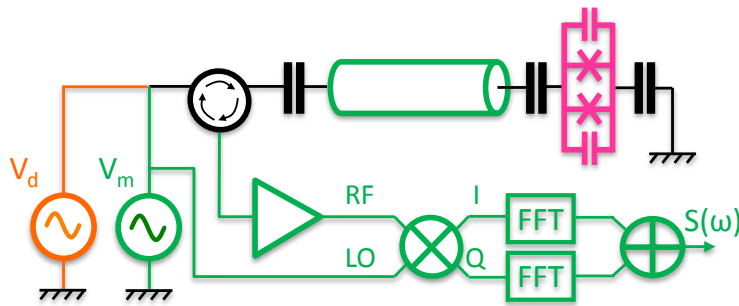
An ideal situation to study the effect of the measurement on the dynamics of a quantum system is shown in Fig. 1.3a: a TLS driven resonantly undergoes Rabi oscillations, while its energy state is being measured by a detector that is continuously active. In such a situation the system is subject to two competing phenomena: the drive tends to create superpositions of the two eigenstates, while the measurement tends to project the TLS state onto one of them. When the measurement is weak enough, the TLS dynamics is only slightly perturbed and keeps its oscillatory behaviour (blue inset of Fig. 1.3c). Conversely, in the strong measurement regime the information is quickly extracted from the system resulting in a rapid projection onto the eigenstate of the measured outcome, as expected from the measurement postulate. The dynamics is then no longer coherent and consists instead in a series of stochastic quantum jumps between the eigenstates<sup>23</sup> (red inset of Fig. 1.3c).

The crossover between these two regimes was widely discussed from a theoretical point of view<sup>24,25,26</sup> but no experimental test had been performed with a mesoscopic system coupled to a continuously measuring detector. The cQED setup is ideal to perform such a study because the atom is fixed, allowing to perform continuous experiments, and because the measurement strength can easily be varied.

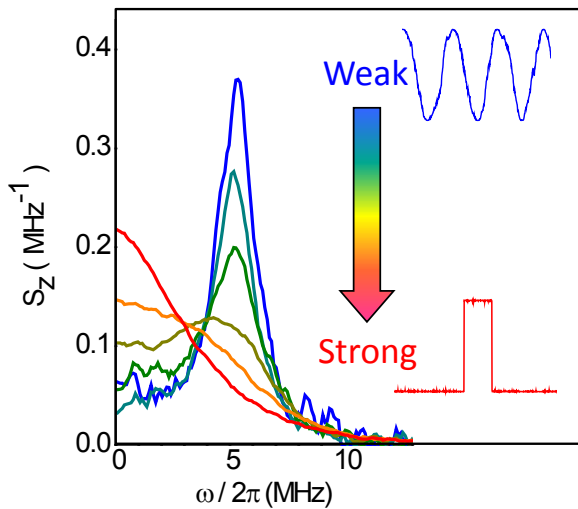
As explained in Chapter 3, we implemented such a continuous measurement experiment in the cQED setup (see Fig. 1.3b) with a transmon TLS coupled to a resonator which acts as a classical detector for the TLS state. Because of the cavity pull, the resonator frequency continuously follows the state of the qubit. To continuously monitor this frequency, we could not simply average the successive periods of the Rabi oscillation, since the dephasing between them which is induced by the measurement itself would produce a null average. However, all the information on the system dynamics is present in the noise spectrum measured at the detector output, which we acquire using a newly designed setup (in green).



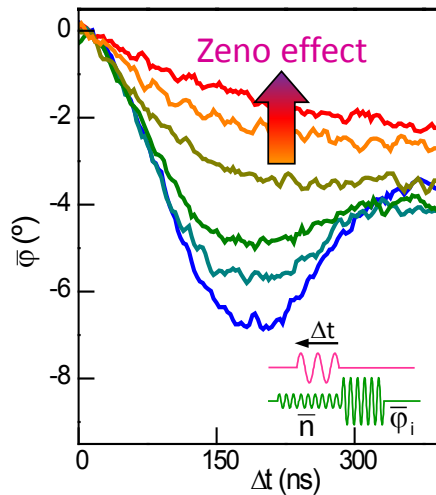
(a) Principle of the experiment



(b) Experimental setup



(c) Weak to strong measurement crossover



(d) Quantum Zeno Effect

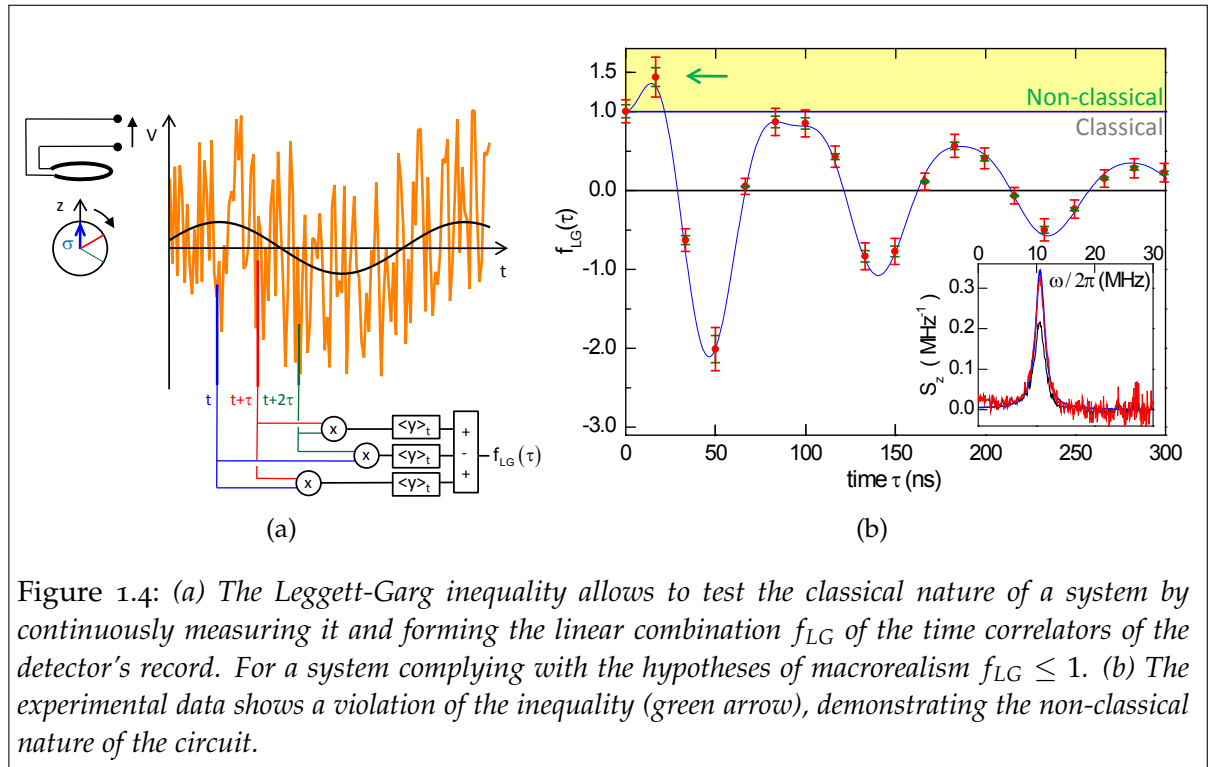
Figure 1.3: The continuous measurement experiment. (a) Principle: a driven TLS performs Rabi oscillations while being continuously monitored by a measuring apparatus. (b) Implementation in the cQED setup: a transmon TLS (pink) is driven by a microwave source (orange), and is coupled to a resonator (green). The continuous measurement is performed by sending a microwave tone to the resonator and by performing an homodyne detection of the reflected signal. The noise spectrum of this reflected signal gives access to the dynamics of the TLS. (c) Noise spectra when the TLS performing Rabi oscillations at 5 MHz. The curves range from weak measurement ( $\bar{n} = 0.23$ , blue) to strong measurement ( $\bar{n} = 15.6$ , red). Blue and red inset curves sketch the quantum trajectories for weak and strong measurements. (d) Ensemble-averaged Rabi oscillations at 2.5 MHz for different measurement strengths. The slowdown of the exponential decay which is observed for the strongest measurements is a signature of the QZE.

Fig. 1.3c shows the noise spectra measured for increasing measurement strengths. When the measurement is weak (blue curve) the spectrum shows a clear Lorentzian peak at the Rabi frequency, which corresponds to the oscillatory dynamics of the system. When increasing the measurement strength, this peak progressively decreases and broadens because of measurement-induced dephasing. At the same time, a Lorentzian at zero frequency grows, yielding the signature of the stochastic quantum jumps in the strong measurement regime. These noise spectra constitute the first quantitative observation of the transition from weak to strong measurement in a continuously measured circuit. They are in very good agreement with the theoretical predictions<sup>24</sup>.

### A GENUINE EFFECT OF QUANTUM MEASUREMENT: THE QUANTUM ZENO EFFECT

In the quantum jump regime the dynamics is progressively frozen by the measurement, a genuinely quantum effect known as Quantum Zeno Effect (QZE)<sup>27,28</sup>. We observed for the first time a signature of this effect in a quantum circuit. On Fig. 1.3d we see how Rabi oscillations performed under growing measurement strengths first lose their oscillatory behaviour (blue curve) to become exponential (golden curve). Further increases in the measurement strength (orange and red curves) increase the time constant of the decay. This is a signature of the inhibition of the  $|g\rangle \rightarrow |e\rangle$  transition caused by the strong continuous measurements as expected from QZE.

### VIOLATION OF THE LEGGETT-GARG INEQUALITY: A PROOF OF NON-CLASSICALITY





The QZE is a first evidence of the quantumness of the TLS, but a stronger proof of the genuine quantum nature of the TLS can be obtained in the weak measurement regime by testing if our measurements comply or violate an inequality introduced by Leggett and Garg<sup>29</sup>. This inequality is derived from two hypotheses which seem natural for macroscopic objects:

1. *Macrorealism per se*: “A macroscopic object, which has available to it two or more macroscopically distinct states, is at any given time in a definite one of those states.” (citing literally from Leggett<sup>30</sup>)
2. *Noninvasive measurability*: “It is possible in principle to determine which of these states the system is in without any effect on the state itself, or on the subsequent system dynamics.”

From these two hypotheses, called *macrorealism*, Leggett and Garg derived in 1985 an inequality on the time-correlators of several successive projective measurements performed on the system. For more than 20 years the inequality was widely discussed theoretically<sup>31,30,32,33</sup> but not tested experimentally because the immediate projective measurements that it requires were difficult to implement. The Leggett-Garg inequality is often described as a *Bell's inequality in time*, since it involves correlations of the detector signal taken at different *times*, while the CHSH Bell inequality<sup>34</sup> involves a correlations between measurements performed with *space* separation.

In this thesis we provide one of the first experimental violations<sup>57,35,36</sup> of the Leggett-Garg inequality in a form derived by Korotkov and coworkers<sup>32</sup> which is adapted to a continuous and weak measurement setup. In the weak measurement regime, we measure an averaged noise spectrum of the detector while the TLS is continuously driven and monitored (Fig. 1.4b inset). A single calibration experiment allows to rescale this spectrum in its natural units, and to extract the time-correlation function involved in the inequality (Fig. 1.4b). This time correlation function is in very good agreement with the quantum predictions, and exceeds the bound predicted by Leggett and Garg for *macrorealistic* systems. This gives a strong proof of the system non-classicality.

Our violation of this inequality opens interesting perspectives. First the Leggett-Garg inequality can be deduced from very different hypotheses related to determinism<sup>37,38</sup>. We explain further in this thesis how the violation of the Leggett-Garg inequality could in this way provide a strong criterion to rule out any deterministic hidden-variables models. We also discuss how the violation of the inequality could be witnessing the existence of a quantum resource, in the same spirit that the violation of the original Bell's inequality demonstrated entanglement, which is used nowadays as a quantum resource in quantum cryptography and computing. Specifically, the excess of correlations which is revealed by the violation of Leggett-Garg inequality suggests that quantum feedback schemes, consisting in analyzing the continuously acquired data and feeding back a control signal onto the system, could be more powerful than their classical analog allowing, for instance, to correct all the dephasing of the TLS and maintain non-decaying Rabi oscillations<sup>39</sup>. However, the practical implementation of such schemes require amplifiers working at the quantum limit<sup>40,41</sup>.

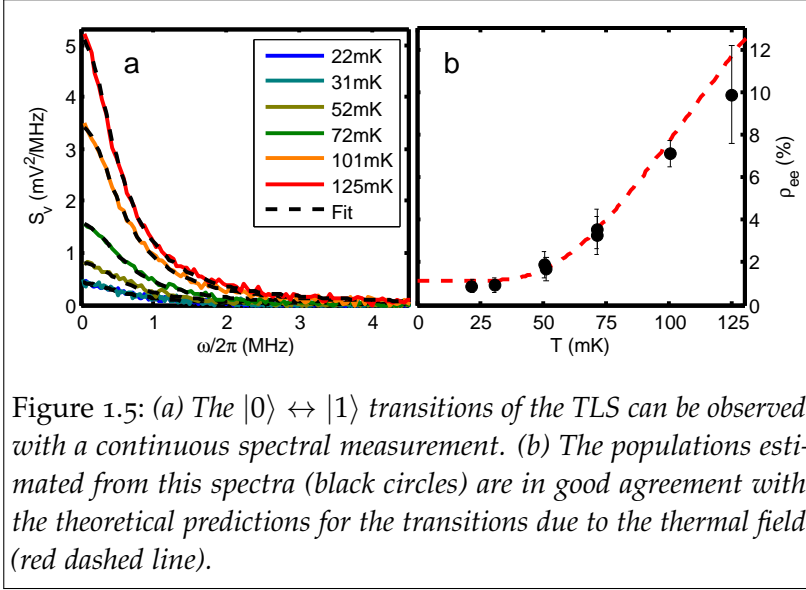


Figure 1.5: (a) The  $|0\rangle \leftrightarrow |1\rangle$  transitions of the TLS can be observed with a continuous spectral measurement. (b) The populations estimated from this spectra (black circles) are in good agreement with the theoretical predictions for the transitions due to the thermal field (red dashed line).

Continuous measurements constitute also a useful tool for characterizing fluctuations of the TLS state due to the thermal field. Indeed, even at the very low dilution cryostat temperatures the cQED artificial atom is often excited by the thermal field present in its environment. As a result, in the absence of external excitation, the population  $\rho_{ee}$  of the excited state  $|e\rangle$  is not zero. However since the thermal fluctuations are not reproducible from one experimental sequence to the next one, they only reduce the amplitude of the measured signal, which is not easy to calibrate.

In Chapter 3 we show that the noise power measurement setup built for the experiments described above allows a direct evaluation of the residual population due to those thermal fluctuations (see Fig. 1.5) and of their decay rate<sup>42</sup>.

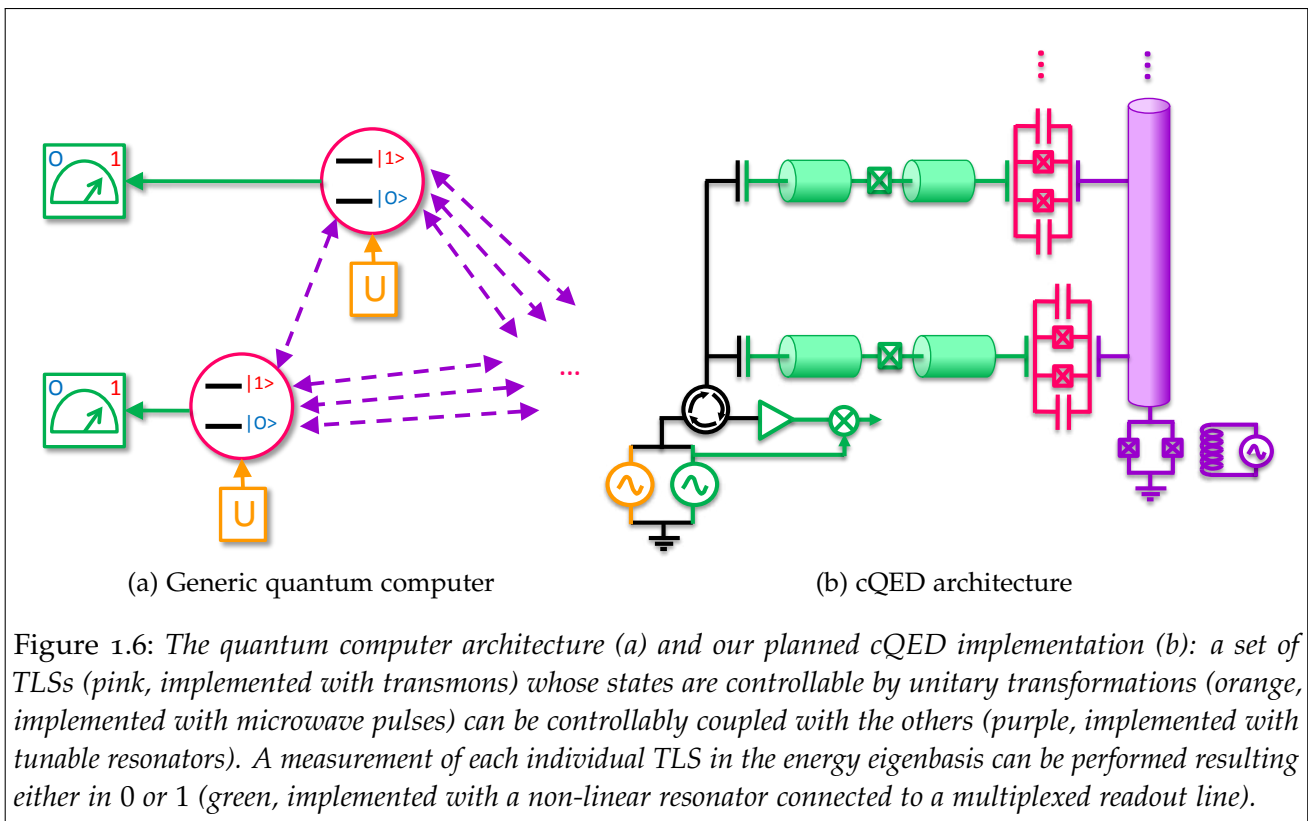
#### 1.4 CIRCUIT QED ARCHITECTURE FOR QUANTUM COMPUTING

Besides these fundamental quantum physics experiments, the circuit QED setup also provides various building blocks which can be used to design useful quantum devices. Indeed, from the 1980s, it is known that the peculiar features of quantum mechanics can be exploited to build *quantum devices* whose capabilities overcome classical ones. A successful example is *quantum cryptography*, which makes use of the *non-cloning theorem* to forbid eavesdropping on a communication channel<sup>43</sup>.

Circuit QED provides a promising architecture to implement another concept, the *quantum computer*, which would process information encoded in quantum states<sup>3</sup>. In this way it would make profit of the superposition principle to achieve a *massive parallelism*: when an operation is performed on a superposition of all the possible inputs, all the corresponding outputs are obtained in a single computational step. In 1985 Deutsch showed that, even if the final measurement selects only one of the results, it is possible to apply ingenious interference schemes to solve some specific problems substantially faster than with a classical Von Neumann computer<sup>2,44</sup>. In circuit QED the qubits are fabricated by lithographic techniques; it therefore seems easy to build a large number of them. However their readout and coupling systems should also be scalable.

To achieve this scalability for the readout, we plan to couple a resonator to each qubit and use it to readout its state with a microwave pulse, as explained above. These

resonators are designed with different frequencies, so that they can be addressed using a single input line multiplexed in frequency, in analogy to what is already done in arrays of Microwave Kinetic Inductance Detectors (MKIDs)<sup>45</sup>. However in the experiments where the cQED resonator was used as a readout system the amount of errors has been substantially higher than the one needed for efficiently running quantum algorithms, undermining the speed gains of quantum algorithms. In this thesis we demonstrate how using a *non-linear* resonator operated as a Josephson bifurcation amplifier (JBA) can substantially improve this situation.

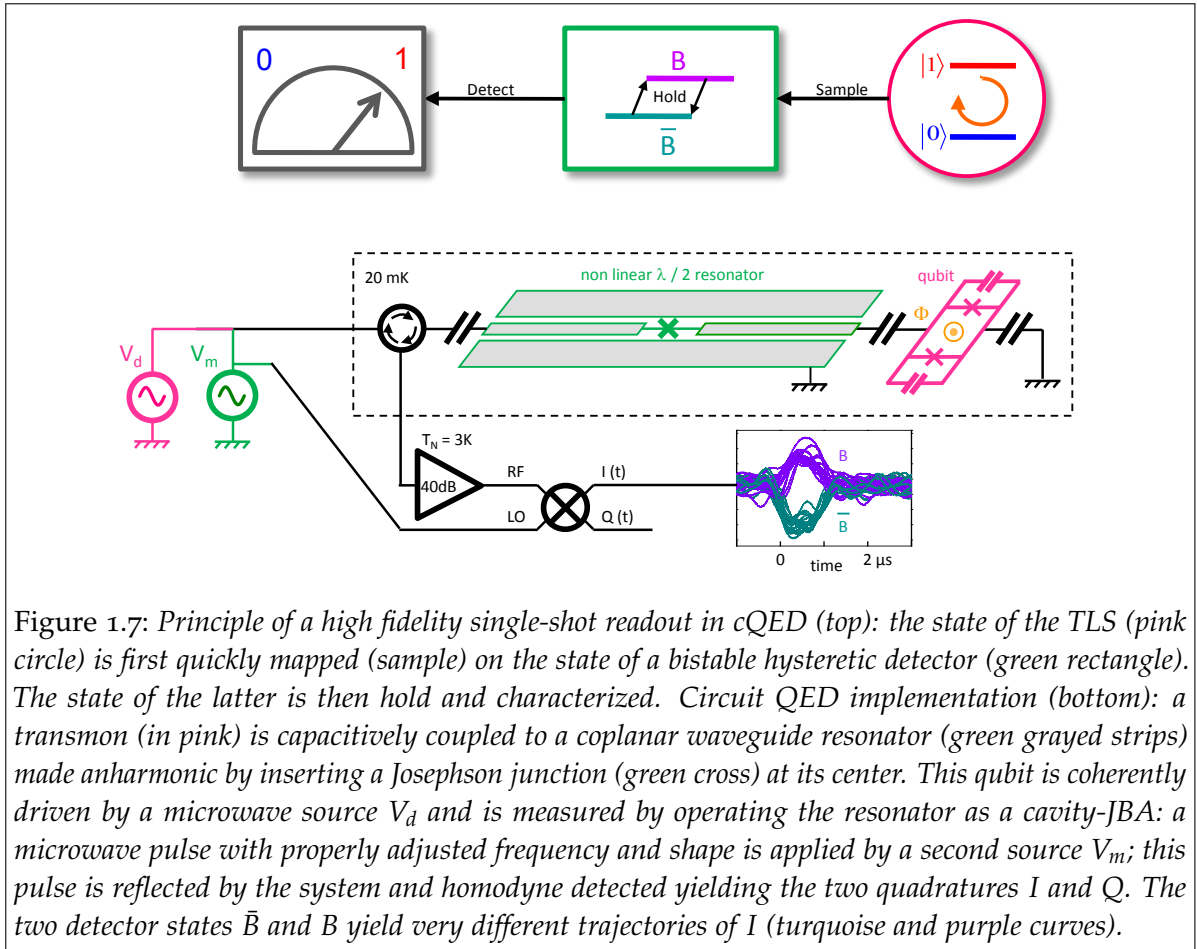


With this readout, the architecture we envision for implementing a scalable cQED processor is shown in Fig. 1.6. It consists in a set of TLS implemented with transmons, each of them encoding a qubit. Each qubit can be controlled individually by unitary operations, implemented as sequences of resonant driving pulses similar to NMR ones. Each qubit can also be individually read by a dedicated non-linear resonator, which is addressed through a single input line multiplexed in frequency as in the Yale Qlab experiments<sup>46</sup>. Finally, two-qubit operations can be performed for any pair of qubits, with a tunable resonator acting as a coupling bus<sup>47</sup>: to mediate their interaction this resonator would be first tuned with one qubit and once the qubit state has been transferred to it, it would be tuned with the second one to actually perform the operation.



### 1.4.1 SAMPLE-AND-HOLD MEASUREMENT IN cQED

As explained above a quantum processor requires qubits with long coherence times as well as a circuit able to readout the qubit state with a low probability of error<sup>48</sup>. An ideal readout circuit should perform a projective measurement of the qubit state on demand. When not being operated its presence should not affect the qubit coherence. When a measurement is performed on a state  $\alpha |0\rangle + \beta |1\rangle$  it should return 0 with probability  $|\alpha|^2$  and 1 with probability  $|\beta|^2$  and the state at the end of the measurement should be  $|0\rangle$  if 0 is measured and vice versa. Two kinds of errors could affect this readout process:



**READOUT ERRORS** They consist in detecting 0 when  $|1\rangle$  has been prepared before the readout, or vice versa. If the probability of such errors is low enough, the system state can be measured with a single readout sequence, without averaging on an ensemble of identically prepared experiments. Such a *single-shot* character of the readout is highly desirable to be able to efficiently run quantum algorithms and also to accurately characterize the system state, for instance in a test of Bell's inequalities.

**BACK-ACTION ON THE QUBIT STATE** In the absence of error the readout unavoidably perturbs the qubit by collapsing its state  $\alpha |0\rangle + \beta |1\rangle$  to  $|0\rangle$  if 0 is read and

vice versa. A desirable feature is that no other perturbation in addition to this projection affects the qubit state. Specifically, the measurement process should not induce extra relaxation of the qubit, or spurious excitations<sup>49</sup>. A strong criterion for this consists in testing if a set of successive readouts return the same result. If they do the readout is said to be *Quantum Non-Demolition* (QND).

In this thesis we demonstrate the first *high-fidelity* readout of a transmon qubit in a cQED architecture with 6% errors consisting in reading 0 instead of 1 and 2% errors in the reverse way. This readout keeps the good coherence properties of the transmon, and induces no extra relaxation of the qubit during the measurement process.

### *Improving fidelity while keeping good coherence properties*

In the dispersive regime of cQED the qubit is readout using the cavity pull, that is, the different shift of the resonator frequency in the  $|0\rangle$  and  $|1\rangle$  states. The standard dispersive readout method consists in detecting the cavity pull by measuring the phase of a microwave pulse reflected from the resonator. This method has failed up to date to achieve high-fidelity, because it faces two related difficulties: the readout has to be completed in a time much shorter than the time  $T_1$  in which the qubit relaxes from  $|1\rangle$  to  $|0\rangle$  and with a power low enough to avoid spurious qubit transitions; these two constraints lead to a signal-to-noise-ratio (SNR) which is too low to discriminate the qubit state with a high-fidelity. We note however that very recently progress has been made in this direction<sup>50</sup>.

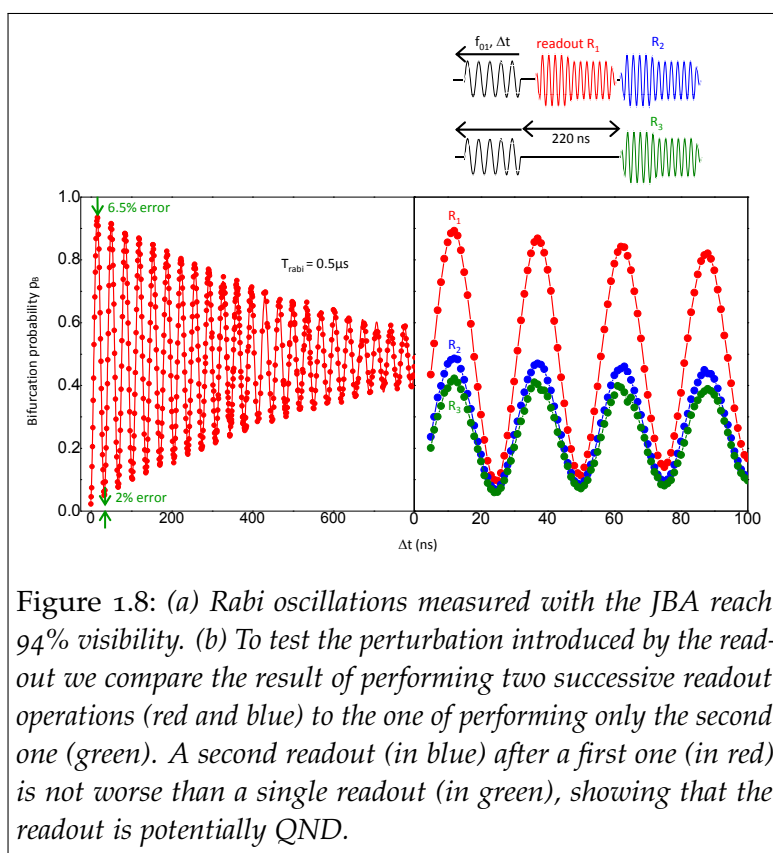


Figure 1.8: (a) Rabi oscillations measured with the JBA reach 94% visibility. (b) To test the perturbation introduced by the readout we compare the result of performing two successive readout operations (red and blue) to the one of performing only the second one (green). A second readout (in blue) after a first one (in red) is not worse than a single readout (in green), showing that the readout is potentially QND.

In Chapter 4 we describe a readout system able to overcome this limitation by using a sample-and-hold detector (Fig. 1.7 top). The strategy of this detector is to separate the measurement process in two parts: a first one during which the qubit state is quickly mapped on the detector state before it relaxes (“sample”), and a second one during which the detector state is held and probed during a time long enough to find out which was the qubit state (“hold”). This strategy requires a bistable hysteretic system. Bistability allows to unambiguously map the qubit state onto the state of the measurement device. Hysteresis allows to hold the state of the measurement device as long as needed to fully characterize it.

In our experiment this bistable system is implemented by inserting a Josephson junction in the middle of the resonator (Fig. 1.7 bottom), making it non-linear. Indeed, when a non-linear resonator is driven slightly below its resonance frequency it shows a bifurcation phenomenon between two stable solutions, characterized by different amplitudes and phases of the intra-resonator field. Such a non-linear resonator, named *Josephson Bifurcation Amplifier* (JBA)<sup>51,52</sup>, provides a sample-and-hold detector for qubit if these two solutions are put in correspondence with the qubit states by performing an appropriate set of pulses.

In such a way, we report a Rabi oscillations visibility of 94%<sup>53</sup> (Fig. 1.8a). This visibility is limited mainly by the relaxation of the qubit, which is not intrinsic to the readout process. This good visibility is achieved while keeping good coherence times for the qubits. Furthermore no extra relaxation is observed during the readout operation (Fig. 1.8b), which suggests that this readout is potentially QND.

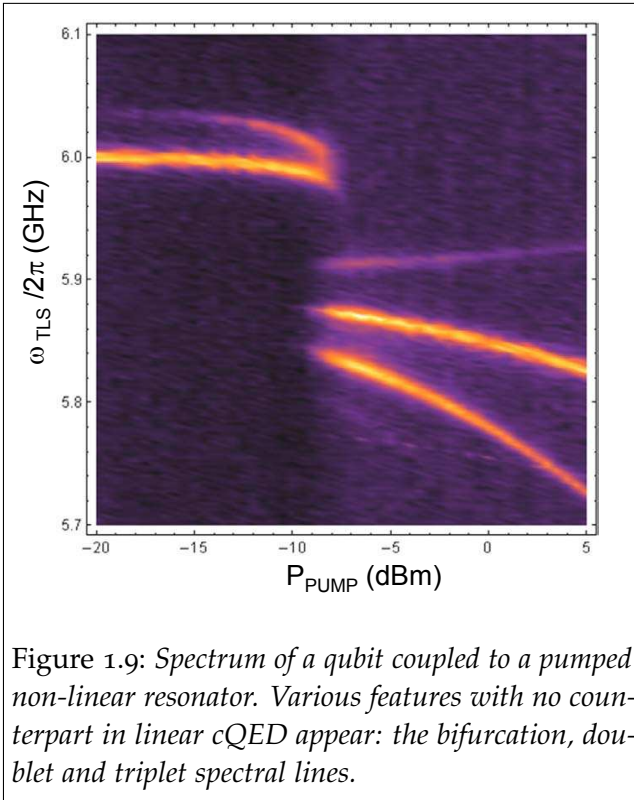


Figure 1.9: Spectrum of a qubit coupled to a pumped non-linear resonator. Various features with no counterpart in linear cQED appear: the bifurcation, doublet and triplet spectral lines.

### Non-linear cQED

The introduction of a non-linear element in the readout resonator modifies its behaviour dramatically. This modification, which allowed us to improve the readout fidelity, also opens the way to a wide variety of experiments beyond the scope of the CQED dispersive interaction model. Such *non-linear cQED* experiments might become a new playground for probing the interplay between strong coupling and non-linear phenomena.

We performed a first set of experiments in which the TLS is used as a probe for the field stored in the resonator. Since the TLS frequency is AC-Stark shifted proportionally to the amplitude of the intra-resonator field, we could characterize the intra-resonator field that result from pumping the cavity with a microwave tone by measuring the TLS spectrum. With such a technique we observed

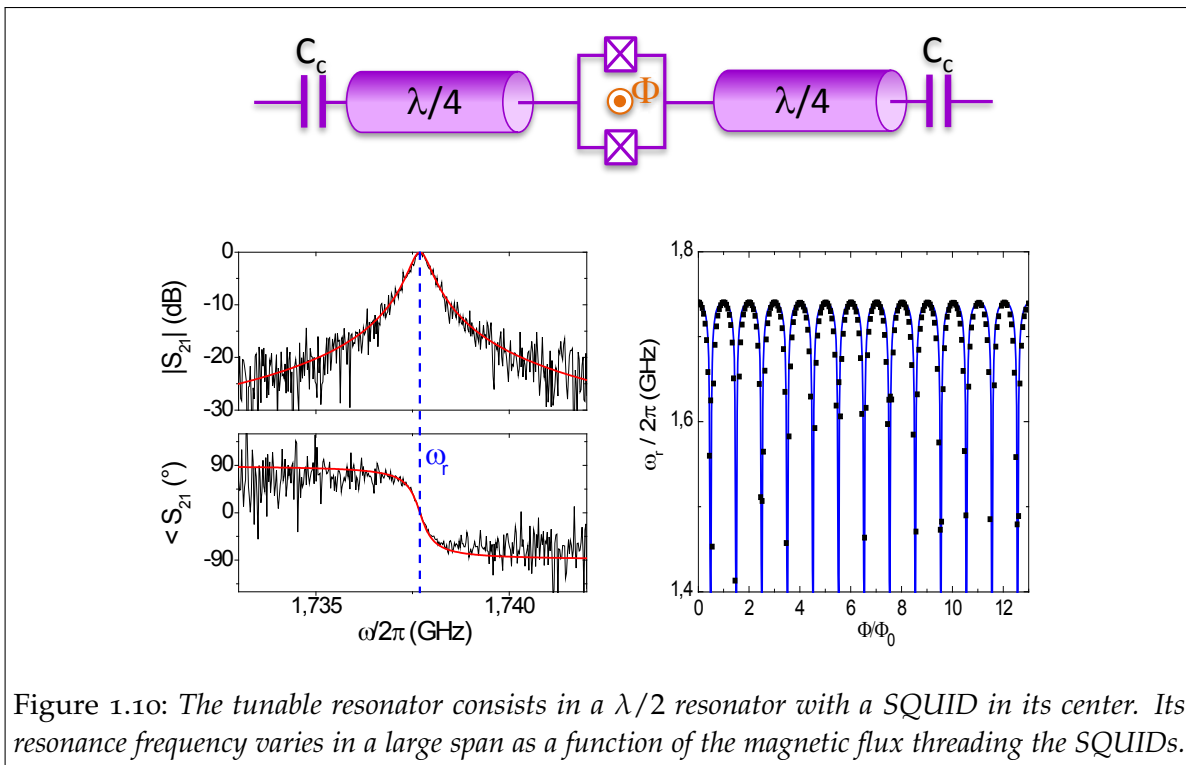
(Fig. 1.9) the sudden jump of the field amplitude at bifurcation. Several other interesting features reveal the rich physics of the system. The most striking among them is the presence of asymmetric sidebands around the transmon transition frequency. We interpreted these spectra through a simple model related to parametric amplification and squeezing of the intra-resonator field.

#### 1.4.2 A TUNABLE QUBIT COUPLER

In addition to a good readout circuit, our cQED scalable architecture requires that any pair of qubits are able to interact for implementing a *quantum gate*. Ideally such

an interaction should be configurable to implement any succession of quantum gates. A good way to implement this coupling in cQED is to couple all the qubits to a common resonator which acts as a *coupling bus*. The couplings can then be switched on and off by tuning the qubits transition frequency in or out of resonance with the resonator, as was experimentally demonstrated<sup>54</sup>. The architecture we plan to use<sup>47</sup> is slightly different: to keep the qubits at fixed working points, we want to have a tunable resonator which is brought in and out of resonance with each qubit to make the couplings effective. Such a tunable resonator should:

- be tunable in the larger possible range to be able to couple many qubits
- have as little losses as possible to avoid errors in 2-qubit operations
- be tunable as fast as possible to perform operations much faster than qubit relaxation



In the Chapter 5 we describe how we operated a tunable superconducting resonator containing a SQUID in its center. The SQUID behaves as a lumped inductance that can be tuned by the flux threading it. In this way (Fig. 1.10) we tuned the resonance frequency in a 300 MHz range below 1.8 GHz and we measured an intrinsic quality factor of  $3 \times 10^4$  on our best sample<sup>55</sup>, a value sufficiently large to operate it as a coupling element, but an order of magnitude lower than for a bare superconducting resonator.

However, when tuning the resonator far from its bare resonance frequency we observed a degradation of the quality factor, which we could not explain as an effect of the typical values of flux noise. We interpret it as an effect of the large non-linearity

of the SQUID for large detunings, which can lead to an inhomogeneous broadening of the resonance due to the thermal fluctuations of the resonator population. This degradation seems to set a compromise between the tunability range and the quality factor which could be a threat for using the resonator as a coupling element. Fast tuning of the resonance frequency was performed at Chalmers University on a very similar design<sup>56</sup> by using an on-chip flux line to quickly vary the flux threading the SQUID.

Summing up, superconducting resonators containing a SQUID as tuning element are promising candidates as configurable coupling elements for the cQED scalable architecture.

## CIRCUIT QED: THE BUILDING BLOCKS

---

The cQED architecture is composed of two basic elements : superconducting resonators and artificial atoms built with Josephson circuits. Along this chapter we present the elements of theory and the techniques which lay the framework of all the experiments described in this thesis.

We start by describing the superconducting coplanar resonators, which are used as measurement devices for the artificial atoms in the following chapters. For this purpose, a full quantum treatment of the input and output signals is introduced in Section 2.1. In Section 2.2, we study the two-level systems (TLS) which is used in our cQED experiments: the transmon. Coupling these circuits together results in the Jaynes-Cummings Hamiltonian. In Section 2.3 we discuss both the resonant regime, in which both elements can exchange energy, and the dispersive regime, in which each one induces frequency shifts on the other. This dispersive regime is central to the measurements schemes discussed in 2.4 and used in the rest of this thesis.

### 2.1 SUPERCONDUCTING RESONATORS

#### 2.1.1 HARMONIC OSCILLATORS

The Fabry-Pérot resonators used in Cavity QED<sup>58,13</sup>, the lumped-element LC resonator and the planar resonator used in circuit QED are different implementations of the same model: the harmonic oscillator. When isolated, all these physical systems behave as *photon boxes* storing the electromagnetic energy of one or several modes of the field. Although the geometrical distribution of the fields varies from system to system, one mode of any of these resonators is always described by the same Hamiltonian

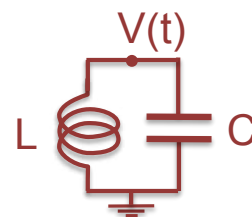
$$\hat{H} = \hbar\omega_r (\hat{n} + 1/2), \quad (2.1)$$

where  $\omega_r$  is the natural frequency of the mode and  $\hat{n}$  the operator representing the number of photons in this mode. The stationary states  $|n\rangle$ , called Fock states, represent a well-defined number  $n$  of photons in the mode –for instance the vacuum  $|0\rangle$ .

*An example: the LC resonator*

The simplest harmonic oscillator that can be built with superconducting circuits is the LC resonator, which comprises an inductance  $L$  in parallel with a capacitor  $C$ .

The formalism to analyze circuits in a full quantum way was introduced by Yurke and Denker<sup>59,60</sup>, who showed that



the circuits should be described in terms of the generalized phase  $\phi = \int_{-\infty}^t V(\tau) d\tau$  and charge  $q$  variables. For instance, the classical Lagrangian of the LC resonator is written:

$$\mathcal{L}(\phi, \dot{\phi}) = \frac{C\dot{\phi}^2}{2} - \frac{\phi^2}{2L}.$$

We first introduce the conjugate variable to  $\phi$ : the charge  $q = C \partial_t \phi$ . To quantize the circuit, we write the Hamiltonian

$$\hat{H} = \frac{\hat{q}^2}{2C} + \frac{\hat{\phi}^2}{2L}$$

where we have introduced the operators  $\hat{\phi}$  and  $\hat{q}$  corresponding to the phase and charge, which obey  $[\hat{\phi}, \hat{q}] = 2i\hbar$ .

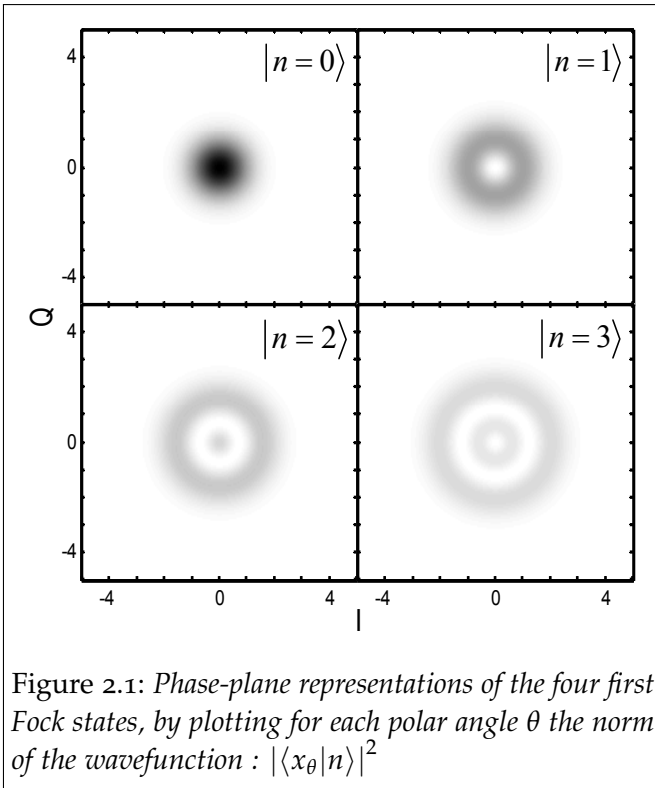


Figure 2.1: Phase-plane representations of the four first Fock states, by plotting for each polar angle  $\theta$  the norm of the wavefunction :  $|\langle x_\theta | n \rangle|^2$

In order to write this Hamiltonian in the canonical form Eq. 2.1, we define the natural pulsation  $\omega_r = 1/\sqrt{LC}$  and the characteristic impedance  $Z_c = \sqrt{L/C}$ . By introducing the annihilation operator

$$\hat{a} = (Z_c \hat{q} + i\hat{\phi}) / \sqrt{2\hbar Z_c},$$

which verifies  $[\hat{a}, \hat{a}^\dagger] = 1$ , we find

$$\hat{H} = \hbar\omega_r (\hat{a}^\dagger \hat{a} + 1/2).$$

We calculate the voltage  $\hat{V}$  across the capacitor and the current  $\hat{i}$  through the inductance in terms of the field operators:

$$\hat{V} = \frac{\hat{q}}{C} = \omega_r \sqrt{\frac{\hbar Z_c}{2}} (\hat{a}^\dagger + \hat{a})$$

$$\hat{i} = \frac{\hat{\phi}}{L} = i\omega_r \sqrt{\frac{\hbar}{2Z_c}} (\hat{a}^\dagger - \hat{a})$$

We now recall some useful results used in this thesis, which can be found in more details in quantum optics textbooks<sup>61,62</sup>. The

field statistical properties are well displayed in a phase plane representation. A first representation consists in defining for each polar angle  $\theta$  the dimensionless field quadratures:

$$\hat{X}_\theta = (\hat{a} e^{-i\theta} + \hat{a}^\dagger e^{i\theta}) / 2,$$

in function of which all the electrical variables  $\hat{q}$ ,  $\hat{\phi}$ ,  $\hat{i}$  and  $\hat{V}$  can be expressed.

Given some reference angle  $\beta$ , the orthogonal **in-phase**  $\hat{I} = \hat{X}_\beta$  and **quadrature**  $\hat{Q} = \hat{X}_{\beta+\pi/2}$  components span the *phase plane* and satisfy  $[\hat{I}, \hat{Q}] = i/2$ . These



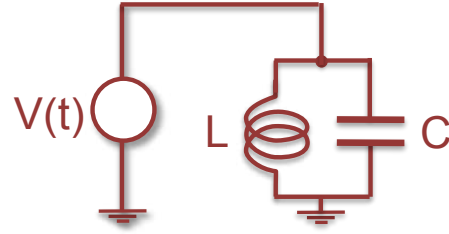
components are used further in this thesis to characterize the TLS evolution. Pure states can be represented in the phase plane by plotting radially for each polar angle  $\theta$  the square modulus of the wavefunction in the  $\hat{X}_\theta$  basis<sup>1</sup>. For instance the first four Fock states are plotted in Fig. 2.1.

### Coherent states and classical evolution

When the field is in a Fock state, the average voltage and current in the LC resonator are zero. However, when the resonator is coupled to an external classical source of voltage or current, it is excited to a state for which the average voltage and current do not vanish.

More precisely, we consider the case of the LC resonator coupled to a classical voltage source  $V(t) = V_0 \cos(\omega_r t + \varphi)$  resonant with it. This source introduces in the Hamiltonian a term

$$\begin{aligned} \hat{W}(t) &= V(t)\hat{q} \\ &\approx \frac{V_0}{2} \sqrt{\frac{\hbar Z_c}{2}} \left( e^{-i\omega_r t} e^{-i\varphi} \hat{a}^\dagger + e^{i\omega_r t} e^{i\varphi} \hat{a} \right) \end{aligned}$$



within the rotating wave approximation (RWA).

If we now move to the frame rotating at  $\omega_r$  using the unitary transformation  $\hat{U}(t) = \exp(-i\omega_r \hat{a}^\dagger \hat{a} t / \hbar)$ , the resulting term in the interaction picture is

$$\hat{W}_I = \hat{U}^\dagger \hat{W} \hat{U} = \frac{V_0}{2} \sqrt{\frac{\hbar Z_c}{2}} \left( e^{-i\varphi} \hat{a}^\dagger + e^{i\varphi} \hat{a} \right).$$

This term is time-invariant and corresponds to a time-evolution operator

$$\begin{aligned} \hat{T}(t) &= \exp(-i\hat{W}_I t / \hbar) \\ &= \exp \left[ -t V_0 \sqrt{\frac{Z_c}{8\hbar}} \left( e^{-i\varphi} \hat{a}^\dagger + e^{i\varphi} \hat{a} \right) \right] = \exp \left[ \alpha^* \hat{a}^\dagger + \alpha \hat{a} \right] = \hat{D}(\alpha) \end{aligned}$$

with  $\alpha = -e^{i\varphi} t V_0 \sqrt{Z_c / (8\hbar)}$ . Operators  $\hat{D}(\alpha)$  are displacement operators that transform the vacuum  $|0\rangle$  into the so-called **coherent states**  $|\alpha\rangle = \hat{D}(\alpha) |0\rangle$ .

Remarkably these coherent states are eigenstates of the annihilation operator  $\hat{a} |\alpha\rangle = \alpha |\alpha\rangle$ . Then, when working with coherent modes and if we neglect the quantum fluctuations, the annihilation and creation operators  $\hat{a}$  and  $\hat{a}^\dagger$  can be replaced by the continuous classical field amplitudes  $\alpha$  and  $\alpha^*$ , making the connection between the quantum and classical behaviour of the circuit. For this reason coherent states are also named *semi-classical states*.

Another interesting property is that the uncertainties of coherent states are always minimal, i.e.  $\Delta q \Delta \phi = \hbar/2$  as for the vacuum. A coherent state can thus be represented

<sup>1</sup>A more formal representation of the states is the Wigner function<sup>13</sup>



by a small uncertainty region in the phase plane. This region is centered at the expectation values of the field quadratures:

$$\begin{aligned}\langle \alpha | \hat{I} | \alpha \rangle &= \text{Re}(\alpha) \\ \langle \alpha | \hat{Q} | \alpha \rangle &= \text{Im}(\alpha).\end{aligned}$$

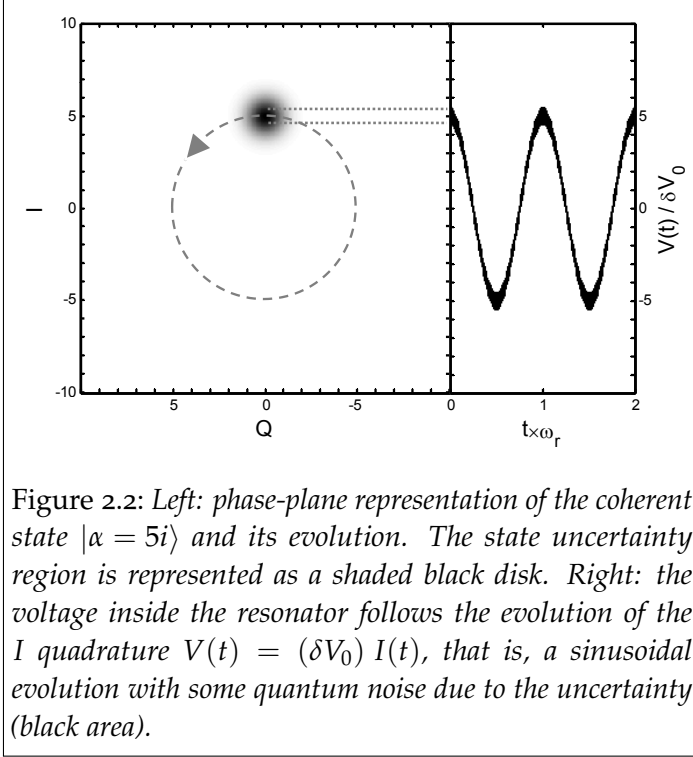


Figure 2.2: Left: phase-plane representation of the coherent state  $|\alpha = 5i\rangle$  and its evolution. The state uncertainty region is represented as a shaded black disk. Right: the voltage inside the resonator follows the evolution of the  $I$  quadrature  $V(t) = (\delta V_0) I(t)$ , that is, a sinusoidal evolution with some quantum noise due to the uncertainty (black area).

Thus, the  $\alpha$ -complex plane plays the role of the phase plane for coherent states. The uncertainty on any quadrature  $\hat{X}_\theta$  being

$$\Delta \hat{X}_\theta = 1/2,$$

the *uncertainty region* has a circular shape and a diameter  $1/2$  as shown in Fig. 2.2.

The free evolution of coherent states is given by

$$|\alpha(t)\rangle = |\alpha e^{i\omega_r t}\rangle,$$

which corresponds to a precession around the origin of the phase plane at an angular speed  $\omega_r$ , as shown in Fig. 2.2. The field quadratures, and consequently all the electrical variables have then an oscillatory behaviour at this angular frequency  $\omega_r$ .

### 2.1.1.2 TRANSMISSION-LINE RESONATORS

In our experiments we operate with signals in the microwave range. At such frequencies, the wavelength becomes comparable to circuit size and the spatial propagation of the signals becomes relevant. To take this into account in circuit theory a new circuit element is introduced: the transmission line. This element is important for our experiments in two ways. Firstly, it models all the microwave lines which we use to couple the circuits to the external measurement fields. Secondly, the cQED resonator itself is built using a section of transmission line, as explained below.

#### 2.1.1.2.1 Transmission lines

A transmission line is a longitudinal structure which supports the propagation of an electromagnetic mode. For a transverse-electromagnetic (TEM) mode each infinitesimal segment of a transmission line can be modelled by the elementary circuit shown in Fig. 2.3 where  $\ell$  and  $c$  are the inductance and capacitance per unit-length.

The analysis of this circuit is conveniently performed by defining a local phase  $\phi(x, t) = \int_{-\infty}^t V(x, \tau) d\tau$ . The voltage drop in each segment is then  $-\partial_x V(x, t) dx =$

$-\partial_x \partial_t \phi(x, t) dx$ , and the flux through the inductance  $-dx \partial_x \phi(x, t)$ . Using the constitutive relation the local current is written  $i(x, t) = -\partial_x \phi(x, t) / \ell$  yielding the Lagrangian

$$\mathcal{L} = \int dx \left[ \frac{c (\partial_t \phi)^2}{2} - \frac{(\partial_x \phi)^2}{2\ell} \right].$$

The equation of motion is the wave equation

$$\partial_t^2 \phi - \ell c \partial_x^2 \phi = 0 \quad (2.2)$$

with a propagation speed  $\bar{c} = 1/\sqrt{\ell c}$ . Fourier transforming in time, the resulting voltages and currents follow the two wave equations

$$\begin{aligned} \partial_x^2 V - \beta^2 V &= 0 \\ \partial_x^2 i - \beta^2 i &= 0, \end{aligned}$$

where  $\beta = \omega/\bar{c} = \omega\sqrt{\ell c}$ . Using those equations and the constitutive relations to link voltages and currents we find

$$\begin{aligned} V(x, \omega) &= V^+(\omega)e^{-i\beta x} + V^-(\omega)e^{i\beta x} \\ i(x, \omega) &= Z_0^{-1} \left( V^+(\omega)e^{-i\beta x} - V^-(\omega)e^{i\beta x} \right), \end{aligned}$$

where  $Z_0 = \sqrt{\ell/c}$  is the *characteristic impedance* of the line.  $V^+(\omega)$  and  $V^-(\omega)$  are the complex amplitudes of the right and left propagating microwave fields deduced from the boundary conditions. The voltage and current in the line are the superposition of these two waves.

Using  $V(x, \omega)$  and  $i(x, \omega)$ , we can now deduce the impedance  $Z_{in}(\omega)$  seen from the left of a line of length  $\Lambda$  terminated on the right by a load impedance  $Z_L = V(\Lambda, \omega)/i(\Lambda, \omega)$ :

$$Z_{in}(\omega) = \frac{V(0, \omega)}{i(0, \omega)} = Z_0 \frac{Z_L \cos(\beta\Lambda) + iZ_0 \sin(\beta\Lambda)}{Z_0 \cos(\beta\Lambda) + iZ_L \sin(\beta\Lambda)}. \quad (2.3)$$

### 2.1.2.2 Transmission-line resonators

In our experiments the resonator is built with a segment of transmission line of length  $\Lambda$  terminated with an open circuit at both sides (Fig. 2.4). We show here that this structure is equivalent to harmonic oscillator and find the physical characteristics of its resonant modes.

Since the variable conjugated to the phase is the charge density  $q = c \partial_t \phi$ , the Hamiltonian takes the form

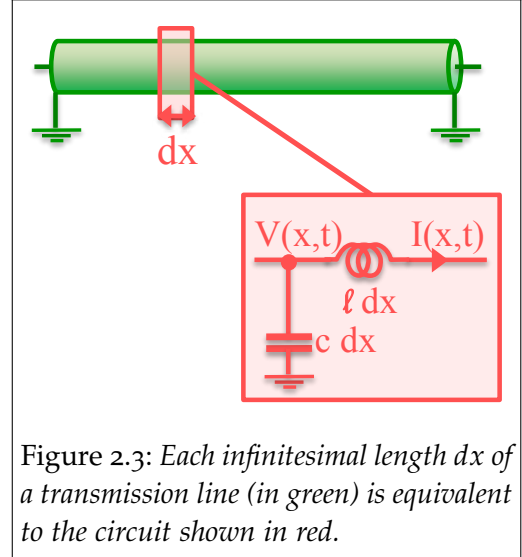


Figure 2.3: Each infinitesimal length  $dx$  of a transmission line (in green) is equivalent to the circuit shown in red.

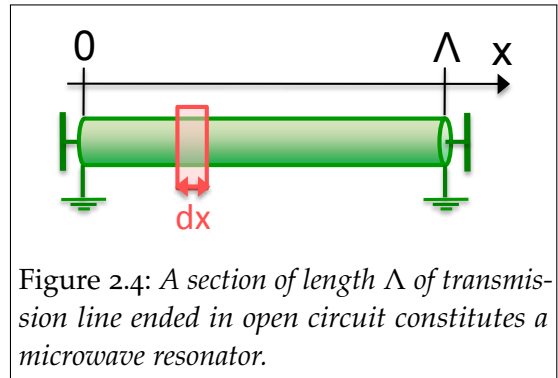


Figure 2.4: A section of length  $\Lambda$  of transmission line ended in open circuit constitutes a microwave resonator.

$$H = \int \left[ \frac{\varrho^2}{2c} + \frac{(\partial_x \phi)^2}{2\ell} \right] dx.$$

The open ends impose the boundary conditions:  $I(0,t) = I(\Lambda,t) = 0$ , and  $\partial_x \phi(0,t) = \partial_x \phi(\Lambda,t) = 0$ . Therefore, the spatial configuration of  $\phi$  and  $\varrho$  in the transmission line can be written:

$$\begin{aligned} \phi(x,t) &= \sqrt{\frac{2}{\pi k}} \sum_k \phi_k(t) \cos\left(\frac{k\pi x}{\Lambda}\right) \\ \varrho(x,t) &= \frac{\sqrt{2\pi k}}{\Lambda} \sum_k q_k(t) \cos\left(\frac{k\pi x}{\Lambda}\right), \end{aligned}$$

where each  $k$  term corresponds to a spatial mode. The pre-factors are chosen so that  $\phi_k$  and  $q_k$  represent the phase and charge of an equivalent LC resonator. In these new variables, the Hamiltonian writes:

$$H = \sum_k \frac{\pi k}{\Lambda} \left[ \frac{q_k^2}{2c} + \frac{\phi_k^2}{2\ell} \right].$$

For each  $k$  the equivalent LC resonator has  $C = c\Lambda/(\pi k)$  and  $L = \ell\Lambda/(\pi k)$ , and a resonance frequency

$$\omega_k = \frac{\pi k}{\Lambda\sqrt{\ell c}} = \frac{\pi k \bar{c}}{\Lambda}.$$

To quantize each of these LC resonators an annihilation operator

$$\hat{a}_k = \sqrt{\frac{Z_0}{2\hbar}} \hat{q}_k + i\sqrt{\frac{1}{2\hbar Z_0}} \hat{\phi}_k,$$

is introduced, satisfying  $[\hat{a}_k, \hat{a}_k^\dagger] = 1$ . Thus, the phase and the current density can be expressed by the operators

$$\begin{aligned} \hat{\phi}(x) &= -i \sum_k \sqrt{\frac{\hbar Z_0}{\pi k}} (\hat{a}_k - \hat{a}_k^\dagger) \cos\left(\frac{k\pi x}{\Lambda}\right) \\ \hat{q}(x) &= \sum_k \frac{1}{\Lambda} \sqrt{\frac{\hbar \pi k}{Z_0}} (\hat{a}_k + \hat{a}_k^\dagger) \cos\left(\frac{k\pi x}{\Lambda}\right). \end{aligned}$$

Finally the local voltages and currents inside the resonator are

$$\hat{V}(x) = \frac{\hat{q}(x)}{c} = \sum_k \omega_k \sqrt{\frac{\hbar Z_0}{\pi k}} (\hat{a}_k + \hat{a}_k^\dagger) \cos\left(\frac{k\pi x}{\Lambda}\right) \quad (2.4)$$

$$\hat{i}(x) = -\frac{\partial_x \hat{\phi}(x)}{\ell} = \sum_k -i\omega_k \sqrt{\frac{\hbar \pi k}{Z_0}} (\hat{a}_k - \hat{a}_k^\dagger) \sin\left(\frac{k\pi x}{\Lambda}\right). \quad (2.5)$$

In this thesis we use the first resonant mode  $k = 1$  with resonance frequency

$$\omega_r = \omega_1 = \frac{\pi}{\Lambda\sqrt{\ell c}} = \frac{\pi\bar{c}}{\Lambda}. \quad (2.6)$$

The two following expressions for the total capacitance and inductance of the resonator are often useful:

$$c\Lambda = \frac{\pi}{Z_0\omega_1} \quad (2.7)$$

$$\ell\Lambda = \frac{\pi Z_0}{\omega_1}. \quad (2.8)$$

### 2.1.3 PROBING THE DYNAMICS OF THE RESONATOR FROM THE OUTSIDE : INPUT-OUTPUT THEORY

To characterize the resonators, we connect them to voltage sources through transmission lines as shown in Fig. 2.5a. Such situation is naturally described in terms of input and output waves. In the classical microwave theory, each port  $i$  is associated to an input  $a_{in,i}$  and output  $a_{out,i}$  power waves<sup>63</sup> defined by

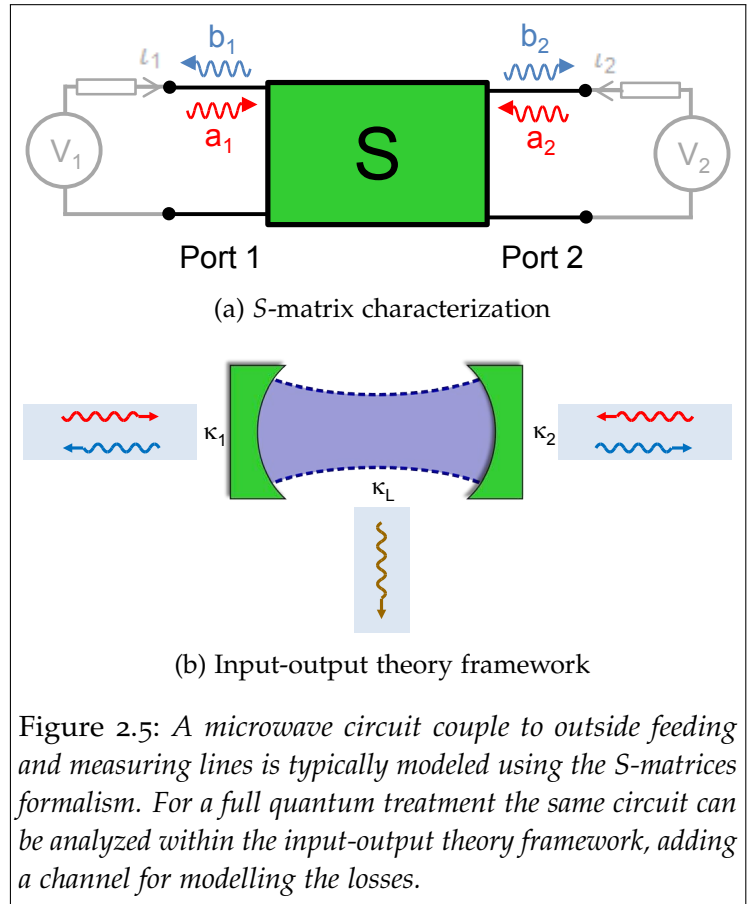
$$a_{in,i} = \frac{1}{2} \frac{V_i + Z_0 I_i}{\sqrt{\text{Re}(Z_0)}} = \frac{V_i^+}{\sqrt{\text{Re}(Z_0)}}$$

$$a_{out,i} = \frac{1}{2} \frac{V_i - Z_0^* I_i}{\sqrt{\text{Re}(Z_0)}} = \frac{V_i^-}{\sqrt{\text{Re}(Z_0)}}.$$

Thus, following a scattering-matrix approach, a linear device with  $N$  ports can be modelled as a *black box* with  $N^2$  ratios between its input and output waves which fully characterize the behaviour of the device as seen from the outside :

$$S_{ij} = \left. \frac{a_{out,i}}{a_{in,j}} \right|_{a_{k \neq j} = 0}.$$

The  $S$  matrix completely characterizes the transmission and reflexion measurements that can be performed on a resonator in the classical regime. However, in this thesis we investigate the quantum dynamics of a resonator coupled to an artificial atom circuit,



and also the quantum back-action of the measurement. We therefore need a theoretical framework providing a quantum counterpart of the scattering matrix formalism. This full quantum treatment is provided by the input-output theory developed by Gardiner and Collett<sup>64,65</sup>. This theory deals with the very general situation showed in Fig. 2.5b in which a quantum system described by its Hamiltonian  $\hat{H}$  is coupled to a set external fields with coupling strengths  $\kappa_i$ .

We will now apply it to the case of a resonator coupled through a single port, following the treatment by Milburn and Walls<sup>62</sup>. The field in the transmission line contains a continuum of modes, and thus is described as a bath with creation and annihilation operators which satisfy the standard boson commutation relation  $[\hat{b}^\dagger(\omega), \hat{b}(\omega')] = \delta(\omega - \omega')$ . In the rotating wave approximation, the linear coupling between the external and internal modes is described by the Hamiltonian

$$\hat{H}_C = \int d\omega \sqrt{\frac{\kappa_1}{2\pi}} \left[ \hat{b}(\omega) \hat{a}^\dagger - \hat{a} \hat{b}^\dagger(\omega) \right].$$

The Heisenberg equation of motion for the bath is thus

$$\partial_t \hat{b}(\omega) = -i\omega \hat{b}(\omega) + \sqrt{\kappa_1/2\pi} \hat{a}. \quad (2.9)$$

We can solve it by imposing an *initial condition*  $\hat{b}_0(\omega)$  at time  $t_0 < t$ , a situation which corresponds to sending an incoming wave to the resonator, the field operator for this incoming field is

$$\hat{a}_{in}(t) = \frac{-1}{\sqrt{2\pi}} \int e^{-i\omega(t-t_0)} \hat{b}_0(\omega) d\omega.$$

Physically this *input field* is of the same nature as the *input waves*  $V^+$  considered above. The equation of motion of the intra-resonator field  $\hat{a}$  can be written in terms of these input fields and results in

$$\partial_t \hat{a}(t) = \frac{[\hat{a}(t), \hat{H}]}{i\hbar} - \frac{\kappa_1}{2} \hat{a}(t) + \sqrt{\kappa_1} \hat{a}_{in}(t) \quad (2.10)$$

where  $\hat{H}$  is the Hamiltonian of the resonator. This equation has the form of a Langevin equation for the damped intra-resonator field with a noise term brought by the input field.

Instead of solving Eq. 2.9 with an initial condition, we can impose a *final condition*  $\hat{b}_1(\omega)$  at time  $t_1 > t$ , it corresponds to getting an output wave from the resonator, and the corresponding field operator is

$$\hat{a}_{out}(t) = \frac{1}{\sqrt{2\pi}} \int e^{-i\omega(t-t_1)} \hat{b}_1(\omega) d\omega.$$

Using again the equation of motion of the intra-resonator field with this final condition and inverted time, the relation between the input, output, and intra-resonator fields is found to be

$$\hat{a}_{out}(t) + \hat{a}_{in}(t) = \sqrt{\kappa_1} \hat{a}(t). \quad (2.11)$$

In our experiments the resonator is often coupled to more than one external field. For these cases, the analysis performed above can be trivially extended for several external fields, characterized by their input and output field operators  $\hat{a}_{in,i}$  and  $\hat{a}_{out,i}$ . Specifically, the equation Eq. 2.10 becomes

$$\partial_t \hat{a}(t) = \frac{[\hat{a}(t), \hat{H}]}{i\hbar} - \left( \sum_i \frac{\kappa_i}{2} \right) \hat{a}(t) + \sum_i \sqrt{\kappa_i} \hat{a}_{in,i}(t) \quad (2.12)$$

and the equation Eq. 2.13 becomes for each port  $i$ :

$$\hat{a}_{out,i}(t) + \hat{a}_{in,i}(t) = \sqrt{\kappa_i} \hat{a}(t). \quad (2.13)$$

The input and output fields can be represented in the phase-plane, in the same way as the intra-resonator field, with the components:

$$\begin{aligned} \hat{I}_{out} &= 1/2 \left( \hat{a}_{out}^\dagger + \hat{a}_{out} \right) \\ \hat{Q}_{out} &= i/2 \left( \hat{a}_{out}^\dagger - \hat{a}_{out} \right). \end{aligned}$$

### 2.1.3.1 Modelling the losses

The superconducting resonators we use are not ideal: even when they are not connected to any external fields, the energy which is stored is progressively lost due to various mechanisms which will be discussed in 2.1.5. A very natural way to model these losses is to represent them as an additional virtual port  $L$  that brings no excitation  $\hat{a}_{in,L} = 0$ , but adds another damping term to Eq. 2.12. The coupling constant  $\kappa_L$  represents in this case the damping of the energy in the isolated resonator. This damping can also be expressed in the form of a quality factor  $Q_L = \omega_r / \kappa_L$ .

### 2.1.3.2 Measurements

Before using them in circuit QED experiments, resonators need to be characterized by classical microwave reflexion or transmission measurements. We want here to derive a few simple formulas yielding the reflexion and transmission coefficients of a resonator. For that we will use the input-output relations Eq. 2.12 and Eq. 2.13 with classical fields, that is, replacing creation and annihilation operators by the complex amplitudes  $\alpha_{in,out}$  of the coherent fields used to probe the resonator at frequency  $\omega$ . These complex amplitudes  $\alpha_{in,out}$  are directly related to the input and output microwave powers by

$$P_{in,out} = \hbar\omega |\alpha_{in,out}|^2.$$

We will consider in this thesis one-port resonators measured in reflexion and two-port resonators measured in transmission.

### Reflexion measurements

The resonator is coupled to the measuring line with a coupling constant  $\kappa_1 = \kappa$ , and it has internal losses  $\kappa_L$ . Introducing the harmonic oscillator Hamiltonian in Eq. 2.12 and considering a single port and losses, we obtain

$$\dot{\alpha}(t) = -i\omega_r\alpha(t) - \left(\frac{\kappa + \kappa_L}{2}\right)\alpha(t) + \sqrt{\kappa}\alpha_{in,1}(t),$$

and by Fourier transform

$$\alpha(\omega) = \underbrace{\left[ \frac{2\sqrt{\kappa}}{(\kappa + \kappa_L) - 2i(\omega - \omega_r)} \right]}_{\zeta(\omega)} \alpha_{in,1}(\omega). \quad (2.14)$$

The square modulus of  $\zeta(\omega)$  has a Lorentzian shape as shown in Fig. 2.6a, with a width determined by the total damping  $\kappa + \kappa_L$ . The average photon number in the resonator is thus

$$\bar{n} = \frac{4\kappa}{\hbar\omega_r(\kappa + \kappa_L)^2} P_{in}, \quad (2.15)$$

and the phase undergoes a phase shift of  $\pi$  when crossing resonance as shown in Fig. 2.6a.

Using Eq. 2.13 we find the reflected field:

$$\alpha_{out}(\omega) = \underbrace{\left[ \frac{(\kappa - \kappa_L) + 2i(\omega - \omega_r)}{(\kappa + \kappa_L) - 2i(\omega - \omega_r)} \right]}_{\rho(\omega)} \alpha_{in}(\omega), \quad (2.16)$$

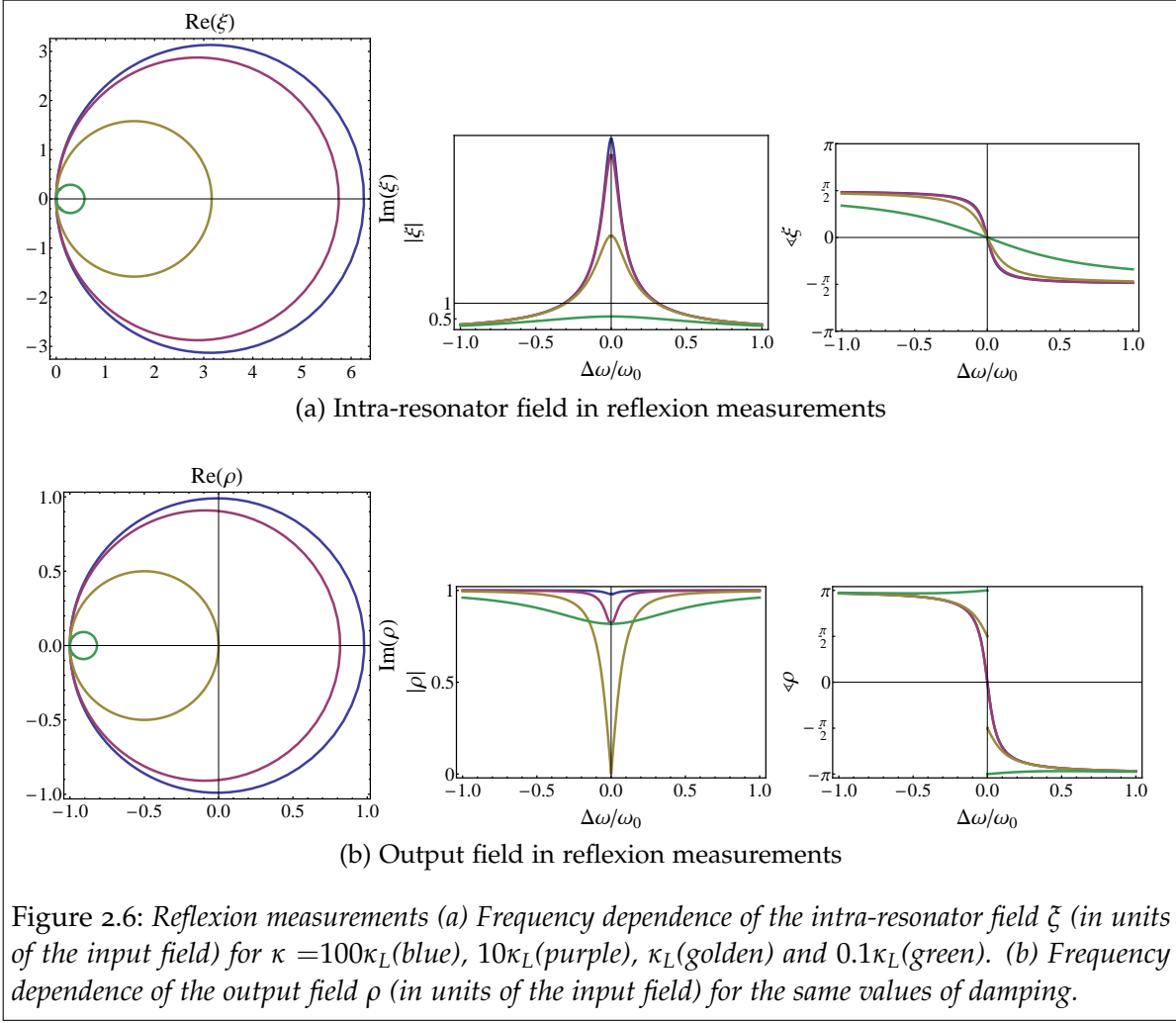
with  $\rho$  shown in Fig. 2.6b.

Depending on the rate between the coupling constant  $\kappa$  and the losses  $\kappa_L$  we can define three regimes characterized by different behaviours of the reflexion  $\rho$ :

- The **over-coupled** regime (blue curves) defined by  $\kappa \gg \kappa_L$ . In this regime  $|\rho| \approx 1$  for all frequencies and the phase  $\angle\rho$  undergoes a  $2\pi$  shift at resonance :

$$\angle\rho = 2 \arctan \left( 2 \frac{\omega - \omega_r}{\kappa} \right)$$

- The **critical coupling** regime (golden curves) defined by  $\kappa = \kappa_L$ . For this regime the amplitude of  $\rho$  reaches 0 at resonance, while a discontinuity in its phase brings a phase shift of  $\pi$ .
- The **under-coupled** regime (green curves) defined by  $\kappa_L \gg \kappa$ . In this regime the resonance corresponds to a dip in the amplitude of  $\rho$  and a shift  $< \pi$  in its phase. The width of both the dip and the phase shift decrease when  $\kappa_L/\kappa$  increases. We stress that an under-coupled resonator is particularly difficult to measure in reflexion since both the amplitude and the phase differ very slightly from their out-of-resonance value.



### Transmission measurements

Some of the resonators operated during this thesis have separated input and output ports, characterized by their coupling constants  $\kappa_1$  and  $\kappa_2$ . Using Eq. 2.12 for the case where the incoming signal is only on port 1 ( $\alpha_{in,2} = 0$ ), the intra-resonator field is:

$$\alpha(\omega) = \frac{\sqrt{\kappa_1}}{\kappa_1 + \kappa_2 + \kappa_L - 2i(\omega - \omega_r)} \alpha_{in,1}(\omega),$$

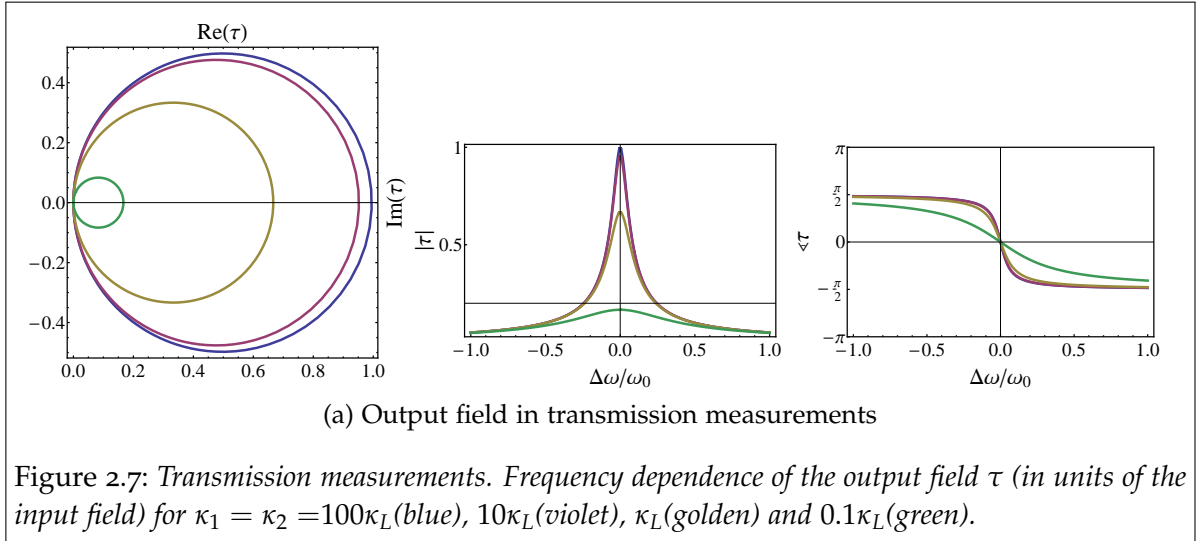
yielding at resonance an average intra-resonator field of

$$\bar{n} = \frac{\kappa_1}{\hbar\omega_r (\kappa_1 + \kappa_2 + \kappa_L)^2} P_{in} \quad (2.17)$$

average photons. Using Eq. 2.13 we calculate the transmission from one port to the other:

$$\alpha_{out,2}(\omega) = \underbrace{\left[ \frac{2\sqrt{\kappa_1\kappa_2}}{\kappa_1 + \kappa_2 + \kappa_L - 2i(\omega - \omega_r)} \right]}_{\tau(\omega)} \alpha_{in,1}(\omega).$$





In our two-port resonators we often have  $\kappa_1 = \kappa_2 = \kappa/2$  which results in a Lorentzian response

$$\alpha_{out,2}(\omega) = \frac{\kappa}{\kappa + \kappa_L - 2i(\omega - \omega_r)} \alpha_{in,1}(\omega).$$

As for reflexion measurements, depending on the rate between the coupling constant  $\kappa$  and the losses  $\kappa_L$  we can define three regimes characterized by different behaviours of the transmission  $\tau$ :

- The **over-coupled** regime (blue curves) defined by  $\kappa \gg \kappa_L$ , in which  $|\tau(\omega)|$  is a Lorentzian that almost reaches 1 at resonance if  $\kappa_1 = \kappa_2$ . The phase of  $\tau(\omega)$  undergoes a  $\pi$  shift in phase at resonance, whose width, as well as the width of the  $|\tau(\omega)|$  Lorentzian, are controlled by  $\gamma$ .
- The **critical coupling** regime (golden curves) defined by  $\kappa = \kappa_L$ . In this regime the amplitude of  $\tau(\omega)$  reaches  $2/3$  at resonance and the widths are controlled by both  $\kappa$  and  $\kappa_L$ .
- The **under-coupled** regime (green curves) defined by  $\kappa_L \gg \kappa$ . In this regime the amplitude of  $\tau(\omega)$  decreases when  $\kappa_L/\kappa$  grows and its width is essentially controlled by  $\kappa_L$ .

Therefore to characterize the losses a slightly under-coupled regime  $\kappa \lesssim \kappa_L$  is the most convenient, since the width of the Lorentzian  $|\rho|$  brings information on  $\kappa_L$  while its amplitude is large enough to be measured.

### Mapping the distributed resonator onto a RLC resonator

It is sometimes useful to map a transmission-line resonator to a Thévenin equivalent lumped-element circuit with the same electrical properties as seen from a particular location. For instance, the fundamental mode  $k = 1$  of the transmission-line resonator

of Fig. 2.8 seen from  $B_1B_2$  is equivalent to an RLC circuit with an impedance:

$$Z_{RLC}(\omega) = \frac{R}{1 + i2Q\frac{\omega - \omega_r}{\omega_r}}$$

with the equivalence shown in the table. However, such a mapping is only valid for a narrow frequency range around the resonance.

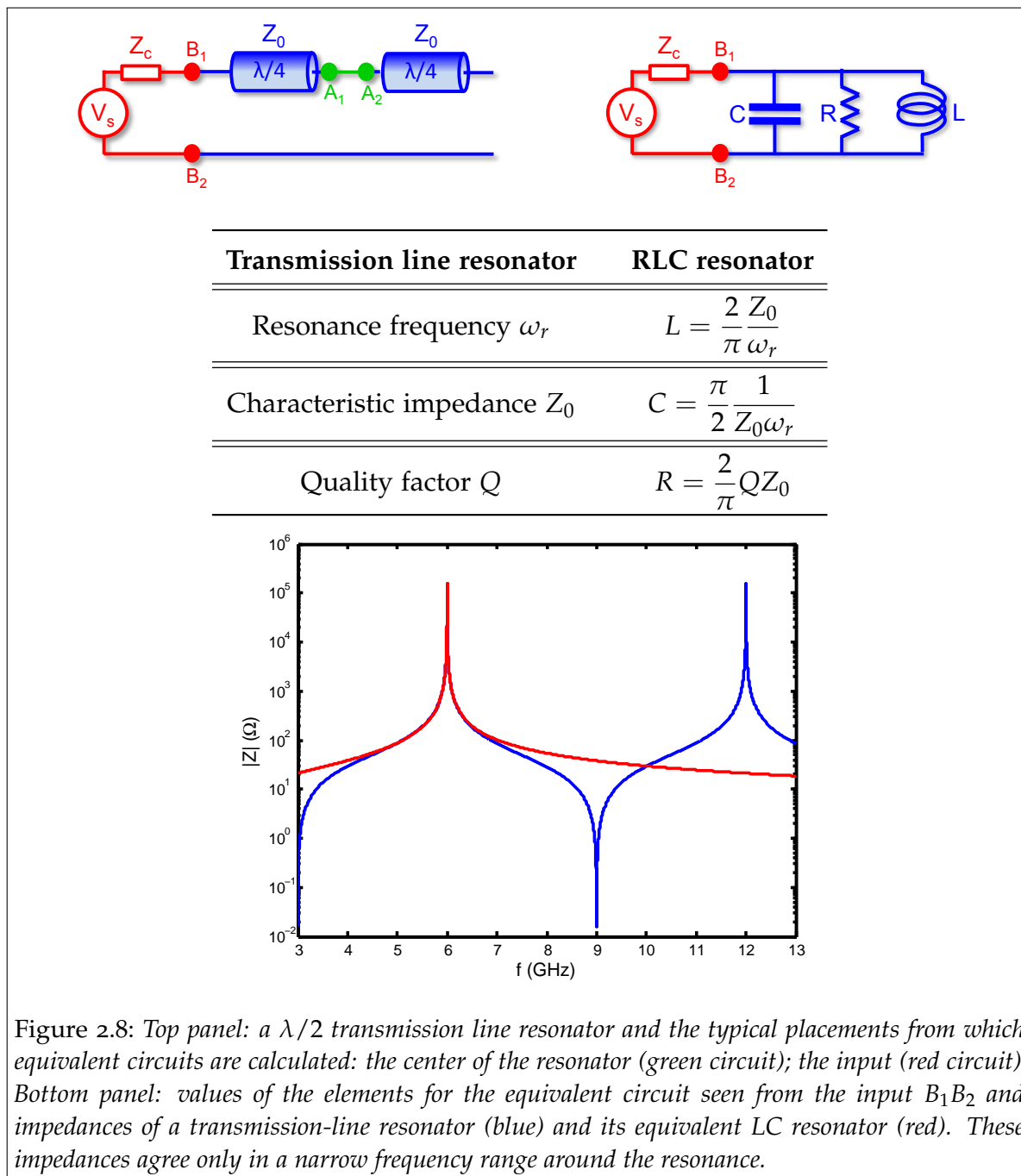


Figure 2.8: Top panel: a  $\lambda/2$  transmission line resonator and the typical placements from which equivalent circuits are calculated: the center of the resonator (green circuit); the input (red circuit). Bottom panel: values of the elements for the equivalent circuit seen from the input  $B_1B_2$  and impedances of a transmission-line resonator (blue) and its equivalent LC resonator (red). These impedances agree only in a narrow frequency range around the resonance.

In Fig. 2.8 the input impedance of a transmission-line resonator is compared to its equivalent LC resonator as seen from the input port  $B_1B_2$ . As expected, the impedances are very similar around the resonance and become more and more

different when going apart from it, since the presence of higher order modes in a transmission line resonator is qualitatively different from the LC resonator.

We also stress that this equivalent circuit depends on the specific nodes from which the rest of the circuit is considered. For instance the equivalent circuit seen from the nodes  $A_1A_2$  does not preserve the currents and voltages passing through  $B_1B_2$ . Therefore, the greatest care has to be taken when calculating with these equivalent circuits.

#### 2.1.4 IMPLEMENTATION

We explain here the implementation of the transmission-line resonators in a convenient planar geometry: the coplanar-waveguide (CPW) (see 2.1.4.1). For this implementation we closely followed the work previously done in other groups<sup>66,67</sup>. We also present their fabrication process (see 2.1.4.3), some elements on the microwave techniques which are used to characterize them, which are the basis of the measurement techniques introduced further in this thesis.

##### 2.1.4.1 Resonator implementation

Our resonators operate in the gigahertz frequency range. This choice is made to reduce the influence of thermal excitations. Indeed the samples are operated in a dilution refrigerator ( $\sim 20$  mK). To avoid spurious thermal population we need a large enough frequency  $\omega_r/2\pi \gg k_B T/h \simeq 400$  MHz, so we chose to work in the 4–8 GHz range.

The 4–8 GHz range correspond to the microwave IEEE C band. In such frequencies a transmission line can be implemented using a wide variety of geometries. In cQED experiments 2D geometries are preferred, since building the resonator on the surface of a chip allows stronger coupling to artificial atoms.

There are two typical planar geometries: coplanar-stripline (CPS) and coplanar-waveguide (CPW shown in Fig. 2.9). CPS geometry consists in two parallel conductors separated by a gap while CPW is formed by a central conductor with ground planes on both sides. We decided to use the unbalanced CPW geometry, similar to coaxial cables delivering the signals, rather than CPS, which would require a balun for making the transition to coaxial cables.

The configuration of the electrical and magnetic fields on a CPW line is shown in Fig. 2.9. The effective dielectric constant felt by these fields can be estimated<sup>68</sup> from the dielectric constant of the substrate  $\epsilon_r \epsilon_0$  as  $\epsilon_r \epsilon_0 = \epsilon_0(1 + \epsilon_{rS})/2$ , The resulting phase velocity is  $\bar{c} = c/\sqrt{\epsilon_r}$ .

The resonator is defined as a  $\lambda/2$  segment of transmission line terminated at both ends by open circuits. Its length is then  $\Lambda = \pi\bar{c}/\omega_r$ . The mode is well-confined and quasi-1D. The characteristic impedance of the line can be exactly calculated from its geometry<sup>68</sup>:

$$Z_0^{CPW}[\Omega] = \frac{30\pi}{\sqrt{\epsilon_r}} \frac{K(\sqrt{1-k^2})}{K(k)},$$

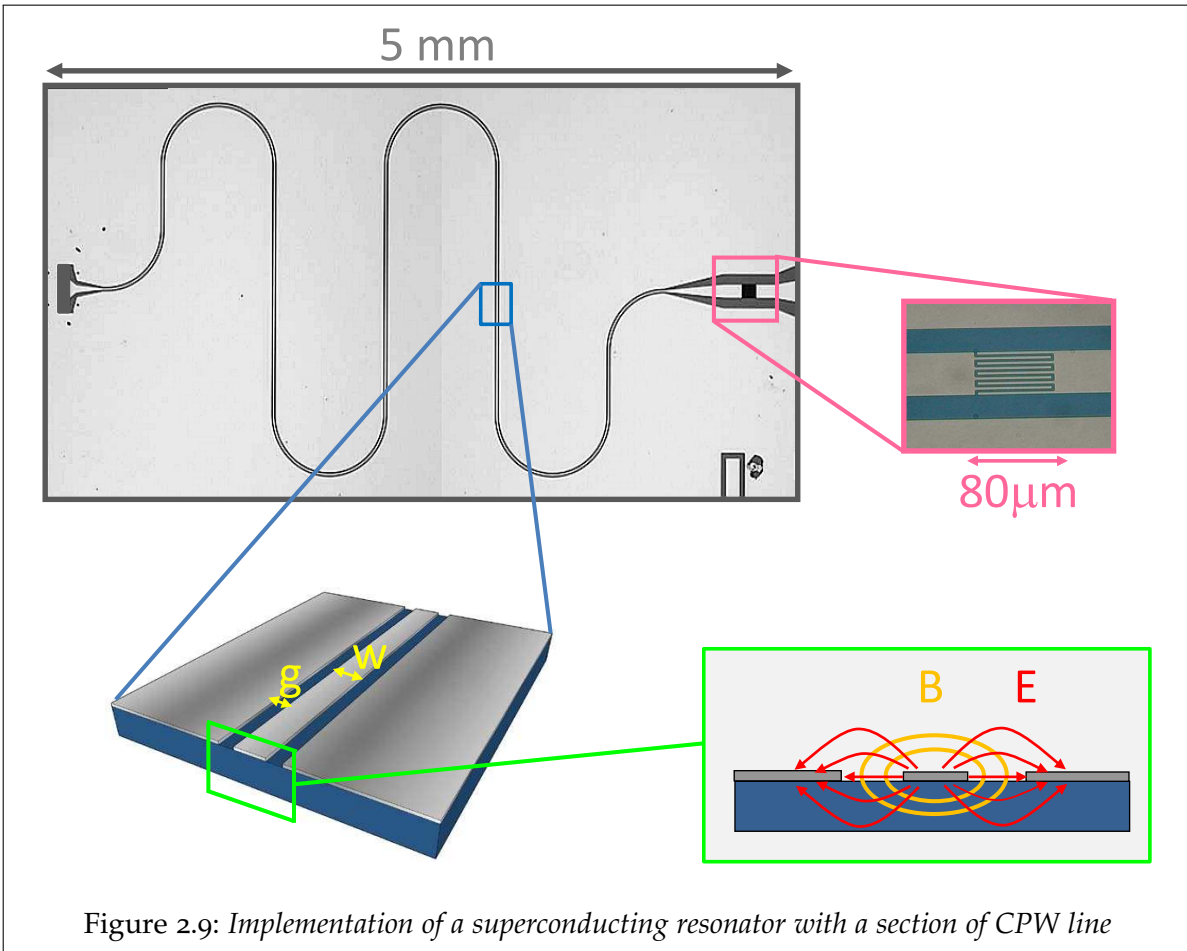


Figure 2.9: Implementation of a superconducting resonator with a section of CPW line

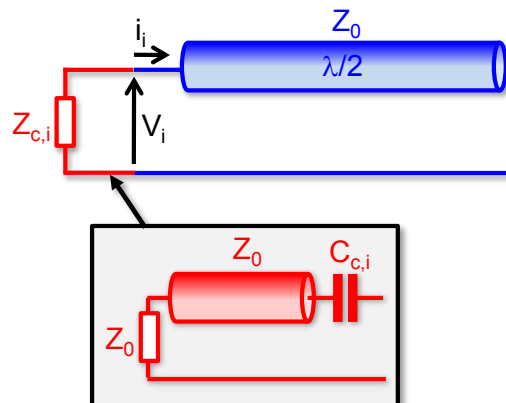
where  $k = w / (w + 2g)$ , with  $w$  and  $g$  the width and the gap defined in Fig. 2.9, and

$$K(k) = \int_0^{\pi/2} \frac{d\theta}{\sqrt{1 - k^2 \sin^2 \theta}}$$

the complete elliptic integral of the first kind. For the experiments presented in this thesis we have used  $w = 10 \mu\text{m}$  and  $g = 5 \mu\text{m}$ , yielding  $Z_0 \simeq 50 \Omega$  on silicon ( $\epsilon_r = 11.9$ ).

#### 2.1.4.2 Capacitive coupling

The specific way of coupling the resonators to the measuring lines determines the coupling strengths  $\kappa_i$ . In this section we want to obtain a relationship between the parameters of the specific coupling circuit and these coupling strengths. We first consider the very general case where the port  $i$  of a resonator is connected to an impedance  $Z_{c,i}$ . The coupling constant  $\kappa_i$  is the ratio between the power dissipated in this impedance and the energy



stored in the line:

$$\begin{aligned}\kappa_i &= \frac{P_{diss,i}}{E_{stored}} = \\ &= \frac{1/2 |V_i|^2 \operatorname{Re}(Z_c^{-1})}{1/4c\Lambda |V_i|^2} = \frac{2\omega_r Z_0}{\pi} \operatorname{Re}\left(\frac{1}{Z_c}\right)\end{aligned}$$

Since microwave components have standard impedances  $Z_0 = 50\Omega$ , typically of the same order as the resonator characteristic impedance, a resonator that would be directly coupled to a microwave line would be strongly damped  $\kappa_i/\omega_r \sim 1$ .

Therefore, our resonators are connected to the external lines through a high impedance element: a small coupling capacitor  $C_c$ . Such a capacitor acts as a semi-reflective mirror in optics, inducing a strong impedance mismatch so that the signals are mostly reflected on it, and the intra-resonator field is coupled to the outside with a coupling

$$\kappa_i = \frac{2\omega_r Z_0}{\pi} \operatorname{Re}\left[\left(Z_0 - i\omega_r^{-1}C_c^{-1}\right)^{-1}\right] \approx \frac{2\omega_r^3 C_c^2 Z_0^2}{\pi},$$

On the other hand the imaginary part of the impedance introduced by such a capacitor,  $\operatorname{Im}(Z_c^{-1}) \approx \omega_r C_c$ , shifts the resonance frequency to  $\omega_r = \omega_1/\sqrt{1 + C_c Z_c \omega_r}$ , slightly below the natural frequency of the first mode  $\omega_1$ .

Since the value of these capacitors controls the coupling to the measuring lines, their value should be carefully chosen for each purpose. If one wishes to study the internal losses, for instance, the capacitors should place the resonator slightly in the under-coupled regime (see 2.1.3.2). In the case of one-port resonators, in order to obtain a coupling quality factor  $Q_c = \omega_r/\kappa$  the coupling capacitor should be

$$C_c = \sqrt{\frac{\pi}{2Q_c}} \frac{1}{Z_0 \omega_r}.$$

In the case of two-port resonators,  $Q_c = \omega_r/\kappa = \omega_r/(\kappa_1 + \kappa_2)$  can be obtained with two equal coupling capacitors

$$C_{c1} = C_{c2} = \sqrt{\frac{\pi}{4Q_c}} \frac{1}{Z_0 \omega_r}.$$

We implement our coupling capacitors with an interdigitated design such as shown in Fig. 2.9. The number of fingers, their length and spacing is chosen with the help of a 2D+ electromagnetic simulator, Sonnet, to achieve the desired capacitance values.

#### 2.1.4.3 Fabrication

The resonators are fabricated by **optical lithography** on a niobium thin-film. The substrate used is a 2-inch high resistivity ( $> 1000 \Omega\text{cm}$ ) silicon wafer, covered with 50 nm of thermally grown  $\text{SiO}_2$ . The lithography consists in five steps:

1. **Sputtering of a niobium thin-film** by a DC electric discharge in a low density ( $10^{-2}$  mbar) argon plasma, that bombards a niobium target. The duration of the process determines the thickness of the film: 100 nm to 200 nm in our case.
2. A layer of **photosensitive resist** (Shipley S1805) is spun on the wafer and baked.
3. The wafer is **UV-exposed** through a chromium on quartz mask and developed to dissolve the exposed resist.
4. **Etching** of the uncovered niobium, by one of the following two techniques:
  - a) **Wet etching** in a solution of HF, H<sub>2</sub>O and FeCl<sub>3</sub> with etching rate of 1 nm/s at room-temperature.
  - b) **Reactive-ion etching** (RIE) with a SF<sub>6</sub> plasma at a pressure of 0.3 mbar and a power such that the self-bias voltage is 30 V and the etching rate 1 nm/s. We observed that adding O<sub>2</sub> to the plasma produces consistently low quality factors, as low as 60 for high O<sub>2</sub> densities. We attribute this to the creation of a dissipative niobium oxide on the surface of the sample.
5. **Dissolution** of the remaining resist.

This process is performed with wafers containing 40 chips, which are then diced on  $3 \times 10$  mm<sup>2</sup> chips, containing each one two resonators such as the one shown in Fig. 2.9.

### 2.1.5 CHARACTERIZATION OF THE RESONATORS

In this section we characterize the resonators to study the impact of the fabrication process on the losses and optimize their quality factor.

#### 2.1.5.1 Measurement techniques

*Setup for measuring the resonators at 1.3 K*

As shown in Fig. 2.11, to quickly characterize a resonator, it is placed in a small refrigerator filled with helium which is pumped to lower the temperature down to 1.3 K –a temperature much lower than the niobium critical temperature in order to reduce quasi-particle density.

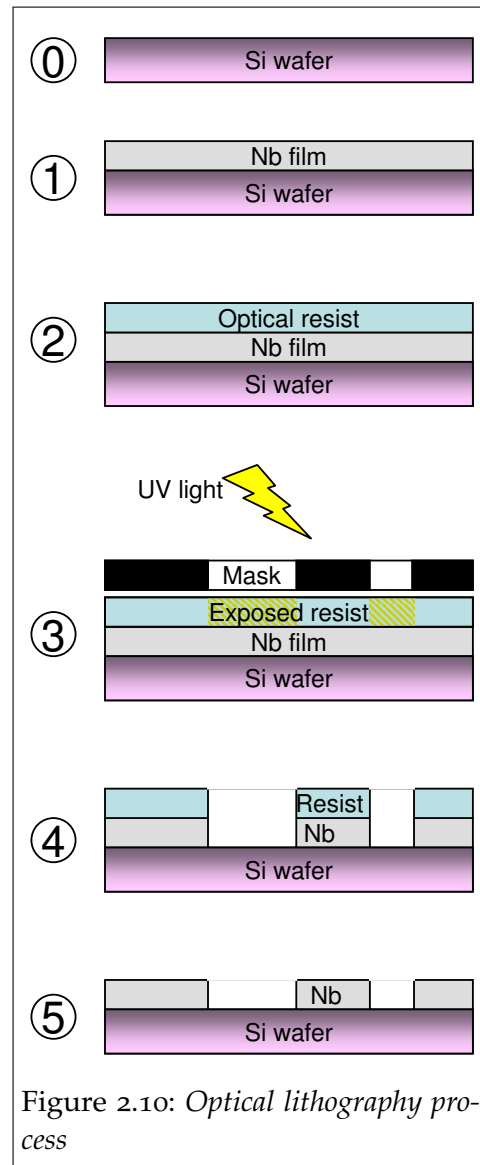
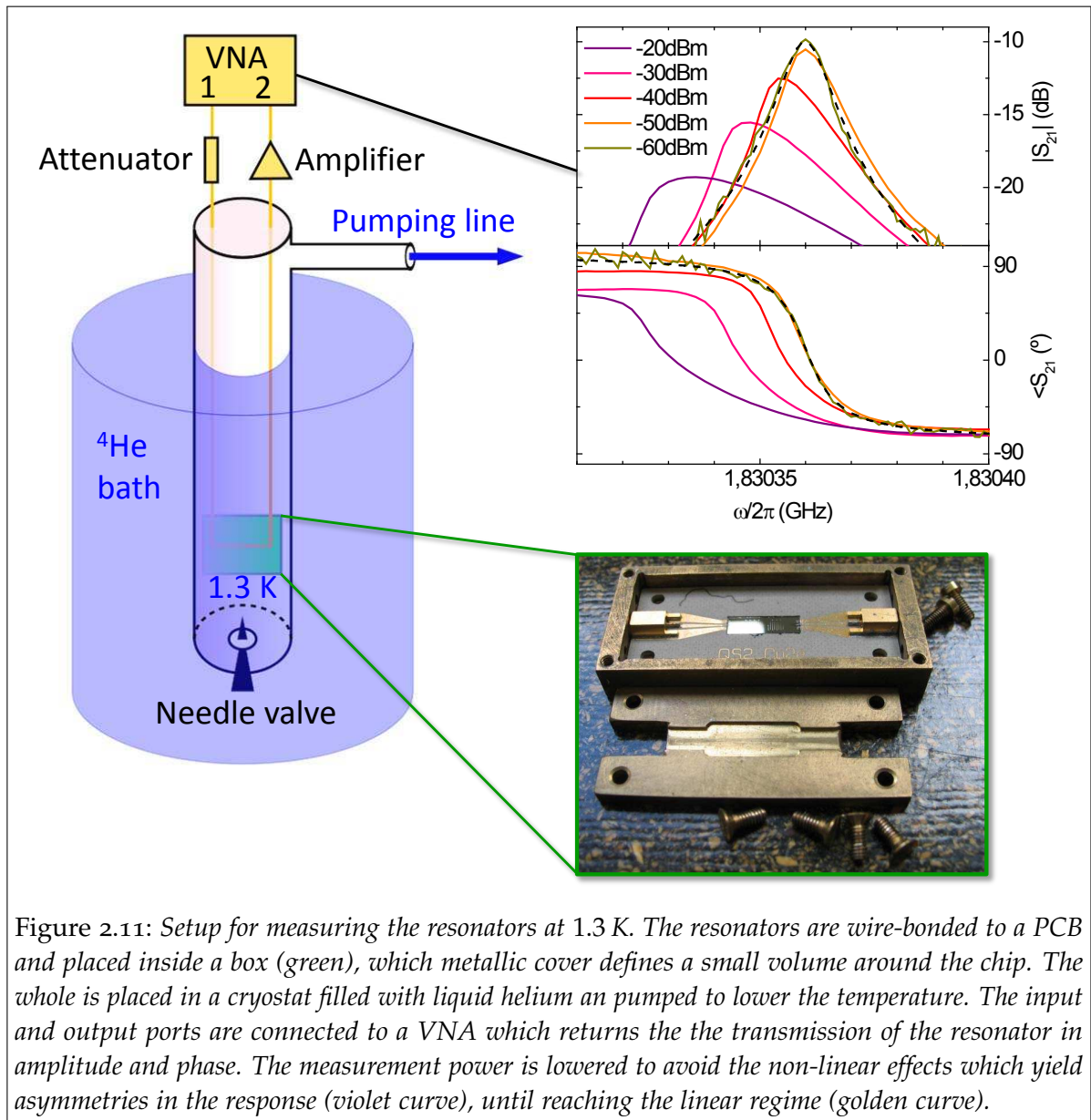


Figure 2.10: Optical lithography process



The resonators may be measured in reflexion or in transmission. Measurements in reflexion are performed using a circulator as shown in Fig. 2.12, to separate the probe signal sent to the sample from the reflected signal which is measured. Circulators allow the propagation of signals in a given direction, the reverse way being attenuated by typically 20 dB (a figure called isolation). Alternatively, if the input signal is high enough (which is the case in our experiments), the circulator can be replaced by a directional coupler<sup>69</sup>. This device attenuates the input signal, and delivers the output signal to a different port with an isolation equal to its attenuation. This can be a good choice for several reasons: contrary to circulators it is not magnetic, it is usually smaller, and has a larger bandwidth.

In both cases we use a Vector Network Analyzer (VNA), an apparatus which measures the scattering matrix of a two-port microwave circuit by sending a microwave signal and detecting the amplitude and phase of the transmitted or reflected signal.



As an example in Fig. 2.11 the typical transmission of an under-coupled resonator is shown.

In a particular setup –reflexion or transmission– a fit of the resonance curves with the expected responses shown in Table 2.13 yields the resonance frequency  $\omega_r$ , the coupling quality factor  $Q_c$  and the quality factor  $Q_L$  corresponding to internal losses. We stress that in order to characterize accurately  $Q_L$ , an under-coupled resonator is needed.

The microwave signal sent by the VNA creates an intra-resonator field, which can be calculated with Eq. 2.15 or Eq. 2.17. If this intra-resonator field is high enough non-linear effects may arise. These effects result in asymmetries in the reflexion or transmission, as the ones shown in Fig. 2.13<sup>2</sup>. To reduce the input power and avoid these effects, an attenuator is inserted on the input line. On the output line, an external low-noise microwave amplifier is used to decrease the high input noise of the VNA.

In the following paragraphs we introduce the main microwave techniques which are used in the VNA measurements. A good general introduction to microwave engineering is provided in Pozar<sup>69</sup> and Collin<sup>70</sup> books.

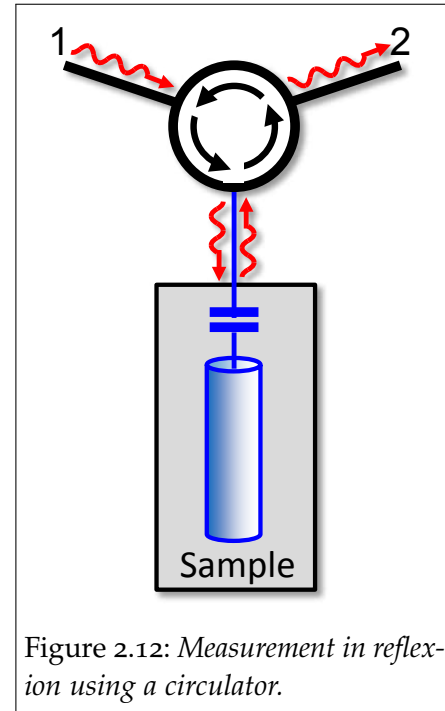


Figure 2.12: Measurement in reflexion using a circulator.

#### *Homodyne demodulation: the field quadratures*

To measure the  $S$  parameters the VNA internally uses homodyne demodulation. Since we use this technique further in our experiments it is worth explaining it here. To characterize an  $S$  parameter, the VNA sends a microwave signal  $V_i = A_i \cos(\omega t)$  of frequency  $\omega$  through one of its ports. In the absence of noise the output is a signal

$$V_o = A_o \cos(\omega t + \varphi).$$

The goal is to obtain the amplitude of the response  $A_o/A_i$  and its phase  $\varphi$ . For this purpose this signal is homodyned, that is, mixed with the same local oscillator  $\cos(\omega t + \Theta)$  or  $-\sin(\omega t + \Theta)$  as used to produce the signal, dephased by  $\Theta$  and with a normalized amplitude. The result is low-pass filtered to eliminate the component at frequency  $2\omega$ . The results are the in-phase and quadrature components

$$I_D = A_o \cos(\varphi - \Theta)$$

$$Q_D = A_o \sin(\varphi - \Theta).$$

#### *Noise issues and averaging*

The signals we use are typically very small to avoid non-linear effects as explained above. A great care has then to be taken in order to obtain a good signal-to-noise ratio (SNR), and a lock-in detection, provided by the VNA averaging mode, is needed.

<sup>2</sup>Peaks shifting both to the higher and the lower frequencies were observed



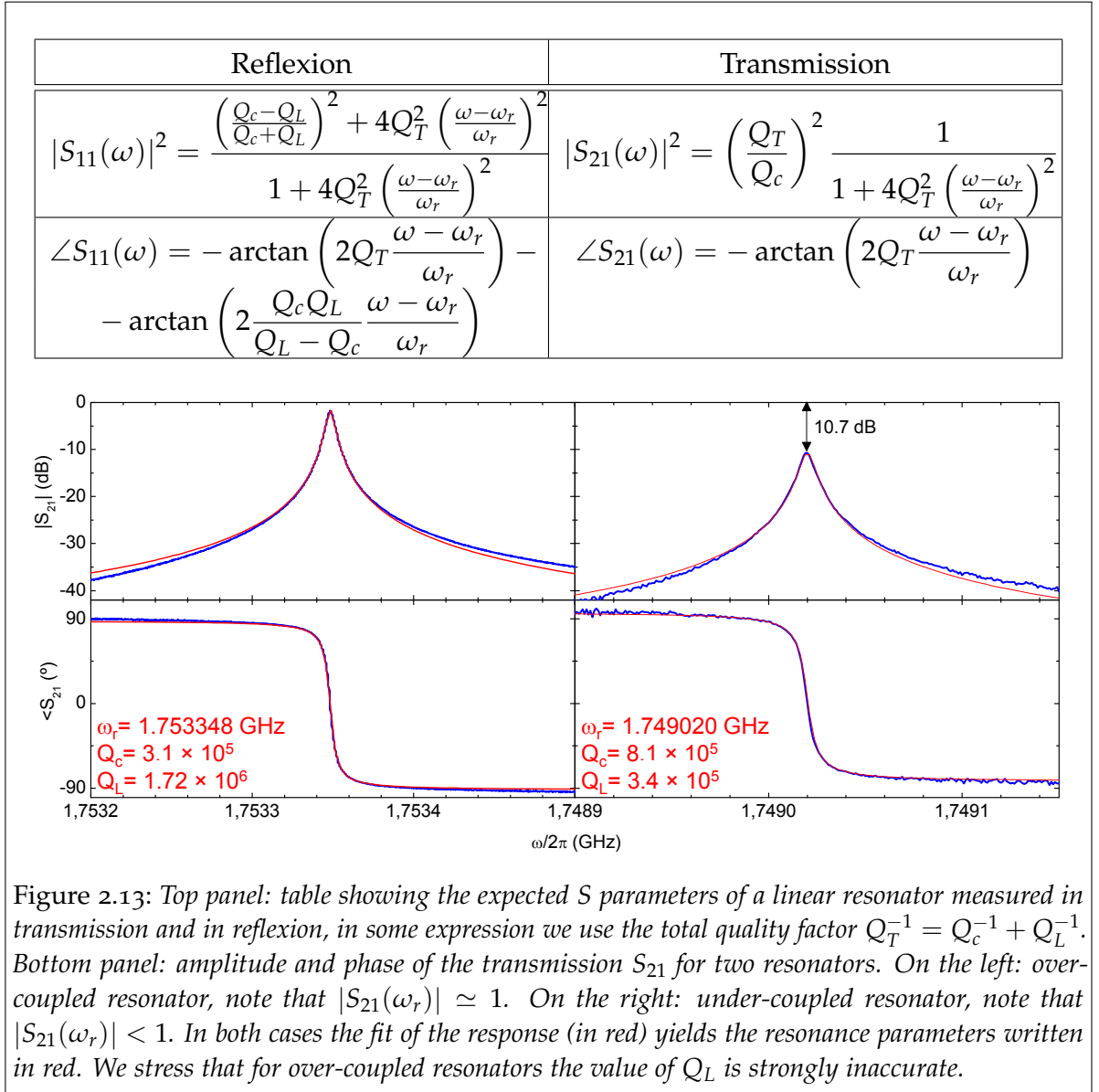


Figure 2.13: Top panel: table showing the expected  $S$  parameters of a linear resonator measured in transmission and in reflexion, in some expression we use the total quality factor  $Q_T^{-1} = Q_c^{-1} + Q_L^{-1}$ . Bottom panel: amplitude and phase of the transmission  $S_{21}$  for two resonators. On the left: over-coupled resonator, note that  $|S_{21}(\omega_r)| \simeq 1$ . On the right: under-coupled resonator, note that  $|S_{21}(\omega_r)| < 1$ . In both cases the fit of the response (in red) yields the resonance parameters written in red. We stress that for over-coupled resonators the value of  $Q_L$  is strongly inaccurate.

This lock-in type detection consists in long-time averaging of the homodyne-detected signals  $I_D$  and  $Q_D$ . With this technique the signal can be recovered with virtually any SNR<sup>3</sup>. The input of the homodyne demodulation is the signal

$$V(t) = A_o \cos(\omega t + \varphi) + V_n(t),$$

where  $V_n(t)$  represents a white noise voltage. The in-phase component is then

$$I_D = A_o \cos(\varphi)/2 + V_n(t) \cos(\omega t).$$

Averaging over a long time  $\tau \gg \omega^{-1}$  we obtain

$$\frac{1}{\tau} \int_0^\tau (A_o \cos(\varphi)/2 + V_n(t) \cos(\omega t)) dt = \underbrace{\frac{A_o \cos(\varphi)}{2}}_S + \underbrace{\frac{\sigma_n}{2\sqrt{\tau}}}_N$$

<sup>3</sup>We say *virtually* because the time drifts of the parameters limit the gain of SNR when averaging the signal over very long times

where  $\sigma_n$  is the rms value of  $V_n$ . The  $\text{SNR} = S/N \propto \sqrt{\tau}$  (in amplitude) can therefore be raised as much as wanted by averaging during longer times.

From another point of view, the averaging amounts to detecting around  $\omega$  with a very small bandwidth  $B \propto \tau^{-1}$ . Since the white noise power  $\sigma_n^2$  is proportional to the bandwidth  $B$ , one can suppress as much noise as wanted. However, measurements may become too long to be practically performed. Moreover, long-term drifts on the system may limit very long measurements, and  $1/f$  noises cannot be averaged out in this way. A careful optimization of SNR is thus necessary.

### 2.1.5.2 Characterization of the resonator losses

Having a good understanding of the internal losses of resonators is important in the perspective of coupling them to qubits. With this in mind, we present here measurements of the resonance parameters as a function of the temperature and the magnetic field.

#### *Resistive losses in a superconductor*

Superconductors are lossless only at zero frequency. At any non-zero frequency they dissipate power<sup>71</sup>. Indeed, the transport of charges through the superconductor can occur via two channels. A first lossless channel is the transport by the Cooper pairs. A second dissipative channel is the transport by normal charge carriers –quasi-particles. At DC frequency, transport by quasi-particles is perfectly shunted by the Cooper pairs. At AC frequencies however the lossless channel presents a purely imaginary inductive response to the passage of a current, which thus generates electric fields that accelerate the quasi-particles causing dissipation. This dissipation is proportional to the quasi-particle density, which is expected to diminish exponentially at low temperatures.

The Mattis-Bardeen theory<sup>72</sup>, based on BCS theory, provides a quantitative treatment of this simplified two-fluid vision. Here, our goal is to summarize all the results needed to calculate the internal losses of a resonator<sup>73</sup>. The Mattis-Bardeen theory yields analytical formula for the complex conductivity of a superconductor  $\sigma = \sigma_1 - i\sigma_2$  at frequency  $\omega$  (valid if  $\hbar\omega < \Delta(T)$ ):

$$\frac{\sigma_1}{\sigma_N} = \frac{2}{\hbar\omega} \int_{\Delta(T)}^{\infty} [f(E) - f(E + \hbar\omega)] g(E) dE \quad (2.18)$$

$$\frac{\sigma_2}{\sigma_N} = -i \frac{2}{\hbar\omega} \int_{\max(\Delta(T) - \hbar\omega, -\Delta(T))}^{\Delta(T)} [1 - 2f(E + \hbar\omega)] g(E) dE \quad (2.19)$$

where  $\sigma_N$  is the normal state conductivity,  $f(E)$  is the Fermi-Dirac distribution at energy  $E$ ,  $\Delta(T)$  is the temperature-dependent energy gap, and

$$g(E) = i \frac{E(E + \hbar\omega) + \Delta(T)^2}{\sqrt{(E + \hbar\omega)^2 - \Delta(T)^2} \sqrt{\Delta(T)^2 - E^2}}.$$

The temperature dependence of  $\sigma_1$  and  $\sigma_2$  cause both the resonance frequency and the quality factor of the resonator to vary in temperature. We now calculate this dependence. The surface impedance  $Z_S = R_S + iL_S$  of a superconducting film of arbitrary thickness  $d$  is given by

$$Z_S = \sqrt{\frac{i\mu_0\omega}{\sigma_1 - i\sigma_2}} \coth\left(\frac{d}{\lambda} \sqrt{1 + i\frac{\sigma_1}{\sigma_2}}\right)$$

with  $\lambda(\omega, T)$  the magnetic penetration depth

$$\lambda(\omega, T) = \frac{1}{\sqrt{\mu_0\omega\sigma_2}}.$$

In the limit where  $\sigma_2 \gg \sigma_1$ , we have

$$R_S = \mu_0\omega\lambda \frac{\sigma_1}{2\sigma_2} \beta \coth\left(\frac{d}{\lambda}\right)$$

$$L_S = \mu_0\lambda \coth\left(\frac{d}{\lambda}\right)$$

where  $\beta = 1 + (2d/\lambda) / \sinh(2d/\lambda)$  is a geometrical factor varying between 1 for a very thin film and 2 for the bulk. A propagating wave in a coplanar waveguide therefore sees a kinetic inductance per unit length  $\ell_K = g_{CPW}L_S$ , where  $g_{CPW}$  is a geometry factor specific to the CPW geometry<sup>73</sup>, in addition to the geometric inductance per unit length  $\ell$ . The resonator frequency is finally given by

$$\omega_r = \frac{\pi}{\Lambda \sqrt{(\ell + \ell_K) c}}$$

so that its relative variation is

$$\frac{\delta\omega_r}{\omega_r} = -\frac{\alpha}{2} \frac{\delta\ell_K}{\ell_K} = \frac{\alpha\beta}{4} \frac{\delta\sigma_2}{\sigma_2}$$

where  $\alpha = \ell_K/(\ell_K + \ell)$  is a geometrical factor describing the fraction of kinetic to total waveguide inductance. Analytical formulas exist allowing to explicitly calculate  $\alpha$  for a specific coplanar waveguide geometry, however it is much more precise to fit it using the temperature dependence of the resonator frequency resulting from the previous relation

$$\frac{\omega_r(T)}{\omega_r(0)} = \left(\frac{\sigma_2(T)}{\pi\Delta(0)/(\hbar\omega)}\right)^{\alpha\beta/4}. \quad (2.20)$$

The quality factor of the resonator is finally given by

$$Q = \frac{\omega\Lambda(\ell + \ell_K)}{R} = \frac{1}{\alpha} \frac{\omega L_S}{R_S} = \frac{2}{\alpha\beta} \frac{\sigma_2}{\sigma_1}. \quad (2.21)$$

## Study in temperature

We have measured the temperature dependence of the resonance frequency  $\omega_r$  and internal quality factor  $Q_L$  of a niobium coplanar resonator of thickness  $d = 130$  nm, with a measured critical temperature  $T_c = 7.98$  K (see Fig. 2.14). The temperature dependence of the resonator frequency is very well fitted with Eq. 2.20 for a reasonable  $\alpha = 1.6\%$ . The quality factor predicted by Eq. 2.21 reproduces well the data in the high temperature range, but saturates at low temperatures at a value around  $10^5$ . This saturation seems to indicate that the internal losses at low temperature are dominated by an unknown source of dissipation that is not described by BCS theory. Similar behavior has been observed in all coplanar waveguide resonators. This extra dissipation may come from radiation or dielectric losses.

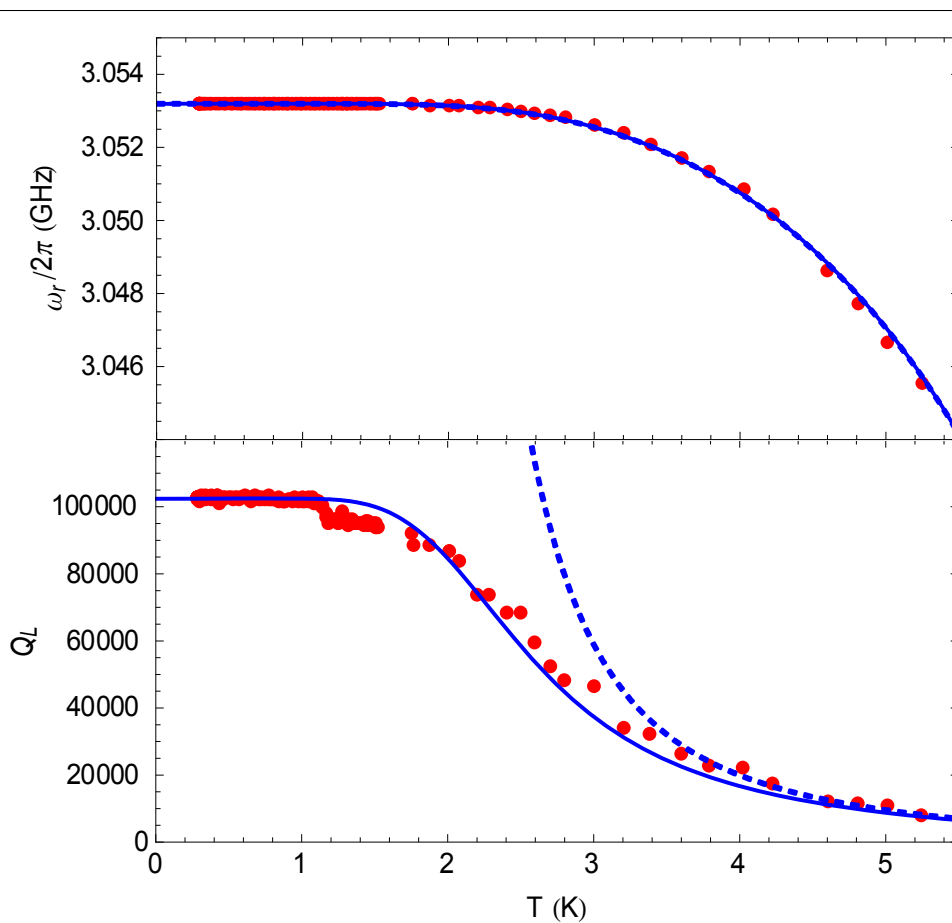


Figure 2.14: Variation in temperature of the resonance frequency (on the top) and the quality factor (on the bottom) of a niobium coplanar resonator of thickness  $t = 130$  nm. Top panel: the measured frequencies (red dots) are in very good agreement with the predictions of the Mattis-Bardeen model (blue solid line). Bottom panel: the measured quality factors (red dots) disagree with the predictions of the Mattis-Bardeen model (blue dashed line), but are very well reproduced by the Mattis-Bardeen model plus an additional constant relaxation (blue solid line).

### *Radiative losses*

Since the resonator is 2D, the fields are not completely confined and they may radiate energy to the outside contributing to the energy losses.

A first analysis of this radiation has been performed for CPW lines by Rutledge<sup>74</sup>. He considers the surface waves on a chip whose thickness is of the same order of magnitude of the wavelength of the stored electromagnetic modes. These surface waves constitute a radiating source<sup>4</sup>. For the geometry, the materials and the typical 6 GHz frequency of our resonators he predicts a radiative quality factor  $Q_{rad} \simeq 8.6 \times 10^6$  with a dependence in frequency  $Q_{rad} \propto \omega^{-2}$ .

Vayonakis<sup>75</sup> has performed a similar calculation with a different method. He considered the CPW line gaps as an aperture antenna. To analyze the radiation, he used the plane waves as a basis. The overlap of the CPW mode with these plane waves allows to calculate the excitation of each of these radiated modes. The total power carried away by all the propagative plane waves corresponds to the power leaking to the open space. This estimation of the radiated power gives for our samples a radiative quality factor  $Q_{rad} \simeq 1.2 \times 10^7$ , and the same scaling  $Q_{rad} \propto \omega^{-2}$ .

Both figures above are in good agreement together for our particular parameters, and predict quality factors way above the ones observed. We can conclude that the radiative losses do not constitute a relevant source of losses in our resonators.

### *Dielectric losses*

The radiative and resistive losses do not explain the quality factors observed in our resonators, limited below  $10^6$  at the lowest temperatures and powers. Other groups have observed a similar limitation. In addition, the measured quality factor are higher when measured with higher microwave powers<sup>76</sup>. This suggests that the mechanism absorbing the energy can be saturated. The temperature dependence of the quality factor reinforces this idea: indeed, it shows a maximum at an intermediate temperature which corresponds to a saturation of the absorbing mechanism by thermal excitations<sup>77,78</sup>.

A proposed explanation for this behaviour is the presence of two-level systems (TLS) in the materials forming the resonators<sup>79</sup>. These TLS could also explain the phase noise which appears in the electromagnetic field stored in the resonator<sup>80</sup> and although their actual nature is not well known, it has been shown that they number scale as the surface of the electrodes<sup>81</sup>. This suggests that an oxide covering the surface of the superconductor, or maybe a dielectric layer in the substrate, may contain glassy TLS systems which absorb energy. The link between the phase noise induced by these TLS and the losses is not clear, although the oxides and the dielectric layers are known to have quite high loss tangents at low temperatures<sup>82</sup>.

---

<sup>4</sup>The simplified expression is

$$Q_{rad} = \frac{128}{\pi^2} \frac{(\epsilon + 1)}{(\epsilon - 1)^2} \frac{c^2 K(k) K(k')}{(s + 2w)^2 \omega^2}$$

The presence of absorbers in the surface of the chip may also explain why the *rejuvenating process* setup by G. Ithier allows to improve the quality factors on newly fabricated resonators up to an order of magnitude, and to recover original quality factors in aged ones. This process consists in a mild etching of the chip surface with a RIE mixture of 10 cc of argon and 20 cc of SF<sub>6</sub> at 50 W and  $1.33 \times 10^{-2}$  mBar during 5 s.

### *Study in magnetic field*

Finally we have also studied the variation of  $\omega_r$  and  $Q$  with magnetic field. Indeed, artificial-atoms and tunable resonators are tuned by using a magnetic field; it is thus important to know if this magnetic field has any effect on the resonator parameters.

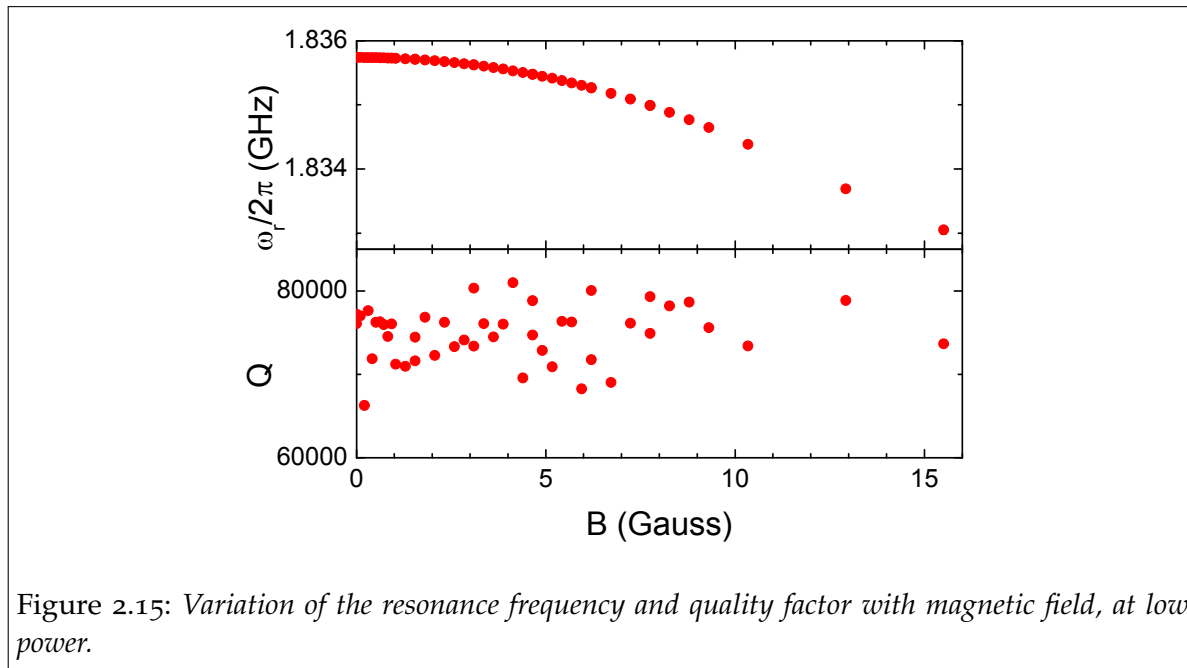


Figure 2.15: Variation of the resonance frequency and quality factor with magnetic field, at low power.

The magnetic field has a minor influence on the resonance frequency, which decreases by less than 3 MHz in the strongest fields that we could apply, as shown on Fig. 2.15. Qualitatively, this is a consequence of the kinetic inductance of the sample, which becomes greater when a magnetic field is applied. Since the exact intensity of the magnetic field on the surface of the sample and its spatial variations are unknown, we cannot make a quantitative analysis of this effect. No relevant effects of these fields on the quality factor were observed. We stress however that it is likely that the presence of a magnetic field during the cooldown of the sample through the superconducting transition would bring significant additional losses due to vortices trapped in the thin-films.

## 2.2 THE TRANSMON ARTIFICIAL ATOM

A superconducting resonator already has well-defined energy levels. To obtain an anharmonic atom-like spectra, in which individual levels can be addressed separately,

we introduce some non-linearity in the circuit with a non-linear and loss-less circuit element: the Josephson junction.

### 2.2.1 THE COOPER-PAIR BOX: AN ANHARMONIC ARTIFICIAL ATOM

The specific Josephson circuit we used to implement artificial atoms in our experiments is the transmon<sup>19</sup> pioneered by Schoelkopf's group at Yale. This circuit is a variant of the Cooper Pair Box (CPB), a simple superconducting circuit developed in 1996 in the Quantronics group<sup>15,83</sup>. In 1999 a team from NEC used the CPB to demonstrate for the first time a coherent superposition of states<sup>4</sup>, although with a rather short coherence time  $< 10$  ns. During the following years important improvements on the CPB were achieved: thanks to an in-depth investigation of the decoherence sources<sup>17</sup> its coherence times reached the microsecond range. At the same time, the readout circuit, which in the first circuits was dissipative and destroyed the state of the CPB, was progressively improved towards circuits which were nearly single-shot, non-dissipative –and where the remaining dissipation is off-chip–, and non-destructive<sup>16,84</sup>. We recall here the most prominent properties of the CPB, closely following A. Cottet's thesis<sup>16</sup> and the article by J. Koch *et al.*<sup>19</sup>.

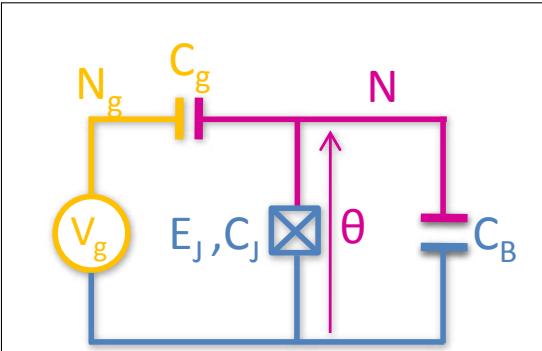


Figure 2.16: The CPB: a superconducting island (purple) is connected to a reservoir (blue) through a Josephson junction with Josephson energy  $E_J$ , and a capacitance  $C_J$ . This island is also electrostatically coupled to ground through a geometric capacitor  $C_B$ , and to a gate circuit through a capacitor  $C_g$ . The gate circuit (yellow) can be used to induce an offset charge  $N_g = C_g V_g / 2e$  on the island.

As shown in Fig. 2.16 the Cooper pair box consists of a superconducting island connected to a reservoir through a Josephson junction with Josephson energy  $E_J$ , and a capacitance  $C_J$ . This island is also electrostatically coupled to ground through a geometric capacitor  $C_B$ , and to a gate circuit through a capacitor  $C_g$ . The gate circuit can be used to induce an offset charge  $N_g = C_g V_g / 2e$  on the island.

The only degree of freedom in this circuit is the tunneling of Cooper pairs through the junction on and off the island. The state of the system can thus be described in terms of the number  $\hat{N}$  of excess Cooper pairs on the island or its canonical conjugate: the superconducting phase difference  $\hat{\theta}$  across the junction. These circuit variables  $\hat{N}$  and  $\hat{\theta}$  satisfy the commutation relation  $[\hat{N}, \hat{\theta}] = i$  and are analog to the momentum and position of an electron in a natural atom. Then, either variable can be used to write the CPB Hamiltonian and wavefunctions.

The dynamics of the CPB is governed by the competition between two phenomena:

- the Josephson effect responsible for the tunnelling of individual Cooper pairs through the junction, with the following Hamiltonian

$$\hat{H}_J = -\frac{E_J}{2} \sum_n (|N\rangle \langle N+1| + |N+1\rangle \langle N|)$$

where  $E_J = I_0 \varphi_0$ ,  $\varphi_0 = \hbar/(2e)$  is the reduced flux quantum and  $I_0$  the critical current of the junction. In the phase basis, this term is simply written

$$\hat{H}_J = -E_J \cos \hat{\theta}$$

since  $|N+1\rangle = \exp(i\hat{\theta})|N\rangle$ .

- the Coulombic effect that tends to fix the number of Cooper pairs in the island. For one Cooper pair the charging energy is  $E_C = (2e)^2/2C_\Sigma$  where  $C_\Sigma = C_B + C_J + C_g$  is the total capacity of the island. Thus, the Coulombic term is

$$\hat{H}_C = E_C (\hat{N} - N_g)^2 = E_C \left( -i \frac{\partial}{\partial \theta} - N_g \right)^2.$$

The Hamiltonian of the CPB is the sum of these two terms:

$$\hat{H} = E_C (\hat{N} - N_g)^2 + \frac{E_J}{2} \sum_N (|N\rangle \langle N+1| + |N+1\rangle \langle N|). \quad (2.22)$$

In the charge regime  $E_C \gg E_J$ ,  $\hat{N}$  is a good quantum number, and the energy eigenstates can be well approximated using only two nearest charge states. This regime suffers from a serious drawback because it is sensitive to charge noise, which dramatically reduces the coherence times as explained in 2.2.3.8.

This issue is solved in the regime  $E_J \gg E_C$ , which is reached in the so-called transmon design by increasing the geometrical capacitance  $C_B$  in order to decrease the charging energy  $E_C = 2e^2/C_\Sigma$ . In this  $E_J \gg E_C$  regime, many charge states have to be taken into account to accurately write the energy eigenstates  $|k\rangle$ , and it becomes convenient to move to a phase representation. In the phase eigenbasis the Hamiltonian is written:

$$\hat{H} = E_C \left( -i \frac{\partial}{\partial \theta} - N_g \right)^2 - E_J \cos(\hat{\theta}). \quad (2.23)$$

In this basis the Schrödinger equation takes the form of a Mathieu equation and the stationary solutions can be expressed exactly in terms of the Mathieu functions<sup>16</sup>. Specifically the energy spectrum is

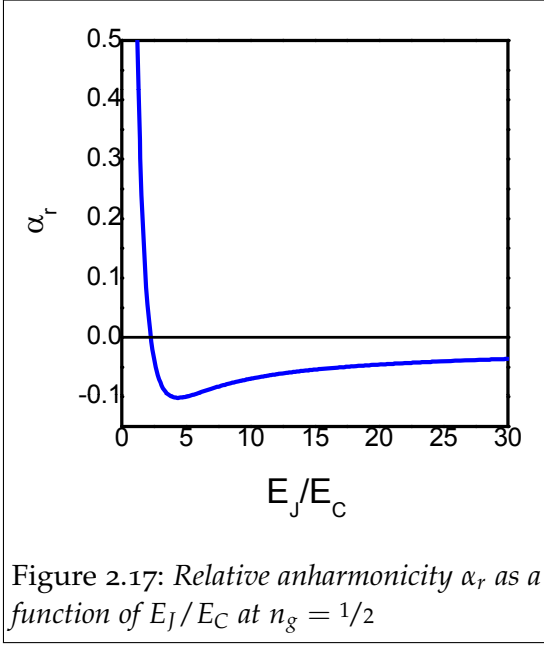
$$E_k = \frac{E_C}{4} \mathcal{M}_A \left[ k+1 - (k-1)(\text{mod } 2) + 2N_g(-1)^k, -\frac{2E_J}{E_C} \right]$$

where  $\mathcal{M}_A[r, q]$  stands for the characteristic value  $a_r$  for even Mathieu functions<sup>5</sup> with characteristic exponent  $r$  and parameter  $q$ .

This spectrum is anharmonic. To characterize the anharmonicity we define the absolute and relative anharmonicities

<sup>5</sup>This value can be obtained with Mathematica function `MathieuCharacteristicA[r, q]`





$$\alpha = E_{12} - E_{01},$$

$$\alpha_r = \frac{E_{12} - E_{01}}{E_{01}}.$$

where  $E_{ij} = E_j - E_i$ .

The anharmonicity only depends on  $N_g$  and  $E_J/E_C$ . Its dependence on  $E_J/E_C$  is shown in Fig. 2.17. It starts by decreasing, crossing zero at  $E_J/E_C \approx 9/4$  and reaching its minimum  $\alpha_r = -0.1$  at  $E_J/E_C \approx 4.4$ . In this thesis we work with  $E_J/E_C > 4.4$ , but at values not too large to stay away from the asymptotic limit  $\alpha_r(E_J/E_C \rightarrow \infty) = 0$ .

### Obtaining a tunable $E_J$ : the split CPB

It is very convenient to make the CPB transition frequency tunable in-situ. This is easily achieved by adding a second Josephson junction in parallel with the first one, so that both form a SQUID and  $E_J$  becomes tunable as a function of the flux  $\Phi$  threading the SQUID's loop.

The split CPB is shown in Fig. 2.18. The two junctions have Josephson energies  $E_{J1} = E_J(1 + d)/2$  and  $E_{J2} = E_J(1 - d)/2$  where  $E_J = E_{J1} + E_{J2}$  is the total Josephson energy and  $d$  is the asymmetry. The Josephson part of the Hamiltonian can be written

$$\hat{H}_J = -E_{J1} \cos(\hat{\theta}_1) - E_{J2} \cos(\hat{\theta}_2)$$

where  $\hat{\theta}_1$  and  $\hat{\theta}_2$  are the superconducting phase differences across each of the junctions, conjugate to the number of Cooper pairs transferred through each of them,  $\hat{N}_1$  and  $\hat{N}_2$ . Introducing the phase of the island  $\hat{\theta} = (\hat{\theta}_1 - \hat{\theta}_2)/2$ , which is the conjugate of the number of Cooper pairs in the island  $\hat{N} = \hat{N}_1 - \hat{N}_2$ , and  $\hat{\delta} = \hat{\theta}_1 + \hat{\theta}_2$ , the complete Hamiltonian is<sup>16</sup>

$$\hat{H} = E_C (\hat{N} - N_g)^2 - E_J \left[ \cos\left(\frac{\hat{\delta}}{2}\right) \cos(\hat{\theta}) + d \sin\left(\frac{\hat{\delta}}{2}\right) \sin(\hat{\theta}) \right]$$

Since the loop inductance is very small, the value of  $\hat{\delta}$  is determined by the flux quantization and can be considered a classical parameter  $\delta$ , proportional to the flux threading the SQUID loop:  $\delta = \Phi/\varphi_0$ . The Hamiltonian then reduces to:

$$\hat{H} = E_C \left( \frac{1}{i} \frac{\partial}{\partial \theta} - N_g \right)^2 - E_J^*(d, \delta) \cos(\hat{\theta}) \quad (2.24)$$

which is exactly the same as for a CPB but with a Josephson energy  $E_J^*(d, \delta)$  that is tunable by varying the flux:

$$E_J^*(d, \delta) = E_J \sqrt{\frac{1 + d^2 + (1 - d^2) \cos \delta}{2}}.$$

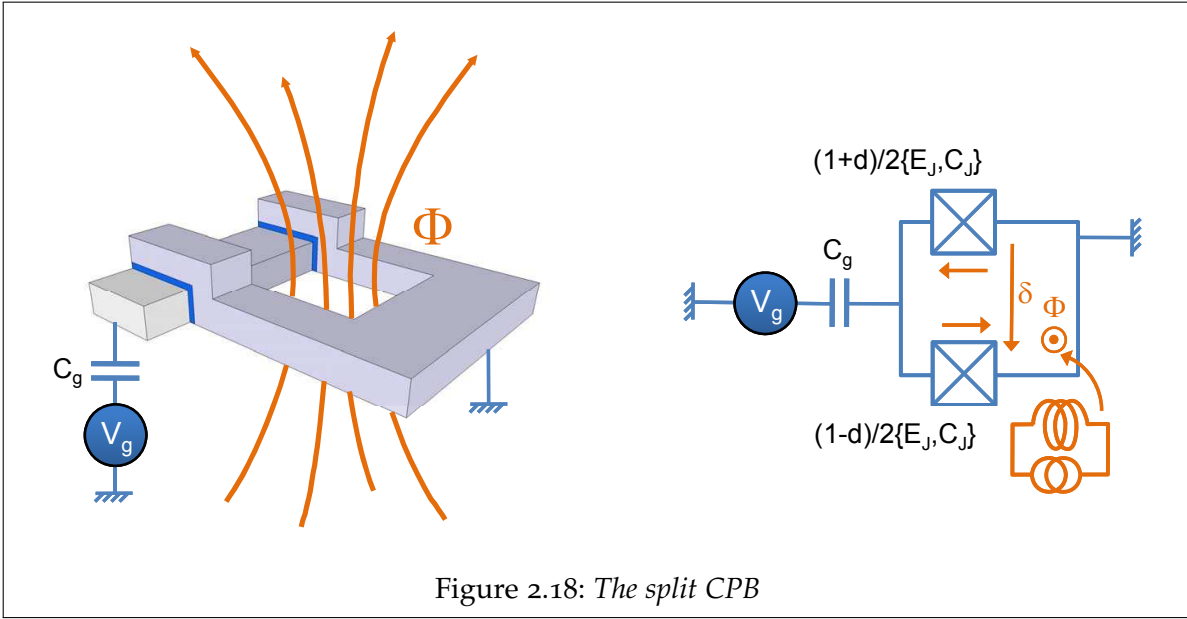


Figure 2.18: *The split CPB*

### 2.2.2 COHERENT MANIPULATION OF THE CPB

Because of the anharmonicity of the transmon, its two lowest energy eigenstates  $|g\rangle$  and  $|e\rangle$  can define a TLS, which can be operated as a qubit. One of the requirements to implement quantum algorithms is to be able to manipulate each qubit state in any desired way, implementing any single-qubit gate<sup>3</sup>. With the CPB such manipulations are performed by using sequences of quasi-resonant gate pulses, in a way similar to NMR<sup>6</sup>. In this section we summarize how to perform these manipulations, which are routine operations used in the rest of this thesis.

Any pure state of the TLS is a linear combination  $|\psi\rangle = \alpha |g\rangle + \beta |e\rangle$  (with  $\alpha, \beta \in \mathbb{C}$ ,  $|\alpha|^2 + |\beta|^2 = 1$ ), which can be also written as

$$|\psi\rangle = \cos(\theta/2) e^{-i\varphi/2} |g\rangle + \sin(\theta/2) e^{i\varphi/2} |e\rangle,$$

with  $\theta \in [0, \pi)$  and  $\varphi \in [0, 2\pi)$ , the polar and azimuth angles in spherical coordinates. The state of the qubit can be mapped to the points on a sphere of radius 1, the **Bloch sphere**, with north pole corresponding to the state  $|0\rangle$  and south pole to  $|1\rangle$ . The corresponding position is  $\vec{\psi} = \vec{u}_x \sin \theta \cos \varphi + \vec{u}_y \sin \theta \sin \varphi + \vec{u}_z \cos \theta$ .

The Bloch sphere is a useful tool to visualize the states as well as their evolution. Indeed any operator acting on a two-level system can be expressed as

$$\hat{A} = -1/2 \vec{a} \cdot \vec{\sigma} + \text{Tr}(\hat{A}) \mathbb{1}$$

where  $\vec{\sigma} = \vec{u}_x \hat{\sigma}_x + \vec{u}_y \hat{\sigma}_y + \vec{u}_z \hat{\sigma}_z$ . Using this representation  $\vec{h}$  for the Hamiltonian, the Schrödinger equation is equivalent to the precession

$$\dot{\vec{\psi}} = (\vec{h} \times \vec{\psi}) / \hbar$$

The unperturbed Hamiltonian of the CPB,  $\hat{H}_0 = \hbar \omega_{ge} \hat{\sigma}_z$ , corresponds then to a precession of the state around the  $z$  axis at angular speed  $\omega_{ge}$ . It is often convenient to cancel this rotation by moving to a frame rotating at  $\omega_{ge}$ .

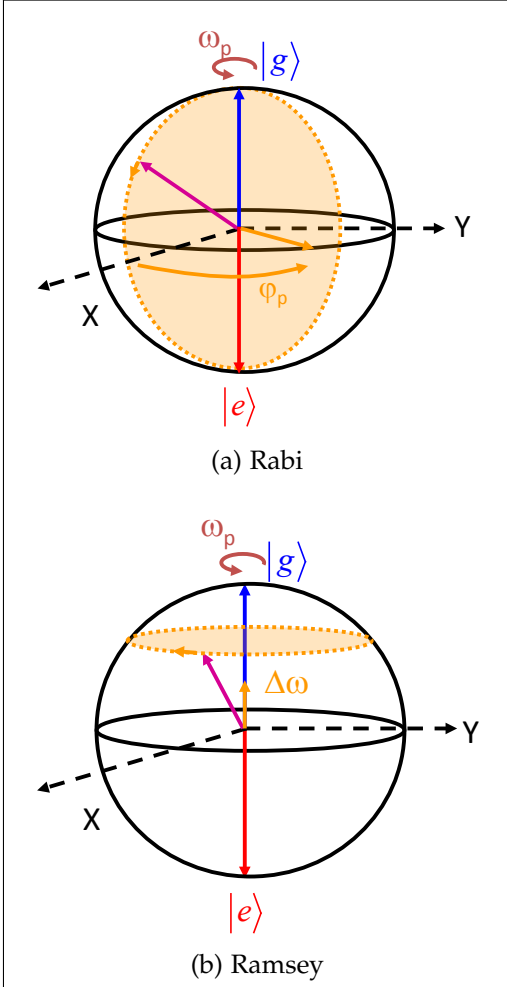


Figure 2.19: Coherent manipulations of the TLS state with microwave pulses represented in the Bloch sphere rotating at the microwave frequency  $\omega_p$ . (a) Rabi precession of the state induced by the microwave pulse. (b) Ramsey precession of the state when the pulse is tuned off.

In order to manipulate the state, a microwave pulse  $A_p \cos(\omega_p t + \varphi_p)$  is sent to the gate, creating a small harmonic perturbation

$$\hat{H}_P = -2E_C \Delta N_g \cos(\omega_p t + \varphi_p) \hat{n}$$

represented as a transverse field

$$2E_C \Delta N_g |\langle e | \hat{n} | g \rangle| \cos(\omega_p t + \varphi_p) \vec{x}.$$

In the frame rotating at  $\omega_p$ , this field becomes static after neglecting terms rotating at  $2\omega_p$  (RWA):

$$\vec{H}_P = -\frac{\hbar \omega_{R0}}{2} (\vec{x} \cos \varphi_p + \vec{y} \sin \varphi_p) - \vec{z} \frac{\hbar \delta \omega}{2},$$

where  $\omega_{R0} = 2E_C \Delta N_g |\langle e | \hat{n} | g \rangle| / \hbar$  is called the Rabi frequency, and  $\delta \omega = \omega_{ge} - \omega_p$  is the detuning between the TLS frequency and the applied microwave. This field induces a Rabi precession of the state around  $\vec{H}_P$  at the Rabi frequency  $\omega_R = \sqrt{\omega_{R0}^2 + \delta \omega^2}$ . When the pulse is turned off, the evolution of the qubit consists in a precession around  $z$  at an angular frequency  $\delta \omega$ . Combining these two behaviours it is possible to bring the state anywhere on the Bloch sphere.

### 2.2.3 DECOHERENCE

The coupling of the transmon to its environment causes the damping of its density matrix  $\rho$  towards its thermal equilibrium value:

$$\begin{pmatrix} |\alpha|^2 & \alpha\beta^* \\ \alpha^*\beta & |\beta|^2 \end{pmatrix} \xrightarrow{t \gg \Gamma_1^{-1}, \Gamma_2^{-1}} \begin{pmatrix} 1 - e^{-\frac{\hbar \omega_{ge}}{k_B T}} & 0 \\ 0 & e^{-\frac{\hbar \omega_{ge}}{k_B T}} \end{pmatrix}.$$

Although important progress has been made in recent years<sup>6,19,9</sup>, this damping occurs in all superconducting circuits with characteristic times in the microsecond range. This constitutes an important obstacle for implementing quantum processors with superconducting circuits. In this section we analyze this important issue and the different sources of decoherence.

This damping involves two processes:

- The **energy relaxation** consists in the decay of the diagonal part of  $\hat{\rho}$ . This decay involves the emission of the TLS excitation  $\hbar \omega_{ge}$  to the environment and it is characterized by a relaxation rate  $\Gamma_1$  or relaxation time  $T_1 = \Gamma_1^{-1}$ .

- The **decoherence** consists in the decay of the non-diagonal elements

$$\rho_{ge}(t) = \rho_{01}(0)e^{i\delta\omega t}e^{-\Gamma_1 t/2}f_{z,R}(t).$$

This decay is most often exponential with a rate  $\Gamma_2$  and is caused by two independent phenomena: the relaxation, which contributes to it by  $\Gamma_1/2$  and the **pure dephasing** of a superposition  $(|g\rangle + e^{i\varphi}|e\rangle)/\sqrt{2}$  (loss of  $\varphi$ ), due to random fluctuations of the transition frequency  $\omega_{ge}$  which most often yields  $f_{z,R}(t) = \exp(-\Gamma_\phi t)$ . The decoherence is best characterized by a Ramsey sequence of two  $\pi/2$  pulses followed by readout<sup>6</sup>.

Relaxation and decoherence have been studied in detail both experimentally<sup>17,85</sup> and theoretically<sup>19</sup> for the CPB and other superconducting qubit designs<sup>86,87,88,8</sup>.

### 2.2.3.1 General formalism for studying decoherence

We summarize here the main results for the transmon adopting the general formalism exposed in G. Ithier *et al*<sup>17</sup>. In this formalism we consider how the different sources of decoherence induce noise in the variables  $\lambda$  entering the Hamiltonian 2.24 –fluctuations of the gate charge  $N_g$ , for instance. Each of these sources induces a quantum noise  $\delta\lambda = \hat{\lambda} - \bar{\lambda}$  which can be characterized by its spectral density

$$S_\lambda(\omega) = \frac{1}{2\pi} \int \overline{\delta\hat{\lambda}(t)\delta\hat{\lambda}(t+\tau)} e^{i\omega\tau} d\tau$$

whose positive part  $S_\lambda(\omega > 0)$  corresponds to an absorption of energy by the TLS and vice versa.

We now derive the decoherence rates from these spectral densities. Assuming a weak coupling of the transmon to its environment, the Hamiltonian  $\hat{H} = -\vec{\sigma} \cdot \vec{H}/2$  can be linearized and each source of noise yields a perturbation

$$\delta\hat{H} = -\frac{\hbar}{2} \left( \vec{D}_\lambda \cdot \vec{\sigma} \right) \delta\lambda$$

where  $-1/2\hbar \vec{D}_\lambda \cdot \vec{\sigma}$  is the restriction of  $\partial\hat{H}/\partial\lambda$  to the  $|0\rangle$  and  $|1\rangle$  states. The longitudinal part  $D_{\lambda,z}\hat{\sigma}_z$  yields dephasing while the transverse part  $\vec{D}_{\lambda,\perp} \cdot \vec{\sigma}_z$  yields relaxation.

### 2.2.3.2 Relaxation

The relaxation rate  $\Gamma_1$  is given by the sum of energy absorption and emission, which can be calculated from the Fermi golden rule:

$$\Gamma_1 = \frac{\pi}{2} D_{\lambda,\perp}^2 \left[ \underbrace{S_\lambda(\omega_{ge})}_{\text{TLS relaxation}} + \underbrace{S_\lambda(-\omega_{ge})}_{\text{TLS excitation}} \right]$$

### 2.2.3.3 Pure dephasing caused by white noise sources

For white noise the pure dephasing yields an exponential decay of the coherences:

$$f_{z,R}(t) = \exp(-\Gamma_\phi t)$$

with a pure dephasing rate  $\Gamma_\phi$  which is calculated within Bloch-Redfield theory:

$$\Gamma_\phi = \pi S_{\delta\omega_{ge}}(0) = \pi D_{\lambda,z}^2 S_\lambda(0) \quad (2.25)$$

### 2.2.3.4 Pure dephasing caused by $1/f$ noise sources

The Bloch-Redfield approach fails when the noise has a singular spectral density at  $\omega = 0$ , as  $1/f$  noise has:

$$S_\lambda(\omega) = \frac{A^2}{|\omega|}$$

Then the evolution of the coherence  $\rho_{ge}(t)$  has to be calculated directly<sup>17</sup> and is characterized by the function

$$f_{z,R}(t) = \exp\left(-\frac{t^2}{2} D_{\lambda,z}^2 \int_{-\infty}^{\infty} S_\lambda(\omega) \text{sinc}^2\left(\frac{\omega t}{2}\right) d\omega\right).$$

In the case of  $1/f$  noise, a low cutoff frequency  $\omega_{\text{IR}}$  has to be introduced. It enters only logarithmically in the calculations, and is determined by the exact measurement protocol<sup>16</sup>. A rather good approximation is to consider that it is simply the rate at which data points are produced.

Then:

$$f_{z,R}(t) = \exp\left(-t^2 D_{\lambda,z}^2 A^2 |\ln \omega_{\text{IR}} t|\right).$$

A rough approximation can be made by substituting the logarithmic part by a constant. Typically  $\omega_{\text{IR}} \simeq 1$  Hz and  $t \simeq 1$   $\mu$ s, so  $|\ln \omega_{\text{IR}} t| \simeq 13.8$ . yielding a Gaussian decay  $\exp(-\Gamma_\phi^2 t^2)$  with a rate:

$$\Gamma_\phi = 3.7A \left| \frac{\partial \omega_{ge}}{\partial \lambda} \right|.$$

If the linear susceptibility  $D_{\lambda,z}$  vanishes, a second order perturbative expansion is needed. In this case there is a crossover between two behaviours: at short times  $t \ll t_c = 2/(A \partial \omega_{ge}^2 / \partial \lambda^2)$  the decay is algebraic and on longer times  $t \gg t_c$  it becomes exponential with a rate

$$\Gamma_\phi = \frac{A^2 \pi}{2} \frac{\partial^2 \omega_{ge}}{\partial \lambda^2}.$$

### 2.2.3.5 Pure dephasing during driven evolution

During a driven evolution with a Rabi frequency  $\omega_{R0}$  and detuning  $\delta\omega$ , the state precesses around an axis forming an angle  $\eta = \arctan(\omega_{R0}/\delta\omega)$  with the  $z$  axis. The resulting relaxation rate<sup>17</sup>

$$\tilde{\Gamma}_1 = \Gamma_{\omega_R} \sin^2 \eta + \Gamma_1 \frac{1 + \cos^2 \eta}{2}$$

and pure dephasing rate

$$\tilde{\Gamma}_\phi = \frac{\Gamma_1}{2} \sin^2 \eta + \Gamma_\phi \cos^2 \eta$$

depend on the rate

$$\Gamma_{\omega_R} = \pi S_{\delta\omega_{ge}}(\omega_R) = \pi D_{\lambda,z}^2 S_\lambda(\omega_R),$$

which shows that the relaxation rate becomes dependent of the spectral density *at the Rabi frequency*. The resulting decoherence rate, which gives the decay rate of Rabi oscillations (for  $\delta\omega = 0$ ) is

$$\tilde{\Gamma}_2 = \Gamma_R = 1/2\tilde{\Gamma}_1 + \tilde{\Gamma}_\phi = 3/4\Gamma_1 + 1/2\Gamma_{\omega_R}. \quad (2.26)$$

### 2.2.3.6 Sources of decoherence

The different sources of decoherence correspond to the external variables in the Hamiltonian 2.24. These sources are:

- **charge noise**, which consists in a fluctuating contribution to  $N_g$  coming from gate voltage noise, two-level fluctuators in the transmon and possibly the creation of quasi-particles.
- **flux noise** on  $\delta$  which comes from the universal  $1/f$  flux noise, as well as the fluctuations of the current in the coil which generates the flux threading the transmon loop.
- **$E_J$  noise** coming from microscopic defects which create fluctuations of the the CPB junction's  $I_0$ .

### 2.2.3.7 Relaxation

*Through the gate circuit*

The main mechanism for relaxation is the **emission to the gate circuit**. An advantage of the cQED setup is that the gate circuit is filtered by the resonator that protects the TLS from environmental noise, as analyzed below in 2.3.1.

Noting  $Z_g(\omega)$  the impedance seen from the gate, the fluctuations of gate voltage are characterized by their spectral density

$$S_{V_g}(\omega) = \frac{\hbar\omega}{2\pi} \left[ \coth\left(\frac{\hbar\omega}{2k_B T}\right) + 1 \right] \text{Re}(Z_g(\omega)).$$

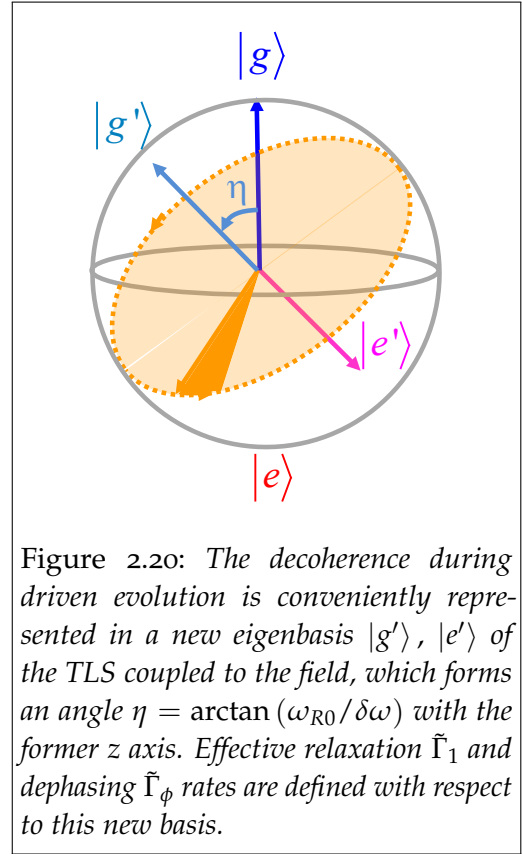


Figure 2.20: The decoherence during driven evolution is conveniently represented in a new eigenbasis  $|g'\rangle, |e'\rangle$  of the TLS coupled to the field, which forms an angle  $\eta = \arctan(\omega_{R0}/\delta\omega)$  with the former  $z$  axis. Effective relaxation  $\tilde{\Gamma}_1$  and dephasing  $\tilde{\Gamma}_\phi$  rates are defined with respect to this new basis.

The sensitivity to gate charge fluctuations is given by  $\hbar D_{N_g, \perp} = 4E_C \langle g | \hat{N} | e \rangle$ . The resulting relaxation rate is

$$\Gamma_1^{gate} = \frac{\pi}{2} |D_{N_g, \perp}|^2 \left( \frac{C_g}{2e} \right)^2 [S_{V_g}(\omega_{ge}) + S_{V_g}(-\omega_{ge})].$$

At low temperatures  $k_B T \ll \hbar \omega_{ge}$ ,  $S_{V_g}(-\omega_{ge})$  becomes negligible, so that<sup>16</sup>

$$\Gamma_1^{gate} = 16\pi\beta^2\omega_{ge} \frac{\text{Re}(Z(\omega_{ge}))}{R_K} |\langle g | \hat{n} | e \rangle|^2, \quad (2.27)$$

where  $R_K = h/e^2$  and  $\beta = C_g/C_\Sigma$ . This expression is used below to calculate the relaxation of the transmon through the resonator (see 2.3.1).

### *Through on-chip flux lines*

In our setup a coil is used for creating a magnetic flux  $\Phi$  through the transmon loop to tune its transition frequency  $\omega_{ge}$ . However, in future experiments involving many transmons, in order to control individually their transition frequencies, such coil should be complemented with on-chip flux-lines. The fluctuations on the currents flowing through these lines couple to the current in the transmon loop through their mutual inductance  $M$  yielding a relaxation channel. The goal of this paragraph is to calculate the relaxation rate associated to this channel.

The fluctuations of the flux-line current result in fluctuations of the flux, which are characterized by the spectral density

$$S_{\Phi/\varphi_0}(\omega) = \left( \frac{M}{\varphi_0} \right)^2 S_I(\omega) = \left( \frac{M}{\varphi_0} \right)^2 \frac{\hbar\omega}{2\pi} \text{Re} \left( \frac{1}{Z_{coil}(\omega)} \right) \left[ \coth \left( \frac{\hbar\omega}{2k_B T} \right) + 1 \right].$$

The sensitivity to these fluctuations is

$$|D_{\Phi/\varphi_0, \perp}| = \frac{E_J}{2} \sqrt{1 - (1 - d^2) \cos^2 \left( \frac{\Phi}{2\varphi_0} \right)},$$

so the resulting relaxation rate is

$$\Gamma_1^{FL} = \frac{\pi}{2} S_{\delta\omega, \perp}(\omega_{ge}) = \frac{\pi}{2} |D_{\Phi/\varphi_0, \perp}|^2 S_{\Phi/\varphi_0}(\omega_{ge}).$$

Therefore, when designing flux lines, the mutual inductance has to be small enough so that  $\Gamma_1^{FL}$  is a negligible contribution to the total relaxation rate.

### *Microscopic relaxation mechanisms: saturation of the relaxation time*

Relaxation mechanisms of microscopic origin, and thus with rates which are not easily calculated, seem to play an important role for the transmon. Indeed, in most



experiments the relaxation through the resonator is not able to fully explain the observed relaxation times<sup>9</sup>, which somehow seem to saturate at a sample-dependent value, typically between 500 ns and some  $\mu$ s.

We have already seen in 2.1.5 that superconducting resonators also lose energy in an unexplained way. For the resonators, this may be linked to mechanisms of not yet understood phase noise induced by the dielectrics covering the surface of the superconductors. A first hypothesis is that this very same mechanism could be responsible for the excess relaxation observed in the transmon.

Another possible explanation is that the extra relaxation comes from non-equilibrium quasi-particles which would poison the island and induce relaxation even in charge-insensitive qubits<sup>89</sup>.

Some other relaxation mechanisms have been analyzed<sup>90</sup> –the radiation of the TLS electric and magnetic dipole, the dissipative currents created by induction on non-superconducting metals around the sample– but their relaxation times should be much longer than the ones measured.

### 2.2.3.8 Dephasing

#### *E<sub>J</sub> noise*

The Josephson junctions of the transmon have fluctuations in their critical current  $I_0$  with  $1/f$  spectrum. The most accepted hypothesis is that these fluctuations come from trapping and releasing of charges in microscopic defects of the barrier. The presence of these charges affects the barrier height and thus the critical current as analyzed by Van Harlingen *et al.*<sup>86</sup>.

The corresponding dephasing rate is:

$$\Gamma_{\phi}^{\delta E_J} \sim 3.7A \left| \frac{\partial \omega_{ge}}{\partial I_c} \right| = 1.4\bar{A}\omega_{ge},$$

where  $\bar{A} = A/I_0$  is the dimensionless amplitude of  $I_0$  fluctuations. For typical parameters ( $\bar{A} = 10^{-6}$  and  $\omega_{ge} = 6$  GHz) this dephasing time is  $T_{\phi} \simeq 120 \mu$ s, much longer than the experimental  $T_{\phi}$  measured in this thesis.

#### *Flux noise*

Noise in the magnetic flux threading the transmon loop induces dephasing. Fluctuations on the current of the coil circuit or fluctuations of the magnetic field also yield this kind of noise.

A universal  $1/f$  flux noise, which is likely to be caused by microscopic mechanisms, has been also observed and is currently a research topic<sup>91,92</sup>. It is characterized by a typical amplitude  $A = 10^{-5}\Phi_0$ , yielding a dephasing rate

$$\Gamma_{\phi}^{\delta \Phi} \sim 3.7A \left| \frac{\partial \omega_{ge}}{\partial \Phi} \right| = 3.7 \frac{\pi A}{\hbar \Phi_0} \sqrt{2E_C (E_{J1} + E_{J2})} \left| \sin \left( \frac{\pi \Phi}{\Phi_0} \right) \tan \left( \frac{\pi \Phi}{\Phi_0} \right) \right|$$

valid for  $E_J \gg E_C$ . For representative values  $\Phi = \Phi_0/4$  and  $E_J = 30 \text{ GHz} = 20 E_C$  this yields a dephasing time of  $\Gamma_\phi^{-1} \sim 2 \mu\text{s}$ , whereas at sweet spot  $\Phi = 0$  this rate vanishes and the second order contribution

$$\Gamma_\phi^{\delta\Phi} \sim \frac{A^2\pi}{2} \left| \frac{\partial^2 \omega_{ge}}{\partial \Phi^2} \right|$$

yields  $\Gamma_\phi^{-1} \sim 3.6 \text{ ms}$ <sup>19</sup> which is not relevant compared to other dephasing sources in the experiment.

### Charge noise

Charges hopping from a microscopic trapping site to another yielding  $1/f$  charge noise have been a major problem for former charge qubits<sup>18</sup>. A first approach to overcome this problem is to improve the materials and fabrication techniques<sup>88</sup> in order to suppress this effect, although up to now no significant suppression of  $1/f$  charge noise has been achieved in this way.

Another approach consists in reducing the sensitivity of the CPB to such noise. This was performed first in the Quantronium design by operating the TLS at precise biasing points where it is insensitive to charge noise to the first order<sup>6</sup>. The transmon goes one step further since the sensitivity to charge fluctuations decreases exponentially with  $E_J/E_C$ . Indeed

$$\Gamma_\phi^{\delta N_g} \sim 3.7A \left| \frac{\partial \omega_{ge}}{\partial N_g} \right|$$

yields in the  $E_J \gg E_C$  regime<sup>19</sup>

$$\Gamma_\phi^{\delta N_g} \sim 3.7 \frac{A\pi}{\hbar} |(\epsilon_1 - \epsilon_0) \sin(2\pi N_g)| \lesssim 3.7 \frac{A\pi}{\hbar} |\epsilon_1|,$$

where  $\epsilon_1$  is the amplitude of modulation in  $N_g$  of the first excited energy level  $m = 1$ . For  $E_J \gg E_C$  the general expression of  $\epsilon_m$  is

$$\epsilon_m \simeq (-1)^m E_C \frac{2^{4m+3}}{m!} \sqrt{\frac{2}{\pi}} \left( \frac{2E_J}{E_C} \right)^{\frac{m}{2} + \frac{3}{4}} \exp\left(-\sqrt{\frac{32E_J}{E_C}}\right).$$

Therefore the sensitivity to charge noise is exponentially reduced when increasing  $E_J/E_C$ , yielding  $(\Gamma_\phi^{\delta N_g})^{-1} \simeq 3 \text{ s}$  for a transmon with typical parameters ( $E_J = 30 \text{ GHz}$ ,  $E_C = 1.4 \text{ GHz}$ ) and with  $A = 10^{-4}$  (from Zorin *et al.*<sup>93</sup>).

#### 2.2.4 THE TRANSMON: PERTURBATIVE APPROXIMATION OF THE ANHARMONICITY

Although it was introduced as a capacitively-shunted CPB working in the  $E_J \gg E_C$  regime, the transmon admits a simpler description as an *LC resonator with a non-linear inductance* –the Josephson junction. In this description, the transmon is treated as a

harmonic oscillator, plus an anharmonic term that can be developed perturbatively<sup>19</sup>. Even though it is only an approximate description compared to the more exact model given above, this point of view gives an interesting complementary physical picture to the transmon. It also yields simplified useful analytical results, valid in the  $E_J \gg E_C$  limit.

The Hamiltonian Eq. 2.23 shows that the Josephson term is dominant and then that the fluctuations of  $\hat{\theta}$  are small. Thus we expand the cosine for small angles and obtain

$$\hat{H} = \sqrt{2E_J E_C} (\hat{b}^\dagger \hat{b} + 1/2) - E_J - \frac{E_C}{3} (\hat{b}^\dagger + \hat{b})^4 + O(\hat{b}^6),$$

where  $\hat{b} = (E_J/8E_C)^{1/4} \hat{\theta} + i(E_C/2E_J)^{1/4} (\hat{N} - N_g)$ . Expanding the quartic term, we find the first order approximation  $E_k^{(1)}$  for the energy levels:

$$E_k^{(1)} = \sqrt{2E_J E_C} (k + 1/2) - E_C (2k^4 + 2k + 1).$$

This yields a convenient approximation for the anharmonicity:

$$\alpha = E_{12} - E_{01} \approx (E_2^{(1)} - E_1^{(1)}) - (E_1^{(1)} - E_0^{(1)}) = E_C,$$

which can be refined by introducing higher order terms and developing to higher orders in perturbation.

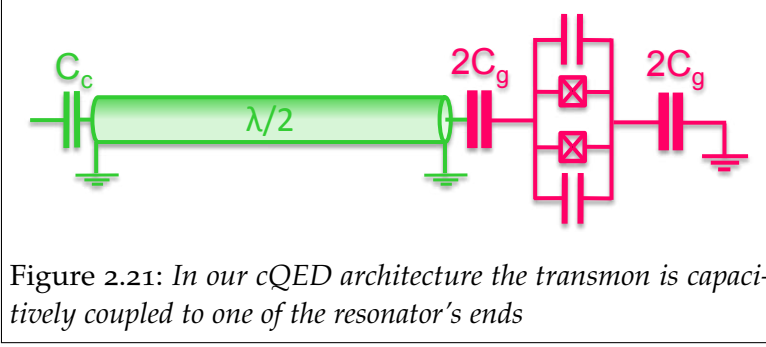
The matrix elements  $|\langle j+k | \hat{N} | j \rangle|$  determine the coupling of the transmon to the resonator. A convenient approximation for those terms, obtained from  $\hat{N} - N_g = -i(E_J/8E_C)^{1/4} (\hat{b} - \hat{b}^\dagger)$ , is

$$|\langle j+k | \hat{N} | j \rangle| \approx \begin{cases} \sqrt{j+1/2(k+1)} \left(\frac{E_J}{8E_C}\right)^{1/4} & k = \pm 1 \\ 0 & \text{otherwise.} \end{cases}$$

It means that, like the harmonic oscillator, *only adjacent levels are coupled* and that the coupling  $j \leftrightarrow j-1$  grows as  $\sqrt{j}$ . Note that expanding to further orders, the elements  $|\langle 2i | \hat{N} | 2j \rangle|$  ( $i$  and  $j$  being arbitrary integers) are much smaller than the  $|\langle 2i+1 | \hat{N} | 2j \rangle|$  ones. Indeed, the application of  $\hat{N}$  to a state of even parity  $|2i\rangle$  results in a superposition of states of odd parity yielding a very small superposition with states of even parity, and conversely.

We want to stress, however, that this convenient perturbative treatment is incomplete. It does not reproduce any charging effects, since it disregards the periodicity in phase of the wavefunction  $\psi(\phi + 2\pi) = \psi(\phi)$ , assuming a variation of the phase  $-\infty < \phi < \infty$ . It is impossible in this perturbative approach to calculate, for instance, the charge dispersion  $\epsilon_m$ , and therefore to demonstrate the low sensitivity of the transmon to charge noise. This is the reason why our study of the transmon was first presented from the CPB perspective.

### 2.3 TRANSMON-RESONATOR COUPLING



In our experiments the transmon is capacitively coupled to the voltage  $\hat{V}(\Lambda)$  at one of the resonator ends. Thus, the gate charge  $N_g$  has two components, the first coming from a DC bias voltage  $V_g^{DC}$  and the second one to the oscillating resonator voltage  $\hat{V}(\Lambda)$  (Eq. 2.4):

$$N_g 2e = C_g \left[ V_g^{DC} + \hat{V}(\Lambda) \right].$$

The Hamiltonian Eq. 2.23 then becomes

$$\hat{H} = E_C \left( \hat{N} - N_g^{DC} \right)^2 - E_J^*(\delta, d) \cos \hat{\theta} - \underbrace{E_C \frac{C_g}{e} \hat{N} \hat{V}(\Lambda)}_{\hat{H}_{int}} + E_C \frac{C_g}{2e} \left[ \hat{V}^2(\Lambda) - 2N_g^{DC} \hat{V}(\Lambda) \right].$$

The last term produces a renormalization of the resonator capacitance, whereas  $\hat{H}_{int}$  corresponds to the coupling between the resonator and the transmon, which can be written as

$$\hat{H}_{int} = -E_C \frac{C_g}{e} \hat{N} \hat{V}(\Lambda) = -2e \frac{C_g}{C_\Sigma} \hat{N} \sqrt{\frac{\hbar \omega_r}{\Lambda c}} (\hat{a} + \hat{a}^\dagger) = -\hbar g_0 \hat{N} (\hat{a} + \hat{a}^\dagger)$$

with  $\hbar g_0 = 2e\beta\sqrt{\hbar\omega_r/\Lambda c}$  the coupling constant, and where we are only considering the first resonator mode ( $\hat{a} = \hat{a}_1$ ). The Hamiltonian of the coupled system is then

$$\hat{H}_{cQED} = \underbrace{\hat{H}_{CPB} + \hbar\omega_r (\hat{a}^\dagger \hat{a} + 1/2)}_{\text{resonator}} - \underbrace{\hbar g_0 \hat{N} (\hat{a} + \hat{a}^\dagger)}_{\text{interaction}}.$$

Now, in the RWA,

$$\hat{H}_{cQED} \approx \sum_{i=0}^{\infty} \hbar\omega_i |i\rangle \langle i| + \hbar\omega_r (\hat{a}^\dagger \hat{a} + 1/2) + \hbar \sum_{i=0}^{\infty} g_{i,i+1} (\hat{a} |i+1\rangle \langle i| + \hat{a}^\dagger |i\rangle \langle i+1|), \quad (2.28)$$

with  $g_{i,i+1} = g_0 \langle i | \hat{N} | i+1 \rangle$  the coupling strength constant between transmon levels  $i$  and  $i+1$  and  $\hbar\omega_i$  the energy of the  $i$ -th transmon level. In some situations, it is appropriate to restrict this Hamiltonian to the first two energy levels of the transmon, which yields the Jaynes-Cummings Hamiltonian

$$\hat{H}_{TLS} = \frac{\hbar\omega_{01}}{2} \hat{\sigma}_z + \hbar\omega_r (\hat{a}^\dagger \hat{a} + 1/2) + \hbar g (\hat{\sigma}^+ \hat{a} + \hat{\sigma}^- \hat{a}^\dagger), \quad (2.29)$$

where  $g = g_{01}$  and  $\omega_{01} = \omega_1 - \omega_0$ . In the rest of this section, we will detail the most relevant physical consequences of this Jaynes-Cummings Hamiltonian for this

thesis. As we will see, they strongly depend on the ratio between the qubit-resonator detuning  $\Delta = \omega_r - \omega_{01}$  and  $g$ . We will also see in 2.3.3 that in the dispersive regime  $|\Delta| \gg g$ , the multi-level character of the transmon brings significant alterations to the usual results of cavity QED physics.

### 2.3.1 RELAXATION THROUGH THE RESONATOR: THE PURCELL EFFECT

In cQED the gate of the CPB is connected to the resonator. Here we want to calculate the CPB relaxation induced by its coupling to the  $50 \Omega$  environment through the resonator.

An approximate and useful formula is obtained by modelling the distributed resonator by its equivalent lumped parallel RLC circuit seen from the CPB, as described in Fig. 2.8. The impedance seen from the CPB is then  $Z_{RLC}(\omega) = R/(1 + 2j(\omega - \omega_r)/\kappa)$ , with  $R = 2\omega_r Z_0/(\pi\kappa)$ . According to Eq. 2.27, the CPB relaxation rate through the gate circuit is governed by

$$\text{Re} [Z(\omega_{ge})] = \frac{R}{1 + (2\Delta/\kappa)^2} = \frac{Z_0\omega_r}{2\pi} \frac{\kappa}{\Delta^2 + \kappa^2/4}.$$

Using Eq. 2.27 we obtain

$$\begin{aligned} \Gamma_1^{gate} &= 16\pi\beta^2\omega_{ge} \frac{\text{Re} [Z(\omega_{ge})]}{R_K} |\langle g | \hat{n} | e \rangle|^2 = 2\pi \frac{\omega_{ge}}{Z_0\omega_r^2} g^2 \text{Re} [Z(\omega_{ge})] \\ &= \kappa \frac{g^2}{\Delta^2 + \kappa^2/4}. \end{aligned}$$

Therefore, the CPB relaxation to the gate is controlled by the resonator relaxation rate  $\kappa$ . If the resonator has a very high  $Q$  (i.e. low  $\kappa$ ), its response is sharply centered around its resonance frequencies, reducing the emission to the environment. In this sense, the resonator acts as a *filter* for the environmental noise that induces relaxation. This is a manifestation of the so-called *Purcell effect*<sup>94</sup>, which can be used to control the relaxation time of the transmon, provided that the other relaxation channels are slow enough.

A more accurate calculation of the relaxation due to this mechanism which takes into account higher order modes can be performed by using the complete expression of the resonator impedance as seen from the transmon,

$$\text{Re}(Z_{res}) = \text{Re} \left[ \frac{-j}{\omega C_g} + Z_0 \frac{Z_L \cos(\beta\Lambda) + iZ_0 \sin(\beta\Lambda)}{Z_0 \cos(\beta\Lambda) + iZ_L \sin(\beta\Lambda)} \right],$$

with  $Z_L = Z_0 - j/(\omega C_c)$  the load impedance that corresponds to the coupling capacitor and the  $Z_0$  line. Houck *et al.*<sup>85</sup> demonstrated experimentally that it is possible using such an analysis to account for the relaxation rate of the TLS until, for large detunings  $\Delta$ , some yet unexplained microscopic mechanism of relaxation become predominant, producing a saturation of the relaxation time.

The resonator might also have parasitic modes, which have not been considered in the analysis above. For instance, CPW resonators have an antisymmetric mode,

in which one of the ground planes has a finite voltage compared to the other. The symmetric position of the qubit with respect to the symmetry plane in our circuits was chosen in order to avoid couplings to those modes with uncontrolled impedances.

### 2.3.2 RESONANT REGIME: VACUUM RABI SPLITTING

In addition to affecting the relaxation properties of the TLS, the coupling to the resonator strongly modifies its dynamics. When the TLS transition frequency matches the resonator frequency ( $\omega_{ge} = \omega_r$ ), the TLS and resonator are able to coherently exchange energy<sup>13</sup>. The coupled system energy eigenfunctions then are not anymore separable resonator-TLS states but become instead coherent superpositions of the qubit and photon (resonator) states, the so-called *quton*  $(|g, 1\rangle + |e, 0\rangle) / \sqrt{2}$  and *phobit*  $(|g, 1\rangle - |e, 0\rangle) / \sqrt{2}$  as seen in Fig. 2.22.

The Jaynes-Cummings Hamiltonian (Eq. 2.29) can be exactly diagonalized<sup>13</sup> in the RWA, yielding the dressed eigenstates

$$\begin{aligned} |+, n\rangle &= \cos \theta_n |e, n\rangle + \sin \theta_n |g, n+1\rangle \\ |-, n\rangle &= -\sin \theta_n |e, n\rangle + \cos \theta_n |g, n+1\rangle \end{aligned}$$

with

$$\theta_n = 1/2 \cot \left( \frac{2g\sqrt{n+1}}{\Delta} \right)$$

and the eigenenergies

$$\begin{aligned} E_{\pm, n} &= \hbar\omega_1 (n+1) \\ &\pm 1/2\hbar\sqrt{4g^2(n+1) + \Delta^2}. \end{aligned}$$

At resonance,  $\Delta = 0$ , an *avoided crossing* of width  $2g$  opens in the energy spectrum between the levels of the resonator and the TLS. The most immediate manifestation of this anti-crossing is visible in the central curve of Fig. 2.22: the usual  $2\pi$  shift at resonance disappears, and is split in two shifts separated by  $2g$ : This phenomenon is known as the *vacuum Rabi splitting*. This splitting is the first manifestation of the strong coupling regime ( $g \gg \Gamma_1, \Gamma_2$ ); its observation at Yale in 2004<sup>11</sup> demonstrated

that cavity QED experiments could be performed with superconducting circuits, opening the field of circuit QED.

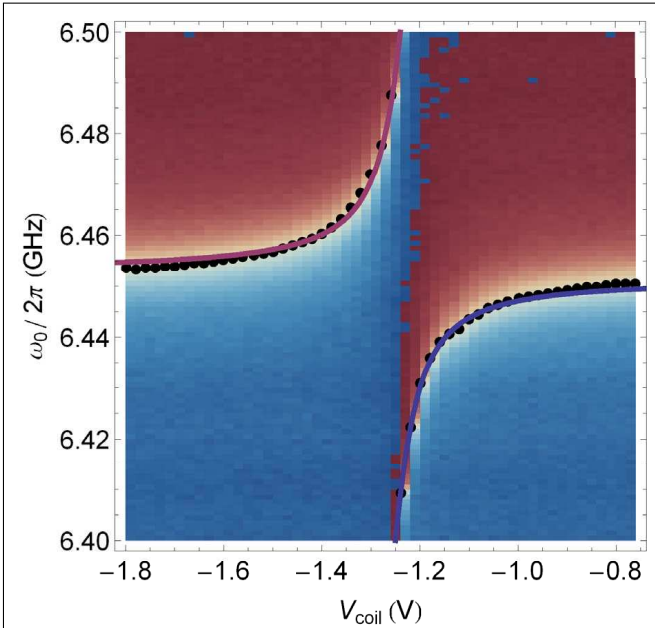


Figure 2.22: Anti-crossing between the resonator and the TLS: the phase of the resonator as a function of the frequency at the vicinity of the flux for which  $\Delta \rightarrow 0$ .

### 2.3.3 DISPERSIVE REGIME: CAVITY PULL AND AC-STARK SHIFT

The experiments performed in this thesis are mostly performed in the dispersive regime, for which the TLS and resonator are far detuned ( $|\Delta| \gg g$ ) so that they do not exchange energy, but only shift each other's frequency.

To get insight into this regime, we diagonalize the Hamiltonian 2.28 by applying the unitary transformation  $\hat{D} = \exp(\hat{S} - \hat{S}^\dagger)$  with<sup>19</sup>

$$\hat{S} = \sum_i \frac{g_{i,i+1}}{\omega_{i,i+1} - \omega_r} \hat{a} |i+1\rangle \langle i| \approx \frac{\chi_{01}}{g_{01}} \hat{a} |1\rangle \langle 0| + \frac{\chi_{12}}{g_{12}} \hat{a} |2\rangle \langle 1|,$$

where  $\omega_{i,j} = \omega_j - \omega_i$ ,  $\chi_{i,i+1} = g_{i,i+1}^2 / (\omega_{i,i+1} - \omega_r)$  and neglecting the transmon levels above the second one. Then, using the Baker-Campbell-Hausdorff relation

$$e^{-\lambda \hat{X}} \hat{H} e^{\lambda \hat{X}} = \hat{H} + \lambda [\hat{H}, \hat{X}] + \lambda^2 [[\hat{H}, \hat{X}], \hat{X}] + O(\lambda^3),$$

we obtain

$$\begin{aligned} \frac{\hat{H}_{eff}}{\hbar} &= \frac{\hat{D} \hat{H} \hat{D}^\dagger}{\hbar} = \sum_{i=0}^{\infty} \omega_i |i\rangle \langle i| + \omega_r \left( \hat{a}^\dagger \hat{a} + 1/2 \right) + \sum_{i=0}^{\infty} \chi_{i,i+1} |i+1\rangle \langle i+1| - \chi_{01} \hat{a}^\dagger \hat{a} |0\rangle \langle 0| \\ &+ \sum_{i=1}^{\infty} (\chi_{i-1,i} - \chi_{i,i+1}) \hat{a}^\dagger \hat{a} |i\rangle \langle i| + \sum_{i=1}^{\infty} \eta_i \hat{a} \hat{a} |i+2\rangle \langle i| + O \left[ \left( \frac{g_{i,i+1}}{\Delta_{i,i+1}} \right)^3 \right], \end{aligned} \quad (2.30)$$

where the last but one term that corresponds to two-photon transitions can be neglected since

$$\eta_i = \frac{g_{i,i+1} g_{i+1,i+2} (2\omega_{i+1} - \omega_i - \omega_{i+2})}{2(\omega_{i+1} - \omega_i - \omega_r)(\omega_{i+2} - \omega_{i+1} - \omega_r)} \ll \chi_{i,j}.$$

Specifically if we keep only the two lowest energy levels  $|0\rangle$  and  $|1\rangle$ , plus the shifts induced by level  $|2\rangle$ , we get

$$\frac{\hat{H}_{disp}}{\hbar} = 1/2 \underbrace{(\omega_{01} + \chi_{01})}_{\omega_{ge}} \hat{\sigma}_z + \underbrace{(\omega_r - 1/2\chi_{12})}_{\omega_c} \left( \hat{a}^\dagger \hat{a} + 1/2 \right) + \underbrace{(\chi_{01} - 1/2\chi_{12})}_{\chi} \hat{\sigma}_z \left( \hat{a}^\dagger \hat{a} + 1/2 \right),$$

which is the Jaynes-Cummings dispersive Hamiltonian for a TLS, with renormalized parameters, as the dispersive shift  $\chi$ .

The coupling term  $\chi \hat{\sigma}_z \hat{a}^\dagger \hat{a}$  allows no energy exchange since it commutes with the other terms in the Hamiltonian. However, it shifts the energy levels of both the resonator and the atom. Indeed, this Hamiltonian may be written in the form

$$\hat{H}_{disp} = 1/2 \hbar \omega_{ge} \hat{\sigma}_z + \underbrace{\hbar (\omega_c + \chi \hat{\sigma}_z)}_{\text{pulled cavity}} \left( \hat{a}^\dagger \hat{a} + 1/2 \right), \quad (2.31)$$

where the term labelled as *pulled cavity* remains the Hamiltonian of a harmonic oscillator, but with frequency  $\omega_c + \chi$  when the TLS is in its  $|g\rangle$  state and  $\omega_c - \chi$  when



it is in its  $|e\rangle$  state. This TLS-dependent resonator shift, called *cavity pull* is used all along this thesis for characterizing the TLS state. It is worth noting that due to the renormalization of the resonator frequency to  $\omega_c$ , in contrast with the case of a TLS, the uncoupled resonance frequency  $\omega_r$  of the resonator is not in the middle of the resonator shifted lines the  $|g\rangle$  and  $|e\rangle$  states.

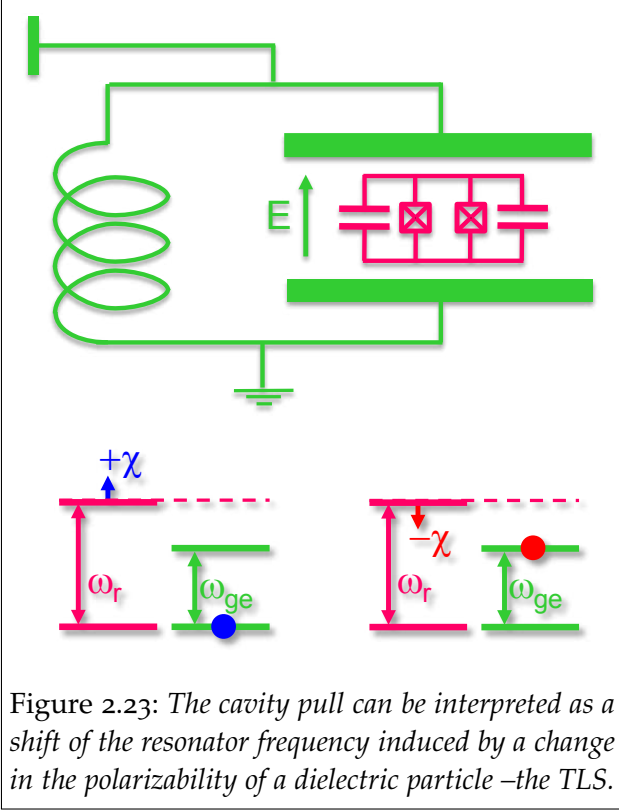


Figure 2.23: The cavity pull can be interpreted as a shift of the resonator frequency induced by a change in the polarizability of a dielectric particle –the TLS.

Reordering the terms in the dispersive Hamiltonian 2.31 we obtain

$$\hat{H}_{disp} = \hbar\omega_c \left( \hat{a}^\dagger \hat{a} + 1/2 \right) + \underbrace{+ 1/2\hbar \left[ \omega_{ge} + \chi \left( \hat{a}^\dagger \hat{a} + 1/2 \right) \right]}_{\text{shifted TLS}} \hat{\sigma}_z. \quad (2.32)$$

The term labelled *shifted TLS* corresponds to a TLS transition frequency  $\omega'_{ge} = \omega_{ge} + \chi (n + 1/2)$ , shifted by an amount proportional to the number of photons stored in the resonator (the AC-Stark shift of atomic physics) plus half a photon for the zero-point fluctuations (Lamb shift). Experimentally, this AC-Stark shift is particularly interesting since it allows an in-situ calibration of the number of photons stored in the resonator, as shown in the next chapters.

### 2.3.3.1 Breakdown of the dispersive approximation

The diagonalization Eq. 2.30 is only approximate. Considering only the two lowest states of the TLS, an exact diagonalization<sup>6</sup> of the Hamiltonian 2.28 can be performed<sup>49</sup> and yields:

$$\hat{H}_{exact} = \frac{\hbar\omega_{ge}}{2} \hat{\sigma}_z + \hbar\omega_c \left( \hat{a}^\dagger \hat{a} + 1/2 \right) - \frac{\hbar\Delta}{2} \hat{\sigma}_z \left( 1 - \sqrt{1 + \frac{4g^2}{\Delta^2} \hat{v}} \right),$$

where  $\hat{v} = \hat{a}^\dagger \hat{a} + |e\rangle \langle e|$  is the total number of excitations in the system. If this number is low compared to  $\Delta^2/4g^2 = n_{crit}$  which is called the critical number of photons, the last term results in the dispersive term of Eq. 2.31. Conversely, if the number of photons in the resonator  $n$  becomes comparable to  $n_{crit}$ , the linear approximation of the dispersive Hamiltonian breaks down and the expression of the dispersive shifts becomes dependent on  $n$ .

<sup>6</sup>With the unitary transformation

$$\hat{D}_e = \exp \left[ \frac{\arctan \left( 2g\Delta^{-1} \sqrt{\hat{a}^\dagger \hat{a} + |e\rangle \langle e|} \right)}{2\sqrt{\hat{a}^\dagger \hat{a} + |e\rangle \langle e|}} \left( \hat{a}^\dagger \hat{\sigma}^- - \hat{a} \hat{\sigma}^+ \right) \right]$$

2.3.3.2 Modelling the full system for ensemble-averaged measurements: the master equation

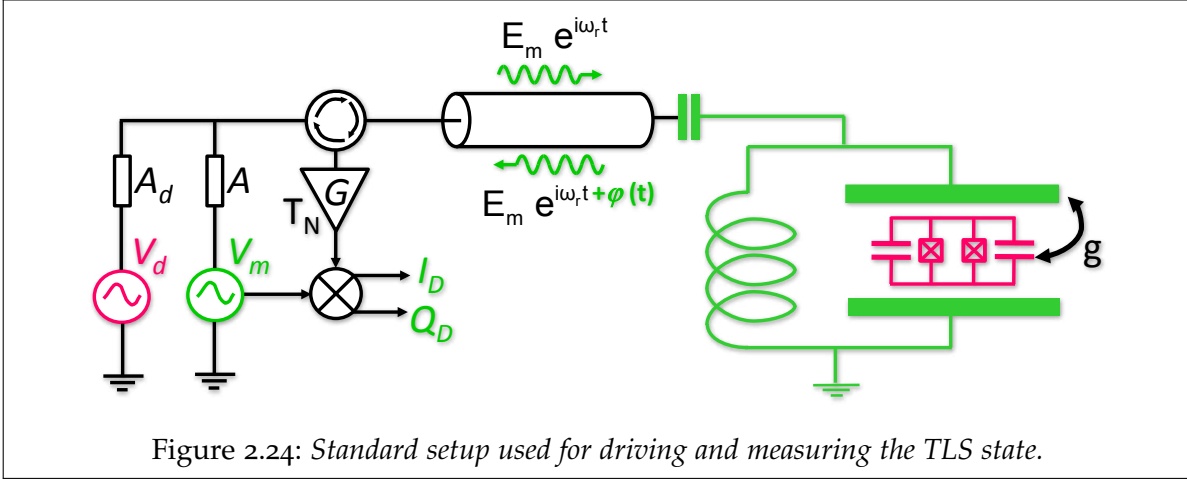


Fig. 2.24 sketches the common situation in which the experiments described in Chapter 3 and 4 are performed. It consists in connecting the TLS-resonator coupled system to two sources:  $V_d$  which drives the TLS transition to control its state, and  $V_m$  which allows to measure the TLS state by probing the cavity pull. According to 2.1.3, the measurement is still described in the input-output framework. However, the quantum system being probed is no longer the resonator alone, but rather the TLS-resonator coupled system, whose internal dynamics cannot anymore be described by Eq. 2.12, but rather by the following master equation which replaces it, completely describing the ensemble-averaged evolution of the density matrix:

$$\partial_t \hat{\rho} = \mathcal{L} \hat{\rho} = -\frac{i}{\hbar} [\hat{\rho}, \hat{H}] + \kappa \mathcal{D}[\hat{a}] \hat{\rho} + \Gamma_1 \mathcal{D}[\hat{\sigma}_-] \hat{\rho} + 1/2 \Gamma_\phi \mathcal{D}[\hat{\sigma}_z] \hat{\rho}. \quad (2.33)$$

The Lindblad super-operator  $\mathcal{L}$  contains four terms: the first one represents the Hamiltonian evolution. The Hamiltonian  $\hat{H}$  is the Jaynes-Cummings dispersive Hamiltonian, plus two terms representing the sources driving the resonator and the TLS, written in the interaction picture:

$$\begin{aligned} \hat{H} = & 1/2 \hbar (\omega_{ge} - \omega_d) \hat{\sigma}_z + \hbar (\omega_c - \omega_m) (\hat{a}^\dagger \hat{a} + 1/2) + \\ & + \hbar \chi (\hat{a}^\dagger \hat{a} + 1/2) \hat{\sigma}_z + \\ & + E_m (\hat{a}^\dagger + \hat{a}) + E_d (\hat{\sigma}_+ + \hat{\sigma}_-). \end{aligned}$$

The amplitudes of the drives  $E_m = V_m / A$  and  $E_d$  are the amplitudes  $V_m$  and  $V_d$  sent by the two microwave sources, but attenuated by the setup.

After this first term, the  $\kappa \mathcal{D}[\hat{a}] \hat{\rho}$  term represents the damping of the resonator field. It is written in terms of the collapse super-operator  $\mathcal{D}[\hat{C}]$  which is defined as:

$$\mathcal{D}[\hat{C}] \hat{\rho} = \hat{C} \hat{\rho} \hat{C}^\dagger - 1/2 \hat{C} \hat{C}^\dagger \hat{\rho} - 1/2 \hat{\rho} \hat{C} \hat{C}^\dagger.$$

The last two terms of the master equation represent respectively the relaxation and dephasing of the TLS and are also written in terms of the collapse super-operator.

In addition we want to compute the signal reflected on the cavity and detected. Using the input-output relation Eq. 2.13 we obtain the output field

$$\hat{a}_{out} = \sqrt{\kappa}\hat{a}(t) + \frac{iE_m}{\sqrt{\kappa}}$$

with the field quadratures  $\hat{X}_{out} = 1/2\sqrt{\kappa}\hat{X}$ , disregarding the component in  $E_m$  which brings no information on the TLS-resonator system.

To obtain the demodulated components  $X_D$  we need to add the effect of the amplifier, which, in the one hand, amplifies with a power gain  $G$ , and on the other hand, adds noise, yielding a total noise  $\xi_X(t)$ . However, the ensemble-averaging cancels this noise, yielding:

$$E[I_D] = \langle \hat{I}_D \rangle = \sqrt{G} \langle \hat{I}_{out} \cos \Theta + \hat{Q}_{out} \sin \Theta \rangle = \sqrt{\kappa G} \langle ae^{-i\Theta} + a^\dagger e^{i\Theta} \rangle / 2$$

$$E[Q_D] = \langle \hat{Q}_D \rangle = \sqrt{G} \langle -\hat{I}_{out} \sin \Theta + \hat{Q}_{out} \cos \Theta \rangle = \sqrt{\kappa G} \langle -iae^{-i\Theta} + ia^\dagger e^{i\Theta} \rangle / 2$$

where  $\Theta$  is the phase of the local oscillator used for demodulation, and  $E[\bullet]$  indicates ensemble-averaging of classical signals and  $\langle \bullet \rangle$  the ensemble average over the density matrix.

### 2.3.3.3 Following a single realization in the ensemble: the quantum trajectories framework

The master equation formalism presented above gives access to all ensemble-averaged measurements of the system, and fully describes its dynamics if we don't take into account the information leaking out of the resonator due to the measurement. Now if we want to consider the dynamics of a single realization inside the ensemble, taking into account how the resonator-TLS state evolves under the acquisition of information, we need to move to a more general framework, derived from the standard quantum theory and known in the literature as quantum trajectories<sup>95</sup>, quantum Monte-Carlo method<sup>13</sup> or Bayesian theory<sup>96</sup>, which has been applied to circuit QED in many articles<sup>23,97</sup>. This framework describes how the state of knowledge about an *individual quantum system* evolves given the *record of the measurements* performed on it. These successive measurements induce a succession of projections on new quantum states, with a stochastic character due to the intrinsic randomness of each measurement result. Therefore, the theory describes the measurement process with two coupled stochastic differential equations:

- the first describes the output field at time  $t$ , which can be explicitly written as

$$X_D(t) = \sqrt{\kappa G} \langle \hat{X} \cos \Theta + \hat{Y} \sin \Theta \rangle_t + \xi_X(t) \quad (2.34)$$

where the notation  $\langle \bullet \rangle_t$  describes the expectation value of an operator at time  $t$  conditioned to all the previous measurement records ( $X \equiv \{X_{out}(t')\}_{t' < t}$ ) and  $\xi_X(t)$  is a realization of a random process with white noise spectrum

$\langle \xi_X(t + \tau) \xi_X(t) \rangle = 1/2 S_0 \delta(\tau)$  which describes the randomness of the measurement  $X_D(t)$ . Very often these components  $X_D(t)$  are expressed in units of the average noise photons  $1/2G S_0$ , by introducing the quantum efficiency  $\eta = G/S_0$  and the reduced noise  $\tilde{\xi}_X(t) = \xi_X(t)/\sqrt{1/2S_0}$ :

$$\tilde{X}_D(t) = \sqrt{\kappa\eta} \langle 2\hat{X} \cos \Theta + 2\hat{Y} \sin \Theta \rangle_t + \tilde{\xi}_X(t),$$

- the second equation describes the evolution of the field inside a resonator conditioned to a homodyne measurement of its outcome<sup>98</sup>. Applied to the resonator-TLS system, this theory yields

$$\partial_t \hat{\rho}^{(X)} = \mathcal{L} \hat{\rho}^{(X)} + \left( [\hat{Y}, \hat{\rho}^{(X)}] + \mathcal{M} [2\hat{X}] \hat{\rho}^{(X)} \right) \sqrt{\kappa\eta} \tilde{\xi}_X(t) \quad (2.35)$$

where  $\hat{\rho}^{(X)}$  is the resonator-TLS density matrix conditioned to the measurement records  $(X) \equiv \{X_{out}(t')\}_{t' < t}$ ,  $\mathcal{L}$  is the resonator-TLS Lindblad operator given in the previous section, which describes the ensemble-averaged evolution of the density matrix, and  $\mathcal{M}[\hat{c}]$  is the measurement super-operator defined as

$$\mathcal{M}[\hat{c}] \hat{\rho} = 1/2 (\hat{c} - \langle \hat{c} \rangle_t) \hat{\rho} + 1/2 \hat{\rho} (\hat{c} - \langle \hat{c} \rangle_t).$$

This means that the evolution of the density matrix  $\hat{\rho}^{(X)}$  conditioned to the measurement records  $(X)$ , is the same than the usual density matrix of the ensemble  $\hat{\rho}$ , but adding the effect of the projection and the back-action associated with the results of the measurements  $(X)$ .

The master equation 2.33 is extensively used to analyze the TLS-resonator system in the Chapter 3. The quantum trajectories formalism will be used to illustrate some specific aspects of the TLS-resonator dynamics.

## 2.4 MEASURING THE TLS WITH A RESONATOR

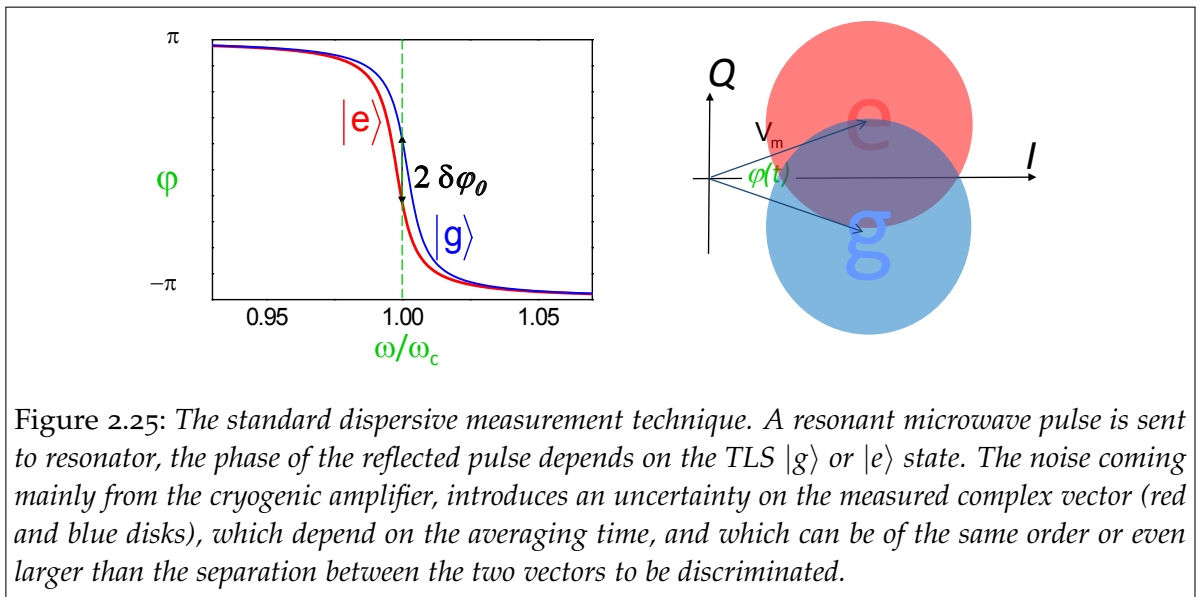
Since the cavity pull shifts the resonator frequency up or down depending on the TLS state, we can characterize this state by measuring the resonance frequency of the resonator. A convenient way to do so is to send a microwave pulse at frequency  $\omega_r$  to the resonator input and to measure the relative phase  $\bar{\varphi} = \arctan(\bar{Q}_D/\bar{I}_D)$  of the reflected pulse, where  $\bar{X}_D$  is obtained by time averaging  $X_D(t)$  to reduce the influence of the noise  $\xi_X$ . As shown in Fig. 2.25, when the TLS is in  $|g\rangle$ , the resonator frequency is shifted to  $\omega_r + \chi$ , yielding a reflected phase  $\delta\varphi_0 = 2 \arctan(2\chi/\kappa)$  in the  $\omega_r$  pulse. Conversely, when the TLS is in  $|e\rangle$ , the resonator frequency is shifted down to  $\omega_r - \chi$ , yielding a phase  $-\delta\varphi_0 = -2 \arctan(2\chi/\kappa)$ .

To implement these kind of measurements experimentally, some additional microwave techniques need to be introduced.

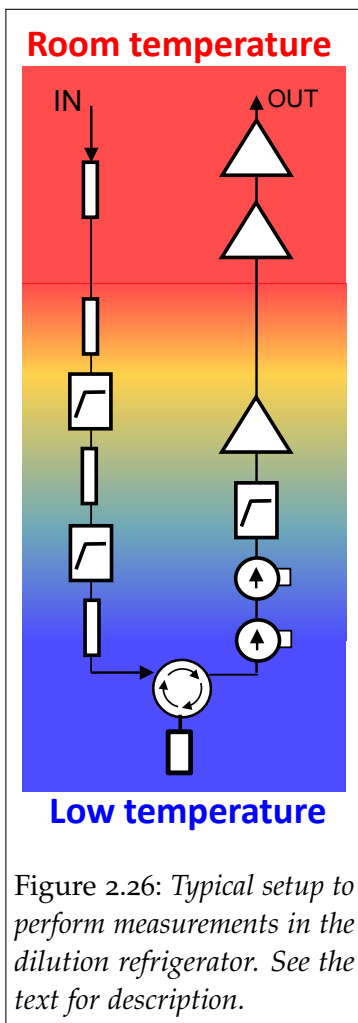
### 2.4.1 MICROWAVE TECHNIQUES FOR MEASURING THE TLS-RESONATOR COUPLED SYSTEM

#### 2.4.1.1 Microwave setup for the measurements performed in the dilution refrigerator

To study the TLS-resonator system, we use a dilution refrigerator at 20 mK. The typical setup for performing measurements in this refrigerator is shown in Fig. 2.26.



The aim of this setup is to reduce as much as possible the thermal and technical noise reaching the sample and to get the best possible noise temperature at the output.



To reduce noise from the input line which reaches the sample, this line contains several filters and successive attenuators thermalized at several stages with decreasing temperatures. If the last attenuator has a large value (typically 20 dB), it fixes the noise temperature of the full line, as explained below in 2.4.1.2.

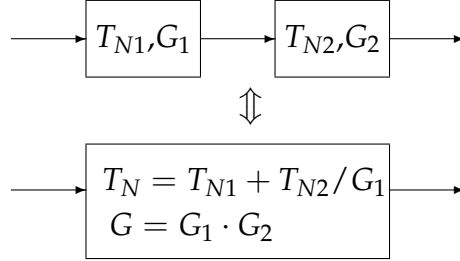
To improve the noise temperature of the output line and speedup the measurements, we use a cryogenic amplifier, as explained in 2.4.1.2. However, amplifiers can inject noise backwards to their input. This noise constitutes an important issue when operating the full TLS-resonator system. To reduce its effect we insert between the sample and the cryogenic amplifier two isolators, that is, two circulators with one of their ports connected to a  $50\ \Omega$  charge, so that the signals are attenuated by 20 dB in the reverse direction.

#### 2.4.1.2 SNR of cascaded amplifiers: interest of cryogenic amplifiers

The noise of each microwave device can be characterized by its equivalent noise temperature. This temperature  $T_N$  corresponds to the temperature of the  $50\ \Omega$  matched resistor, which, connected to the input of the noiseless quadrupole, produces the same noise  $\sigma_n^2$  as the quadrupole itself. For a quadrupole with power gain  $G$ , the noise temperature is:

$$T_N = \frac{\sigma_n^2}{G \cdot k_B \cdot B}.$$

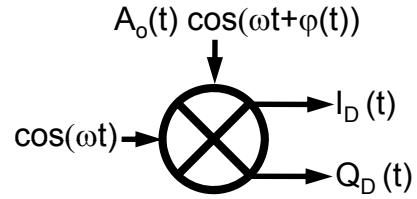
For some measurements we use a cascade of amplifiers or attenuators instead of a single one. To analyze the noise in such a cascade, we use the equivalence<sup>69</sup>:



From this equivalence, we see that the SNR depends mainly on the *first amplifier* and on the *last attenuator* of the chain. Thus a key point in our experiments is to use a cryogenic amplifier, an amplifier operated at cryogenic temperatures with a very low noise temperature  $T_{N1} \sim 4$  K, yielding a good overall  $T_N \simeq T_{N1}$ .

#### 2.4.1.3 Homodyne detection

To detect the phase of the microwave pulse which is reflected on the resonator, we use a homodyne detection scheme, following the same principle exposed in 2.1.5.1. As shown in Fig. 2.24 the detection is performed in an IQ demodulator, a device which mixes the input signal with the local oscillator  $\cos(\omega_m t + \Theta)$ , yielding the  $I_D(t)$  component of the signal; and with the local oscillator dephased by  $-\pi/2$ ,  $-\sin(\omega_m t + \Theta)$ , yielding the  $Q_D(t)$  component. The result is low-pass filtered to eliminate the terms around  $2\omega_m$ . The results are the in-phase and quadrature components



$$I_D(t) = A_o(t) \cos(\varphi(t) - \Theta)$$

$$Q_D(t) = A_o(t) \sin(\varphi(t) - \Theta).$$

We stress that the temporal dependence of these signals is only limited by the bandwidth of the low pass-filter used for suppressing the  $2\omega_m$  terms.

#### 2.4.1.4 Heterodyne detection of the phase

The measurements of the TLS state rely on the detection of the phase of a microwave pulse reflected on the resonator. It is therefore very important to accurately measure the phase. In our experiments, in order to avoid variations on the DC offsets of the IQ demodulator, which may lead to a bad determination of this phase, we often use a heterodyne demodulation technique to measure  $\varphi$ .

A microwave tone of frequency  $\omega_c/2\pi$  is sent to the resonator input. The reflected pulse is demodulated using a local oscillator detuned by  $\omega_{IF}/2\pi = 3.2$  MHz from  $\omega_c$ . The acquired signal is therefore an oscillating signal describing a periodic trajectory in the IQ plane (a circle in the case of a perfect IQ demodulator). The  $I_D(t)$  and  $Q_D(t)$  signals are sampled, typically with  $t_S = 1$  ns sample period.

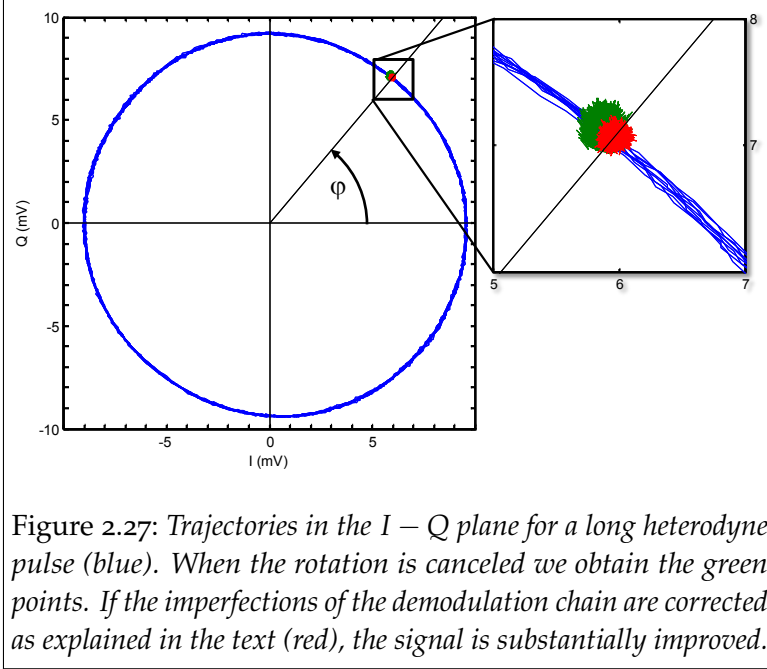


Figure 2.27: Trajectories in the  $I - Q$  plane for a long heterodyne pulse (blue). When the rotation is canceled we obtain the green points. If the imperfections of the demodulation chain are corrected as explained in the text (red), the signal is substantially improved.

Various imperfections can be calibrated and corrected at this stage:

- An imperfect orthogonality of the  $I_D$  and  $Q_D$  signals, i.e.  $I_D \propto \cos(\omega_{IF}t + \phi_0)$  whereas  $Q_D \propto \sin(\omega_{IF}t + \phi_1)$  with  $\phi_0 \neq \phi_1$
- An imbalance between the gains of the  $I_D$  and  $Q_D$  chains
- DC offsets in each chain

In our experiments these imperfections are calibrated by acquiring a very long trace to get the correction coefficients. Then the  $I[n]$  and  $Q[n]$  data vectors are corrected for each measurement yielding the two corrected sets  $I'[n]$  and  $Q'[n]$ , which

allow to extract the phase  $\varphi'[n] = \arctan(Q'[n]/I'[n])$ . The phase is corrected for  $\omega_{IF}$ :

$$\varphi''[n] = \varphi'[n] - nt_S\omega_{IF}$$

The resulting  $I''[n]$  and  $Q''[n]$  are averaged, and yield the estimated phase  $\bar{\varphi}$ .

#### 2.4.2 AN EXAMPLE: TLS SPECTROSCOPY

As an example, the above measurement procedure allows to perform easily a spectroscopy of the TLS (see Fig. 2.28). To excite the TLS we send a long microwave pulse  $V_d$  whose frequency  $\omega_d$  is scanned. If this pulse is resonant with the TLS transition frequency  $\omega_{ge}$ , it induces some steady-state population in the TLS excited state  $|e\rangle$ . Now to detect this population a microwave pulse  $V_m$  is sent to the resonator: its reflected phase undergoes a shift  $\pm\delta\varphi_0$  depending on the TLS  $|g\rangle$  or  $|e\rangle$  state as explained above. Therefore, the average reflected phase of an ensemble of identically prepared experiments,  $E[\bar{\varphi}]$ , shows a dip when  $\omega_d$  excites the TLS.

#### 2.4.3 LIMITS OF THE STANDARD DISPERSIVE MEASUREMENT TECHNIQUE

To have a good accuracy in the determination of the TLS state, the SNR should be as large as possible. The measurement pulse should then be as large as possible,



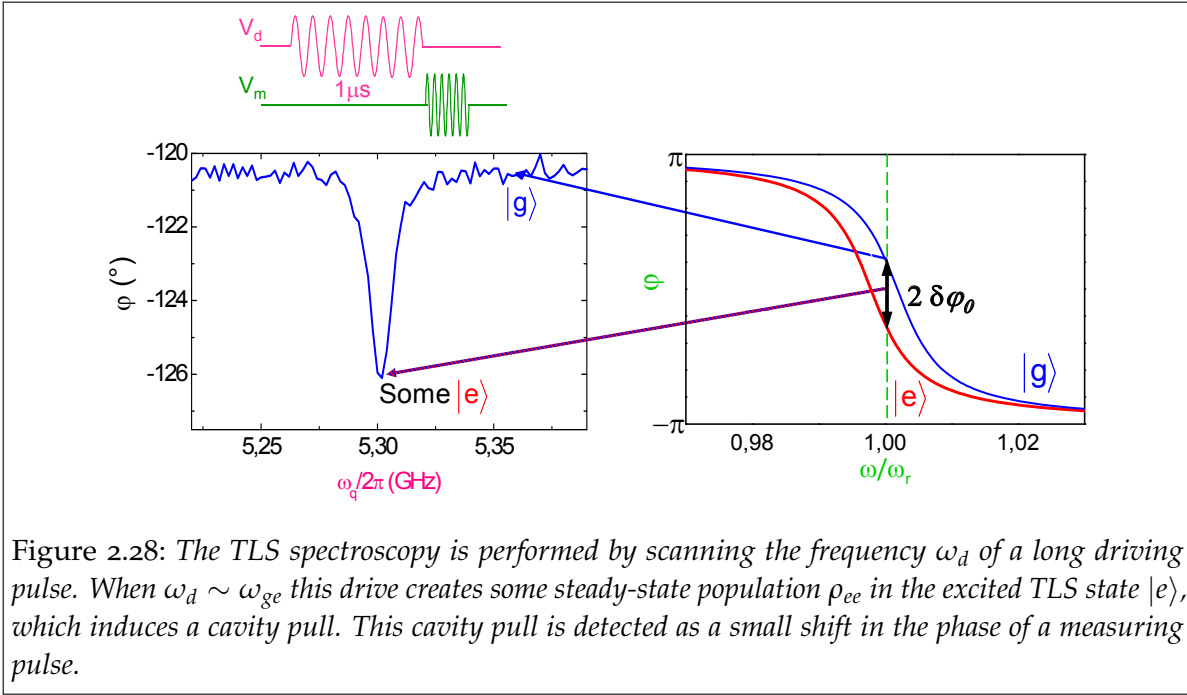


Figure 2.28: The TLS spectroscopy is performed by scanning the frequency  $\omega_d$  of a long driving pulse. When  $\omega_d \sim \omega_{ge}$  this drive creates some steady-state population  $\rho_{ee}$  in the excited TLS state  $|e\rangle$ , which induces a cavity pull. This cavity pull is detected as a small shift in the phase of a measuring pulse.

although low enough to induce a resonator field lower than the critical photon number  $n_{crit}$ . The duration of the pulse should also be long to improve the SNR by averaging, although if it becomes comparable to the relaxation time  $\Gamma_1^{-1}$  the TLS may relax during the measurement yielding a wrong result. Although it is still not possible in cQED experiments to reach a SNR high enough to have a negligible error rate and to characterize the state of the qubit in a single-shot, there is a way around this issue which consists in averaging over the results of a large number of successive realizations of the same experimental sequence. Such ensemble-averaged readout procedure is extremely useful since it allows to characterize the state of the qubit: it is the base of a large part of the experiments performed in the next chapter.

However, a large span of questions about this measurement procedure remain open. Which kind of back-action does the measurement induce on the TLS state to make it collapse? How does the measurement happens if a very low amplitude measurement pulse is used? Is it possible to fully characterize the qubit state in a single-shot measurement, without averaging over an ensemble of equal experiments?

In Chapter 3 we investigate the dynamics of the qubit while it is being measured to answer the first two questions, among others. In Chapter 4 we demonstrate a different readout procedure which is able to characterize the TLS state in a single experimental sequence.



## Part II

### THE MEASUREMENT IN QED



## MEASUREMENT AND DYNAMICS IN CIRCUIT QED

*Quantum behaviour does not occur in Hilbert space:  
it occurs in the laboratory.*  
— Asher Peres

An important prediction of quantum mechanics is that a measuring apparatus unavoidably applies some back-action to the system it measures. The measuring process consists in a progressive acquisition of information about an observable, which in parallel leads to the projection of the system on the observable eigenspace corresponding to the detector outcome. At the same time, the quantum coherence is progressively erased until it is completely lost when the measurement outcome is completely characterized.

In this chapter we discuss an experiment designed in the goal of shedding light on the interplay between the Hamiltonian evolution of a TLS and the state projection induced by its measurement. This experiment, sketched in Fig. 3.1, consists in continuously measuring a TLS while it is performing Rabi oscillations in order to capture the perturbation of its dynamics due to the measurement, under different measuring strengths. The circuit QED setup is an ideal framework for such an investigation for two reasons: first because it contains a fixed artificial atom on which truly continuous and non-destructive measurements can be performed, and second, because the measurement strength can be tuned in-situ by varying the power which is sent to the resonator. This allows to explore the crossover from weak measurements, which only slightly perturb the TLS state, to much stronger ones, in which the TLS state is blocked in an eigenstate and can only evolve by sudden and stochastic quantum jumps.

It is possible to go further and to test, using a weak and continuous measurement, if our system behaves as a *classical macroscopic* object satisfying the so-called Leggett-Garg inequality<sup>29</sup>. By demonstrating the violation of this inequality, we show that the classical description is ruled out and that a quantum description is needed, even for a *macroscopic* circuit. This constitutes one of the most important results of this chapter.

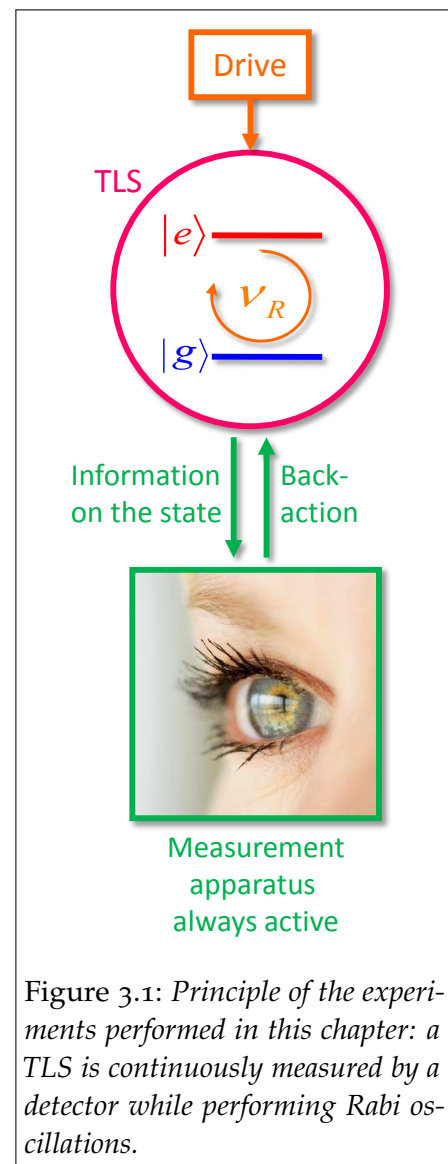


Figure 3.1: Principle of the experiments performed in this chapter: a TLS is continuously measured by a detector while performing Rabi oscillations.

### 3.1 PREDICTIONS ON THE CONTINUOUS WEAK MEASUREMENT OF A DRIVEN TLS

Sudden projective measurements are at heart of quantum mechanics postulates. When they occur, all the information about the measured observable is immediately acquired and at the same time, the system state is suddenly projected onto the observable's eigenspace corresponding to this outcome. Compared to this, weak measurements only extract some part of the information on the observable, and induce a partial collapse of the state. The weak and continuous measurements which are performed in this chapter are the continuous limit of such partial measurement process, in which the extraction of information and the collapse occur as continuous processes.

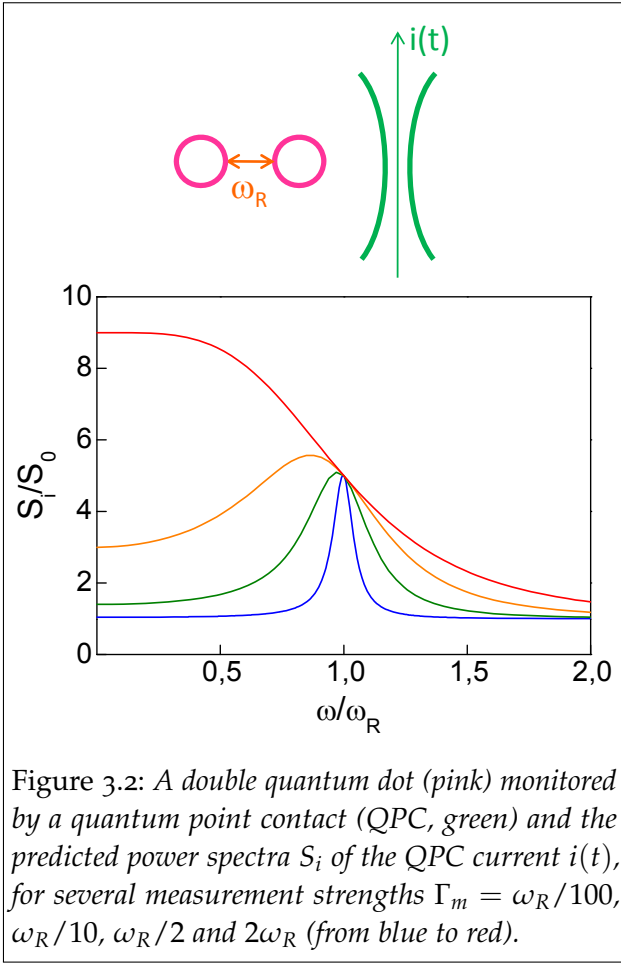


Figure 3.2: A double quantum dot (pink) monitored by a quantum point contact (QPC, green) and the predicted power spectra  $S_i$  of the QPC current  $i(t)$ , for several measurement strengths  $\Gamma_m = \omega_R/100$ ,  $\omega_R/10$ ,  $\omega_R/2$  and  $2\omega_R$  (from blue to red).

The first goal of our experiment is to probe the theoretical predictions for the spectrum of a TLS coupled to such a weak continuous detector (Fig. 3.1). Indeed, Korotkov<sup>24</sup> studied theoretically in great detail a very similar system: a double quantum dot (DQD) whose state is monitored by a quantum point contact (QPC). In this situation (see Fig. 3.2), the current  $i(t)$  flowing through the QPC depends on the presence of the electron in the dot nearest to the QPC or in the other one. Thus, the current through the QPC provides a meter for the DQD state and the following predictions are made:

1. For weak measurements the power spectrum  $S_i$  of  $i(t)$  contains a signature of the coherent dynamics of the system which consists in a Lorentzian peak at the Rabi frequency  $\omega_R$ . (blue curve in Fig. 3.2).
2. When raising the measurement strength the Rabi peak decreases and broadens, and another Lorentzian peak at zero frequency, related to stochastic quantum jumps, starts to grow (see Fig. 3.2 and Section 3.4).
3. The information contained in these Rabi peaks allows to test if the system complies with the hypotheses of macrorealism as stated by Leggett and Garg<sup>29,32</sup> (see Section 3.5).
4. The maximum signal-to-noise ratio which is obtained when continuously monitoring coherent oscillations is 4. This is the ratio between the maximum Rabi peak height and the noise background if this background comes solely from the quantum vacuum fluctuations (Fig. 3.2).
5. It is possible to build a quantum feedback scheme in which the signal obtained at

the detector output is used to calculate an adequate reaction onto the system, which corrects the dephasing of coherent oscillations better than any classical feedback scheme (see 3.5.5.3).

Although these predictions have been extensively discussed in the literature<sup>99,100,101</sup>, only two experiments which deal with the first of them are reported: Il'ichev *et al.*<sup>102</sup> observed an indirect signature of the Rabi peak with a flux qubit measured by an RF oscillator, and Deblock *et al.*<sup>103</sup> were able to observe a narrow peak at the frequency of coherent charge oscillations of a CPB, using a SIS junction as detector.

The main goal of our experiment is to test the Korotkov's predictions using our cQED system instead of the DQD system originally considered<sup>1</sup>. For this purpose we implemented the setup shown in Fig. 3.3. In this setup a transmon TLS is driven by an external microwave source  $V_d$  and capacitively coupled to a resonator. As described in the former chapter, in the dispersive regime the resonance frequency of the resonator is shifted up or down by  $\chi$  depending on the TLS state. This shift is continuously monitored by a microwave signal  $V_m$  which is continuously sent to the resonator input and gets reflected with a different phase depending on the TLS state. The noise power spectrum of the  $I_D$  and  $Q_D$  components of this signal, which are obtained by IQ demodulation, contain the signature of the TLS behaviour: a peak at the Rabi frequency.

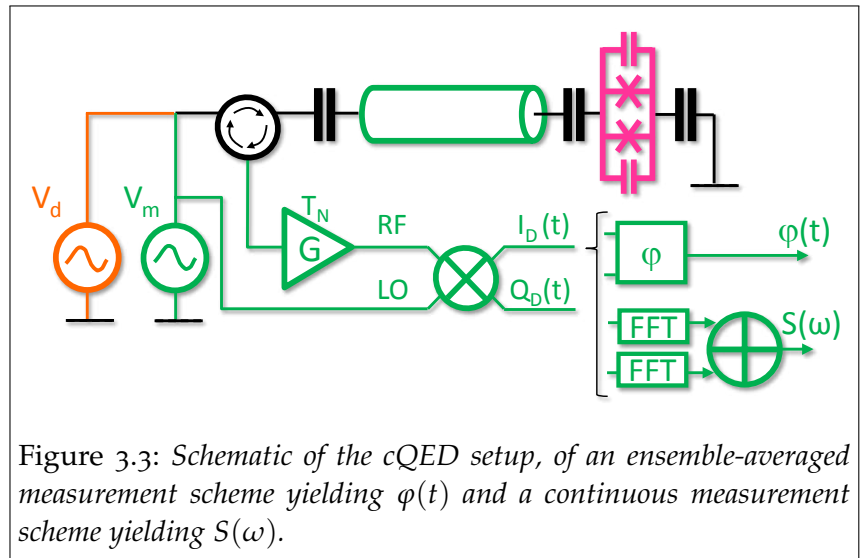


Figure 3.3: Schematic of the cQED setup, of an ensemble-averaged measurement scheme yielding  $\phi(t)$  and a continuous measurement scheme yielding  $S(\omega)$ .

## 3.2 EXPERIMENTAL IMPLEMENTATION

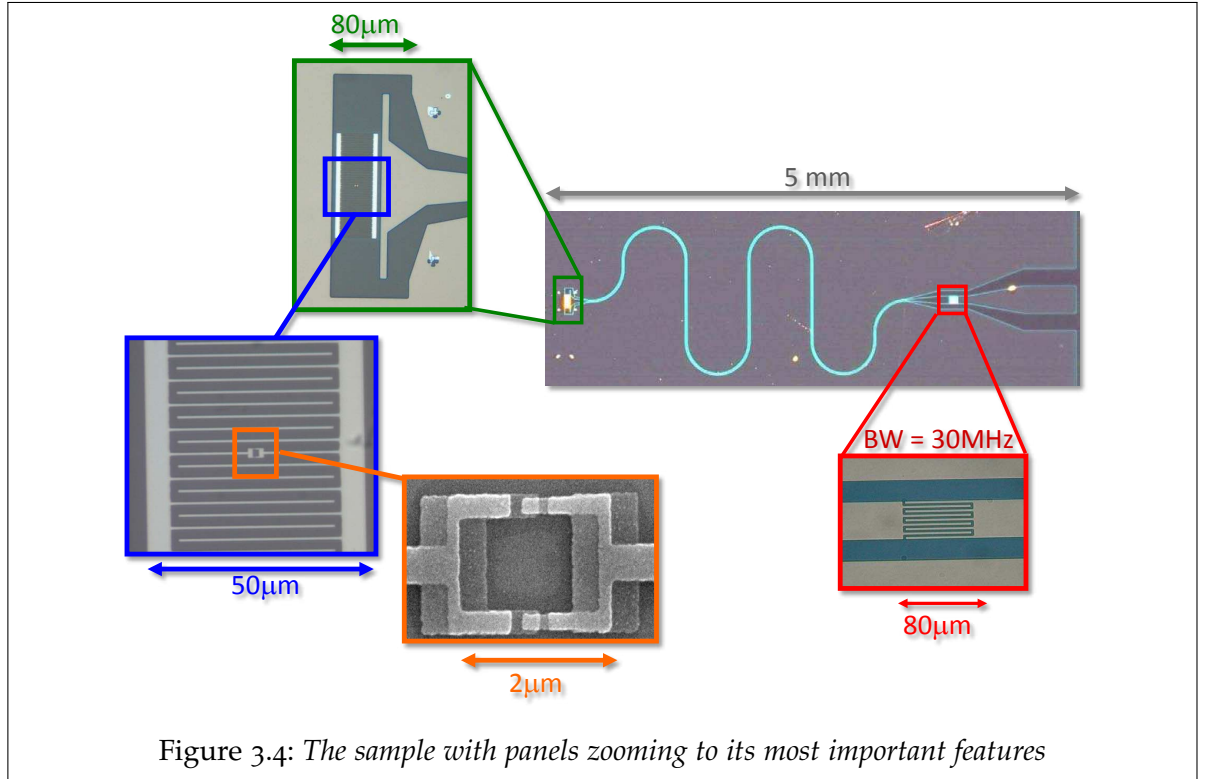
In order to mimic the wide-band and weak detection of the DQD by the current in the QPC with our setup, we have taken care that the superconducting resonator which is used as measurement apparatus for the TLS has a large enough coupling to the measuring lines so that it becomes quickly entangled with its environment, leading to a fast decay of its coherences; in this way it behaves as a classical measurement apparatus for the TLS state. Therefore we chose an over-coupled resonator with a low  $Q \simeq Q_c$ . Note that we could even imagine not to use a resonator at all, but just a transmission line capacitively coupled to the TLS: in such an experiment, the detection bandwidth would have been nearly infinite, and the system would have been even more similar to the DQD-QPC, but on the other hand the amplitude of the

<sup>1</sup>The two latter predictions could not be tested since they require an amplifier working at the quantum limit which is still a subject of active research nowadays<sup>40,41</sup>.



signal would have been reduced and the experiment much longer.

### 3.2.1 THE SAMPLE



As shown in Fig. 3.4 the sample consists of a  $\lambda/2$  CPW resonator with resonance frequency  $\omega_r/2\pi \approx 5.8$  GHz. On one side of the resonator, we fabricate a transmon (green rectangle), consisting in a split Cooper-pair box (orange rectangle) and a large shunt capacitor (blue rectangle). The other side of the resonator is connected to the input line through a coupling capacitor (red rectangle) that sets the quality factor  $Q \simeq Q_c \approx 190$ , which corresponds to a  $\kappa/2\pi \approx 30$  MHz bandwidth. This large bandwidth ensures that the resonator acts as a classical measurement apparatus for the TLS.

The resonator is fabricated in niobium with the process described above (see 2.1.4.1). The transmon is then patterned using e-beam lithography followed by a double-angle evaporation of two aluminium thin-films. The first of these layers is oxidized to form the junction insulator. The sample is then glued on a microwave printed-circuit board made out of TMM10 ceramics. The whole is enclosed in a copper box and thermally anchored to the mixing chamber of a dilution refrigerator at typically 20 mK (Fig. 3.5).

### 3.2.2 MEASUREMENT SETUP

The measurement setup is shown in Fig. 3.5. Two kinds of microwave signals are sent to the sample through the same input line: measurement pulses with voltage  $V_m$  (in green) and pulses to resonantly control the TLS state with voltage  $V_d$  (in pink). Both

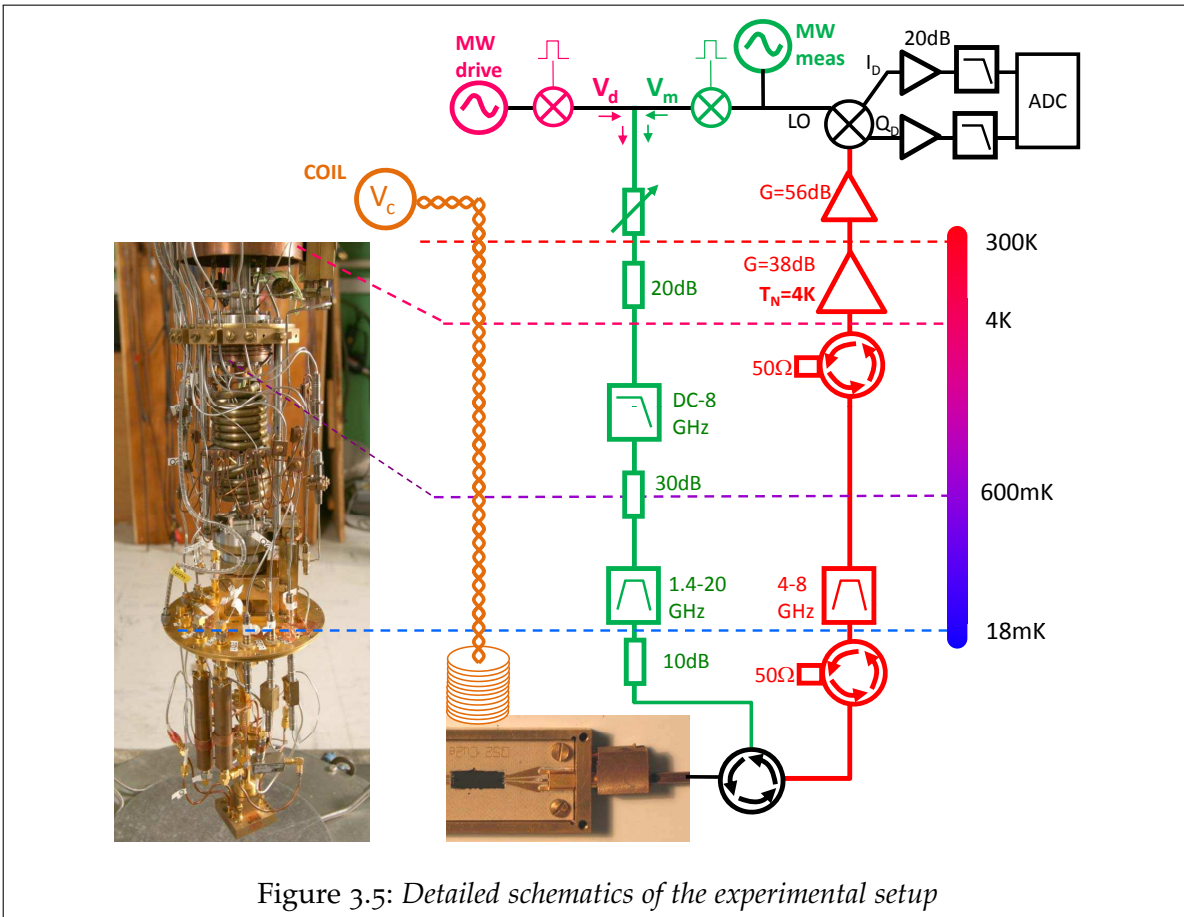


Figure 3.5: Detailed schematics of the experimental setup

of them are shaped in a DC-coupled mixer: a continuous microwave tone (generated by an Anritsu MG3692 microwave generator) is mixed with the DC pulses generated by an arbitrary waveform generator (Tektronix AFG3252). These are combined and sent through a microwave line which contains several filters and attenuators (67 dB in total) thermalized at the different temperature stages of the cryostat. The signal reflected on the sample is separated from the input signal by a cryogenic circulator. It is routed through several isolators, a 4–8 GHz bandpass filter, a cryogenic amplifier (CITCRYO1-12 from Caltech) with 38 dB gain and noise temperature  $T_N = 4$  K.

The signals are then amplified at room temperature with a total gain of 56 dB, and finally mixed down using a I/Q mixer with a local oscillator synchronous to the microwave tone used for generating the measurement microwave pulses. The  $I_D$  and  $Q_D$  quadratures are filtered, amplified and balanced with a precision better than 0.5%. They are finally sampled by an Acqiris DC282 fast digitizer and transferred to a computer that processes them.

A superconducting coil is attached to the copper box containing the sample to vary the flux. A very-low cutoff RL filter formed by the coil itself and a  $50\ \Omega$  resistor filters this line to reduce the thermal noise coming from room-temperature.

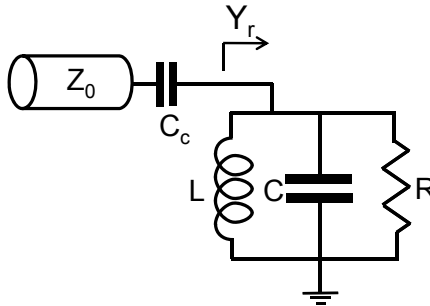
### 3.2.3 CALIBRATION OF THE RESONATOR PARAMETERS

Due to the low  $Q$  of the resonator, it is not easy to calibrate its parameters. Indeed, an over-coupled resonator measured in reflection yields no signature of the resonance in amplitude but only a shift of  $2\pi$  in the phase. Since the measuring lines have small spurious resonances, the phase of the response contains a ripple in addition to the resonator  $2\pi$  shift. This is not a problem when the resonator has a large  $Q$ , since the ripple, which is smooth compared to the resonator response, induces almost no variation of the phase in the span where the  $2\pi$  shift corresponding to the resonance takes place. It is therefore easy to fit the width of the shift and deduce  $Q$  from it. However, when the resonator has a low  $Q$ , it becomes very difficult to separate the phase shift induced from the resonator from the ripple coming from the lines. Thus, spectral measurements performed with a VNA yield uncertainties around 10% for  $Q$ .

To accurately measure the resonator parameters we used a different technique consisting in sending to the resonator microwave pulses of different frequencies and performing a time-resolved measurement of the reflected  $I_D$  and  $Q_D$  quadratures. When the pulse is nearly resonant, we observe an initial transient during which the intra-resonator field builds up from the incoming field, whereas when it is very detuned it is almost instantly reflected at resonator output. The color plot of the power of the reflected pulses as a function of the microwave frequency is shown in the Fig. 3.6.

To determine the resonator parameters we fit this surface with the response calculated for a certain resonance frequency  $\omega_r$  and quality factor  $Q$ . This is efficiently performed by synthesizing the time-response of the resonator using an inverse Laplace transform. First the response around resonance is calculated for the RLC-parallel equivalent resonator:

$$Y_r = Cs + R^{-1} + (Ls)^{-1}$$

$$C(s) = \frac{Y_r^{-1} + C_c^{-1}s^{-1} - Z_0}{Y_r^{-1} + C_c^{-1}s^{-1} + Z_0}.$$


The time-response when the input is  $I_{in}(t) = \cos(\omega t)u(t)$  (where  $u(t)$  is the Heaviside step function) is

$$I_{out}(t) = \mathcal{L}^{-1} [C(s) \star \mathcal{L}(\cos(\omega t))] = \left[ \mathcal{L}^{-1} \left( C(s) \star \frac{\omega}{s^2 + \omega^2} \right) \right]^2$$

where  $\star$  indicates a convolution. The other quadrature is found similarly  $Q_{out}(t) = \mathcal{L}^{-1} [C(s) \star \mathcal{L}(\sin(\omega t))]$  and thus, the resulting time envelope of the total reflected power is  $P(t) = I_{out}^2(t) + Q_{out}^2(t)$ .

The finite rising time of the microwave pulses has also to be take into account, and can be simulated by convolving the time response with a triangle. We measured

$t_{rise} = 3.1 \pm 0.1$  ns with a fast quadratic detector and a 16 GHz oscilloscope.

The fit finally yields  $\omega_c/2\pi = 5.796$  GHz and  $Q = 191 \pm 5$  (equivalent to a bandwidth  $\kappa/2\pi = 30.3 \pm 0.8$  MHz) with very good agreement as shown in Fig. 3.6.

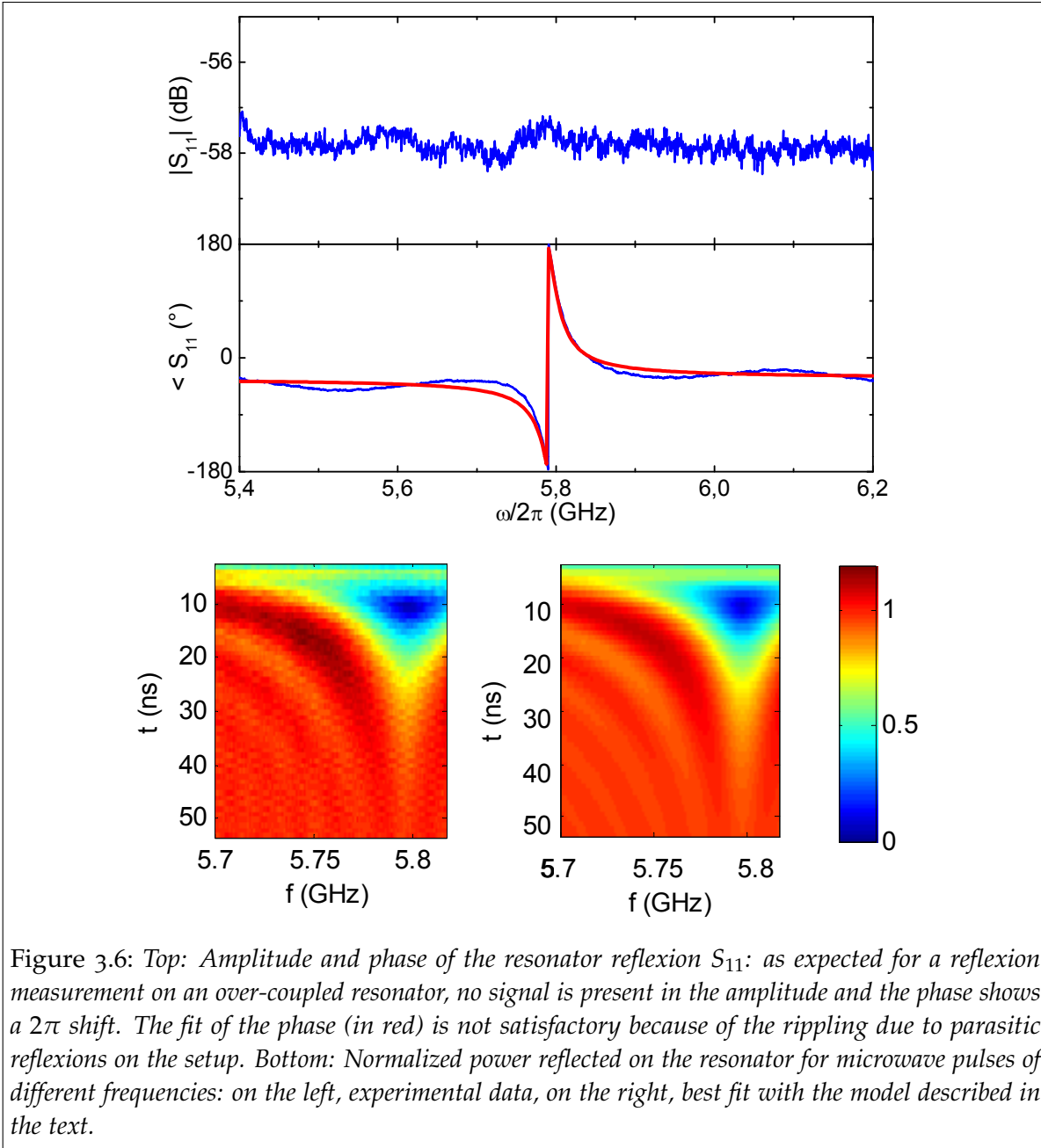
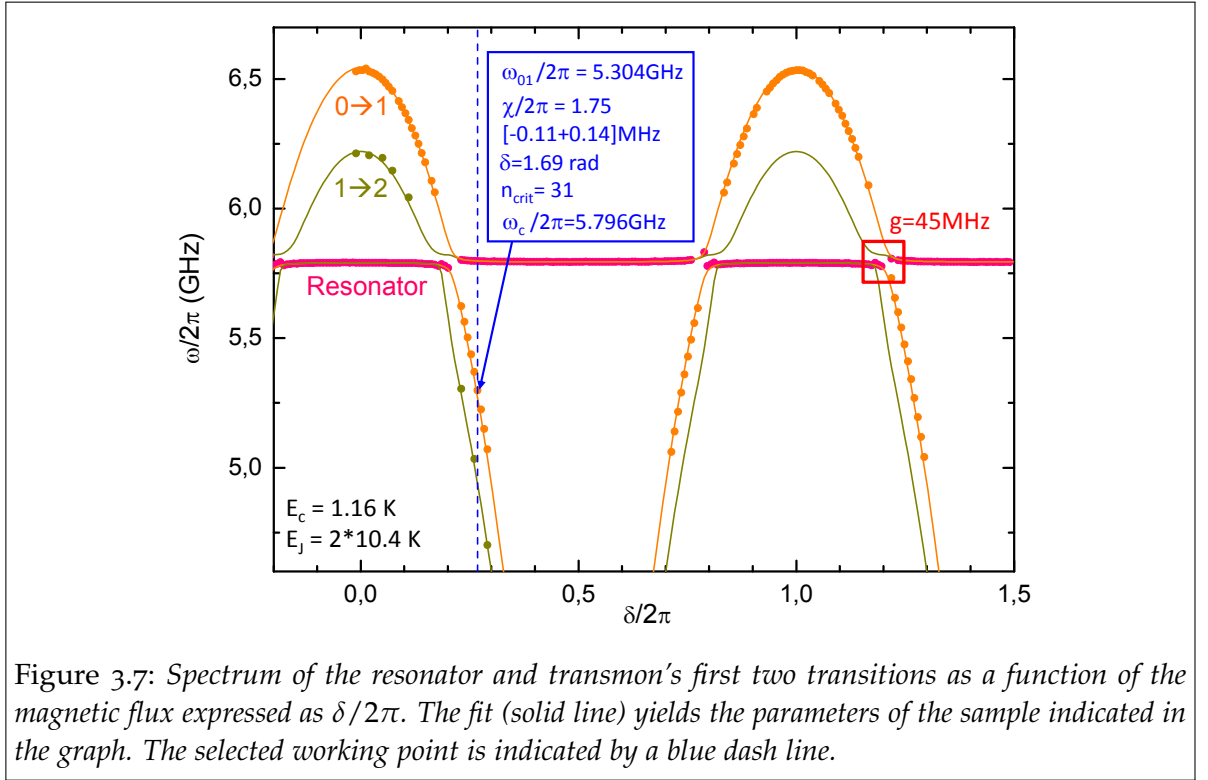


Figure 3.6: Top: Amplitude and phase of the resonator reflexion  $S_{11}$ : as expected for a reflexion measurement on an over-coupled resonator, no signal is present in the amplitude and the phase shows a  $2\pi$  shift. The fit of the phase (in red) is not satisfactory because of the rippling due to parasitic reflexions on the setup. Bottom: Normalized power reflected on the resonator for microwave pulses of different frequencies: on the left, experimental data, on the right, best fit with the model described in the text.

### 3.2.4 CHOICE OF THE WORKING POINT

A spectroscopy of the system yield the spectrum shown in Fig. 3.7 for the resonator and the first two transitions of the transmon. We fitted these spectra with the full theoretical expressions of the dressed transmon levels to obtain the transmon and coupling parameters which are shown in the figure.

We choose to work at a large detuning  $\Delta \approx 500$  MHz, far in the dispersive regime,



while keeping a cavity pull  $\chi \propto \Delta^{-1}$  large enough to detect easily the TLS state. At this point we characterized the relaxation rate  $\Gamma_1^{-1} = 200 \pm 10$  ns, and the decoherence rate  $\Gamma_2^{-1} = 150 \pm 10$  ns by a Ramsey experiment. In all the experiments reported in this chapter the TLS will be biased at this same working point.

### 3.3 MEASUREMENT-INDUCED DEPHASING

Before testing the continuous measurement predictions, we first probed our understanding of the back-action in ensemble-averaged measurements. Indeed, it is well established that the quantum fluctuations in the readout pulse intensity lead to dephasing of the TLS<sup>22</sup>. This was first demonstrated in Cavity QED<sup>104</sup>; a similar experiment in circuit QED was performed at Yale<sup>21</sup> by characterizing spectroscopically the dephasing times of a qubit in the presence of a field in the resonator.

In this thesis, after introducing the theory for measurement-induced dephasing, we discuss the experimental results obtained with a spectroscopic characterization, and we extend this study to the dephasing of Rabi oscillations induced by the resonator field. Compared to the spectroscopic investigation of dephasing, the study of Rabi oscillations allows us to demonstrate an additional interesting effect that had been previously overlooked: a reduction of the dephasing at high Rabi frequencies due to filtering of the shot noise by the resonator.

### 3.3.1 THEORY OF THE MEASUREMENT-INDUCED DEPHASING

In this section, we discuss the situation where a TLS is dispersively coupled to a resonator that is driven by a source at its resonance frequency, as described at the end of Chapter 2 by the master equation (Eq. 2.33). We are interested here in the way the intra-resonator field affects the quantum coherence of the TLS. The dephasing of the TLS by the resonator field can be seen as occurring in two distinct steps:

- first, the TLS gets entangled with the resonator degrees of freedom;
- then, the entangled TLS-resonator state loses its coherence due to coupling of the resonator to the measuring line.

Seen from the TLS alone, each of these two processes amounts to a loss of quantum coherence ; however the coherence loss occurring in the first process is in principle reversible since the TLS coherence is still stored in the coupled TLS-resonator state, while the second process leads to an irreversible loss of coherence towards the heat bath constituting the environment.

The time scales over which both processes occur strongly depend on the ratio between the parameters characterizing the system:

- the resonator damping rate  $\kappa$
- the dispersive coupling constant  $\chi$
- the TLS dephasing rate  $\Gamma_\phi$  caused by other dephasing processes than coupling to the resonator

We will here investigate three different limiting cases. In the limit where  $\kappa \ll \chi, \Gamma_\phi$ , the resonator field is not coupled to the environment during its interaction with the TLS, so that the TLS loss of coherence is only due to its entanglement with the resonator. In the opposite limit where  $\chi, \Gamma_\phi \ll \kappa$  relevant for the experiments discussed in this chapter, the resonator field leaks towards the environment before it gets appreciably entangled with the TLS. A master equation for the qubit only can be derived that yields an analytical formula for the dephasing rate. We also show that this dephasing rate can be interpreted as being due to the shot-noise of the intra-resonator field.

We will finally briefly discuss the most general case where both entanglement and resonator field relaxation are relevant, which has been solved analytically in the case where the TLS excited state probability stays constant.

#### 3.3.1.1 *Measurement-induced dephasing by a resonator of infinite quality factor*

We first consider the situation of Fig. 3.8 where the resonator and TLS damping rates are negligible compared to the dispersive constant  $\chi$  so that only the TLS-resonator Hamiltonian evolution needs to be considered. Even though this is far from the experiments described in this chapter, this situation is very instructive to consider because it yields analytical formula that give useful insight into the measurement



process of a TLS by a resonator. This ideal situation is in particular precisely the one implemented in cavity QED experiments, in which the resonator and atoms damping times are much longer than the transit time of the atoms through the cavity, and also in certain circuit QED experiments where a high-Q resonator is used. We will here heavily rely on Brune *et al.*<sup>104</sup> who deeply investigated this situation.

We assume that before the experiment a coherent state  $|\alpha\rangle$  was generated in the resonator with mean photon number  $\bar{n} = |\alpha|^2$ , and that the TLS is prepared in state  $(|g\rangle + |e\rangle)/\sqrt{2}$ . Due to the dispersive coupling, the resonator frequency is shifted by  $\pm\chi$  depending on the TLS state, so that the field undergoes a TLS-state dependent phase shift of  $\pm\chi t$  after an interaction time  $t$ . The TLS-resonator entangled state can thus be written

$$|\psi(t)\rangle = \frac{|g, \alpha_g(t)\rangle + |e, \alpha_e(t)\rangle}{\sqrt{2}}$$

where  $|\alpha_g(t)\rangle = |\alpha \exp(i\chi t)\rangle$  and  $|\alpha_e(t)\rangle = |\alpha \exp(-i\chi t)\rangle$ . This state can be seen as a sort of Schrödinger cat state between a TLS and a mesoscopic detector, justifying the nickname of *pointer states* for  $|\alpha_{g,e}\rangle$ . It is then easy to show that the TLS density matrix, obtained after tracing out the field degrees of freedom, has an off-diagonal coefficient describing the TLS coherence  $f_{z,R}(t)/2$  given by  $\langle \alpha_g(t) | \alpha_e(t) \rangle / 2$ . The contrast of Ramsey fringes obtained after a TLS-resonator interaction of duration  $t$  is then given by

$$\begin{aligned} |f_{z,R}(t)| &= |\langle \alpha_g(t) | \alpha_e(t) \rangle| \\ &= \exp\left(-D(t)^2/2\right) \end{aligned}$$

with  $D(t) = |\alpha_g(t) - \alpha_e(t)| = 2\sqrt{\bar{n}} \sin \chi t$  the distance between the two pointer states. At short times where  $\sin \chi t \sim \chi t$ , the TLS-resonator interaction can thus be seen as inducing some Gaussian decay of the TLS coherence with a rate  $2\chi\sqrt{\bar{n}}$ ; we stress however that the coherence is not truly lost but merely stored in the entanglement with the resonator. Indeed, the coherence factor  $|f_{z,R}(t)|$  is expected to exhibit periodic revivals whenever  $\chi t$  is a multiple of  $\pi$ , fully restoring the initial TLS coherence. If nevertheless the TLS intrinsic dephasing time  $\Gamma_\phi^{-1}$  is shorter than these revivals, the

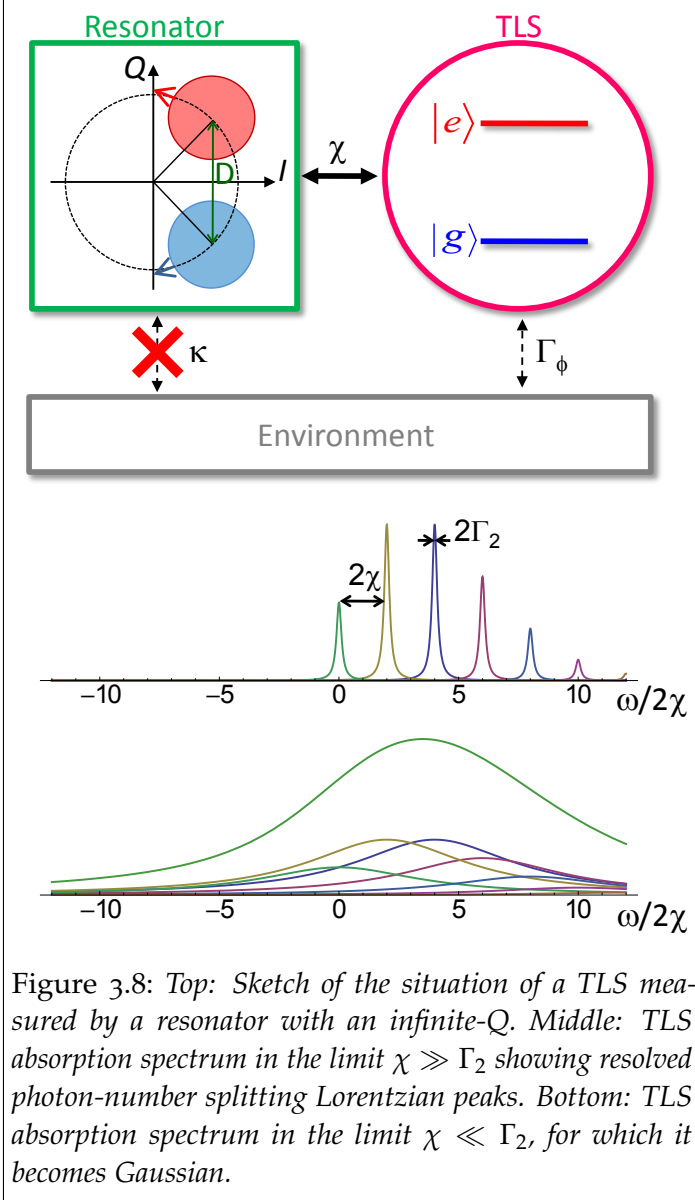


Figure 3.8: Top: Sketch of the situation of a TLS measured by a resonator with an infinite-Q. Middle: TLS absorption spectrum in the limit  $\chi \gg \Gamma_2$  showing resolved photon-number splitting Lorentzian peaks. Bottom: TLS absorption spectrum in the limit  $\chi \ll \Gamma_2$ , for which it becomes Gaussian.

entanglement with the resonator will appear as a genuine dephasing process for the TLS.

It is very instructive to discuss the counterpart of these effects in the spectral domain<sup>22</sup>. Indeed, the TLS absorption spectrum should be the Fourier transform of the coherence factor  $|f_{z,R}(t)|$ . In the limit where the resonator damping is negligible, the photon distribution

$$p_n = \exp(-|\alpha|^2) \frac{|\alpha|^{2n}}{n!}$$

is stationary and the TLS absorption spectrum simply consists in the sum of Lorentzian peaks of width  $2\Gamma_2$  centered on the AC-Stark shifted TLS frequency  $\omega_{ge} + 2\chi n$  and weighted by  $p_n$ . The resulting shape of the resonance clearly depends on the ratio between  $\chi$  and  $\Gamma_2$ . If  $\chi \gg \Gamma_2$  all the TLS absorption peaks corresponding to different photon numbers in the resonator are resolved (see Fig. 3.8 middle panel). The observation of resolved photon-number splitting peaks therefore appears as the spectral counterpart of revivals in the coherence factor of a TLS coupled to a resonator. While the atom-cavity interaction time in cavity QED with Rydberg atoms is usually too short to allow the direct observation of revivals in the Ramsey fringes, well-resolved peaks corresponding to different photon numbers have been observed in circuit QED with a transmon coupled to a high-Q resonator<sup>105</sup>.

In the opposite limit  $\chi \ll \Gamma_2$ , the presence of the field in the resonator induces an extra broadening of the peak by  $2\chi\sqrt{\bar{n}}$ , directly given by the width of the Poissonian photon distribution  $\sqrt{\bar{n}}$ , in agreement once more with the discussion in the time domain above. Note that at low photon numbers  $2\chi\sqrt{\bar{n}} \ll \Gamma_2$  the resonance shape should still be Lorentzian with width  $2\Gamma_2$ , whereas at larger photon numbers  $2\chi\sqrt{\bar{n}} \gg \Gamma_2$  it should become Gaussian (see Fig. 3.8 bottom panel), directly reflecting the Poissonian distribution of the photon number in the resonator. Such a crossover between a Lorentzian and a Gaussian line-shape for increasing fields in the resonator was indeed observed with a Cooper-Pair Box coupled to a high-Q resonator<sup>21</sup>.

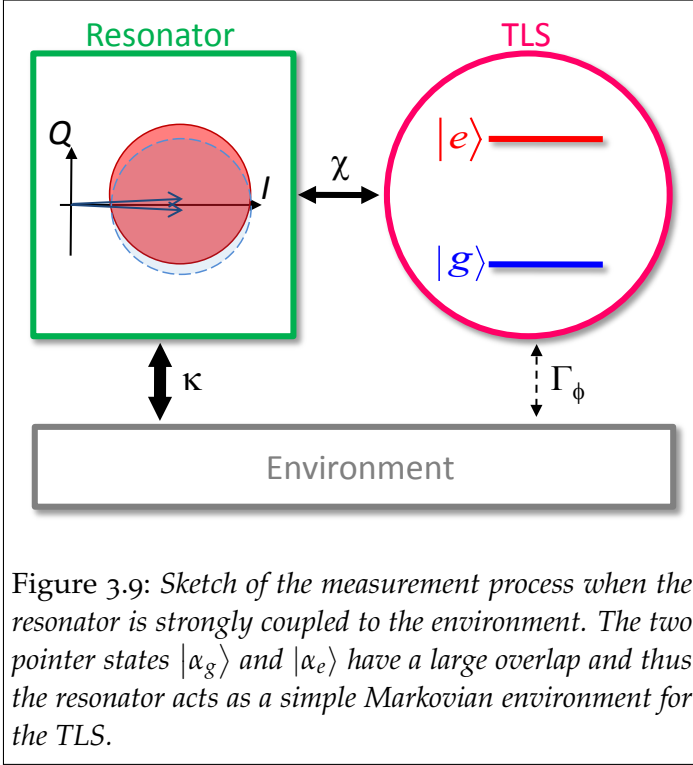
### 3.3.1.2 Measurement-induced dephasing by a resonator of very low quality factor

The situation is somewhat different when the resonator damping rate can not be neglected, and when the resonator is driven. Whereas in the high-Q case the pointer states  $|\alpha_{g,e}\rangle$  were evolving coherently under the action of the dispersive Hamiltonian yielding periodic rephasings of the TLS, they now reach a stationary regime under the combined action of the resonator damping and drive. This situation can only be treated using the full TLS-resonator coupled system density matrix. Fortunately, in the limit relevant for the experiments described in this chapter where  $\chi, \Gamma_\phi \ll \kappa$ , an effective master equation can be derived for the TLS only, yielding analytical formulas for the measurement-induced dephasing rate. We follow here the treatment given by Hutchison *et al.*<sup>97</sup> based on an adiabatic elimination of the resonator field. We wish to give the calculation in some detail because we will need it later in this chapter.

We start by recalling the master equation (Eq. 2.33):



$$\partial_t \hat{\rho} = \mathcal{L} \hat{\rho} = -\frac{i}{\hbar} [\hat{\rho}, \hat{H}] + \kappa \mathcal{D}[\hat{a}] \hat{\rho} + \Gamma_1 \mathcal{D}[\hat{\sigma}_-] \hat{\rho} + 1/2 \Gamma_\phi \mathcal{D}[\hat{\sigma}_z] \hat{\rho}.$$



Note that we will consider here that the measurement field is at the resonator frequency  $\omega_m = \omega_c$ , so that the dispersive Hamiltonian in the interaction picture writes

$$\begin{aligned} \hat{H} = & 1/2 \hbar (\omega_{ge} - \omega_d) \hat{\sigma}_z + \\ & + \hbar \chi (\hat{a}^\dagger \hat{a} + 1/2) \hat{\sigma}_z + \\ & + E_m (\hat{a}^\dagger + \hat{a}) + E_d (\hat{\sigma}_+ + \hat{\sigma}_-). \end{aligned}$$

We then move to the frame defined by the displacement operator  $\hat{D}(\alpha) = \exp(\alpha \hat{a}^\dagger - \alpha^* \hat{a})$ , with a displacement field  $\alpha = -2iE_m/\kappa$  chosen to cancel exactly the steady-state field that would have built up in the resonator in the absence of the TLS. The new master equation in the displaced density matrix  $\hat{\rho}^D(t) = \hat{D}^\dagger(\alpha) \hat{\rho}(t) \hat{D}(\alpha)$  can be shown to be

$$\partial_t \hat{\rho}^D = \mathcal{L}^D \hat{\rho}^D = \mathcal{L}_q \hat{\rho}^D + \kappa \mathcal{D}[\hat{a}] \hat{\rho}^D - i\chi [(\hat{a}^\dagger \hat{a} + \alpha^* \hat{a} + \alpha \hat{a}^\dagger) \hat{\sigma}_z, \hat{\rho}^D].$$

Here  $\mathcal{L}_q$  is the Lindblad super-operator representing the dynamics of the qubit only

$$\mathcal{L}_q \hat{\rho} = -i [\hat{H}_q, \hat{\rho}] + \left( \Gamma_1 + \kappa \frac{g^2}{\Delta^2} \right) \mathcal{D}[\hat{\sigma}_-] \hat{\rho} + \frac{\Gamma_\phi}{2} \mathcal{D}[\hat{\sigma}_z] \hat{\rho}$$

and

$$\hat{H}_q = \frac{(\omega_{ge} - \omega_d) + 2\bar{n}\chi}{2} \hat{\sigma}_z + E_d (\hat{\sigma}^+ + \hat{\sigma}^-)$$

where  $\bar{n} = |\alpha|^2$  is the mean photon number of the intra-resonator field. We now make an adiabatic approximation that consists in supposing that the quantum fluctuations of the displaced resonator state are small. This is a good assumption in the case where the resonator damping is large, because then the field state is then expected to stay very close to  $|\alpha\rangle$  at all time. More precisely, we will suppose that the displaced matrix elements in the photon number basis  $\rho_{n,m}^D$  scale as  $\varepsilon^{n+m}$  where  $\varepsilon = \chi |\alpha| / \kappa \ll 1$ . Expanding the displaced matrix to second order in  $\varepsilon$  yields

$$\hat{\rho}^D = \hat{\rho}_{00} |0\rangle \langle 0| + \hat{\rho}_{10} |1\rangle \langle 0| + \hat{\rho}_{01} |0\rangle \langle 1| + \hat{\rho}_{11} |1\rangle \langle 1| + \hat{\rho}_{20} |2\rangle \langle 0| + \hat{\rho}_{02} |0\rangle \langle 2| + O(\varepsilon^3)$$

and the reduced density matrix for the TLS is  $\hat{\rho}_q = \text{Tr}_{\text{field}}(\hat{\rho}^D) = \hat{\rho}_{00} + \hat{\rho}_{11}$ . Substituting in the master equation we obtain

$$\begin{aligned}\partial_t \hat{\rho}_{00} &= \mathcal{L}_q \hat{\rho}_{00} + \kappa \hat{\rho}_{11} + i\chi (\alpha \hat{\rho}_{01} \hat{\sigma}_z - \alpha^* \hat{\sigma}_z \hat{\rho}_{10}) \\ \partial_t \hat{\rho}_{10} &= \mathcal{L}_q \hat{\rho}_{10} - \kappa \hat{\rho}_{10}/2 + i\alpha\chi (\hat{\rho}_{11} \hat{\sigma}_z - \hat{\sigma}_z \hat{\rho}_{00}) - i\chi (\hat{\sigma}_z \hat{\rho}_{10} + \alpha^* \sqrt{2} \hat{\sigma}_z \hat{\rho}_{20}) \\ \partial_t \hat{\rho}_{11} &= \mathcal{L}_q \hat{\rho}_{11} - \kappa \hat{\rho}_{11} + i\chi (\alpha^* \hat{\rho}_{10} \hat{\sigma}_z - \alpha \hat{\sigma}_z \hat{\rho}_{01}) - i\chi [\hat{\sigma}_z, \hat{\rho}_{11}] \\ \partial_t \hat{\rho}_{20} &= \mathcal{L}_q \hat{\rho}_{20} - \kappa \hat{\rho}_{20} - i\chi (2\hat{\sigma}_z \hat{\rho}_{20} + \alpha \sqrt{2} \hat{\sigma}_z \hat{\rho}_{10})\end{aligned}$$

The off-diagonal matrix elements are damped at a rate  $\kappa$  but populated only at a rate  $|\alpha| \chi / \kappa$ , and therefore decay much faster than the diagonal matrix elements. We thus approximate the off-diagonal matrix elements by their steady-state values

$$\begin{aligned}\hat{\rho}_{10} &= \frac{i\alpha\chi (\hat{\rho}_{11} \hat{\sigma}_z - \hat{\sigma}_z \hat{\rho}_{00})}{\kappa/2} \\ \hat{\rho}_{20} &= \frac{-i\alpha\chi \sqrt{2} \hat{\sigma}_z \hat{\rho}_{10}}{\kappa}.\end{aligned}$$

Substituting these expressions, we find that the TLS density matrix  $\hat{\rho}_q$  then verifies the effective master equation

$$\partial_t \hat{\rho}_q = -i [\hat{H}_q, \hat{\rho}_q] + \left( \Gamma_1 + \kappa \frac{g^2}{\Delta^2} \right) \mathcal{D}[\hat{\sigma}^-] \hat{\rho}_q + \left( \frac{\Gamma_\phi + \Gamma_\phi^{ph}}{2} \right) \mathcal{D}[\hat{\sigma}_z] \hat{\rho}_q \quad (3.1)$$

Let us now give the physical content of this equation. The ensemble-averaged qubit dynamics is modified by the presence of the field in the resonator in three ways:

- the AC Stark shift  $2\chi\bar{n}$  of its resonance frequency (see 2.3.3),
- an additional relaxation rate due to the presence of the cavity, the Purcell damping rate  $\kappa g^2 / \Delta^2$  (see 2.3.1),
- an additional dephasing rate: the measurement induced dephasing  $\Gamma_\phi^{ph} = 8\bar{n}\chi^2 / \kappa$ . Note that the above derivation assumes  $\omega_R \ll \kappa$ , which is not always the case in our experiments.

It is also interesting to calculate the ensemble-averaged expectation of the detector output signal quadratures after demodulation at an angle  $\Theta$  with the signal. We first note that

$$\begin{aligned}\langle \hat{a}(t) \rangle &= \alpha + \text{Tr}_{\text{TLS}} \left[ \text{Tr}_{\text{field}} \left[ \hat{a} \hat{\rho}^D(t) \right] \right] \simeq \alpha + \text{Tr}_{\text{TLS}} [\hat{\rho}_{10}(t)] \\ &\simeq \alpha - \frac{2i\alpha\chi}{\kappa} \text{Tr}_{\text{TLS}} [\hat{\sigma}_z \hat{\rho}_q(t)] = \alpha - \frac{2i\alpha\chi}{\kappa} \langle \hat{\sigma}_z(t) \rangle\end{aligned}$$

Choosing  $E_m$  to be real and positive so that  $\alpha = -i|\alpha|$ , we then have

$$\begin{aligned}\langle \hat{I}_D \rangle &= \sqrt{\kappa G} \langle a e^{-i\Theta} + a^\dagger e^{i\Theta} \rangle / 2 = \bar{I}_D - \sqrt{\kappa G} \frac{2|\alpha|\chi}{\kappa} \cos \Theta \langle \hat{\sigma}_z(t) \rangle \\ \langle \hat{Q}_D \rangle &= \sqrt{\kappa G} \langle -i a e^{-i\Theta} + i a^\dagger e^{i\Theta} \rangle / 2 = \bar{Q}_D + \sqrt{\kappa G} \frac{2|\alpha|\chi}{\kappa} \sin \Theta \langle \hat{\sigma}_z(t) \rangle\end{aligned}$$

with  $\bar{I}_D = -|\alpha| \sin \Theta$  and  $\bar{Q}_D = -|\alpha| \cos \Theta$ . We see that in the low-Q limit, as expected, the quadratures of the output signal measure directly the TLS state, which at the same time obeys the effective master equation above. This has been used in circuit QED experiments to measure ensemble-averaged Rabi oscillations with high fidelity<sup>106</sup>. We note in particular that

$$\sqrt{(\langle \hat{I}_D \rangle - \bar{I}_D)^2 + (\langle \hat{Q}_D \rangle - \bar{Q}_D)^2} = \frac{\Delta V}{2} \langle \hat{\sigma}_z(t) \rangle \quad (3.2)$$

with  $\Delta V/2 = 2\sqrt{\kappa G} |\alpha| \chi/\kappa$ .

To shed light on the physical meaning of the extra dephasing term appearing in Eq. 3.1, it is interesting to follow the analysis by Gambetta *et al.*<sup>22</sup> and to derive this dephasing rate from a simple reasoning based on the quantum fluctuations of the photon number in the resonator. This analysis completely neglects the entanglement occurring between the field and the resonator, an approximation valid in the low-Q regime.

#### *Dephasing caused by fluctuations of intra-resonator photon number*

When a microwave pulse is sent to the resonator, the intra-resonator field which builds up has a fluctuating number of photons  $n(t) = \bar{n} + \delta n(t)$  as a result of the quantum fluctuations –the so-called shot noise. The shot-noise cause fluctuations in the transition frequency of the TLS  $\omega_{ge}$  via the AC-Stark shift:

$$\omega'_{ge}(t) = (\omega_{ge} + 2\chi\bar{n}) + 2\chi\delta n(t)$$

which result in a random dephasing found by integrating the frequency fluctuations over time:

$$\delta\varphi(t) = 2\chi \int_0^t \delta n(\tau) d\tau.$$

To study this dephasing we analyze the time-evolution of the TLS coherence, which is given by the correlator:

$$\langle \hat{\sigma}_-(t) \hat{\sigma}_+(0) \rangle = e^{-\Gamma_2 t} \langle e^{-i\delta\varphi(t)} \rangle,$$

where the first term results from other decoherence process and the second term represents the measurement-induced dephasing only. Assuming that the statistics

of  $\delta\varphi(t)$  are Gaussian, the cumulant expansion  $\langle e^{-i\delta\varphi(t)} \rangle = \exp[-1/2 \langle \delta\varphi^2 \rangle]$  is exact and yields to:

$$\langle \hat{\sigma}_-(t) \hat{\sigma}_+(0) \rangle = \exp \left[ -\Gamma_2 t - 2\chi^2 \int_0^t \int_0^t \langle \delta n(\tau) \delta n(\zeta) \rangle d\tau d\zeta \right].$$

The correlation function  $\langle \delta n(t_1) \delta n(t_2) \rangle$  for a damped driven resonator is<sup>10</sup>

$$\langle \delta n(t_1) \delta n(t_2) \rangle = \bar{n} e^{-\frac{\kappa}{2}|t_1 - t_2|}, \quad (3.3)$$

yielding

$$\langle \hat{\sigma}_-(t) \hat{\sigma}_+(0) \rangle = \exp \left\{ -\Gamma_2 t - \frac{8\bar{n}\chi^2}{\kappa^2} \left[ \kappa |t| - 2 + 2 \exp \left( -\frac{\kappa}{2} |t| \right) \right] \right\}. \quad (3.4)$$

Since  $\Gamma_2 \ll \kappa$ , the dephasing occurs slowly compared to  $\kappa$ , and for the relevant timescales  $t \gg \kappa^{-1}$ , the total dephasing is exponential:

$$\langle \hat{\sigma}_-(t) \hat{\sigma}_+(0) \rangle \approx \exp \left( -(\Gamma_2 + \Gamma_\phi^{ph}) t \right)$$

with the measurement-induced dephasing:

$$\Gamma_\phi^{ph} = \frac{8\chi^2}{\kappa} \bar{n} = \gamma_\phi^{ph} \bar{n}. \quad (3.5)$$

as already seen above. To summarize the measurement-induced dephasing in the low-Q limit can be seen as arising from the incoming microwave pulse shot-noise. We stress however that in this derivation it is assumed that the field has photon number defined independently from the TLS. If however the two pointer states  $|\alpha_g\rangle$  and  $|\alpha_e\rangle$  have widely different amplitude as can happen if the resonator  $Q$  is larger, this assumption does not hold anymore.

### *Calculation in the Bloch-Redfield formalism*

This formula can also be derived in the Bloch-Redfield formalism introduced in 2.2.3 to study the dephasing induced by noise sources coupled to the TLS. In this formalism, the dephasing introduced by the noise on some variable  $\lambda$  is found to be (Eq. 2.25):

$$\Gamma_\phi = \pi D_{\lambda,z}^2 S_\lambda(0)$$

where  $S_\lambda(\omega)$  is the spectral density of the fluctuations of  $\lambda$  and  $D_{\lambda,z}$  is the sensitivity of the longitudinal part of the Hamiltonian to the parameter  $\lambda$ . Here

$$D_{n,z} = \frac{\partial \omega_{ge}}{\partial n} = 2\chi$$

and the spectral density of shot noise found from the time-correlator  $\langle \delta n(t_1) \delta n(t_2) \rangle$  (Eq. 3.3) is

$$S_n(\omega) = \frac{1}{2\pi} \frac{2\bar{n} \frac{\kappa}{2}}{\left(\frac{\kappa}{2}\right)^2 + \omega^2} \quad (3.6)$$

yielding the dephasing rate

$$\Gamma_{\phi}^{ph} = \pi D_{n,z}^2 S_n(0) = \pi (2\chi)^2 \frac{2\bar{n}}{\pi\kappa} = \frac{8\chi^2\bar{n}}{\kappa}$$

already found above (Eq. 3.5). This derivation has the advantage of providing also the decay rate of Rabi oscillations  $\Gamma_R$ , which is related to the noise spectrum  $S_n$  at the Rabi frequency  $\omega_R$ , as explained in 2.2.3.5:

$$\Gamma_R(\omega_R) = \frac{3}{4}\Gamma_1 + \frac{1}{2}\pi D_{\lambda,z}^2 S_{\lambda}(\omega_R) = \frac{3}{4}\Gamma_1 + \frac{4\chi^2\bar{n}}{\kappa} \frac{1}{1 + (2\omega_R/\kappa)^2}. \quad (3.7)$$

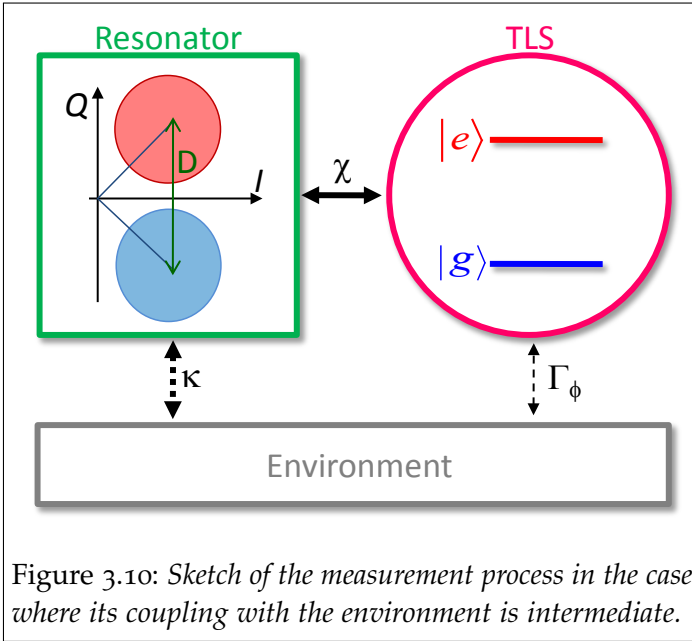


Figure 3.10: Sketch of the measurement process in the case where its coupling with the environment is intermediate.

We describe below the experimental characterization of this Lorentzian dependence on frequency of the measurement-induced dephasing.

### 3.3.1.3 Intermediate case

In the above analyses we have supposed either that the resonator was completely isolated from the environment, or that the coupling of the resonator with the environment is so stronger than the one to the TLS, that the resonator state is almost independent of the TLS state. But for many situations we are between these limiting cases (3.10). Fortunately Gambetta *et al.*<sup>23</sup> studied the decay of the coherences in this most general cQED situation, without making any additional assumption apart from neglecting the

TLS relaxation and driving.

Starting from the master equation for cQED (Eq. 2.33), a master equation for the evolution of the TLS alone can be deduced by using a *polaron-like* transformation. This equation contains a time-dependent measurement-induced dephasing term which is written:

$$\Gamma_{\phi}^{ph}(t) = 2\chi \text{Im} [\alpha_g(t)\alpha_e^*(t)] \quad (3.8)$$

where the resonator coherent field amplitudes vary in time according to:

$$\begin{cases} \dot{\alpha}_e(t) = -iV_m(t) - i(\Delta_r + \chi)\alpha_e(t) - 1/2\kappa\alpha_e(t) \\ \dot{\alpha}_g(t) = -iV_m(t) - i(\Delta_r - \chi)\alpha_g(t) - 1/2\kappa\alpha_g(t) \end{cases}$$

In the low Q limit, the fields  $\alpha_i(t)$  reach very quickly their steady-state value, and thus  $\Gamma_\phi^{ph}(t)$  is constant for relevant timescales of the experiment ( $\gg \kappa^{-1}$ ). Thus,

$$\Gamma_\phi^{ph} = 2\chi\bar{n} \sin(2\delta\varphi_0)$$

and if the states have a large overlap  $\delta\varphi \ll 1$  and we find the same

$$\Gamma_\phi^{ph} = \frac{8\chi^2\bar{n}}{\kappa}$$

as above.

A last very interesting consequence of Eq. 3.8 is that in the steady-state regime (at times  $t \gg \kappa^{-1}$ ), when  $\alpha_{g,e}(t)$  reach their steady-state values  $\alpha_{g,e}$ , the dephasing rate can be written as:

$$\Gamma_\phi^{ph} = \frac{\kappa}{2} |\alpha_g - \alpha_e|^2 = \frac{\kappa}{2} D^2$$

where  $D = |\alpha_g - \alpha_e|$  is known as the *distinguishability* of the states.  $D^2$  represents the amount of information about the TLS stored in the resonator, and  $\kappa D^2$  is the amount of information about the TLS leaking out of the resonator, illustrating the fundamental quantum property that the extraction of information is unavoidably accompanied by an equivalent dephasing of the measured state.

### 3.3.2 SPECTROSCOPIC OBSERVATION OF THE AC-STARK SHIFT AND MEASUREMENT-INDUCED DEPHASING

To verify our understanding of the measurement induced dephasing, we characterize the TLS absorption spectrum while the intra-resonator field contains  $\bar{n}$  photons in average. To create this intra-resonator field, a perturbing field is sent to the resonator while performing the spectroscopy. The TLS line is expected to be AC-Stark shifted to  $\omega'_{ge}(\bar{n}) = \omega_{ge} - 2\chi\bar{n}$  and broadened by the measurement-induced dephasing.

Closely following the experiment performed at Yale<sup>21</sup>, we measure the  $g \rightarrow e$  spectral line of the TLS in presence of a perturbing field that creates a finite photon population in the resonator. This is done, as shown at the top

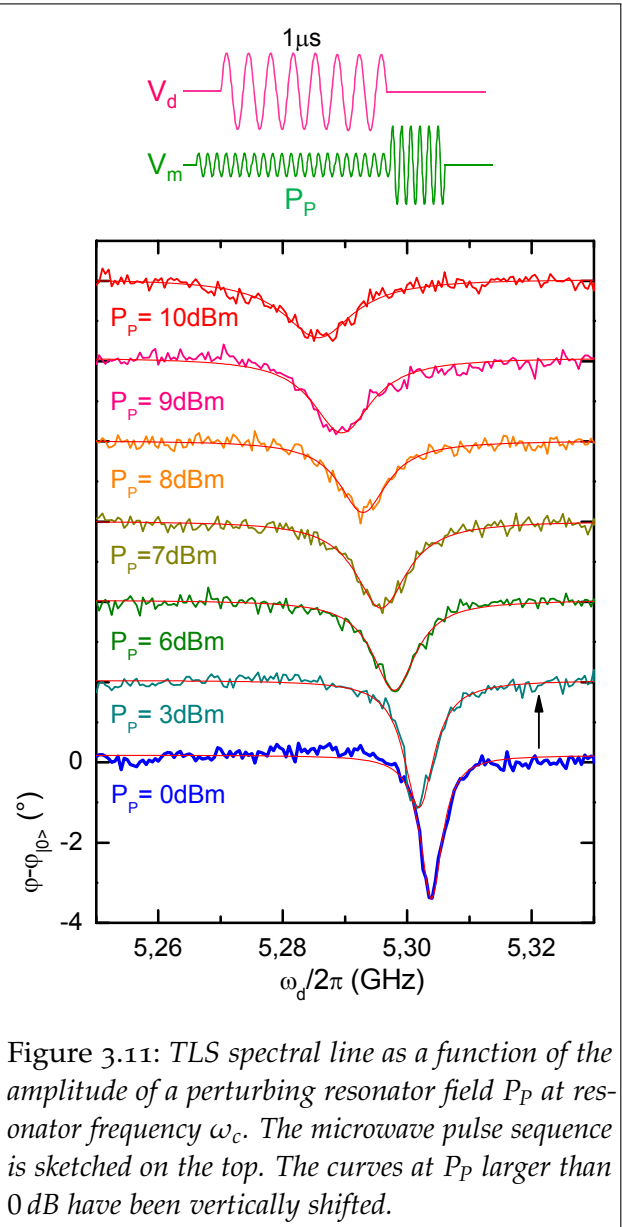


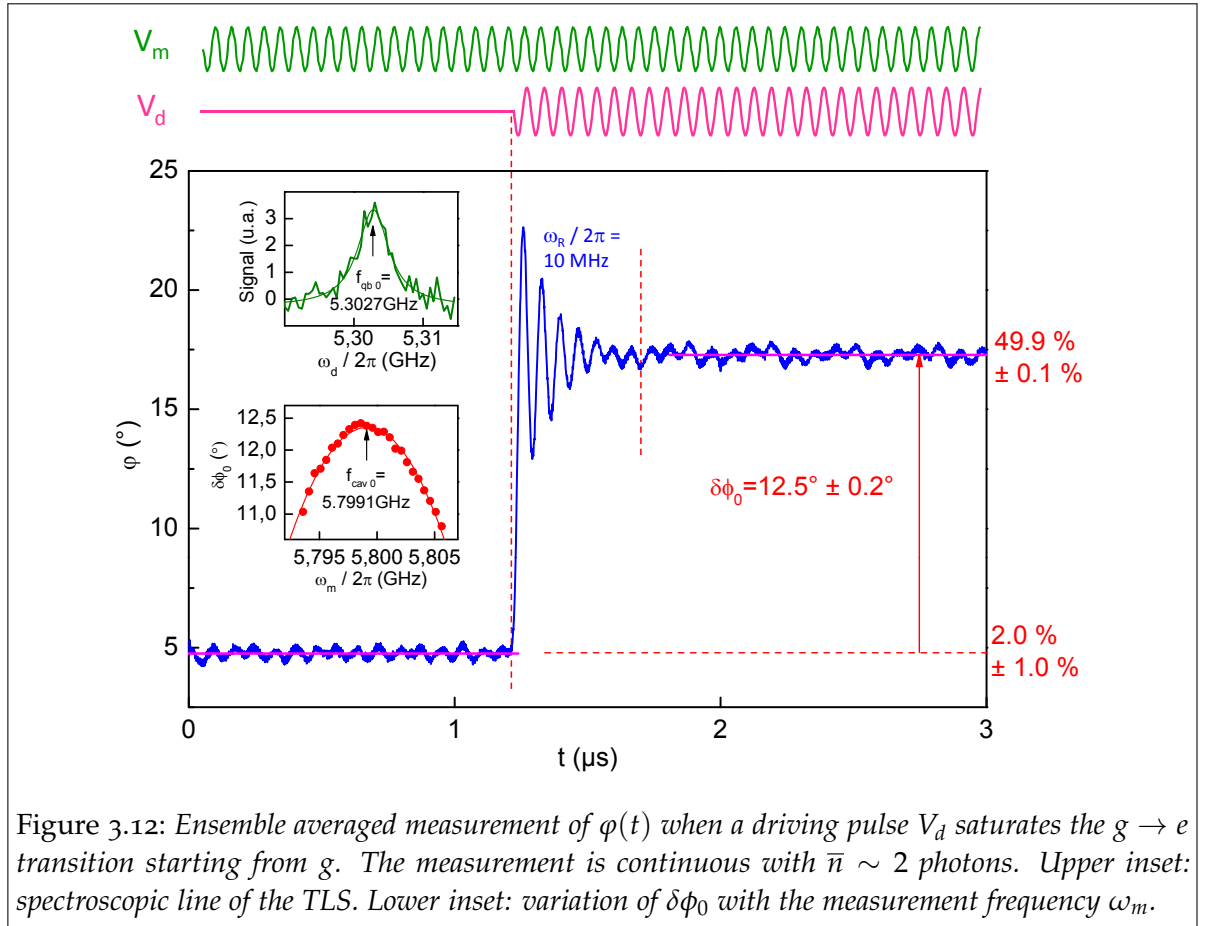
Figure 3.11: TLS spectral line as a function of the amplitude of a perturbing resonator field  $P_p$  at resonator frequency  $\omega_c$ . The microwave pulse sequence is sketched on the top. The curves at  $P_p$  larger than 0 dB have been vertically shifted.

of Fig. 3.11, by sending a perturbing pulse at frequency  $\omega_c$  and power  $P_P$  to the resonator during the spectroscopic excitation of the TLS, which is performed with a long  $V_d$  pulse whose frequency  $\omega_d/2\pi$  is scanned. After these pulses, a large amplitude measurement pulse at  $\omega_c$  performs a projective measurement of the TLS state as explained in 2.4.

The results (Fig. 3.11) show that, as expected, the TLS spectral line shifts down in frequency and broadens as the power of the perturbing field  $P_P$  is increased. To probe if these shifts and broadenings are in quantitative agreement with the theory we need first to calibrate the intra-resonator field in terms of the average number of photons  $\bar{n}$  and for that we need an accurate value of  $\chi$ .

### 3.3.2.1 Determination of $\chi$

In order to determine  $\chi$  accurately we measure the phase shift  $2\delta\phi_0 = 4 \arctan(2\chi/\kappa)$  on the reflected microwave signal which takes place when the TLS state changes from  $|g\rangle$  to  $|e\rangle$ . In this measurement, the resonator is probed continuously with a low-amplitude field  $V_m$  with power  $P_P$ . Then, a long pulse  $V_d$  at  $\omega_{ge}$  saturates the  $g \rightarrow e$  transition. After an initial transient the population of  $g$  and  $e$  become almost equal to 50% so that the detected phase shift should saturate at the value  $\delta\phi_0$ .



To measure the corresponding phase shift the signal reflected onto the resonator is mixed with a local oscillator detuned from  $V_m$  by 3.2 MHz: this heterodyne detection



scheme avoids problems with the offsets of the IQ demodulator. The resulting beating pattern in the two quadratures  $I_D(t)$  and  $Q_D(t)$  is ensemble averaged over a few  $10^5$  identical sequences: the phase  $\varphi(t) = \arctan(E[Q_D(t)]/E[I_D(t)])$  is plotted in Fig. 3.12. This plot yields a shift  $\delta\phi_0 = 12.5 \pm 0.2^\circ$  between no driving and saturation. Note that the frequency of the measuring microwave  $\omega_m$  was scanned to find precisely the frequency for which  $\delta\phi_0$  is maximum, corresponding to the resonator frequency  $\omega_c$ .

For converting this shift into a  $\chi$  value, we take into account that:

- in the absence of microwave drive the TLS is not perfectly in its ground state  $|g\rangle$  due to residual thermal excitation to  $|e\rangle$ . We calibrate this thermal population  $\rho_{ee}^{th} = 0.02 \pm 0.01$  by measuring the noise spectrum with  $V_d$  being switched OFF (see Section 3.6 below).
- the saturation induced by the driving field is slightly below 50% due to longitudinal and transverse relaxation. The population  $\rho_{ee}^{sat}$  in the excited state at saturation is indeed given by the steady state solution to Bloch equations

$$\rho_{ee}^{sat} = \frac{1}{2} - \left( \frac{1}{2} - \rho_{ee}^{th} \right) \frac{1 + (\Gamma_2^{-1}\delta\omega)^2}{1 + (\Gamma_2^{-1}\delta\omega)^2 + (\omega_R^2\Gamma_1^{-1}\Gamma_2^{-1})}. \quad (3.9)$$

Here  $\omega_R/2\pi = 10$  MHz is fixed by the driving strength,  $\Gamma_1^{-1} = 200 \pm 10$  ns and  $\Gamma_2^{-1} = 150 \pm 10$  ns are independently measured. Note that here, as in all the following experiments,  $\delta\omega = 0$  since an automated spectroscopy sequence is programmed to measure  $\omega'_{ge}(P_p)$  just before the experiment, and to assign its value to  $\omega_d$ . Finally we obtain  $\rho_{ee}^{sat} = 0.496 \pm 0.001$  instead of 0.5.

Taking these two effects into account, we calculate  $\delta\phi_0 = (0.95 \pm 0.02)\delta\phi_0$ . Maximizing all the uncertainties including those on  $\kappa$ , we finally obtain  $\chi/2\pi = \kappa \tan(\delta\phi_0/2)/4\pi = 1.75(-0.11/+0.14)$  MHz, which is also consistent with the TLS parameters determined by spectroscopy.

### 3.3.2.2 AC-Stark shift: in-situ calibration of $\bar{n}$

The combination of the cavity-pull and AC-Stark shift provides a convenient way to calibrate in-situ the average number of photons  $\bar{n}$  stored in the resonator when a pulse of power  $P_p$  is sent to it. Indeed, as shown in 3.13, the TLS frequency is AC-stark shifted down proportionally to the power  $P_p$  of the perturbing field. Since the AC-Stark shift is  $-2\chi\bar{n}$ , and we have obtained an accurate value of  $\chi$ , the dependence between  $P_p$  and  $\bar{n}$  is immediately obtained (scale on top of 3.13).

### 3.3.2.3 Measurement induced-dephasing

Since the  $Q$  of our resonator is low, we expect the Eq. 3.5 to be valid and the spectral line to be broadened by the measurement-induced dephasing reaching a width (FWHM)  $\Delta\omega = 2\left(\Gamma_2 + \bar{n}\gamma_\phi^{ph}\right)$  with  $\gamma_\phi^{ph} = 8\chi^2/\kappa$ . The experimentally measured widths of the spectral line are shown in 3.13, and are in good agreement with this theoretical prediction.



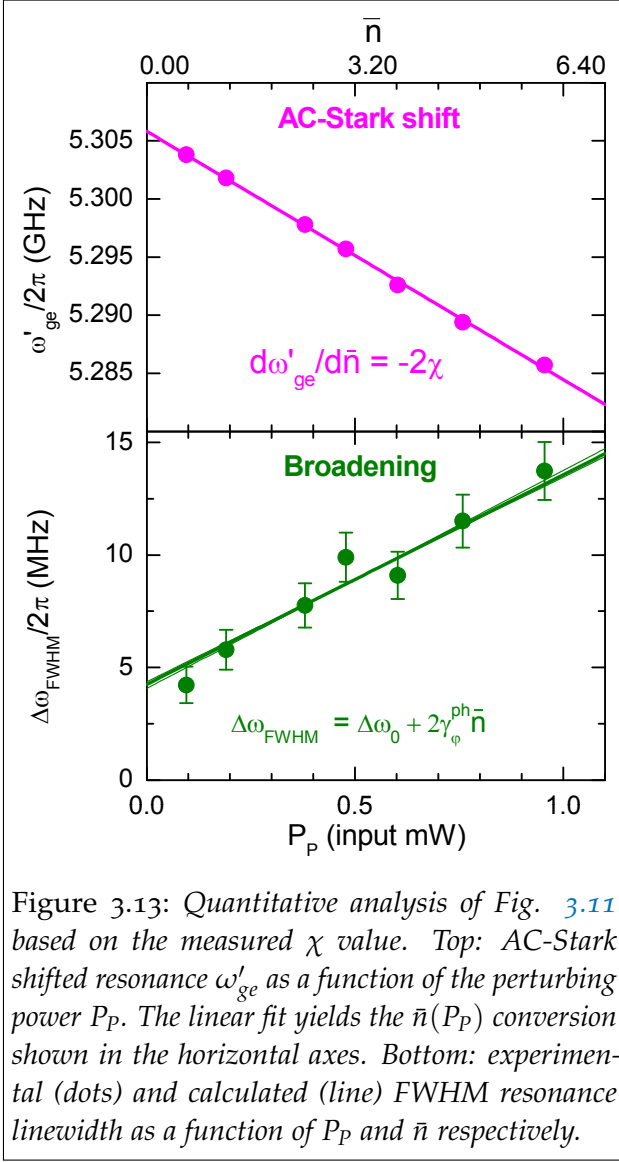


Figure 3.13: Quantitative analysis of Fig. 3.11 based on the measured  $\chi$  value. Top: AC-Stark shifted resonance  $\omega'_{ge}$  as a function of the perturbing power  $P_p$ . The linear fit yields the  $\bar{n}(P_p)$  conversion shown in the horizontal axes. Bottom: experimental (dots) and calculated (line) FWHM resonance linewidth as a function of  $P_p$  and  $\bar{n}$  respectively.

Note that this linear dependence is only valid for small  $\bar{n}$  as the ones used in our experiment and a saturation occurs for higher values of  $n \simeq n_{crit}^{21}$ .

### 3.3.3 CHARACTERIZATION IN FREQUENCY OF THE MEASUREMENT-INDUCED DEPHASING

The line broadening in the spectroscopic measurements shown above gives access to the measurement-induced dephasing. However, as we deduced above (Eq. 3.7), the decay rate of Rabi oscillations at Rabi frequency  $\omega_R$  is sensitive to the spectral density of noise at  $\omega_R$ : we thus expect to observe an interesting effect of reduction of the oscillations dephasing rate at high  $\omega_R$  due to the filtering of the shot noise by the resonator, which is not possible to observe in the TLS spectral line.

To measure Rabi oscillations in presence of a perturbing field, we use the sequence of pulses shown on left inset of Fig. 3.14. During a microwave pulse at  $\omega_c$  that builds up a perturbing intra-resonator field of  $\bar{n}$  photons, a driving pulse of length  $\Delta t$  induces a rotation in the azimuthal plane of the Bloch sphere of an angle  $\omega_R \Delta t$ . The frequency of this driving pulse is set to the AC-Stark shifted TLS fre-

quency which is spectroscopically measured by an automated procedure for each  $\bar{n}$ . Just after the driving pulse ends, a large amplitude measurement pulse is used for measuring the TLS state as explained in 2.4: the signal is time-averaged over the measurement pulse, yielding the phase  $\bar{\varphi}_i(\Delta t)$ . Repeating  $10^4$  times this procedure yields an ensemble-averaged point  $\bar{\varphi}(\Delta t) = E[\bar{\varphi}_i(\Delta t)]$ . Then  $\Delta t$  is incremented to produce the next point of the Rabi oscillation.

The resulting curves are shown in Fig. 3.14. For each Rabi frequency the oscillations were acquired at different perturbing field powers  $P_p$ . The qualitative behaviour is the expected one: when increasing  $\bar{n}$ , the Rabi oscillations decay more rapidly due to the measurement-induced dephasing. At some point the oscillations are completely washed out and replaced by an exponential decay. For even larger  $\bar{n}$ , the damping time constant increases, indicating an inhibition of the TLS transition from  $|g\rangle$  to  $|e\rangle$ , which is a signature of the Quantum Zeno Effect discussed below (see 3.3.3.1).

A quantitative analysis of these curves is performed by fitting each Rabi curve with the analytical solution of Bloch equations<sup>107</sup>. In this fit the longitudinal decay time  $\Gamma_{||}$  is fixed to the independently measured relaxation rate  $\Gamma_1 = (225 \pm 10 \text{ ns})^{-1}$ . The

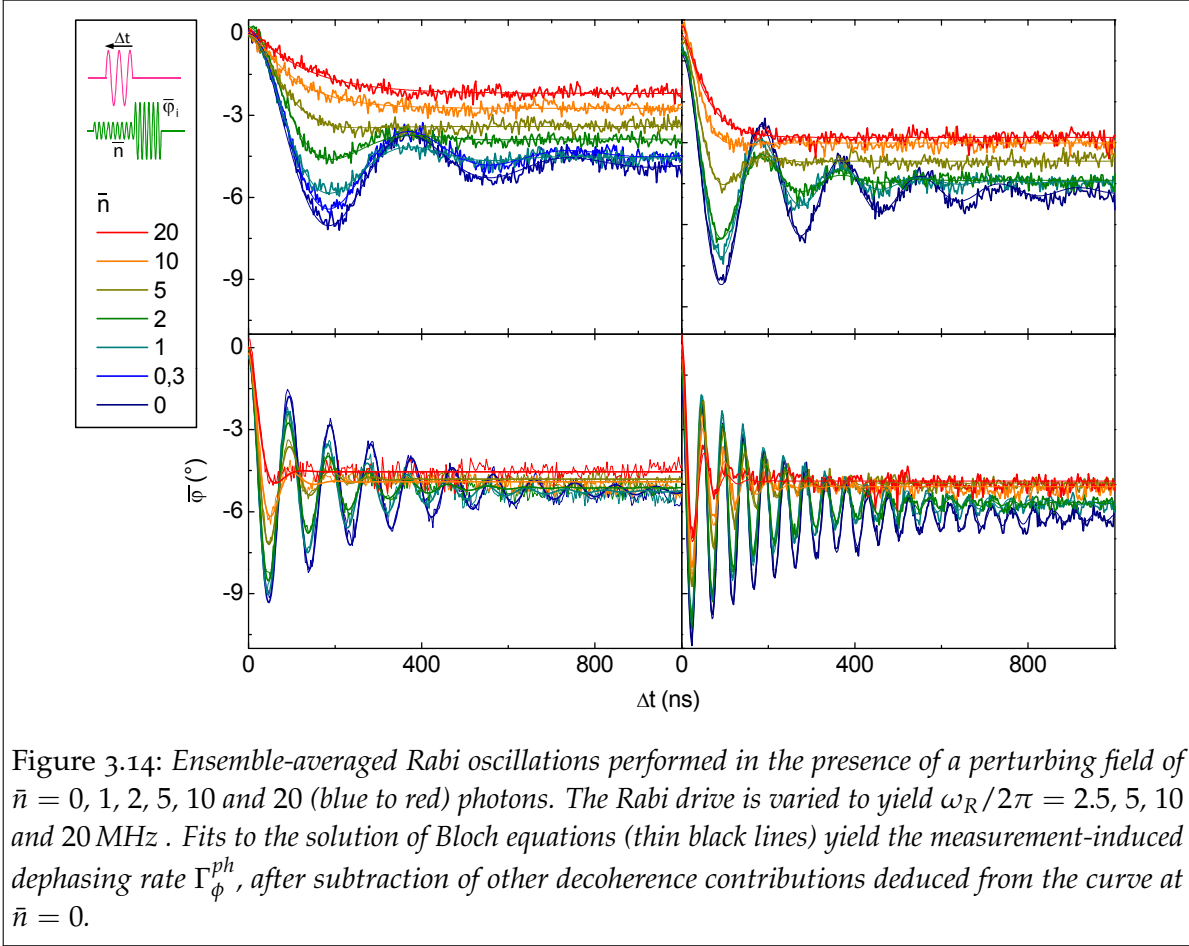


Figure 3.14: Ensemble-averaged Rabi oscillations performed in the presence of a perturbing field of  $\bar{n} = 0, 1, 2, 5, 10$  and  $20$  (blue to red) photons. The Rabi drive is varied to yield  $\omega_R/2\pi = 2.5, 5, 10$  and  $20$  MHz. Fits to the solution of Bloch equations (thin black lines) yield the measurement-induced dephasing rate  $\Gamma_\phi^{ph}$ , after subtraction of other decoherence contributions deduced from the curve at  $\bar{n} = 0$ .

transverse decay  $\Gamma_\perp$  rate is fitted, and compared to the theoretical predictions, using the fact that, as explained in 2.2.3.5, the Rabi oscillations decay rate is

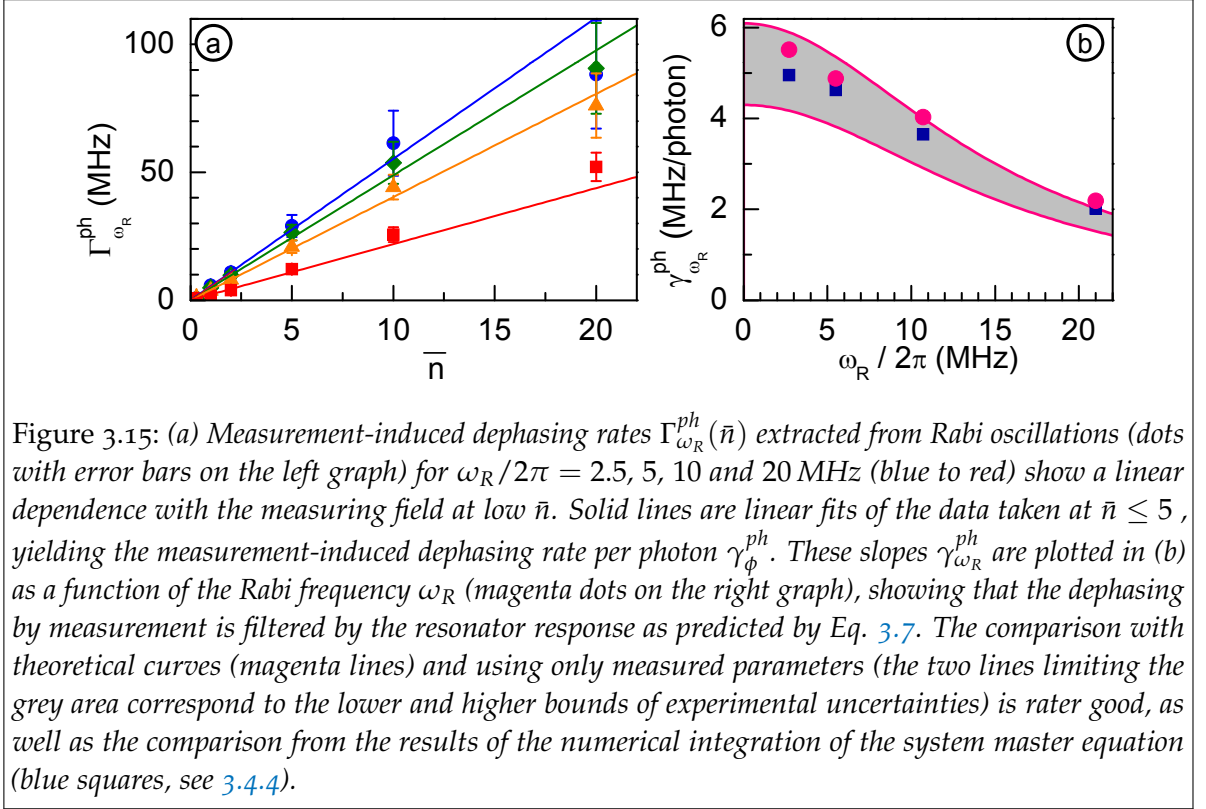
$$\tilde{\Gamma}_2 = 3/4\Gamma_1 + 1/2\Gamma_{\omega_R} = 1/2(\Gamma_1 + \Gamma_\perp).$$

Thus this transverse rate  $\Gamma_\perp$  has two components:

$$\Gamma_\perp(\bar{n}) = \underbrace{\Gamma_{\omega_R}^{ph}(\bar{n})}_{\text{measurement}} + \underbrace{\Gamma_{\omega_R}^0 + 1/2\Gamma_1}_{\text{other dephasing+relaxation}}.$$

The measurement independent contribution  $\Gamma_\perp(0) = \Gamma_{\omega_R}^0 + 1/2\Gamma_1$  coming from other dephasing sources and from energy relaxation has to be the same for all the curves. As shown in Fig. 3.15a, for each  $\omega_R$  the measured  $\Gamma_{\omega_R}^{ph}(\bar{n})$  are proportional to  $\bar{n}$ , as expected. Their slopes  $\gamma_{\omega_R}^{ph}$  are determined by fitting  $\Gamma_{\omega_R}^{ph}(\bar{n})$  up to  $\bar{n} = 5$  and are shown in Fig. 3.15b: these  $\gamma_{\omega_R}^{ph}$  follow a Lorentzian cutoff, as expected from theory, showing that the shot noise is indeed filtered by the resonator. Their values are in good agreement with the predictions of Eq. 3.7 using the independently measured values of  $\chi$  and  $\kappa$ . We thus have a full quantitative understanding of the measurement-induced dephasing in our system and its dependence on frequency. Interestingly, this frequency dependence follows the same cutoff as the signal, illustrating once again the fundamental quantum property that the amount of information extracted is

unavoidably accompanied by an equivalent amount of dephasing of the measured state.



### 3.3.3.1 Quantum Zeno Effect

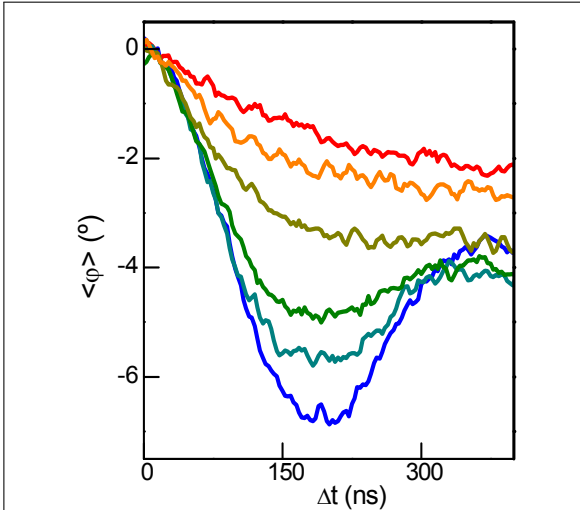


Figure 3.16: Ensemble-averaged Rabi oscillations at  $\omega_R/2\pi = 2.5$  MHz and  $\bar{n} = 0, 1, 2, 5, 10$  and  $20$  (blue to red) photons. The higher  $\bar{n}$  curves show a slowdown of the TLS excitation which is the signature of the Quantum Zeno Effect.

When the TLS is weakly driven and very strongly measured (see first panel of Fig. 3.14, and Fig. 3.16 for the highest  $\bar{n}$ ), the ensemble-averaged signal is no longer oscillating but consists of an exponential decay. When the power is further increased the time-constant grows and the time dependence at short times changes from quadratic to approximately linear with an increasing time constant, which is a manifestation of the Quantum Zeno effect<sup>27,108,28</sup> (QZE).

The QZE is a progressive slow-down of the dynamics of a system when it is being measured. It comes as a consequence of the measurement postulate: after a measurement the system is reset in the eigenstate corresponding to the

measured outcome. Therefore, if measurements are repeated often enough, the system is *blocked* in its initial state. This evokes the paradox of the arrow devised by Zeno of Elea:

*If everything is either in motion or at rest, if it is at rest when it occupies an equal space, and if that which is in locomotion is at any precise instant occupying such a space, the flying arrow is therefore motionless.*

—Aristotle, *Physics* VI, 9

In principle it could be possible to block the system in any initial state in this way. However, to overcome the relaxation which tends to collapse the TLS state to  $|g\rangle$ , the measurement would need to be repeated in a timescale in which the qubit relaxation is not linear but quadratic in time, a timescale which is of the order of the environment correlation time. For the case of cQED these timescales are several orders of magnitude shorter than the fastest measurement which can be performed. Therefore, in this experiment, as well as in former ones performed with other systems<sup>28</sup>, only the inhibition of a coherent *excitation* process is accessible experimentally.

### 3.4 CONTINUOUS MEASUREMENTS

In the experiments described above the link between measurement and dephasing is inferred by mimicking the measurement field by sending a microwave pulse at the resonator frequency  $\omega_c$ . However, although the reflected perturbing pulse contains some information on the TLS state, this information is not used, and all our knowledge of the system comes from a final projective measurement performed with a high amplitude microwave pulse. After this measurement the oscillation is stopped, and the system is prepared again in the same state. The oscillations are therefore averaged over an ensemble of identically prepared situations. To go further in the study of the dynamics of the measured system, we now want to monitor a *single and continuous* Rabi oscillation, extracting the information on the TLS state at the same time that it is evolving. According to the theoretical predictions of Korotkov *et al.*<sup>24</sup> the power spectrum at the detector's output should then contain a Lorentzian peak at the Rabi frequency.

Moreover, such continuous measurement brings more information on the system than the ensemble-averaged measurements discussed above. Specifically, if we take the precession of a classical macro-spin, and a

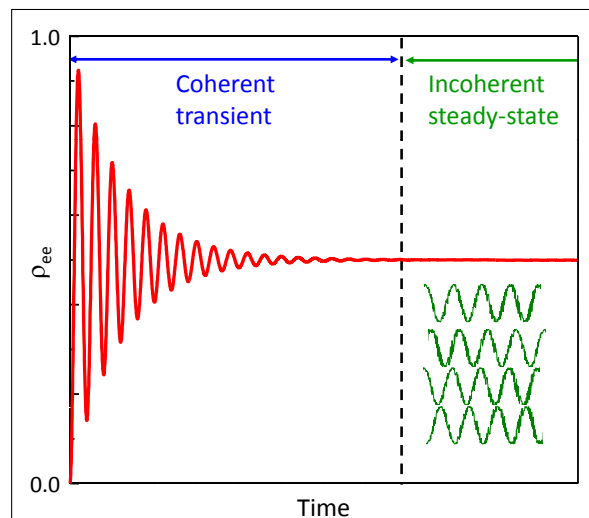


Figure 3.17: Ensemble-averaged Rabi oscillations (in red) decay in amplitude until reaching zero amplitude in the steady-state. However, the individual trajectories of the ensemble (green curves) keep oscillating: the null average of the ensemble comes from the random dephasing between the different trajectories.

quantum TLS, the ensemble-averaged measurements performed on them can be equivalent, in strong contrast with continuous measurement, which allow to distinguish both situations as discussed below.

### 3.4.1 THEORETICAL PREDICTIONS FOR THE POWER SPECTRUM OF THE DETECTOR

As seen in Fig. 3.14, ensemble-averaged Rabi oscillations decay after a time  $\Gamma_R^{-1}$  which becomes shorter when the measurement strength is increased. The reason for such a decay is sketched in the Fig. 3.17: different realization of the oscillations in the ensemble become progressively dephased, and thus their average tends to zero. However, in each particular realization the TLS is still undergoing oscillations, which leave a signature in the power spectrum at the detector output: a Lorentzian peak at the Rabi frequency.

We now want to calculate the exact shape of this peak, i.e. the power spectrum  $S_X(\omega) = \mathcal{F}[K_X(\tau)]$  of the detected signal components  $X_D(t)$  where  $X = I, Q$ , depending on the Rabi frequency and the measurement strength. These power spectra are given by the Fourier transform of the autocorrelation functions  $K_X(\tau) = E[X_D(t)X_D(t + \tau)]$  calculated when the system is in its steady-state. We will now explain how these correlation functions can be computed analytically in the limiting case where the resonator bandwidth is infinite, which would correspond to a very low quality factor as is the case in our experiment. Note that similar calculations have been performed using a great variety of methods<sup>25,109,24,110</sup>, for the situation of a DQD measured by a QPC.

The link between the correlation function

$$K_X(\tau) = E[X_D(t)X_D(t + \tau)] - E[X_D(t)]E[X_D(t + \tau)]$$

involving a classical measurement record and the corresponding quadrature operators  $\hat{X}_{out}$  of the fields leaking out of the resonator (given in the Heisenberg representation) is

$$K_X(\tau) = G [\langle : \hat{X}_{out}(t + \tau) \hat{X}_{out}(t) : \rangle - \langle \hat{X}_{out}(t + \tau) \rangle \langle \hat{X}_{out}(t) \rangle]$$

where  $::$  indicates normal ordering of the operators (i.e. creation operators at the left of all annihilation operators<sup>62</sup>). Using  $\hat{I}_{out}(t) = \sqrt{\kappa} (\hat{a}(t) + \hat{a}^\dagger(t)) / 2$  and  $\hat{Q}_{out}(t) = i\sqrt{\kappa} (\hat{a}^\dagger(t) - \hat{a}(t)) / 2 + E_m / \sqrt{\kappa}$ , one can show that

$$K_I(\tau) + K_Q(\tau) = G \left[ \kappa \operatorname{Re} \left( \langle \hat{a}^\dagger(t + \tau) \hat{a}(t) \rangle \right) - \kappa |\langle \hat{a}(t) \rangle|^2 \right].$$

We therefore need to calculate the two-time correlation function  $\langle \hat{a}^\dagger(t + \tau) \hat{a}(t) \rangle$ . As we will see, one can obtain a simple formula for this correlator in the low-Q limit. We will use for that the adiabatic elimination technique described in 3.3.1.2 and in Hutchinson *et al.*<sup>97</sup> to rewrite this expression as a function of TLS operators only. As explained above, the field is first rewritten as  $\hat{a}(t) = \alpha + \hat{b}(t)$  where  $\alpha = -2iE_m/\kappa$  is a classical field amplitude and  $\hat{b}(t)$  contains the quantum fluctuations due to the TLS

dynamics. This yields  $K(\tau) = K_I(\tau) + K_Q(\tau) = \kappa G \operatorname{Re} \left( \left\langle \hat{b}^\dagger(t + \tau) \hat{b}(t) \right\rangle \right)$ . We then rewrite

$$\left\langle \hat{b}^\dagger(t + \tau) \hat{b}(t) \right\rangle = \operatorname{Tr} \left( \hat{b}^\dagger \exp(\mathcal{L}^D \tau) \left[ \hat{b} \hat{\rho}^D(t) \right] \right)$$

where  $\hat{\rho}^D(t)$  is the steady-state displaced density matrix of the whole system, governed by the Lindblad super-operator  $\mathcal{L}^D$  that describes the full master equation<sup>62</sup>. This can be written

$$\operatorname{Tr} \left( \hat{b}^\dagger \exp(\mathcal{L}^D \tau) \left[ \hat{b} \hat{\rho}^D(t) \right] \right) = \operatorname{Tr}_{\text{TLS}}[K']$$

with  $K' = \operatorname{Tr}_{\text{field}} \left( \hat{b}^\dagger \exp(\mathcal{L}^D \tau) \left[ \hat{b} \hat{\rho}^D(t) \right] \right)$ . We then note  $\tilde{\rho}(t) = \hat{b} \hat{\rho}^D(t)$ , and  $\tilde{\rho}(t + \tau) = \exp(\mathcal{L}^D \tau) \left[ \hat{b} \hat{\rho}^D(t) \right]$ . Given the expansion of the density matrix

$$\hat{\rho}^D = \hat{\rho}_{00} |0\rangle \langle 0| + \hat{\rho}_{10} |1\rangle \langle 0| + \hat{\rho}_{01} |0\rangle \langle 1| + \hat{\rho}_{11} |1\rangle \langle 1| + \hat{\rho}_{20} |2\rangle \langle 0| + \hat{\rho}_{02} |0\rangle \langle 2| + O(\varepsilon^3)$$

in powers of  $\varepsilon = \chi |\alpha| / \kappa \ll 1$ , we can restrict ourselves to the  $\{|0\rangle, |1\rangle\}$  subspace so that  $K' = \operatorname{Tr}_{\text{field}}[\tilde{\rho}^\dagger(t + \tau)] = \langle 0| \tilde{\rho}(t + \tau) |1\rangle = \tilde{\rho}_{01}(t + \tau)$ . This is the matrix element we need to calculate to lowest order in  $\varepsilon$ .

From the  $\hat{\rho}^D$  expansion, we have:  $\tilde{\rho}(t) = \hat{b} \hat{\rho}^D(t) = \hat{\rho}_{10}(t) |0\rangle \langle 0| + \sqrt{2} \hat{\rho}_{20}(t) |1\rangle \langle 0| + \hat{\rho}_{11}(t) |0\rangle \langle 1|$ . Since  $\tilde{\rho}(t + \tau) = \exp(\mathcal{L}^D \tau) (\tilde{\rho}(t))$  for any  $\tau > 0$ , the equations of motion for  $\tilde{\rho}$  are the same as for  $\hat{\rho}$  so the same reasoning as done in the adiabatic elimination can be done. In particular

$$\tilde{\rho}_{01} = -\frac{2i\alpha^* \chi}{\kappa} (\hat{\sigma}_z \tilde{\rho}_{11} - \tilde{\rho}_{00} \hat{\sigma}_z).$$

and to lowest order in  $\varepsilon$ ,

$$\tilde{\rho}_{01}(t + \tau) \simeq \frac{2i\alpha^* \chi}{\kappa} \tilde{\rho}_{00}(t + \tau) \hat{\sigma}_z.$$

We now need to link  $\tilde{\rho}_{00}(t + \tau)$  to  $\tilde{\rho}_{00}(t)$ . For that we again use the fact that  $\tilde{\rho}_{00}(t + \tau) \simeq \tilde{\rho}_q(t + \tau)$  where  $\tilde{\rho}_q = \tilde{\rho}_{00} + \tilde{\rho}_{11}$ . As already shown for the qubit density matrix  $\hat{\rho}_q = \hat{\rho}_{00} + \hat{\rho}_{11}$ ,  $\tilde{\rho}_q$  satisfies the qubit master equation with Lindblad super-operator  $\mathcal{L}_q$  so that

$$\tilde{\rho}_q(t + \tau) = \exp(\mathcal{L}_q \tau) \tilde{\rho}_q(t).$$

All this yields

$$\tilde{\rho}_{01}(t + \tau) = \frac{2i\alpha^* \chi}{\kappa} \left[ \exp(\mathcal{L}_q \tau) \tilde{\rho}_q(t) \right] \hat{\sigma}_z.$$



Similarly,  $\tilde{\rho}_q(t) \simeq \tilde{\rho}_{00}(t)$  to lowest order in  $\varepsilon$ , with  $\tilde{\rho}_{00}(t) = \hat{\rho}_{10}(t) \simeq (-2i\alpha\chi/\kappa)\hat{\sigma}_z\hat{\rho}_{00}(t) \simeq (-2i\alpha\chi/\kappa)\hat{\sigma}_z\hat{\rho}_q(t)$ . Finally we obtain

$$\tilde{\rho}_{01}(t + \tau) = \frac{4|\alpha|^2\chi^2}{\kappa^2} \left\{ \exp(\mathcal{L}_q\tau) [\hat{\sigma}_z\hat{\rho}_q(t)] \right\} \hat{\sigma}_z$$

yielding

$$\begin{aligned} K(\tau) &= \kappa G \text{Tr}_{\text{TLS}}(K') = \kappa G \frac{4|\alpha|^2\chi^2}{\kappa^2} \text{Tr}_{\text{TLS}}(\left\{ \exp(\mathcal{L}_q\tau) [\hat{\sigma}_z\hat{\rho}_q(t)] \right\} \hat{\sigma}_z) = \\ &= G \frac{4|\alpha|^2\chi^2}{\kappa} \text{Tr}_{\text{TLS}}(\hat{\sigma}_z \left\{ \exp(\mathcal{L}_q\tau) [\hat{\sigma}_z\hat{\rho}_q(t)] \right\}) = \left( \frac{\Delta V}{2} \right)^2 \langle \hat{\sigma}_z(t + \tau)\hat{\sigma}_z(t) \rangle \end{aligned}$$

so that

$$K(\tau) = (\Delta V/2)^2 K_{\hat{z}}(\tau) \quad (3.10)$$

with  $K_{\hat{z}}(\tau) = \langle \hat{\sigma}_z(t + \tau)\hat{\sigma}_z(t) \rangle$ . We note that the coefficient linking both correlators is simply the square of the coefficient  $(\Delta V/2)$  linking the ensemble-averaged signal quadratures to  $\langle \hat{\sigma}_z(t) \rangle$  as shown by 3.2. This will be used in the following to convert measured power spectra into dimensionless spin units. We therefore find that in the low quality factor limit, the two-time correlation function of the output homodyne signal is directly given by the correlation function of  $\hat{\sigma}_z$ , with the TLS obeying the Bloch equations as given by the effective master equation Eq. 3.1. Other demonstrations of this result have been obtained by Korotkov for the case of the DQD measured by a QPC<sup>109,24</sup>. The correlation function of a continuous and weak measurement gives therefore the same quantity as if two successive and instantaneous projective measurements were performed at time  $t$  and then at time  $t + \tau$ , although yielding much less signal.  $K_{\hat{z}}(\tau)$  can then be conveniently calculated as

$$K_{\hat{z}}(\tau) = \langle \hat{\sigma}(0)\hat{\sigma}(\tau) \rangle = p[\sigma(0) = -1] \langle \hat{\sigma}(\tau) \rangle_{\sigma(0)=+1} - p[\sigma(0) = +1] \langle \hat{\sigma}(\tau) \rangle_{\sigma(0)=-1}$$

where  $p[\sigma(0) = \pm 1]$  is the probability that  $\sigma$  starts from  $\pm 1$  at the initial time and  $\langle \hat{\sigma}(\tau) \rangle_{\sigma(0)=\pm 1}$  is the evolution of the average value of  $\hat{\sigma}$  conditioned to the initial state  $\pm 1$ , which can be directly determined by the Lindblad super-operator  $\mathcal{L}_q$ . For a TLS undergoing Rabi oscillations at frequency  $\omega_R$  with damping rate  $\Gamma_R$ , we obtain for instance that  $K_{\hat{z}}(\tau) = e^{-\Gamma_R\tau} \cos \omega_R\tau$ . Using the most general formula giving the analytical solutions for the transient of the Bloch equations calculated by Torrey<sup>107</sup>, we obtain after Fourier transform the spectrum:

$$\begin{aligned} S_{\hat{z}}(\omega) &= \frac{4}{[\Gamma_{\parallel}^2 + (\omega - \tilde{\omega}_R)^2][\Gamma_{\parallel}^2 + (\omega + \tilde{\omega}_R)^2]} \cdot \left\{ \Gamma_{\parallel}(1 - z_{st}^2)(\Gamma_{\parallel}^2 + \tilde{\omega}_R^2 + \omega^2) + \right. \\ &\quad \left. + \left[ (1 - z_{st}^2)(\Gamma_{\parallel} - \Gamma_{\perp})/2 - \omega_R^2 z_{st}^2 / \Gamma_{\parallel} \right] (\Gamma_{\parallel}^2 + \tilde{\omega}_R^2 - \omega^2) \right\} \quad (3.11) \end{aligned}$$

In this expression  $\Gamma_{\parallel}$  and  $\Gamma_{\perp}$  are the transverse and longitudinal relaxation respectively (discussed below),  $\tilde{\omega}_R = \sqrt{\omega_R^2 - 1/4(\Gamma_{\parallel} - \Gamma_{\perp})^2}$  and  $z_{st} = -(1 + \Gamma_1^{-1}\Gamma_2^{-1}\omega_R^2)^{-1}$  is the steady state solution.

### 3.4.2 IMPLEMENTING A CONTINUOUS MEASUREMENT

#### 3.4.2.1 Noise power spectrum measurement setup

We now describe our experimental implementation of a CW measurement. The microwave sources:  $V_d$ , which drives the TLS and  $V_m$ , which measures its state, are continuously turned on. The TLS state is thus continuously precessing in the azimuthal plane of the Bloch sphere and, at the same time, the measurement is continuously extracting information on its state and dephasing the oscillations.

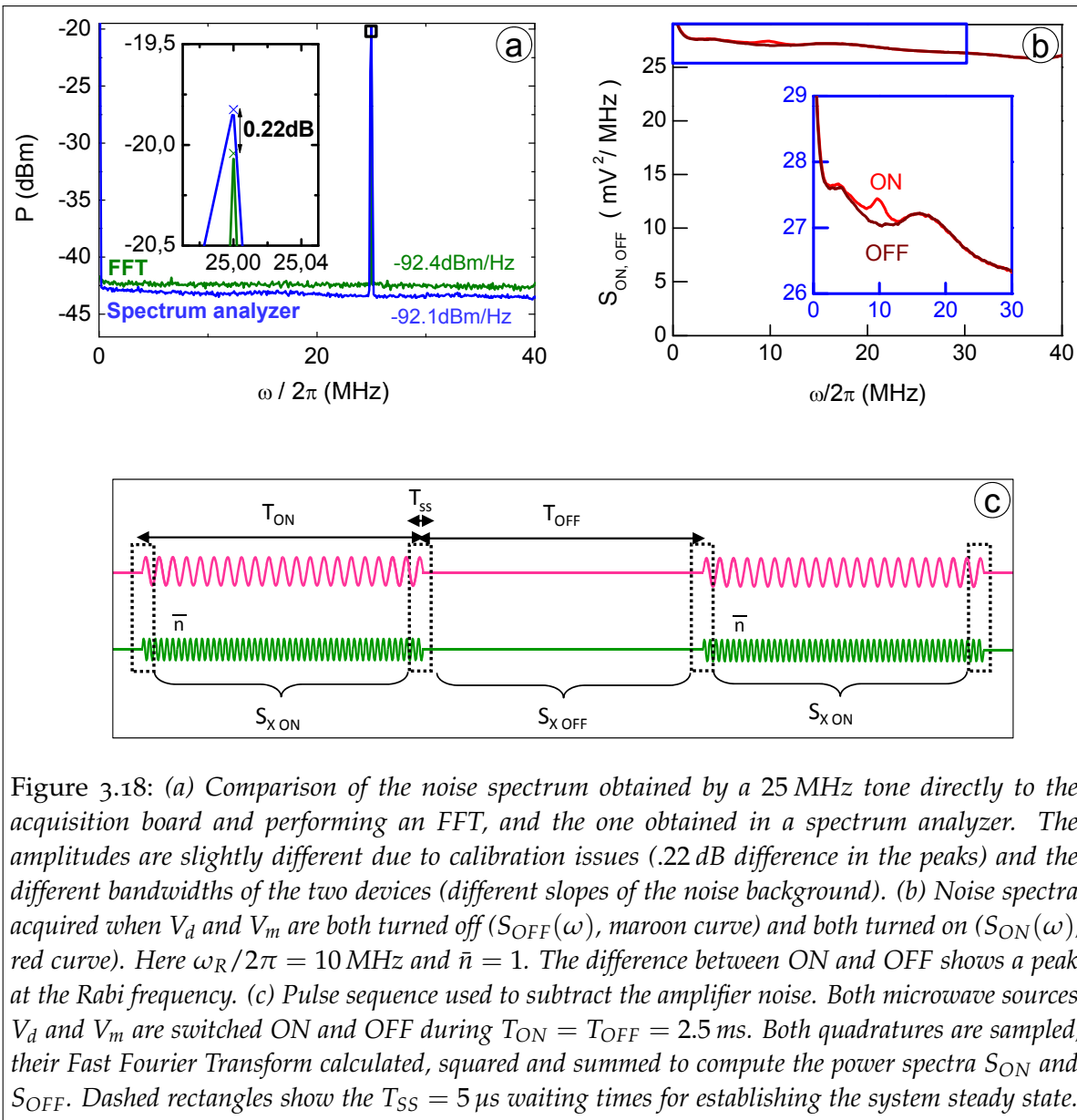


Figure 3.18: (a) Comparison of the noise spectrum obtained by a 25 MHz tone directly to the acquisition board and performing an FFT, and the one obtained in a spectrum analyzer. The amplitudes are slightly different due to calibration issues (.22 dB difference in the peaks) and the different bandwidths of the two devices (different slopes of the noise background). (b) Noise spectra acquired when  $V_d$  and  $V_m$  are both turned off ( $S_{OFF}(\omega)$ , maroon curve) and both turned on ( $S_{ON}(\omega)$ , red curve). Here  $\omega_R/2\pi = 10$  MHz and  $\bar{n} = 1$ . The difference between ON and OFF shows a peak at the Rabi frequency. (c) Pulse sequence used to subtract the amplifier noise. Both microwave sources  $V_d$  and  $V_m$  are switched ON and OFF during  $T_{ON} = T_{OFF} = 2.5$  ms. Both quadratures are sampled, their Fast Fourier Transform calculated, squared and summed to compute the power spectra  $S_{ON}$  and  $S_{OFF}$ . Dashed rectangles show the  $T_{SS} = 5 \mu s$  waiting times for establishing the system steady state.



In order to measure a noise spectrum, the signals  $I_D$  and  $Q_D$  are sampled with a period  $t_S = 10$  ns, which allows to recover the spectrum from DC to 50 MHz<sup>111</sup>. To avoid aliasing, a low-pass filter with cut-off at 50 MHz is used before sampling. Each set of 1024 data points form a bin  $X[n] = X_D(n t_S)$  (where  $X = I, Q$ ) that undergoes a discrete Fourier transform, yielding  $X(\omega)$ , with a frequency resolution  $\Delta\omega/2\pi = 50/512$  MHz, sufficient for the features we are interested in. The Fourier transform is performed using FFTW<sup>112</sup>. The noise spectrum  $S_X(\omega)$  is then obtained by averaging  $|X(\omega)|^2$  over a large number of successive experimental sequences (typically  $10^6$ ).

We first verified that the noise spectrum obtained with the acquisition board and our implementation of the FFT was equivalent to the one acquired on a spectrum analyzer. For that we measured the same signal, consisting of a demodulated carrier frequency used as marker on top of the cryogenic amplifier noise, with the acquisition card and with the spectrum analyzer. As shown in Fig. 3.18a, we found an equal marker power with both setups. The difference in noise power observed in Fig. 3.18 comes from a difference in bandwidth; the noise equivalent powers measured in both setups are in fact equal to less than 0.5 dB.

A first test of this measuring procedure is shown in Fig. 3.18b. A noise spectrum is first acquired with the drive and measuring sources  $V_d$  and  $V_m$  both OFF, yielding the noise spectrum of the amplifier. Then, both sources are turned ON and a single peak appears at the Rabi frequency known from ensemble-averaged measurements performed with the same  $V_d$ . This Rabi peak is the signature of a steady-state Rabi oscillation –the initial transient of which is observed in the ensemble-averaged measurements performed above.

#### 3.4.2.2 *Corrections applied to the raw spectrum*

We present here the data treatment applied to the raw spectra to convert them into dimensionless spin units.

##### *Amplifier noise subtraction*

Since the noise from the amplifier is very large compared to this Rabi peak, it is important to accurately subtract it. For this purpose, we use a “lock-in” technique adapted for noise measurements. Each noise spectrum acquisition consists, as shown in Fig. 3.18c, in alternate periods of duration 2.5 ms. During the first one the spectrum  $S_{X,ON}(\omega)$  is acquired with both sources  $V_d$  and  $V_m$  on, whereas during the second period the same spectrum is measured with both sources off yielding simply the amplifier noise  $S_{X,OFF}(\omega)$ . The duration of 2.5 ms is short enough that all the setup drifts (in gain, power, ...) should be identical over two consecutive sequences and therefore cancel out. However this duration is long enough compared to all relevant timescales in our experiment so that the TLS is always measured in its steady-state despite the modulation. Moreover, we took care to throw away the data measured in a time window of 5  $\mu$ s windows around each transition between two periods. The spectra are acquired over a typical 20 minutes total duration.

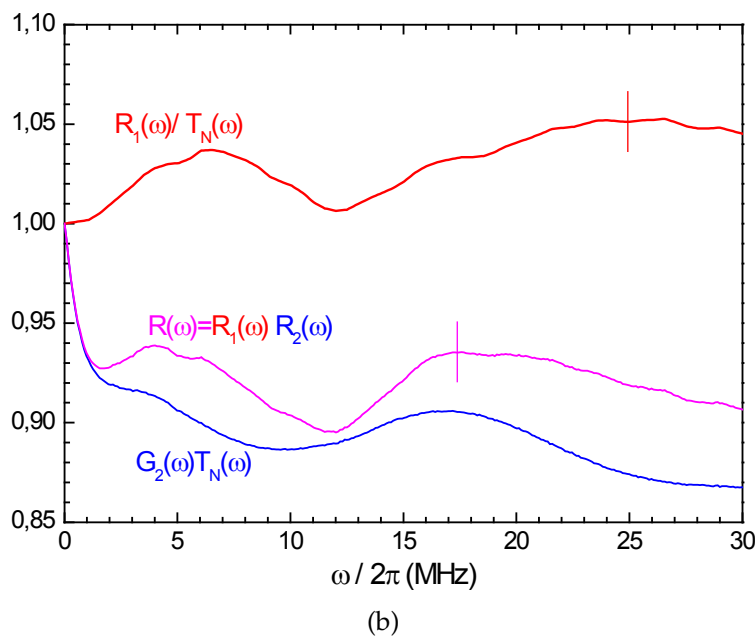
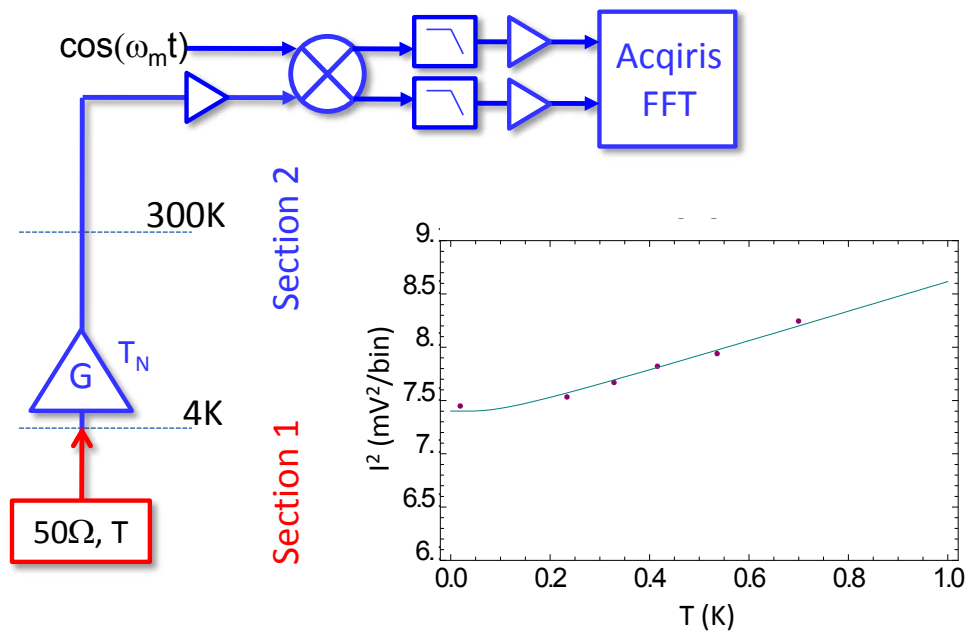


Figure 3.19: (a) The output line of the experimental setup is divided in two sections for analyzing its frequency response. Inset: example of the fit of the temperature dependence of the output spectra for  $\omega/2\pi = 17.57$  MHz. (b) Frequency response  $R(\omega)$  of the measuring line, including the amplification and demodulation chain. The error bar represent a constant maximum relative error.

The spectrum obtained after this first correction is

$$S(\omega) = (S_{I,ON}(\omega) - S_{I,OFF}(\omega)) + \\ + (S_{Q,ON}(\omega) - S_{Q,OFF}(\omega)).$$

### Setup frequency response

Our spectra extend over a bandwidth of  $\pm 30$  MHz around a carrier frequency of 5.8 GHz. All the lines, microwave components, amplifiers, and demodulators used in this experiment have a nominal bandwidth much broader than that and should thus in principle have a flat frequency response. It is nevertheless desirable to correct as well as possible for the possible measurement setup slight residual frequency dependence  $R(\omega)$  in order to obtain the best precision on the final spectra. This is particularly important for the test of the Leggett-Garg inequality that is discussed below.

Measuring this frequency dependence is rather difficult since we are only interested in the output line of our setup that links the sample to the acquisition card whose frequency response we want to measure at a few percent level. Our idea consists in using “in-situ” white noise sources to illuminate the output line; the frequency dependence of the resulting spectrum will therefore reflect the one of the output line. We have used two such noise sources : one is the cryogenic amplifier, another is the thermal noise coming out of the sample that can be heated up at a non-zero temperature.

For this purpose the measuring line is regarded as two sections in series (Fig. 3.19a): section 1 between the resonator and the cryogenic amplifier with frequency response  $R_1(\omega)$ , and section 2 above the cryogenic amplifier input with frequency response  $R_2(\omega)$  (including the amplifier gain  $G(\omega)$ ). The full line has a response  $R(\omega) = R_1(\omega)R_2(\omega)$  that is to be determined. All the responses are normalized to 1 at zero frequency. When the bottom of section 1 is at 20 mK, the noise spectrum of the cryogenic amplifier dominates the noise seen from the measurement line output  $S_{OFF}(\omega) = cR_2(\omega)k_B T_N(\omega)$  where  $c$  is a dimensionless constant, making impossible to calibrate  $R_1(\omega)$ .

For determining  $R_1(\omega)$  a complementary set of measurements was performed: the noise spectrum  $S_{OFF}(\omega, T)$  was acquired for several temperatures  $T$  of the bottom part of section 1 between 20 mK and 1 K. This new measurement yields

$$S_{OFF}(\omega, T) = cR_2(\omega) \left[ k_B T_N(\omega) + \frac{\hbar\omega}{2} R_1(\omega) \coth \left( \frac{\hbar\omega}{2k_B T} \right) \right] \\ = k_B a(\omega) + b(\omega) \frac{\hbar\omega}{2} \coth \left( \frac{\hbar\omega}{2k_B T} \right)$$

The fits of  $S_{OFF}(\omega, T)$  for each frequency  $\omega$  (an example of fit is shown in Fig. 3.19a) yields  $R_1(\omega)/T_N(\omega) = b(\omega)/a(\omega)$ . Multiplying this quantity by  $S_{OFF}(\omega)$  yields precisely  $R(\omega)$  as shown in Fig. 3.19b (even the frequency dependence of the amplifier noise temperature cancels out). As expected, the total frequency dependence of the setup is less than 10% over our detection window. We now analyze the uncertainties

associated with this analysis: although the error in measuring  $R_2(\omega)T_N(\omega)$  is less than 0.3%, the error on  $R_1(\omega)/T_N(\omega)$  is larger: it is due to the imperfection of the fits and to variations of the helium level in the cryostat. This absolute error increases from 0 at  $\omega = 0$  to 1.4% at  $\omega = 2\pi \times 30$  MHz. As an upper bound, we take a constant relative error of  $\pm 1.5\%$  over the whole 30 MHz range as shown in Fig. 3.19b.

After this second correction, we obtain a spectrum

$$S_V(\omega) = \frac{S(\omega)}{R(\omega)}.$$

### Calibration of the detector sensitivity

According to the predictions for the correlation function 3.10, the conversion factor  $\Delta V(\bar{n})/2$  between the demodulated output signals in Volts and spin units is given by  $[\Delta V(\bar{n})]^2 = [\Delta I(\bar{n})]^2 + [\Delta Q(\bar{n})]^2$ , with  $\Delta X(\bar{n})$  the change in quadrature  $X$  when the TLS state changes from  $|g\rangle$  to  $|e\rangle$ . This definition has the great advantage of being insensitive to any drift or jitter of the relative microwave phase between the measurement source  $V_m$  and the local oscillator used for the demodulation. Since  $(\Delta V(\bar{n})/2)^2$  is the normalization factor used to rescale the spectra, it is particularly important to determine it with the best possible precision.

Although it could be calculated from several independently measured parameters, we found more accurate to calibrate it by direct measurement: we thus ensemble average  $V^2(t) = [I_{ON}(t) - I_{OFF}(t)]^2 + [Q_{ON}(t) - Q_{OFF}(t)]^2$  under saturation of the  $g \rightarrow e$  transition (see Fig. 3.20).

In this experiment,  $V_m$  is always ON and only  $V_d$  is switched ON and OFF, and  $\omega_R/2\pi = 20$  MHz so that  $p(e)_{st} = 0.499 \pm 0.001$ ;  $V^2(t)$  varies from  $\epsilon = 4E[\xi_0^2]$  (with  $E[\xi_0^2]$  the variance of the noise on each  $X$  up to  $v^2 + \epsilon$  with  $v = [p(e)_{st} - p(e)_0] \Delta V$  when saturation is reached. From Fig. 3.20, we obtain  $(\Delta V)^2 = 10.29 \pm 0.64$  mV<sup>2</sup> for

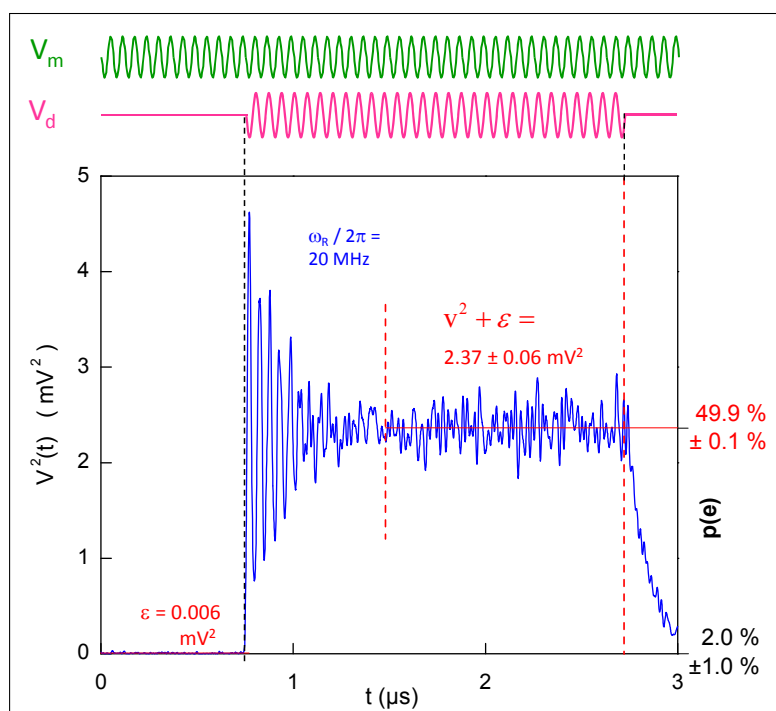


Figure 3.20: Calibration of the conversion factor  $\Delta V/2$  between output demodulated voltage and spin units. A measurement pulse  $V_m$  is applied with an amplitude corresponding to  $\bar{n} = 0.78$ . After about one  $\mu\text{s}$ , a saturating pulse is applied at  $\omega_{ge}$  during about 2  $\mu\text{s}$ . The  $V^2(t)$  signal is measured and averaged over a few  $10^5$  identical sequences. Starting from a thermal mixture of 98%  $g$  and 2%  $e$ , the TLS undergoes Rabi oscillations at about 20 MHz before it reaches its steady state with 50%  $g$  and  $e$  population. The steady-state output yield  $\Delta V$ .

$\bar{n} = 0.78$ .

Instead of performing a measurement as accurate for each value of  $\bar{n}$ , we have used  $\Delta V(\bar{n}) = \Delta V(0.78) \sqrt{\bar{n}/0.78}$  at low  $\bar{n}$  according to 3.2. For  $\bar{n} > 3$ , we also take into account corrections to the dispersive approximation, which is valid only for  $\bar{n} \ll n_{crit} = 31$ <sup>10</sup> in our case. Using a model similar to that of Gambetta *et al.*<sup>23</sup>, we keep the form of the dispersive Hamiltonian unchanged but use a modified dispersive constant  $\chi(\bar{n}) = \chi(0) (1 - \lambda\bar{n})$  yielding a modified conversion factor  $\Delta V(\bar{n}) (1 - \lambda\bar{n})$ . We determine  $\lambda = 7 \cdot 10^{-3}$  both experimentally and theoretically. Note that this correction gives noticeable effect only for  $\bar{n} = 15$ , and only a negligible correction for the data discussed now.

This third correction yields a spectrum rescaled to dimensionless spin units

$$\tilde{S}_z(\omega) = \frac{S_V(\omega)}{(\Delta V(\bar{n})/2)^2}.$$

We finally note that our measurements of the detector power spectrum are equivalent, via Fourier transform, to measurements of the two-time correlation function of the detector output as already explained. Other methods have been employed more recently to obtain this correlation function<sup>113</sup>. Bozyigit *et al.*<sup>114</sup> have measured the two-time amplitude correlation function of a single-photon emitted by a qubit, using two separate cryogenic amplifiers and an on-chip splitting of the field. Using numerical data analysis based on FPGAs, the same authors have also managed to observe intensity correlations manifested by anti-bunching in the case of a single-photon source.

### 3.4.3 COMPARISON WITH THEORETICAL PREDICTIONS

The four panels of Fig. 3.21 show the system output spectra  $\tilde{S}_z(\omega)$  for different measurement strengths  $V_m$ . Inside each panel four spectra corresponding to values of  $V_d$  yielding  $\omega_R/2\pi = 2.5, 5, 10, 20$  MHz are shown.

Before comparing them to the theoretical predictions Eq. 3.11, we note that the demonstration explicitly assumed a detector with infinite bandwidth. Despite the resonator was designed with a low  $Q$ , the finite bandwidth has sizeable effects on the spectra measured for Rabi frequencies of 10 and 20 MHz, as discussed in 3.3.3. To our knowledge there are no derivations of analytical expressions taking into account these effects, but they can be included in a phenomenological approach. This phenomenological approach involves two modifications:

- the measured signal  $\tilde{S}_z$  is filtered by the resonator Lorentzian response  $C(\omega)$  with frequency cutoff  $\kappa$  (dash-dot line in the first panel of Fig. 3.21). To include this cutoff in the theoretical prediction we replace Eq. 3.11 by

$$\tilde{S}_z(\omega) = S_z(\omega)C(\omega) = \frac{S_z(\omega)}{1 + \left(\frac{2\omega}{\kappa}\right)^2}.$$

- the transverse relaxation rate  $\Gamma_{\parallel}$  which should be taken into account is not the static decoherence rate  $\Gamma_2$ , but the driven decoherence rate

$$\Gamma_{\parallel} = \tilde{\Gamma}_2 = \frac{8\kappa\chi^2\bar{n}}{\kappa^2 + (2\omega_R)^2} + \Gamma_{\omega_R}^0$$

introduced in 2.2.3.5.

The validity of this phenomenological approach was checked by numerical simulations as explained in 3.4.4.

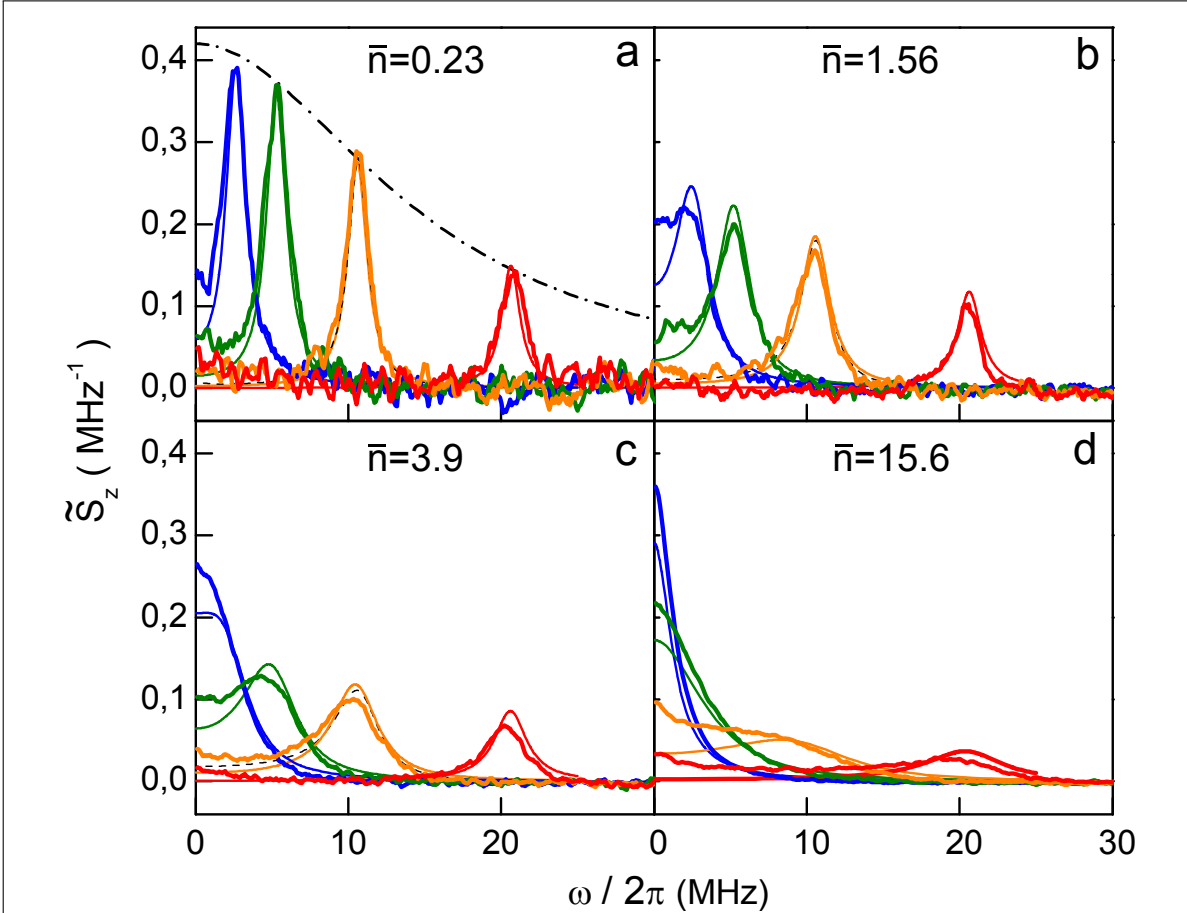


Figure 3.21: Continuous monitoring of the TLS driven at different Rabi frequencies ( $\omega_R/2\pi = 2.5, 5, 10$  and  $20$  MHz (from blue to red) and for different measurement strengths ( $\bar{n} = 0.23, 1.56, 3.9,$  and  $15.6$ ). Each power spectrum is acquired in 40 to 80 minutes. The spectra  $\tilde{S}_z(\omega)$  are normalized by correcting them from the frequency response of the measuring line and by converting the output voltage into units of  $\sigma_z$ . Thick and thin color lines are respectively the experimental spectra and those calculated from a theoretical analytical formula using only independently measured parameters (including  $\chi/2\pi = 1.8$  MHz). Dashed black lines on top of the orange curves in (a,b,c) are Rabi peaks obtained by numerical simulation with the same parameters. The dotted-dashed black curve in a is the Lorentzian frequency response of the resonator.

The calculated spectra are shown with thinner color lines in Fig. 3.21. The agreement between theory and experiment is good for low measurement strengths ( $\bar{n} \leq 5$ ), but becomes only qualitative at larger  $\bar{n}$ , probably due to the breakdown of the dispersive approximation.

### 3.4.4 NUMERICAL SIMULATIONS

In order to probe the phenomenological treatment of the resonator cut-off in the theoretical predictions explained above, we performed a numerical simulation of the full cQED setup for the situation of a TLS performing Rabi oscillations. To solve the evolution of the density matrix  $\hat{\rho}(t)$  we used a quantum optics simulation toolbox for MatLab<sup>115</sup> which allows to solve numerically the master equation (Eq. 2.33):

$$\partial_t \hat{\rho} = \mathcal{L} \hat{\rho} = -i [\hat{\rho}, \hat{H}] / \hbar + \kappa \mathcal{D}[\hat{a}] \hat{\rho} + \Gamma_1 \mathcal{D}[\hat{\sigma}_-] \hat{\rho} + 1/2 \Gamma_\phi \mathcal{D}[\hat{\sigma}_z] \hat{\rho}$$

with

$$\begin{aligned} \hat{H} = & 1/2 \hbar (\omega_{ge} - \omega_d) \hat{\sigma}_z + \hbar (\omega_r - \omega_m) (\hat{a}^\dagger \hat{a} + 1/2) + \\ & + \hbar \chi (\hat{a}^\dagger \hat{a} + 1/2) \hat{\sigma}_z + \\ & + E_m (\hat{a}^\dagger + \hat{a}) + E_d (\hat{\sigma}_+ + \hat{\sigma}_-) \end{aligned}$$

the dispersive driven Hamiltonian.

The solution to the master equation is computed in the basis made up of the direct product of the two TLS states and of the first  $N$  Fock states of the resonator. We checked empirically by repeating the simulations with different  $N$  that from  $N \geq 10\bar{n}$  the solutions converge with good accuracy. We refined also the model by considering the third level of the transmon.

#### *Simulating the initial transient of Rabi oscillations*

A first simulation was performed to confirm the validity of the dephasing rate dependence in frequency Eq. 3.7. We simulated with the master equation the ensemble averaged Rabi oscillations dephased by  $\bar{n}$  photons in the resonator, for various Rabi frequencies  $\omega_R$ , with  $\chi/2\pi = 1.8$  MHz.

To simulate the transient Rabi oscillations the two sources  $E_d$  and  $E_m$  are turned on at the beginning of the simulation and the density matrix  $\rho(t)$  is used to find  $\langle \hat{\sigma}_z(t) \rangle$ . The dephasing, which is fitted from the simulated oscillations (dark blue squares in Fig. 3.15b) is clearly cut-off by the resonator response as observed in the experiment, which confirms the prediction of Eq. 3.7.

#### *Simulating the spectrum of a continuous measurement*

To check if the theoretical expression Eq. 3.11 is indeed modified by a phenomenological cut-off  $\tilde{S}_z(\omega) = S_z(\omega)C(\omega)$ , we simulate numerically the continuous measurement of the Rabi oscillations. To obtain  $\tilde{S}_z(\omega)$ , we calculate the noise spectrum at the resonator output

$$\begin{aligned} S_{out}(\omega) &= \mathcal{F} \left( \langle \langle : \hat{I}_{out}(t+\tau) \hat{I}_{out}(t) : \rangle \rangle + \langle \langle : \hat{Q}_{out}(t+\tau) \hat{Q}_{out}(t) : \rangle \rangle \right) = \\ &= \kappa \mathcal{F} \left( \text{Re} \left( \langle \langle \hat{a}^\dagger(t+\tau) \hat{a}(t) \rangle \rangle - \langle \langle \hat{a}^\dagger(t+\tau) \rangle \rangle \langle \langle \hat{a}(t) \rangle \rangle \right) \right) \end{aligned}$$



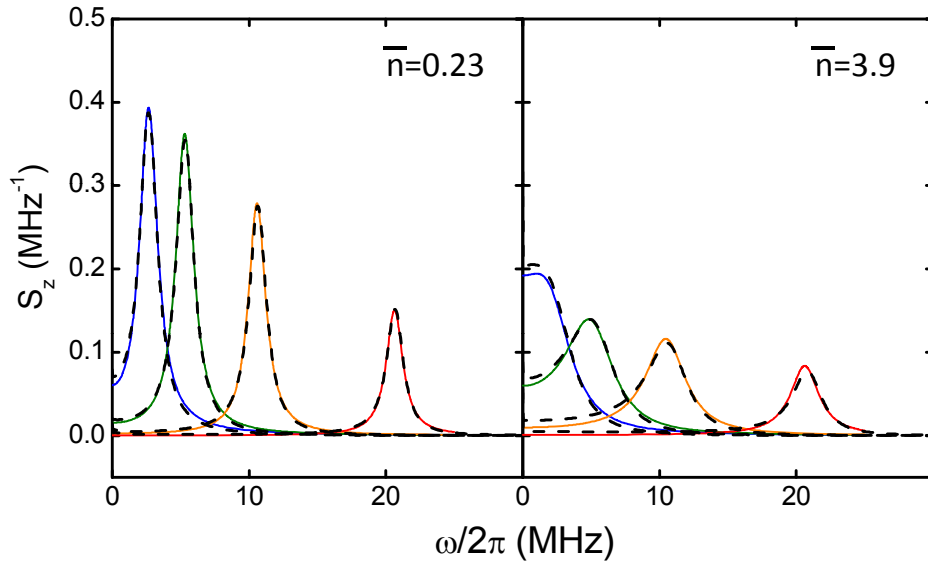


Figure 3.22: Comparison between the analytical spectra  $\tilde{S}_z$  (solid lines) and numerical simulations using the master equation as explained in the text (dashed black lines), for  $\bar{n} = 0.23$  and 3.9, and  $\omega_R/2\pi = 2.5, 5, 10, 20$  MHz. The agreement is excellent.

Although the density matrix  $\hat{\rho}$  does not directly allow to find the correlation functions, these can be computed from the quantum regression theorem<sup>62,65</sup>

$$\langle \hat{A}(t + \tau) \hat{B}(t) \rangle = \text{Tr} [\hat{A} \exp(\mathcal{L}\tau) \hat{B} \hat{\rho}(t)].$$

Therefore, from a computational point of view, the correlation function  $\langle \hat{a}^\dagger(t + \tau) \hat{a}(t) \rangle$  is found by calculating the average of  $\hat{a}^\dagger(\tau)$  using as initial condition a matrix  $\hat{a} \hat{\rho}(t)$ .

The results are shown in Fig. 3.22. The conversion into spin units was done as in the experiment, by calculating the output signal at saturation  $\delta V$  of a continuously monitored Rabi oscillation. The agreement with the analytical formula is excellent for all calculated curves.

Unfortunately it was not possible to simulate the strong measurement limit, since the toolbox used for our simulations does not implement any memory optimization code, and the 2GB of RAM present in the simulating computer were saturated when trying to simulate in Hilbert spaces containing more than  $10\bar{n} = 60$  Fock states  $\times 3$  transmon levels.

#### *Going beyond the dispersive approximation*

It would be of great interest to simulate the noise spectra with the full Hamiltonian of the system –without the dispersive approximation– to clear up if the discrepancies which appear between the predictions and the experiment for  $\bar{n} \geq 5$  are due to the breakdown of the dispersive approximation when  $\bar{n}$  is a substantial fraction of  $n_{crit} = 31$ . However, as explained above, the design of the toolbox imposes some memory limitations, and, in addition, artefacts due to the high amplitude of qubit driving terms prevented us to get accurate simulations for these situations.



When we acquire a series of spectra keeping a constant drive  $V_d$  and progressively increasing the measurement strength  $V_m$ , we obtain the curves shown in Fig. 3.23. For weak measurements we observe a Lorentzian peak at the Rabi frequency  $\omega_R$  known from ensemble-averaged Rabi oscillations. The width of this peak corresponds to the total dephasing, some part of which comes from the measurement itself. When increasing the measurement strength this peak decreases and is progressively broadened by the increased measurement-induced dephasing. At the same time a Lorentzian at zero frequency starts to grow. Such a spectrum is the signature of telegraphic noise.

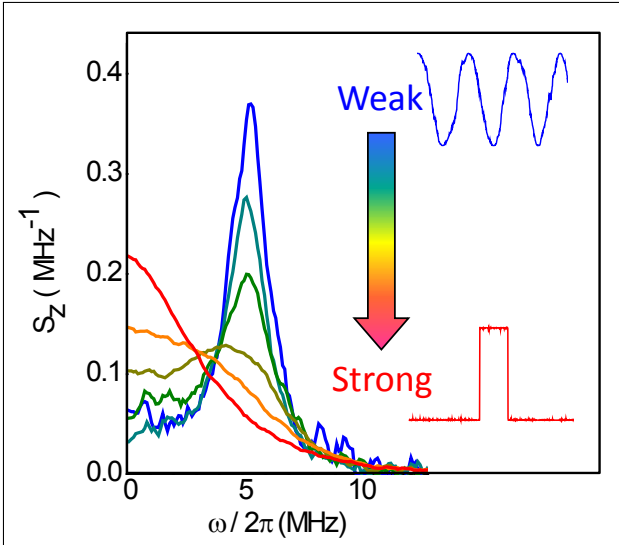


Figure 3.23: Crossover from weak to strong measurement

To gain further insight on the physical meaning of these spectra, it is convenient to analyze the behaviour of the system in the quantum trajectories framework. In this framework, as explained in 2.3.3.3, the detector signal can be written explicitly:

$$\tilde{X}_D(t) = \sqrt{\kappa\eta} \langle 2\hat{X} \cos \Theta \pm 2\hat{Y} \sin \Theta \rangle_t + \tilde{\xi}_X(t),$$

where  $X = I, Q$  and  $\tilde{\xi}_X(t)$  is a realization of a random process with white noise spectrum  $\langle \tilde{\xi}_X(t + \tau) \tilde{\xi}_X(t) \rangle = \delta(\tau)$  which describes the randomness of the measurement.

The stochastic master equation (SME) which describes the evolution of the TLS alone (Eq. 3.1) is analog to the one of a quantum dot coupled to a quantum point contact calculated by Korotkov and Averin<sup>24</sup>. The evolution of

the diagonal elements of the density matrix conditioned to the measurement record  $\{X_D(t')\}_{t' < t}$  is:

$$\begin{aligned} \dot{\rho}_{gg}(t) = -\dot{\rho}_{ee}(t) = & \underbrace{-\omega_R \text{Im} [\rho_{ge}(t)]}_{\text{Rabi}} + \underbrace{\Gamma_1 \rho_{ee}(t)}_{\text{relaxation}} + \\ & \underbrace{+ \sqrt{\kappa\eta} D^2 \cos(\Theta - \arg(\alpha_e - \alpha_g)) 2\rho_{gg}(t)\rho_{ee}(t)\tilde{\xi}_X(t)}_{\text{measurement}} \end{aligned} \quad (3.12)$$

The first two terms of this equation, which are the only ones present in the absence of measurement, correspond to the TLS drive inducing the Rabi oscillations and the TLS relaxation. The third term corresponds to the change of the expectation of the  $|g\rangle$  and  $|e\rangle$  states due to the acquisition of information, that is, the projection of the TLS state along the  $z$  axis of the Bloch sphere. This projection is proportional to the state distinguishability  $D^2$  and is stochastic due to the noise  $\tilde{\xi}_X(t)$  which is present in the measured signal.

The coherences evolve in a slightly more complicated way:

$$\begin{aligned}
\dot{\rho}_{ge}(t) = & - \underbrace{i\omega_a \rho_{ge}(t)}_{\text{free precession}} + \underbrace{i/2\omega_R [\rho_{gg}(t) - \rho_{ee}(t)]}_{\text{Rabi}} - \underbrace{(\Gamma_2 + \Gamma_\phi^{ph}) \rho_{ge}(t)}_{\text{decoherence}} - \\
& - \underbrace{\sqrt{\kappa\eta} D^2 \cos(\Theta - \arg(\alpha_e - \alpha_g)) [\rho_{gg}(t) - \rho_{ee}(t)] \rho_{ge}(t) \tilde{\zeta}_X(t)}_{\text{measurement}} - \quad (3.13) \\
& - \underbrace{i\sqrt{\kappa\eta} D^2 \sin(\Theta - \arg(\alpha_e - \alpha_g)) \rho_{ge}(t) \tilde{\zeta}_X(t)}_{\text{related to } n(t)}
\end{aligned}$$

The first line corresponds to the evolution of the coherences independently of the measurement record: a rotation at the effective TLS transition frequency  $\omega_a$  in the laboratory frame, the coherent Rabi oscillations induced by the TLS drive, and the free decoherence with rate  $\Gamma_2$  plus a term due to the measurement-induced dephasing<sup>2</sup>. The second line is very similar to the second term in Eq. 3.12 and also corresponds to the projection of the TLS along the  $z$  axis due to the measurement. The third line corresponds to the projection along an orthogonal  $x$  axis, which brings no information about the state of the system but measures the TLS AC-Stark shift, that is, the number  $\bar{n}$  of photons stored in the resonator. We see that when all the information on the TLS state is along one quadrature (for instance  $\arg(\alpha_e - \alpha_g) = 0$ ), the other quadrature (for instance  $\arg(\alpha_e - \alpha_g) = \pi/2$ ) only brings information about those fluctuations.

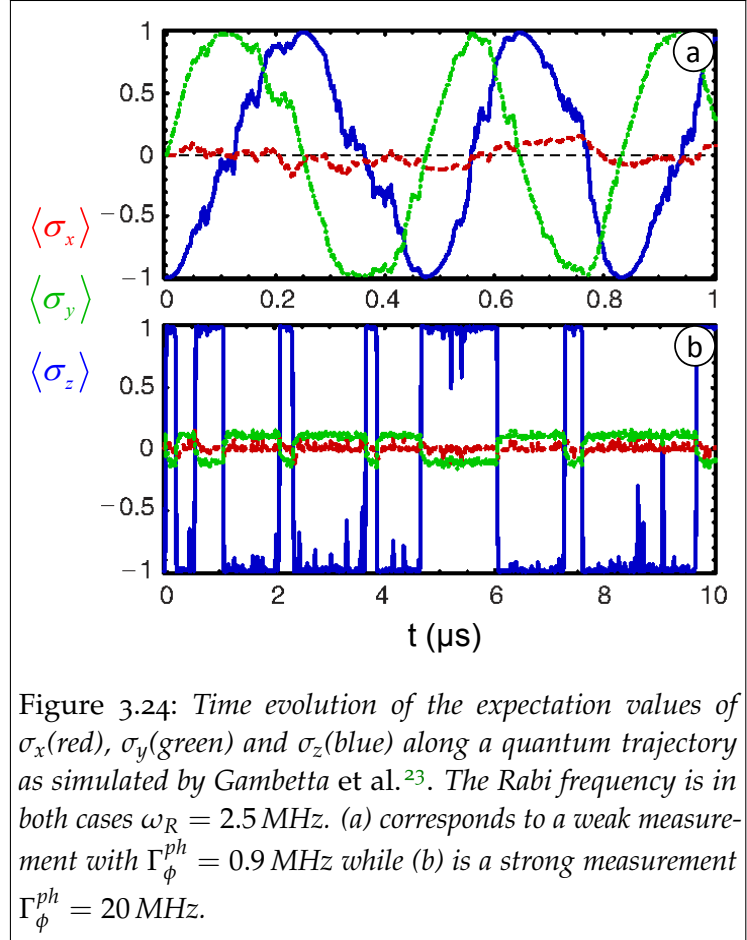


Figure 3.24: Time evolution of the expectation values of  $\sigma_x$  (red),  $\sigma_y$  (green) and  $\sigma_z$  (blue) along a quantum trajectory as simulated by Gambetta et al.<sup>23</sup>. The Rabi frequency is in both cases  $\omega_R = 2.5$  MHz. (a) corresponds to a weak measurement with  $\Gamma_\phi^{ph} = 0.9$  MHz while (b) is a strong measurement  $\Gamma_\phi^{ph} = 20$  MHz.

The quantum trajectories are obtained as solutions of the SME (Eq. 3.12 and 3.13) for a certain realization of noise. Their shape depend very much on the ratio between the measurement strength  $D^2 \propto \Gamma_\phi^{ph}$  and the Rabi frequency  $\omega_R$ . Indeed, as expected from the terms in the SME above, the system is subject to two competing phenomena: the drive tends to create superpositions of the two eigenstates, while the measurement tends to project the state to one of them. This crossover has been extensively studied

<sup>2</sup>Note that formally this term should be written  $\mathcal{F}^{-1} [\Gamma_2 + \Gamma_\phi^{ph}(\omega)] \star \rho_{ge}(t)$ . When writing it as a product,  $\Gamma_\phi^{ph}(\omega)$  is the decoherence rate for the most relevant frequency:  $\omega_R$  for good Rabi oscillations.

with numerical simulations of the trajectories by Gambetta *et al.*<sup>23</sup> In Fig. 3.24 two trajectories corresponding to the limiting cases are shown.

When the measurement is weak enough (Fig. 3.24a) the dynamics of the system is mainly controlled by the oscillatory terms of the SME. Then the dominant behaviour are the coherent oscillations of the system state, which are only slightly perturbed by the measurement acting as a diffusive term.

Conversely, in the strong measurement regime (Fig. 3.24b) the measurement terms in the SME are dominant. As a result the information is quickly extracted from the system resulting in a rapid projection to the eigenstate of the measured outcome, as expected from the measurement postulate. Then, since the state cannot escape from the attractors in the poles of the Bloch sphere, its only way to evolve is by a sudden quantum jump and the evolution consists in a series of stochastic quantum jumps between the eigenstates.

It was not possible in our experiment to observe these quantum jumps, because of the poor signal-to-noise ratio of the state-of-the-art microwave amplifiers. However, the power spectrum at the detector output (Fig. 3.23) shows an indirect signature of quantum jumps in the spectral domain: a Lorentzian centered at zero frequency.

### 3.5 NON-CLASSICALITY OF THE CIRCUIT: VIOLATION OF A BELL'S INEQUALITY IN TIME

The continuous measurements we implemented above provide a way to answer to a very fundamental question: are the outcomes of the measurements performed on our system *truly random* as quantum mechanics predict, or conversely, could they be explained by a classical model?

A good way to rule out any classical model is to demonstrate the existence of a genuine quantum property without classical analogue: entanglement, for instance. The presence of entanglement can be witnessed with the Bell CHSH<sup>34</sup> inequalities. To test them (Fig. 3.25) the TLSs of an entangled pair are brought apart to reach a space-like separated configuration, and the correlations between the measurements performed on each side is compared to the maximal value possible for classical correlations.

However there is a different situation in which the quantum nature of the system can be tested with *a single TLS*. In this case the criterion to distinguish between the classical behaviour and the quantum one is the Leggett-Garg inequality<sup>29</sup>. This inequality appeared in the context of the debate about the existence of macroscopic superpositions of states. It involves the correlations between several measurements performed at *different times* on a *single TLS* (Fig. 3.26), in contrast to Bell's inequality, which involves correlations between measurements performed in *space-separated* regions. Therefore it is also named in the literature a *Bell's inequality in time*. In this section we report one of the first violations of this inequality with our circuit QED system demonstrating its quantum nature.

### 3.5.1 THE CHSH BELL'S INEQUALITY

The usual CHSH Bell's inequality consists in a quantitative criterion to test if a given system complies with the local-realism hypotheses, that is

1. Locality: two events happening in space-like separated regions cannot have influence on each other.
2. Realism: the measurement of a certain observable gives access to a preexisting value whose existence does not depend on the fact of measuring or not.

The simplest situation (Fig. 3.25) in which the quantum predictions contradict the inequality derived from these hypotheses is the case of a pair of TLS in a maximally entangled state such as

$$|\psi^-\rangle = (|\uparrow\downarrow\rangle - |\downarrow\uparrow\rangle)/\sqrt{2}.$$

Each member of the pair is then distributed to two observers A and B, who perform projective measurements of the TLS spin  $\sigma_i^{A,B} = \pm 1$  along one of two directions  $a_i$  ( $i = 1, 2$ ) for A and  $b_i$  for B, with these directions forming angles  $(a_1, b_1) = (b_1, a_2) = (a_2, b_2) \equiv \theta$ , as shown in Fig. 3.25. The two observers then combine all their measurements to compute the Bell sum

$$\Sigma(\theta) = -K_{11} + K_{12} - K_{22} - K_{21}$$

of the correlators  $K_{ij}(\theta) = \langle \sigma_i^A \sigma_j^B \rangle$ . The Bell's theorem, based on a simple statistical argument, states that according to all local realistic theories

$$-2 \leq \Sigma(\theta) \leq 2. \quad (3.14)$$

However, standard quantum mechanics predicts that this inequality is violated, with a maximum violation  $\Sigma(\theta = \pi/4) = 2\sqrt{2}$ . Many experimental tests, those performed by A. Aspect and his team<sup>116</sup> in particular, have verified this violation.

This inequality has also been tested with superconducting circuits<sup>117</sup> and specifically in the circuit QED setup<sup>118</sup>. Note that in these experiments, in contrast with Aspect's one, it was not possible to reach space-like separation between the TLS. In this case, the violation of the CHSH inequality should rather be considered as a benchmark of the possibility of producing entanglement in the system, and not as a fundamental proof that the system fails to comply with the local-realism hypotheses stated above.

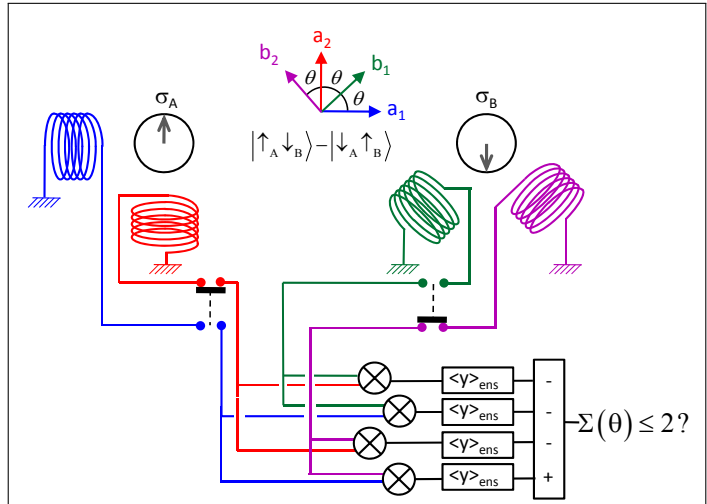


Figure 3.25: Experimental test of the CHSH Bell's inequality: two maximally entangled spins  $\sigma_A$  and  $\sigma_B$  are sent to two spatially separated observers A and B. Each of the observers measures with pick-up coils his spin along one of two possible directions ( $a_1$  and  $a_2$  for A, and  $b_1$  and  $b_2$  for B); the four directions make angles  $\theta$  as depicted. By repeating this experiment on a statistical ensemble, a linear combination  $\Sigma$  of the four possible correlators between measurements on a spin pair is computed. Local realism requires  $-2 \leq \Sigma \leq 2$ , while quantum mechanics predicts  $\Sigma = 2\sqrt{2}$  for  $\theta = 45^\circ$ .

### 3.5.2 THE LEGGETT-GARG INEQUALITY

In the context of the debate on the existence of quantum superpositions of macroscopically distinct states, Leggett and Garg<sup>29</sup> proposed in 1985 an inequality which tests the hypotheses of *macrorealism*, slightly different from those of local realism. These two hypotheses, which seem quite natural for macroscopic classical bodies, are:

1. *Macrorealism per se*: A macroscopic object, which has available to it two or more macroscopically distinct states, is at any given time in a definite one of those states.
2. *Noninvasive measurability*: It is possible in principle to determine which of these states the system is in without any effect on the state itself, or on the subsequent system dynamics.

Now if we consider a two-valued observable evolving in time  $\sigma(t) = \pm 1$  and three successive times  $t_1 < t_2 < t_3$ , the first property above allows to define the joint probability densities  $\rho(\sigma(t_1), \sigma(t_3))$  and  $\rho(\sigma(t_1), \sigma(t_2), \sigma(t_3))$ . To be consistent with one another, they should satisfy

$$\sum_{\sigma(t_2)=\pm 1} \rho(\sigma(t_1), \sigma(t_2), \sigma(t_3)) = \rho(\sigma(t_1), \sigma(t_3)).$$

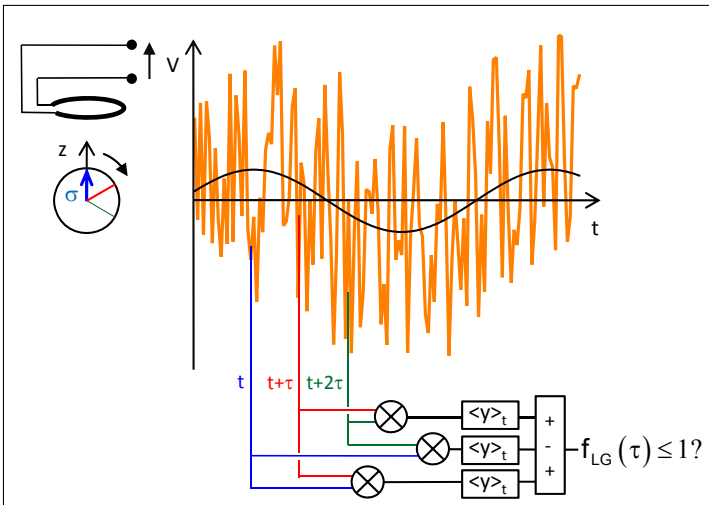


Figure 3.26: Experimental test of the Bell's inequality in time with weak measurement: a single spin  $\sigma$  undergoing coherent oscillations at frequency  $\omega_R$  is continuously measured with a pick-up coil coupled to it so weakly that the time for a complete projective measurement would be much longer than the period of oscillations  $T_R = 2\pi/\omega_R$ . From the noisy time trace recorded in the steady state, one computes a linear combination  $f_{LG}$  of the three time-averaged-correlators between the readout outcomes at three times separated by  $\tau$ . Macrorealism requires  $f_{LG} \leq 1$  for any  $\tau$ , while quantum mechanics predicts  $f_{LG} = 1.5$  at  $\tau = T_R/6$ .

The ensemble-averaged time-correlation functions

$$K_{ij} = E[\sigma(t_i)\sigma(t_j)]$$

should satisfy the inequality

$$f_{LG} = K_{12} + K_{23} - K_{13} \geq 1 \quad (3.15)$$

The second hypothesis stated above means that the correlators  $K_{ij}$  can actually be measured.

Quantum mechanics does not comply with any of the two hypotheses stated above. In a large number of situations it is theoretically possible to find violations of the above inequality. The violation in CQED with Rydberg atoms, for instance, is theoretically analyzed by Huelga *et al.*<sup>31,119</sup>. Actually, Kofler and Brukner<sup>120</sup> have demonstrated that it can be violated by any time-independent non-trivial Hamiltonian. One of the simplest situations in

which such violation occurs is the precession of a spin  $1/2$  at the angular frequency  $\omega_R$ . In this situation the correlators above are

$$K_{ij} = E [\sigma(t_i)\sigma(t_j)] = p_{i=1} \left( p_{j=1}^{(i=1)} - p_{j=-1}^{(i=1)} \right) + p_{i=-1} \left( p_{j=-1}^{(i=-1)} - p_{j=1}^{(i=-1)} \right) = \\ = \cos (2\omega_R(t_j - t_i))$$

where  $p_{i=\pm 1} = 1/2$  stands for the probability of measuring  $\sigma(t_i) = \pm 1$  and  $p_{j=y}^{(i=x)}$  is the conditional probability of measuring  $\sigma(t_j) = y$  after measuring  $\sigma(t_i) = x$ . Then

$$f_{LG} = K_{12} + K_{23} - K_{13} = \cos (2\omega_R(t_2 - t_1)) + \cos (2\omega_R(t_3 - t_2)) - \cos (2\omega_R(t_3 - t_1))$$

which for  $t_2 - t_1 = t_3 - t_2 = \pi/(6\omega_R)$  yields  $f_{LG} = \sqrt{3} - 1/2 > 1$ .

Leggett and Garg proposal consisted in testing the above inequality in a RF-SQUID (Fig. 3.27), a superconducting loop interrupted by a Josephson junction. Such a circuit, when flux-biased around  $\Phi_0/2$ , has two metastable states, coupled by tunneling, and corresponding to zero or one flux quantum trapped in the loop. If the circuit is initially prepared in one of this states, it will display coherent oscillations that would allow to test the Leggett-Garg inequality, and to probe if the quantum behaviour is maintained when the difference between the fluxes on the two states becomes macroscopic.

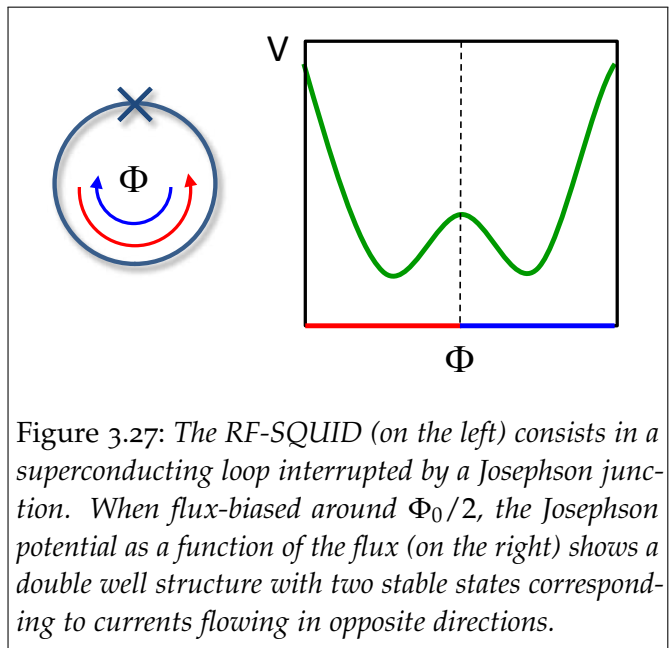


Figure 3.27: The RF-SQUID (on the left) consists in a superconducting loop interrupted by a Josephson junction. When flux-biased around  $\Phi_0/2$ , the Josephson potential as a function of the flux (on the right) shows a double well structure with two stable states corresponding to currents flowing in opposite directions.

### 3.5.3 A LEGGETT-GARG INEQUALITY ADAPTED FOR WEAK CONTINUOUS MEASUREMENT

It is difficult to test the Leggett-Garg inequality 3.15 because it requires instantaneous measurements to characterize the value of  $\sigma$  at a given time. Moreover, the hypothesis of non-invasibility stated above can be violated not only by the projection which is inherent to quantum measurements, but also by some trivial clumsiness in the measurement setup. The suddenness of the measurement makes difficult to prove the absence of that *clumsiness loophole*<sup>33</sup>.

In 2006 Korotkov and coworkers derived another version of the inequality<sup>32</sup>, which relies on the same hypotheses but involves a continuous and weak measurement instead of a fast projective one. They consider the situation of a system characterized by a physical variable  $\sigma(t)$  with any value such that  $|\sigma(t)| \leq 1$ . This upper bound leads to the inequality

$$\sigma(t_1)\sigma(t_2) + \sigma(t_1)\sigma(t_3) - \sigma(t_2)\sigma(t_3) \leq 1 \tag{3.16}$$



for  $t_1 < t_2 < t_3$ . When making a continuous and weak broadband measurement of  $\sigma(t)$  we collect a noisy signal

$$V(t) = \frac{\Delta V}{2}\sigma(t) + \zeta(t)$$

where  $\Delta V/2$  is the sensitivity of the detector and  $\zeta(t)$  a white noise, exactly as in Eq. 2.34. If we average  $V(t)$  we can obtain information on  $\sigma(t)$ . In particular the time correlator of  $V(t)$  is

$$K_V(\tau) = E[V(t)V(t+\tau)] = \left(\frac{\Delta V}{2}\right)^2 E[\sigma(t)\sigma(t+\tau)] + \frac{\Delta V}{2}E[\zeta(t)\sigma(t+\tau)]$$

where the correlator  $E[\sigma(t)\zeta(t+\tau)] = 0$  trivially since the state of the system does not anticipate the future noise. Since the measurement is considered to be non-invasive, no correlation exists between the noise and the future measurements results:

$$E[\zeta(t)\sigma(t+\tau)] = 0.$$

Even in the case of a weak continuous measurement in which the detector noise linearly perturbs the energy of the monitored TLS the correlator above vanishes if the system undergoes symmetric oscillations. From this, using Eq. 3.16 and calling  $\tau_1 = t_2 - t_1$  and  $\tau_2 = t_3 - t_2$  we have the inequality

$$f_{LG}(\tau_1, \tau_2) = K_V(\tau_1) + K_V(\tau_2) - K_V(\tau_1 + \tau_2) \leq \left(\frac{\Delta V}{2}\right)^2. \quad (3.17)$$

It is worth noting that this inequality only involves the measurement of a single time-correlator  $K_V(\tau)$  which is obtained by time-averaging, while in the test of the original Leggett-Garg inequality, the correlators were ensemble-averaged over three ensembles, each one prepared and measured in a different way. The test of this inequality is then more straightforward in the weak measurement case.

Quantum mechanics predicts a violation of the above inequality for the situation of a TLS continuously and weakly monitored while performing Rabi oscillations at  $\omega_R$ . Indeed, as shown in 3.4.1, the detector output correlation function is then

$$K_V(\tau) = \left(\frac{\Delta V}{2}\right)^2 \langle \hat{\sigma}_z(t+\tau)\hat{\sigma}_z(t) \rangle = \left(\frac{\Delta V}{2}\right)^2 \exp(-\Gamma_R\tau) \cos(\omega_R\tau).$$

Choosing  $\tau_1 = \tau_2 = \tau \ll 1/\Gamma_R$  we have in the weak coupling regime  $\Gamma_R \ll \omega_R$

$$f_{LG}(\tau) = \left(\frac{\Delta V}{2}\right)^2 [1 + 2\cos(\omega_R\tau) - 2\cos^2(\omega_R\tau)]$$

which violates maximally the inequality 3.17 with

$$f_{LG}\left(\frac{\pi}{3\omega_R}\right) = \frac{3}{2}\left(\frac{\Delta V}{2}\right)^2.$$



### 3.5.4 EXPERIMENTAL TEST

#### 3.5.4.1 Data acquisition

In order to test inequality 3.17, we measure a Rabi peak at  $\omega_R/2\pi = 10.6$  MHz with  $\bar{n} = 0.78$  photons and a 30 MHz detection window averaged over 13 hours. To compare it to theoretical predictions and test the Leggett-Garg inequality, this spectrum is corrected as explained above by subtracting the amplifier noise, correcting for the setup frequency response  $R(\omega)$ , and dividing by the detector sensitivity  $(\Delta V/2)^2$ , yielding the spectrum  $\tilde{S}_z(\omega)$  shown in Fig. 3.28. We note that the spectrum was taken at exactly the same measurement power as the accurate measurement of  $\Delta V$  reported above and in the same conditions, so that the imprecision on the exact value of  $\bar{n}$  does not play any role. In order to verify that this calibration did not drift, we measured  $\Delta V$  immediately before and immediately after the acquisition of the spectrum. The first measurement yields  $(\Delta V)^2 = 10.29 \pm 0.64$  mV<sup>2</sup> and the second  $(\Delta V)^2 = 10.59 \pm 0.64$  mV<sup>2</sup>. We thus take  $(\Delta V/2)^2 = 2.61 \pm 0.16$  mV<sup>2</sup> for the conversion factor.

We defer the full discussion of the experimental uncertainties to 3.5.4.3, and will now use these data to test the Leggett-Garg inequality.

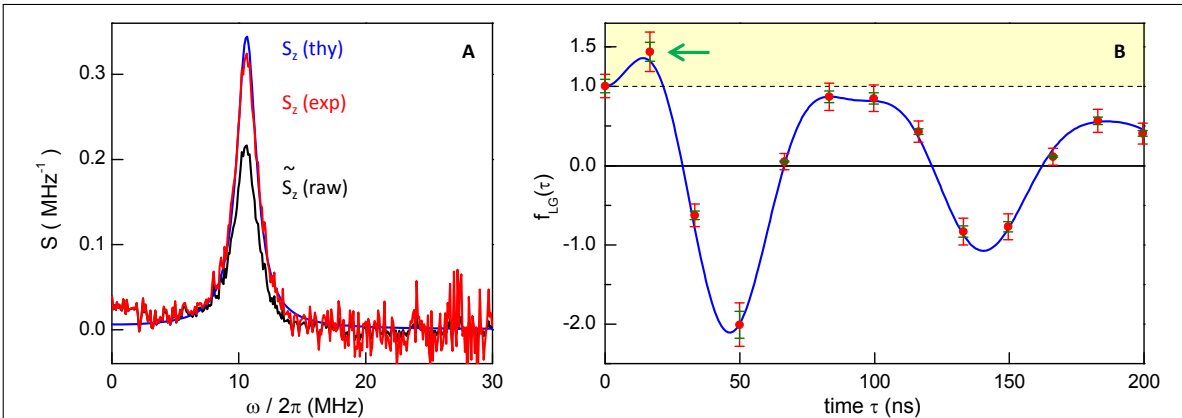


Figure 3.28: Experimental violation of the “Bell’s inequality in time”. (A) experimental (red) and theoretical (blue) spectral densities  $S_z$ , calculated or measured at  $\omega/2\pi = 10.6$  MHz and  $\bar{n} = 0.78$ . The experimental curve is obtained by correcting the raw  $\tilde{S}_z$  spectrum (black line), acquired in 13 hours with a 30 MHz bandwidth, from the frequency response of the resonator. The blue curve is calculated with independently measured  $\Gamma_1^{-1} = 200$  ns and  $\Gamma_2^{-1} = 150$  ns. (B) experimental (dots) and theoretical (blue line) Leggett-Garg quantity  $f_{LG}(\tau) = 2K(\tau) - K(2\tau)$ , with  $K(\tau)$  the signal auto-correlation function obtained by inverse Fourier transform of the  $S_z$  curves in the left panel. Green error bars correspond to the maximum systematic error associated with calibration and  $C(\omega)$ , whereas red ones also include a two standard deviation wide statistical error  $\pm 2\sigma(\tau)$  associated with the experimental noise on  $\tilde{S}_z$ . The Leggett-Garg inequality is violated (yellow region) at  $\tau = 17$  ns (see green arrow) by  $5\sigma$ .

### 3.5.4.2 Violation of the Leggett-Garg inequality

Under macrorealistic assumptions, the only effect of the bandwidth of the resonator would be to reduce the measured signal by its Lorentzian response function  $C(\omega) = 1/[1 + (2\omega/\kappa)^2]$ ; we thus correct the acquired spectrum by dividing the measured spectral density  $\tilde{S}_z(\omega)$  by  $C(\omega)$ , yielding  $S_z(\omega)$  the red curve in Fig. 3.28. The experimental and theoretical Rabi peaks show good overall agreement despite residual low-frequency noise discussed in Section 3.6. The corresponding time-correlators  $K(\tau)$  are found by Fourier transforming these spectrum. The Leggett-Garg quantity  $f_{LG}(\tau) = 2K(\tau) - K(2\tau)$  is then calculated and plotted on the right of Fig. 3.28.

We first note that  $K(0) = f_{LG}(0) = 1.01 \pm 0.15$ , a value close to 1 that directly results from the independent calibration of  $\Delta V$ . Since  $K(0)$  represents the variance of  $\sigma_z(t)$  and  $|\sigma_z(t)| \leq 1$ , this confirms that at any time  $\sigma_z(t) = \pm 1$  as expected for a quantum TLS. This is in strong contrast with the case of a classical macro-spin as the one shown in Fig. 3.26, which takes all the intermediate values during its transition from  $z = -1$  to  $z = +1$ , and would have given a variance  $K(0) = \overline{\cos^2(\omega_R t)} = 1/2$ . This variance  $K(0)$ , therefore, brings substantial information on the nature of the system, allowing to distinguish the case of a macro-spin to the one of a genuine quantum spin. Conversely, ensemble-averaged Rabi oscillations such as those of Fig. 3.14 are the same for both a quantum spin and a macro-spin and therefore provide no criterion to distinguish both. This demonstrates the specific interest of correlation-function measurements compared to time-domain ensemble averaged signals.

Most importantly, we observe that  $f_{LG}(\tau)$  goes above the classical limit of 1, reaching  $1.44(\pm 0.12) \pm 2 \times (\sigma = 0.065)$  at  $\tau = 17 \text{ ns} \sim \pi/3\omega_R$  and thus violating inequality 3.17 by 5 standard deviations. This maximum of  $f_{LG}$ , slightly below the ideal value of 1.5 in absence of decoherence, is a direct signature of the invasive character of the measurement process, which projects partially but continuously the TLS towards the state corresponding to the detector output. It is the interplay between this continuous projection and the coherent dynamics that yields the violation of the inequality. More quantitatively, the maximum of  $f_{LG}$  is in agreement with the quantum prediction of 1.36 when taking into account the independently measured relaxation and dephasing rates of the TLS. This violation of the Leggett-Garg inequality rules out a simple interpretation of  $K(\tau)$  as the correlation function of a classical macro-spin. It therefore brings further evidence that a collective degree of freedom characterizing a Josephson circuit behaves quantum-mechanically. It also demonstrates that the back-action of a weak measurement, far from being only a noise that spoils quantum coherence as could be deduced from ensemble averaged measurements, also reinforces the correlations between measurements made at different times.

It is interesting to discuss in what respect the assumptions made in analysing the experimental data influence the final result: apart from simple corrections relying on classical electromagnetism, we determine the main normalization factor  $\Delta V$  by saturating the TLS transition and assuming that the ensemble averaged spin, either classical or quantum, obeys Bloch equations. We checked this assumption in Fig. 3.14 which shows in particular that the excursion of the signal when driving the spin is symmetric around the saturation value, as it would be for classical macro-spins. The

observed violation is thus not an artifact of our analysis framework, and represents more than a mere self-consistency check of a quantum model.

### 3.5.4.3 Experimental uncertainties in the determination of $f_{LG}(\tau)$

As mentioned in the text, the experimental points  $f_{LG}(\tau) = 2K(\tau) - K(2\tau)$  of Fig. 3.28 are obtained from the inverse Fourier transform  $K(\tau)$  of  $S_z(\omega) = \tilde{S}_z(\omega)/C(\omega)$  with

$$\tilde{S}_z(\omega) = \frac{S_{ON}(\omega) - S_{OFF}(\omega)}{R(\omega)(\Delta V/2)^2}$$

with  $R(0) = C(0) = 1$  and  $\delta V/2$  being measured at zero frequency.

The **systematic error** bars on  $f_{LG}(\tau)$  (in green in Fig. 3.28) result from the sum of the three maximum relative uncertainties:

- The uncertainty on the setup frequency response (see 3.4.2.1):  $\Delta R/R = \pm 1.5\%$
- The uncertainty on the detector sensitivity (see 3.4.2.2):  $\Delta(\Delta V/2)^2/(\Delta V/2)^2 = \pm 6.1\%$
- The uncertainty on the resonator bandwidth (see 3.2.3):  $\Delta C/C = 2(\Delta\kappa/\kappa)/[1 + (\kappa/2\omega)^2]$  with  $\Delta\kappa/\kappa = \pm 2.6\%$ .

Note that the frequency dependent error  $\Delta C/C$  is propagated exactly through the calculation of  $f_{LG}(\tau)$  and contributes to  $\Delta f_{LG}/f_{LG}$  by  $\pm 0.8\%$  where inequation 3.17 is violated. The total systematic error at that point is thus  $\pm 8.4\%$ .

The statistical standard deviation on each  $f_{LG}(\tau)$  data point is computed by propagating the **statistical error** on the measured Rabi spectrum through three steps

1. the division by the cavity filtering  $C(\omega)$
2. the definition of the inverse Fourier transform
3. the difference  $2K(\tau) - K(2\tau)$

Each point  $k = 1$  to  $N$  of the  $S_z(\omega)$  spectrum with bin size  $\Delta f = 100$  kHz has a constant standard deviation  $\sigma_0$  measured in the 22 – 30 MHz region where the spectral density is zero. Consequently, the standard deviation on each point  $k$  of the corrected spectrum is  $\sigma_k = \sigma_0/C[2\pi\Delta f(k-1)]$ . Finally, the standard deviation  $\sigma_r$  on each point  $r$  of  $f_{LG}[\tau = (r-1)/(N\Delta f)]$  is

$$\sigma_r = \Delta f \sqrt{\sigma_{k=1}^2 + 4 \sum_{k=2}^{N/2} \sigma_k^2 \left[ 2 \cos \frac{2\pi(r-1)(k-1)}{N} - \cos \frac{2\pi 2(r-1)(k-1)}{N} \right]^2}.$$

A conventional  $2\sigma_r$  statistical contribution is added to the systematic error to form the total red error bars of Fig. 3.28. At the second point  $\tau = 17$  ns where inequation 3.17 is violated, the standard deviation  $s \equiv \sigma_2 = 0.065$ , and the bottom of the systematic error bar is 4.9 s above 1.

### 3.5.5 INTERPRETATION OF THE VIOLATION OF THE LEGGETT-GARG INEQUALITY

#### 3.5.5.1 Macroscopic quantum superpositions states

The Leggett-Garg inequality was introduced with the aim of distinguishing between classical macroscopic states and macroscopic quantum coherent states (MQCS), that is, coherent superpositions of macroscopically-distinct states, often called Schrödinger cats. Is our violation of the Leggett-Garg inequality a proof of the existence of the existence of such MQCS?

The question is not to know if a superposition state has been observed, which is demonstrated by the violation, but is about the *degree of macroscopicity* of the TLS  $|g\rangle$  and  $|e\rangle$  states whose superpositions are observed. These states are the states of a macroscopic circuit, but are they macroscopic states, or is their difference so small that they are essentially microscopic states that trivially obey quantum laws?

Leggett<sup>121,30</sup> proposes to quantify the *degree of macroscopicity* or the *macroscopic distinctness* of a physical variable, using two numbers, both of them being much larger than one in truly macroscopic objects:

- The *extensive difference*  $\mathcal{L}$  is the difference on the variable expectation value between the two states. This difference should be expressed in some reference units relevant at the atomic scale. For instance, two states which show some difference in charge  $\delta q$  have an extensive difference  $\mathcal{L} = \delta q/e$  which is expressed in terms of the electron charge  $e$ .
- The *disconnectivity*  $\mathcal{D}$  is a measure of the *degree of entanglement* of the state. When the characterization of a state involves up to  $M$ -particle correlations, its disconnectivity is  $\mathcal{D} = M$ . This quantity is defined as an attempt to distinguish a pure MQCS involving  $N$  particles, which has a form  $a|\alpha\rangle^N + b|\beta\rangle^N$  from the typical states found in macroscopic quantum phenomena which are of the form  $(a|\alpha\rangle + b|\beta\rangle)^N$ . Since these latter states can be factorized, their behaviour can be explained by introducing only single and two-particle correlation functions and in this case  $\mathcal{D} = 2$ . In contrast with this, for the former states,  $N$ -particle correlations have to be introduced and thus  $\mathcal{D} = N$ .

As an example, in Cavity QED, a superposition of two coherent states with complex amplitudes  $\alpha$  and  $\beta$  can be built in the cavity:

$$|\psi\rangle = a|\alpha\rangle + b|\beta\rangle$$

In this case the extensive difference is typically  $\mathcal{L} = |\alpha|^2 - |\beta|^2$  in units of photons –typically up to 5-10 photons. On the other hand, the field is not substantially entangled with the electrons in the mirrors –otherwise, the decoherence time would be extremely short– and then it is of the same order of magnitude  $\mathcal{D} \sim \mathcal{L} \sim 10$ . The state is therefore far from being macroscopic.

In the case of an RF-SQUID (Fig. 3.27) which was considered in the Leggett and Garg paper<sup>29</sup>, a simple analysis<sup>30</sup> suggests that the states are much more macroscopic.

Indeed the extensive difference can be taken in terms of the magnetic moment over the flux quantum  $\Phi_0$  which has a difference of typically  $\mathfrak{L} = 10^6\text{--}10^{10}$  between the right and left wells depending on the sample parameters. The disconnectivity is of the same order than the number of Cooper pairs which are different in the states corresponding to the right and left wells. This number can be evaluated with the difference of current between the two states, which is of the order of the magnetic moment divided by  $\hbar$ , and leads to  $\mathfrak{D} \sim \mathfrak{L}$ . This analysis, however, may be too naive: a precise calculation by Korsbakken *et al.*<sup>122</sup> of the number of electrons whose state change between the left and right branches results in a number of the order of 100, which is far from being macroscopic. The subtlety is that the variation in the current does not result from a large number of electrons which moment changes slightly, but rather from a few ones which undergo a large variation of moment  $\Delta p \sim 2k_F$  as a consequence of the exclusion principle.

In the case of a transmon TLS, no exact calculation of  $\mathfrak{D}$  and  $\mathfrak{L}$  exist to our knowledge. The difference in flux between the first two energy eigenstates of the transmon at  $\Phi = 1/4\Phi_0$  is:

$$\Delta\Phi = L \frac{\partial E_{01}}{\partial \Phi} = 4.2 \times 10^{-22} \text{ Wb}$$

The extensive difference expressed in units of the flux quantum is therefore very small:

$$\mathfrak{L} = \frac{\Delta\Phi}{\Phi_0} \simeq 2 \times 10^{-7}$$

As analyzed by Leggett<sup>121</sup> the disconnectivity of a CPB is  $\mathfrak{D} = 2$  because the CPB topology allows to describe the Josephson effect with two-electrons wave functions localized either in one side or the other of the junction. Therefore, according to the two Leggett criteria, our experiment does not involve *superpositions of macroscopic states* but rather *superpositions of microscopically-distinct states of a macroscopic body*. To summarize, what can be said to be macroscopic in our experiment?

- the size of the artificial atom circuit, the transmon, is macroscopic.
- according to the calculations performed above, the difference between the two circuit states is on the microscopic scale.
- however the typical dipole matrix element between the two states is almost macroscopic ( $\sim 10^4 e a_0$ ).

### 3.5.5.2 Determinism

It is interesting to note that, whereas macro-realism is historically the framework in which the Leggett-Garg inequality (Eq. 3.15) was derived, a more general framework based on determinism yields the same result, as noticed by Zela<sup>38</sup>.

To be more specific we consider a dichotomic variable  $\sigma(t) = \pm 1$  describing some physical property, and the situation sketched in Fig. 3.29, where this variable is measured several successive times. For instance,  $\sigma$  may be a magnetic moment

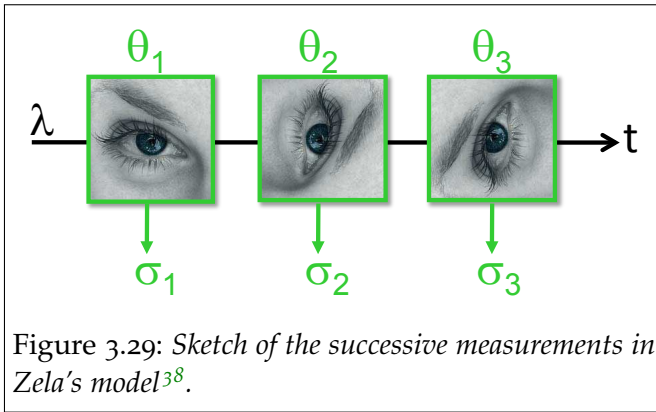
measured in successive Stern-Gerlach apparatuses, each analyzing the moment along an angle  $\theta_i$ . The analysis of Zela is based on two hypotheses:

- *Determinism*: the evolution of the variable is governed by an equation of motion at all times, so that its evolution results from some initial conditions noted  $\lambda$ .
- *Non-contextuality*: the value  $\sigma_i$  measured in a measurement apparatus  $i$  does not depend on the full arrangement of all the measurement apparatuses. That is, the particle does not *know* which are the measurements that will be performed on it during the whole experimental sequence. However, the value  $\sigma_i$  can depend on the setup of the former measurement apparatuses  $\theta_{j<i}$ , which may have introduced some back-action when measuring.

With these two hypotheses the value  $\sigma_i$  measured in a measurement apparatus  $i$  at time  $t$  can be written as a function  $\sigma(\lambda, \theta_i, \theta_{j<i}, t)$  which is only dependent of

- the initial conditions  $\lambda$ .
- the setup of the former measurement apparatuses  $\theta_{j<i}$  (which includes the times  $t_{j<i}$  at which they were performed).
- the setup of the measurement apparatus  $\theta_i$ .
- the time  $t_{j<i}$  at which the measurement is performed.

Since the setup of former measurement apparatus enters in this function, invasive detectors can be described in this formalism, unlike in the original Leggett-Garg inequality.



The deduction of the inequality is straightforward. The two-time correlator of  $\sigma$  is

$$K(t_i, t_j) = E [\sigma(t_i)\sigma(t_j)] = \int P(\lambda)\sigma(t_i, \lambda, \theta_{k \leq i})\sigma(t_j, \lambda, \theta_{l \leq j})d\lambda$$

where the initial conditions have been supposed to follow a classical distribution of probability  $P(\lambda)$ . Now, since  $\sigma$  is dichotomic, two measurements can only yield four possible outcomes, and thus we can decompose  $K(t_i, t_j)$  as:

$$K(t_i, t_j) = [C_{-1,-1}(t_i, t_j) + C_{1,1}(t_i, t_j)] - [C_{1,-1}(t_i, t_j) + C_{-1,1}(t_i, t_j)]$$

where  $C_{r,s}(t_j, t_k)$  is the joint probability of measuring  $r$  at  $t_i$  and  $s$  at  $t_j$ .

Now when three successive measurements are performed at times  $t_1 \leq t_2 \leq t_3$ , the joint probability of getting the outcomes  $r_1, r_2$  and  $r_3$  is:

$$C_{r_1, r_2, r_3}(t_1, t_2, t_3) = \int P(\lambda)\sigma(t_1, \lambda, \theta_1)\sigma(t_2, \lambda, \theta_1, \theta_2)\sigma(t_3, \lambda, \theta_1, \theta_2, \theta_3)d\lambda.$$



Using the relations  $C_{r_1, r_3}(t_1, t_3) = C_{r_1, -1, r_3}(t_1, t_2, t_3) + C_{r_1, 1, r_3}(t_1, t_2, t_3)$  and  $C_{r_i, r_i}(t_i, t_i) = 1$  and rearranging the terms yields<sup>31</sup>

$$K(t_1, t_2) + K(t_2, t_3) - K(t_1, t_3) \leq 1$$

which happens to be the Leggett-Garg inequality.

Now to get more insight on the physical meaning of the inequality, it worths making a comparison between these new hypotheses and the ones of the original Leggett-Garg inequality. A noticeable difference concerns the back-action of the measurement apparatus. One of the original hypotheses is the absence of back-action, whereas with the new hypotheses the measurement can apply some back-action as far as this back-action introduces only a deterministic perturbation of the evolution, which can be treated as an additional initial condition. This suggests that the violation of the Leggett-Garg inequality 3.15 by quantum systems is not a consequence of the dichotomic character of  $\sigma$ , nor of projection of the state, but rather of the stochastic choice of the measured outcome, which results in a stochastic back-action of the measurement apparatus.

A further work by Lapiedra<sup>37</sup> reduces the two above hypotheses to the sole determinism, understood as *the existence of a continuous trajectory  $\sigma_i(t)$  for each system observable  $\sigma_i$ , even when they are being measured*. In this sense, the violation of the Leggett-Garg inequality would constitute a proof of the non-determinism, ruling out all strictly deterministic hidden-variable models.

We stress however that these two developments lead to the original Leggett-Garg inequalities and not to the weak-measurement version (Eq. 3.17) which was violated in our experiment, and no direct way is known for obtaining the latter from the former. However in this case also a classical back-action which mimics the quantum one, for instance two attractors situated along the  $z$  axis to reproduce the projection associated to the measurement of  $\sigma_z$ , create a telegraphic trajectory

$$\sigma_z(t) = \lim_{n \rightarrow \infty} \left( \sin^{2n+1}(\omega_R t) \right)$$

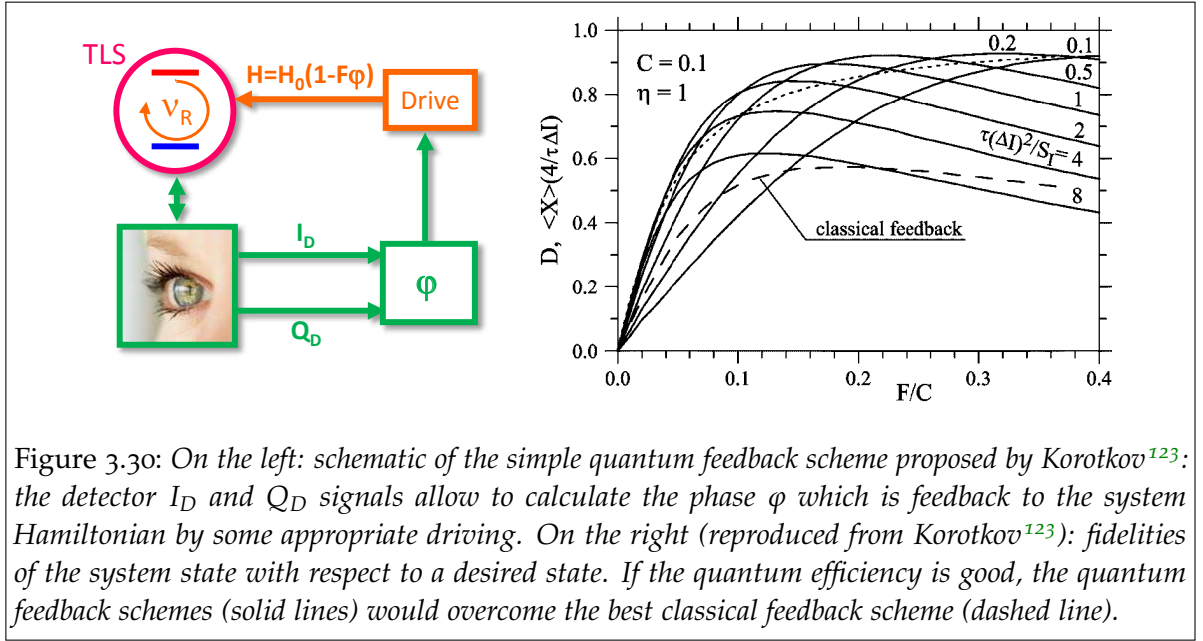
which does not violate the inequality. This suggests that, also in this case, the existence of a deterministic back-action is not enough to bring a violation of the inequality.

### 3.5.5.3 The quantum feedback resource

The violation of the original Bell's inequality brought an experimental evidence for the non-classical correlations associated with entanglement. These peculiar correlations are nowadays regarded as a resource for quantum cryptography and computing. In the same way the violation of the Leggett-Garg inequality witnessing some useful quantum resource?

Indeed, the violation of the inequality comes from the correlations not only of the signal but also of the *noise* at the detector output with the state of the TLS. Can the information contained in these noise correlations be used for some practical purpose? Actually they can: in a feedback configuration, the full detector signal could be used for outperforming any classical feedback scheme, which would only take into account the result of the actual measurement.





Korotkov and Ruskov<sup>39,123</sup> analyzed several of these *quantum feedback* schemes<sup>3</sup> and demonstrated that indeed analyzing the continuously acquired data and feeding back a control signal onto the system, it is possible to correct with high fidelity the measurement-induced dephasing of coherent oscillations and keep their phase constant –with finite accuracy– forever. The Fig. 3.30 shows how this can be made with a simple feedback loop which uses the phase of the detector output to generate slightly different drives which stabilize the phase of the coherent oscillations.

However, to be able to perform such feedback experiments the quantum efficiency of the measurement chain should allow to violate Leggett-Garg inequality in a single-shot: this would require quantum-limited amplifiers which are presently a subject of intense research<sup>40,41</sup>.

### 3.6 CHARACTERIZING THE THERMAL FLUCTUATIONS WITH A CONTINUOUS MEASUREMENT

An interesting application of continuous measurements implemented in this chapter is to characterize the thermal fluctuations of the TLS state. Indeed, in the absence of any driving field, at temperatures in the 10 – 30 mK range and for typical qubit resonance frequencies of a few GHz, there is at thermal equilibrium a small (typically less than 1%) probability  $\rho_{ee}^{th}$  of finding the qubit in the excited state

$$\rho_{ee}^{th} = \frac{1}{\exp\left(\frac{\hbar\omega_{ge}}{k_B T}\right) + 1}$$

Besides it is well known in mesoscopic physics that the effective temperature  $T$  of an electrical degree of freedom such as a superconducting qubit can be in some

<sup>3</sup>A comprehensive introduction to the quantum feedback schemes and their applications can be found in a recent book by Wiseman and Milburn<sup>124</sup>.

cases much larger than the temperature of the experiment, because it can be strongly coupled to out-of-equilibrium electromagnetic radiation coming from the measuring leads, while only weakly to the phonon bath. It is thus important to be able to measure precisely the average excited state population of a single qubit.

This measurement is also important for quantum information purposes. Indeed the implementation of large scale quantum algorithms requires that the qubit registers are properly initialized at the beginning of each computation<sup>48</sup>, with all qubits lying in their ground state  $|0\rangle$ . However in most superconducting qubit experiments, the initialization is simply realized by waiting long enough before each experimental sequence for the system to reach thermal equilibrium. Although the probability  $\rho_{ee}^{th}$  of finding a qubit in the  $|1\rangle$  state is usually considered negligible, given the recent improvement of the overall fidelity of single<sup>125</sup>- and two-qubit gates<sup>126</sup>, the effect of even small thermal fluctuations will require to be considered more quantitatively in the near future.

### 3.6.1 MEASURING THE THERMAL FLUCTUATIONS

The usual method for reading out the qubit state, using ensemble-averaged measurements of the microwave signal, does not directly provide an absolute measurement of the qubit thermal excitations. Indeed, when a thermal fluctuation brings the TLS from the ground to the excited state, the field reflected on the resonator is the one corresponding to the excited state, with the output field components  $I_1$  and  $Q_1$ . In all the cases where no thermal fluctuation occurs the field components are  $I_0 = I_1$  and  $Q_0$ . Thus, the average phase shift between the states results to be

$$\delta\varphi_0(T) = \arctan \left[ \frac{Q_1}{I_1} \right] - \arctan \left[ \frac{Q_0 + (Q_1 - Q_0)\rho_{ee}^{th}(T)}{I_1} \right].$$

Calibrating such small reduction of  $\delta\varphi_0$  is very difficult experimentally. Moreover  $\delta\varphi_0(T=0)$  is not measurable, so only an extrapolation of  $\delta\varphi_0(T)$  could provide an estimation of  $\rho_{ee}^{th}$ .

However, using a continuous measurement scheme as the one described above allows to directly measure the thermal population. Indeed the thermal fluctuations of the qubit state are responsible for a measurable phase noise in the microwave signal reflected by the resonator which can be accurately characterized by averaging the noise spectra at the resonator output. The main difference with the continuous measurements performed above is that the TLS not driven. It is worth noting also that the mere presence of a continuous measurement of the qubit state has no effect on the dynamics of thermal fluctuations because this dynamics is fully incoherent and entirely governed by Markovian rate equations<sup>28</sup>. A similar characterization of thermal population was performed on an ensemble of nuclear spins measured by a SQUID amplifier<sup>127</sup>.

### 3.6.2 SPECTRUM OF A TLS COUPLED TO A THERMAL BATH

To extract the temperature from the spectrum of the continuous measurement of the transmon we compute here the expected noise power spectrum for a TLS coupled to a thermal bath.

We start by describing the TLS dynamics at thermal equilibrium by a simple rate equation<sup>128</sup>

$$\dot{\rho}_{ee} = -\dot{\rho}_{gg} = -\Gamma\rho_{ee} + \Gamma'(\rho_{gg} - \rho_{ee}) \quad (3.18)$$

where  $\Gamma$  is the TLS spontaneous emission rate and  $\Gamma'$  is the stimulated emission rate. Assuming that the bath consists of a bosonic Markovian bath at temperature  $T$ , as expected for the impedance of the electromagnetic environment, the stimulated emission is proportional to the mean number of photons in the bath resonant with the  $g \rightarrow e$  transition  $\Gamma' = \Gamma n_{th}$  which is

$$n_{th}(T) = [\exp(\hbar\omega_{ge}/kT) - 1]^{-1}$$

This yields a steady-state ( $\dot{\rho}_{ee} = 0$ ) population of the qubit excited state

$$\rho_{ee}^{th} = \frac{n_{th}}{1 + 2n_{th}} \quad (3.19)$$

Therefore Eq. 3.18, yields

$$\rho_{ee}(t) = [\rho_{ee}(0) - \rho_{ee}^{th}] e^{-t\Gamma(1+2n_{th})} + \rho_{ee}^{th} \quad (3.20)$$

The conversion to the  $\hat{\sigma}_z$  basis units in which the measurement is performed is directly given by  $\langle \hat{\sigma}_z(t) \rangle = 1 - 2\rho_{ee}(t)$ . In this  $\hat{\sigma}_z$  basis the correlation function is written

$$K_z(t) = \langle \hat{\sigma}_z(t) \hat{\sigma}_z(0) \rangle - \langle \hat{\sigma}_z(0) \rangle^2$$

The first product can be calculated conveniently with the conditional expression

$$\begin{aligned} \langle \hat{\sigma}_z(t) \hat{\sigma}_z(0) \rangle = & P(\sigma_z(0) = 1) \langle \hat{\sigma}_z(t) \rangle|_{\sigma_z(0)=1} \\ & - P(\sigma_z(0) = -1) \langle \hat{\sigma}_z(t) \rangle|_{\sigma_z(0)=-1} \end{aligned} \quad (3.21)$$

where  $P(\sigma_z(0) = 1)$  is the probability of starting with the TLS in the ground state. Substituting Eq. 3.19 and Eq. 3.20 in Eq. 3.21 we find:

$$K_z(\tau) = 4 \left(1 - \rho_{ee}^{th}\right) \rho_{ee}^{th} \exp(-\Gamma(1 + 2n_{th})\tau). \quad (3.22)$$

The power spectrum is the Fourier transform of this expression;

$$S_z(\omega) = 4 \left(1 - \rho_{ee}^{th}\right) \rho_{ee}^{th} \frac{\Gamma(1 + 2n_{th})}{\Gamma^2(1 + 2n_{th})^2 + \omega^2}. \quad (3.23)$$

Note that these expressions are only approximate in the case of a transmon because it is not a genuine two-level system but an anharmonic resonator with an infinite number of excited states. Then the previous expressions are only valid in the limit where the population of the higher excited states is negligible, which in our case remains true up to temperatures around 100 mK.

### 3.6.3 EXPERIMENTAL CHARACTERIZATION OF THE THERMAL FLUCTUATIONS

To characterize the thermal fluctuations of the TLS state, we measure the detector output noise spectrum for a series of temperatures  $T_F$ . The spectra are acquired with the same setup and procedure as described in 3.4.2.1, the only difference being that the source  $V_d$  driving the TLS is now always turned off. As explained in 3.4.2.2, the amplifier noise is subtracted from the measured spectrum, and the resulting spectrum is corrected from the setup response  $R(\omega)$  to yield  $S_V(\omega)$  which is plotted in Fig. 3.31a for varying  $T_F$ . Each spectrum is measured after waiting 15 minutes thermalization time once the cryostat reaches  $T_F$ . We also verify that the sample is well thermalized by acquiring two noise spectra for each  $T_F$ , one upon warming up and the second upon cooling down, which are found to be nearly identical.

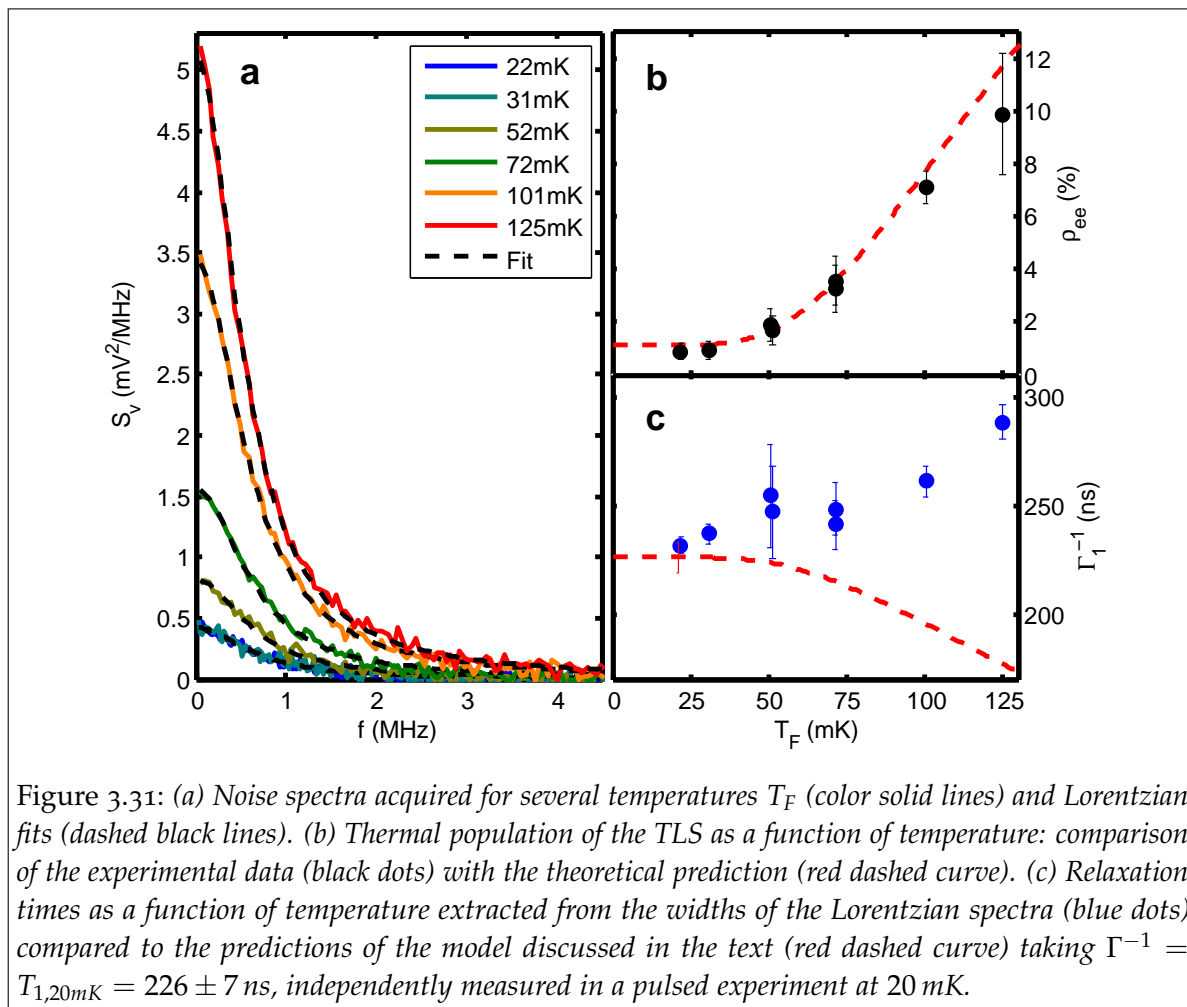


Figure 3.31: (a) Noise spectra acquired for several temperatures  $T_F$  (color solid lines) and Lorentzian fits (dashed black lines). (b) Thermal population of the TLS as a function of temperature: comparison of the experimental data (black dots) with the theoretical prediction (red dashed curve). (c) Relaxation times as a function of temperature extracted from the widths of the Lorentzian spectra (blue dots) compared to the predictions of the model discussed in the text (red dashed curve) taking  $\Gamma^{-1} = T_{1,20mK} = 226 \pm 7$  ns, independently measured in a pulsed experiment at 20 mK.

As seen in Fig. 3.31a, the measured noise spectra  $S_V(\omega)$  have a Lorentzian shape,

with an amplitude rapidly increasing with temperature. This noise spectrum is

$$S_V(\omega) = \left( \frac{\Delta V}{2} \right)^2 S_z(\omega).$$

The amplitude  $A$  and width  $\Gamma_1$  of each spectrum are fitted with a Lorentzian model  $A \Gamma_1 / (\Gamma_1^2 + \omega^2)$ . According to Eq. 3.23, the model predicts that  $A = \Delta V^2 (1 - \rho_{ee}^{th}) \rho_{ee}^{th}$  and  $\Gamma_1 = \Gamma(1 + 2n_{th})$ , which is the experimentally-accessible relaxation rate of the system.

The detector sensitivity  $\Delta V^2$  is experimentally calibrated as explained above. For the power used in this experiment, which corresponds to  $\bar{n} \simeq 2.3$  photons, this yields  $\Delta V/2 = 2.76 \pm 0.14$  mV. In this way we can directly extract from the fits the thermally excited state population  $\rho_{ee}$  and the relaxation rates  $\Gamma_1$  as a function of the cryostat temperature  $T_F$ .

### 3.6.4 ANALYSIS OF THE POPULATIONS AND THE RELAXATION RATES

The fitted population (dots in Fig. 3.31b) agrees with the theoretical average population  $\rho_{ee}^{th}$  (red dashed curve), calculated assuming two sources of radiation (Fig. 3.32): the thermal field corresponding to the temperature of the cryostat coldest stage  $T_F$ , with an average of  $n_{th}(T_F)$  photons, and the thermal field radiated by the 30 dB attenuator thermalized at the still temperature  $T_S = 600 \pm 100$  mK, and attenuated ( $22 \pm 0.5$  dB) at 20 mK, contributing with  $n_{th}(T_S) / 10^{2.2}$  photons. At the lowest  $T_F$ , we find a thermally excited state population of  $1 \pm 0.5\%$ , corresponding to an effective temperature of 55 mK.

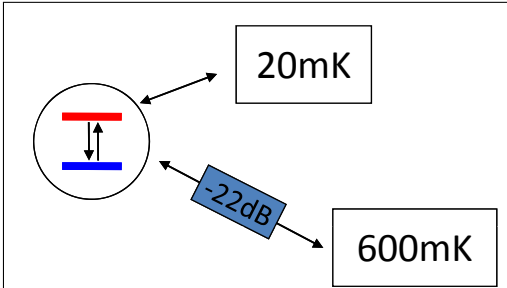


Figure 3.32: Model of the thermal environment seen by the TLS: a first thermal bath thermalized at cryostat temperature is directly coupled to the TLS and a second one, with much higher but constant temperature radiates to the TLS through a line containing 22 dB of attenuation.

At  $T_F = 20$  mK, the relaxation rate  $\Gamma_1^{-1}$  deduced from the width of the Lorentzian noise spectrum (see Fig. 3.31c) is found to be in excellent agreement with the qubit relaxation time  $T_{1,20mK} = 226 \pm 7$  ns, measured in a standard pulsed sequence. However, at higher  $T_F$ , we observe that the fitted width decreases, which implies that the qubit energy relaxation time increases with temperature. Unfortunately we did not verify this surprising result with direct  $T_1$  measurements at each temperature. This counter-intuitive result disagrees with our model which predicts a relaxation rate  $\Gamma(n_{th}) = \Gamma(1 + 2n_{th})$  (Eq. 3.18) increasing with temperature due to stimulated emission by the thermal field, yielding the red dashed curve in Fig. 3.31b (calculated with  $\Gamma = T_{1,20mK}^{-1}$ ). This indicates that the qubit is not only coupled to its electromagnetic environment but also to another type of bath, causing

some additional relaxation with a different temperature dependence.

Additional support for the existence of such unknown non-radiative decay channels is that the measured relaxation time at 20 mK (226 ns) is significantly shorter than the expected relaxation time due to relaxation into the the external impedance at zero

temperature (600 ns), which indicates the existence of a non-radiative energy decay channel. We finally note that a similar increase of the relaxation time with temperature up to 150 mK was directly observed in a superconducting phase qubit, and attributed to non-equilibrium quasi-particles in the superconducting metal electrodes<sup>89</sup>; a similar scenario might explain our results. Note however, that if such relaxation channel exists, the agreement of the populations with the model presented in Fig. 3.32 is fortuitous.





## HIGH-FIDELITY QUBIT READOUT AND NON-LINEAR CIRCUIT QED

---

In the goal of implementing quantum processors with a scalable architecture based on superconducting circuits, the circuit QED architecture is particularly promising. Indeed, the resonator isolates the qubits from their electromagnetic environment, yielding longer and reproducible lifetimes, and, at the same time, it can be used to readout the qubit state thanks to the cavity pull as explained in 2.4. However this cQED dispersive readout method has never reached a signal-to-noise ratio sufficient to allow a single shot readout for qubit, which is an important drawback in the perspective of experiments involving several qubits.

In this chapter, we present a new readout circuit that allows high-fidelity single-shot readout of the qubit state while keeping the good properties of cQED qubit architecture. This is achieved by introducing some non-linearity in the readout resonator to turn it into a bistable hysteretic system, known in the literature as the Cavity Bifurcation Amplifier (CBA) and invented in Michel Devoret's group at Yale<sup>129</sup>. Here we show that this readout allows to reach high fidelities (up to 94%), without affecting the qubit lifetimes or inducing spurious excitations. We also discuss the readout parameter optimization, relying on the results of two experiments in which the non-linearity was made tunable.

The introduction of a non-linear element in the resonator strongly modifies the physics of the resonator-qubit coupled system. In particular, the qubit absorption spectrum in the presence of a field in the resonator is strongly modified compared to the linear resonator case. The observation of these phenomena and their theoretical justification will be the subject of the last section of this chapter.

### 4.1 FIDELITY OF THE DISPERSIVE READOUT METHOD IN cQED

#### 4.1.1 THE STANDARD DISPERSIVE READOUT METHOD

We first discuss the signal-to-noise achieved in the dispersive readout method that was presented in the previous chapters in order to understand better its limitations. This method consists in sending a microwave pulse to the resonator at its resonance frequency  $\omega_c$  and to detect the phase of the reflected pulse, which is shifted by a quantity  $\pm\delta\varphi_0$  depending on the qubit state. To appreciate the difficulty of this detection, we stress that the measurement power  $P_m$  cannot be increased above a power yielding  $n_{crit}$  inside the resonator<sup>49</sup>. The errors which may happen in this detection scheme have two possible origins (4.1):

- a bad estimation of the phase shift due to the small signal and the large amount of noise coming from the cryogenic amplifier ( $T_N \simeq 4$  K).

- the relaxation of the qubit in a time  $T_1$  comparable to the readout process duration.

Both sources of errors are linked: indeed, in order to improve the SNR the signal is averaged during a certain time  $t_m$ . The longer  $t_m$ , the better is the phase estimation, but also the higher is the probability that the qubit relaxes yielding an incorrect readout.

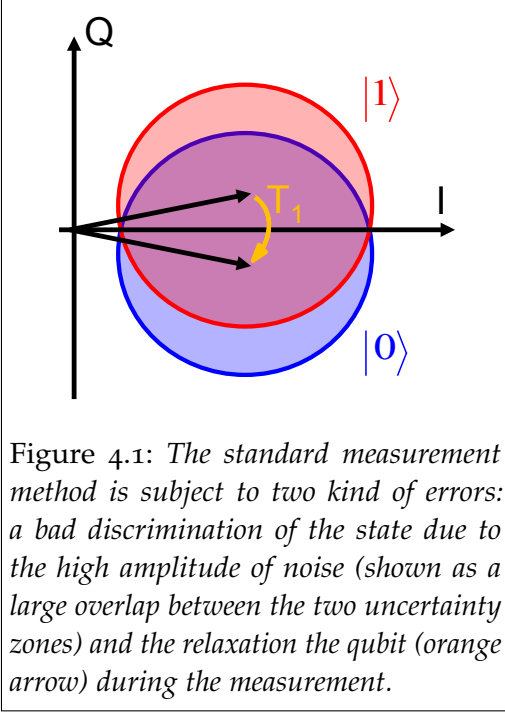


Figure 4.1: The standard measurement method is subject to two kind of errors: a bad discrimination of the state due to the high amplitude of noise (shown as a large overlap between the two uncertainty zones) and the relaxation the qubit (orange arrow) during the measurement.

In order to make this reasoning quantitative, we now estimate the readout fidelity of the dispersive readout method. In order to infer the qubit state correctly, one needs to resolve a phase shift of  $2\delta\varphi_0$  on a microwave signal with amplitude  $\bar{n} \lesssim n_{crit}$  in the presence of the noise of the cryogenic amplifier ( $T_N \simeq 4$  K). This leads to a probability of error:

$$P_N = 1/2 \operatorname{erfc}(\operatorname{SNR})$$

The fidelity  $F = 1 - P_N$  would be arbitrarily large if the qubit were not subject to relaxation, since in this case the SNR can be raised as much as wanted by averaging during a long time (see 2.1.5.1).

The case of a qubit with a finite relaxation time  $T_1$  is more complex. When the qubit is in its  $|0\rangle$  or  $|1\rangle$  state respectively, the resonator field has a complex  $\alpha_g$  or  $\alpha_e$ . The energy of the signal which characterizes the qubit state is therefore  $|\alpha_g - \alpha_e|^2$  in units of photons,

and since the energy leaves the resonator at a rate  $\kappa$ , the power of the signal is:

$$S = \kappa \hbar \omega |\alpha_g - \alpha_e|^2$$

leading to a signal-to-noise ratio:

$$\operatorname{SNR}(t_m) = \frac{S}{N} = \kappa \frac{\hbar \omega}{k_B T_N} |\alpha_g - \alpha_e|^2 t_m$$

where  $t_m$  is the averaging time. The errors in such detection scheme are of two kinds: first, the noise can lead to an incorrect determination of the phase with a probability:

$$P_N(t_m) = 1/2 \operatorname{erfc}(\operatorname{SNR}(t_m))$$

And secondly, when the qubit is prepared in  $|1\rangle$ , it may relax before the measurement is performed with a probability

$$P_R(t_m) = 1 - \exp(-t_m \Gamma_1).$$

Therefore, when the qubit is prepared in  $|0\rangle$  the probability of error is

$$P_{E,0}(t_m) = P_N(t_m)$$

and when it is prepared in  $|1\rangle$  it is:

$$P_{E,1}(t_m) = P_N(t_m) + [1 - P_N(t_m)] P_R(t_m).$$

With the parameters of the sample used in this chapter ( $\Gamma_1^{-1} \simeq 500$  ns,  $\kappa/2\pi \simeq 10$  MHz,  $n_{crit} \simeq 20$  and so  $\bar{n} = 5$  to avoid any spurious excitation and  $\delta\varphi_0 \sim 10^\circ$ ), we find that the fidelity  $F(t_m) = 1 - 1/2P_{E,0}(t_m) - 1/2P_{E,1}(t_m)$  is maximal for  $t_m = 0.26\Gamma_1^{-1}$ , with a maximum fidelity of  $F = 68\%$ . This figure is rather far from the single-shot fidelity and it is highly desirable to improve it. Indeed, the single-shot character of the readout opens the way to operating quantum algorithms without jeopardizing their speed gain by the need to repeat the experiment to get an accurate output, and allows to characterize the immediate value of any qubit observable, providing a useful tool for fundamental quantum physics experiments.

Note however that in even the absence of single shot measurement, averaging over an ensemble of identically prepared experiments, provides an accurate characterization of the qubit state, which has been very successfully used in most of the cQED experiments realized up to the present. In the particular situation where several qubits are coupled to the same resonator, Filipp *et al.*<sup>130</sup> have shown that it is even possible to reconstruct the full density matrix of the qubits, including its non-diagonal elements, from ensemble-averaged measurements.

Various attempts to improve the readout fidelity have been reported: Gambetta *et al.*<sup>131</sup> performed a more detailed analysis of the standard readout procedure, and proposed several modified readout schemes involving optimal filters at the detection stage. A very recent experiment<sup>50</sup> showed that a substantial improvement of the fidelity up to 87% could be achieved without modifying the readout circuit.

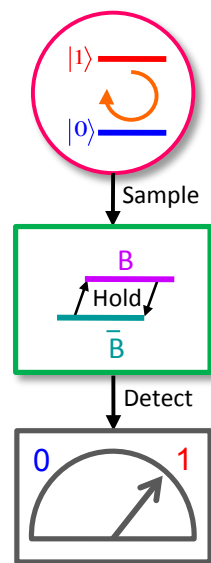
We present in this chapter a modified readout circuit which yields fidelities up to 94%.

#### 4.1.2 A SAMPLE-AND-HOLD DETECTOR FOR IMPROVING THE READOUT FIDELITY

A way to overcome the fidelity limitations of the dispersive readout method is to break the link between the measuring and averaging times by using a so-called sample-and-hold detector. The strategy of this detector is to separate the measurement process in two parts:

- a first step during which the qubit state is quickly mapped on the detector state (*sample*). If this mapping is performed much faster than the relaxation time  $T_1$  the amount of errors induced by relaxation is substantially reduced.
- a second step during which the detector state is maintained and measured until it is discriminated with certainty (*hold*). If the detector is truly metastable, this step can be as long as needed to reduce the errors to zero.

To operate a device as such a sample-and-hold detector, it should be a bistable hysteretic system:



- The bistability allows to unambiguously map the qubit state onto the state of the measurement device
- The hysteresis allows to hold the state of the measurement device as long as needed to determine it without any error

Michel Devoret's group at Yale has invented and demonstrated a family of superconducting circuits that behave as bistable hysteretic detectors: the Josephson Bifurcation Amplifiers (JBA)<sup>51,132,129</sup>, which will be described in detail in the following section. Josephson Bifurcation Amplifiers are oscillators made non-linear by using the non-linearity of the Josephson inductance, which display dispersive bistability. Josephson Bifurcation Amplifiers have been already employed to readout the state of a Quantronium qubit<sup>84,133</sup>, and of a flux qubit<sup>134</sup>, the latter with 87% fidelity and QND character. Here we show how we integrated a JBA to the circuit QED architecture presented in previous chapters to obtain a single-shot readout of a transmon qubit.

## 4.2 JOSEPHSON BIFURCATION AMPLIFIERS: THEORETICAL DESCRIPTION

We now analyze the dynamics of driven non-linear oscillators with a cubic non-linearity, and we show that they can display bistability. We then discuss the specific implementation of non-linear oscillator used in our experiment: the Cavity Josephson Bifurcation Amplifier (CBA).

### 4.2.1 THE DUFFING OSCILLATOR AND THE JOSEPHSON BIFURCATION AMPLIFIER

We first consider a simple pendulum of mass  $m$ , length  $l$ , periodically driven by a force  $F_0$  at frequency  $\omega_m$ , as shown in Fig. 4.2a. The restoring force of this pendulum is proportional to the sine of the angle  $\vartheta$  it makes with the vertical:

$$ml^2\ddot{\vartheta} + \gamma\dot{\vartheta} + mgl \sin(\vartheta) = F(t) = F_0 \cos(\omega_m t),$$

where  $\gamma\dot{\vartheta}$  is the friction force and  $g$  the gravity acceleration. For small oscillations  $\vartheta \ll 1$ , the sine can be expanded to third order, resulting in a restoring force proportional

Parameter	Pendulum	JBA	CBA
$\omega_r$	$\sqrt{\frac{g}{l}}$	$\sqrt{\frac{I_0}{\varphi_0 C}}$	$\sqrt{\frac{1}{(L_e + \varphi_0/I_0)C_e}}$
$Q$	$\frac{2ml^2\omega_r}{\gamma}$	$RC\omega_r$	$\frac{\pi Z_0}{2R_e}$
$u(t)$	$\sqrt{\frac{\omega_r^2}{4\omega_m\Delta_m}}\vartheta(t)$	$\sqrt{\frac{\omega_r^2}{4\omega_m\Delta_m}}\theta(t)$	$\sqrt{\frac{pQ}{2\Omega}}\frac{\omega_m}{I_0}q(t)$
$\beta$	$\left(\frac{F}{mgl}\right)^2 \left(\frac{\omega_r^2}{4\omega_m\Delta_m}\right)^3$	$\left(\frac{I_m}{I_0}\right)^2 \left(\frac{\omega_r^2}{4\omega_m\Delta_m}\right)^3$	$\left(\frac{V_e}{\varphi_0\omega_m}\right)^2 \left(\frac{pQ}{2\Omega}\right)^3$

Table 4.1: Reduced non-linear resonator parameters<sup>129</sup> for the three kinds of non-linear resonators considered above

to the displacement –as in a harmonic oscillator– plus a non-linear term which make the oscillator frequency dependent on the dimensionless amplitude of the drive  $\beta$ :

$$ml^2\ddot{\vartheta} + \gamma\dot{\vartheta} + mgl \left[ \vartheta - \frac{\vartheta^3}{3!} \right] = F_0 \cos(\omega_m t)$$

Such a non-linear oscillator with cubic non-linearity is known as the Duffing oscillator. We note immediately that an exact electrical analog is a resonator formed by a capacitor  $C$  in parallel with a resistor  $R$  and with a Josephson junction (critical current  $I_0$ ) that behaves as a non-linear inductance, driven by a current source  $I(t) = I_m \cos(\omega_m t)$  (Fig. 4.2b). The equation of motion of this circuit can indeed be written:

$$C\varphi_0\ddot{\theta} + \frac{\varphi_0}{R}\dot{\theta} + I_0 \sin \theta = I(t) = I_m \cos(\omega_m t),$$

where  $\theta$  now represents the phase across the junction and  $\varphi_0 = \hbar/2e$  is the reduced flux quantum.

As we will see, both oscillators display bistability. We first write the equations of motion in dimensionless units using the transformations shown in Table 4.1, the drive detuning  $\Delta_m = \omega_r - \omega_m$ , the dimensionless time  $\tau = t\Delta_m$  and the slowly varying envelope  $u(\tau)$ :

$$\frac{\Delta_m}{\omega_m} \frac{d^2 u}{d\tau^2} + \left( \frac{1}{Q\omega_m} + 2i \right) \frac{du}{d\tau} + \left[ 2 \left( \frac{\omega_r^2 - \omega_m^2}{2\omega_m\Delta_m} \right) + \frac{1}{Q\Delta_m} - 2|u|^2 \right] u = 2\sqrt{\beta}.$$

We then simplify these equations in the high- $Q$  limit  $Q \gg 1$ : the drive is near resonance  $\Delta_m/\omega_m \ll 1$  and thus  $\omega_m + \omega_r \approx 2\omega_m$ , and  $u(\tau)$  being small  $\ddot{u} \ll \omega_m \dot{u}$ . This yields:

$$\frac{du}{d\tau} = -\frac{u}{\Omega} - iu(|u|^2 - 1) - i\sqrt{\beta} \quad (4.1)$$

where we have introduced the reduced detuning  $\Omega = 2Q\Delta_m/\omega_r$ .

*Bistability: the bifurcation points*

The stationary solutions  $\dot{u} = 0$  of Eq. 4.1 obey

$$\frac{u}{\Omega} + iu(|u|^2 - 1) = i\sqrt{\beta(\Omega)}.$$

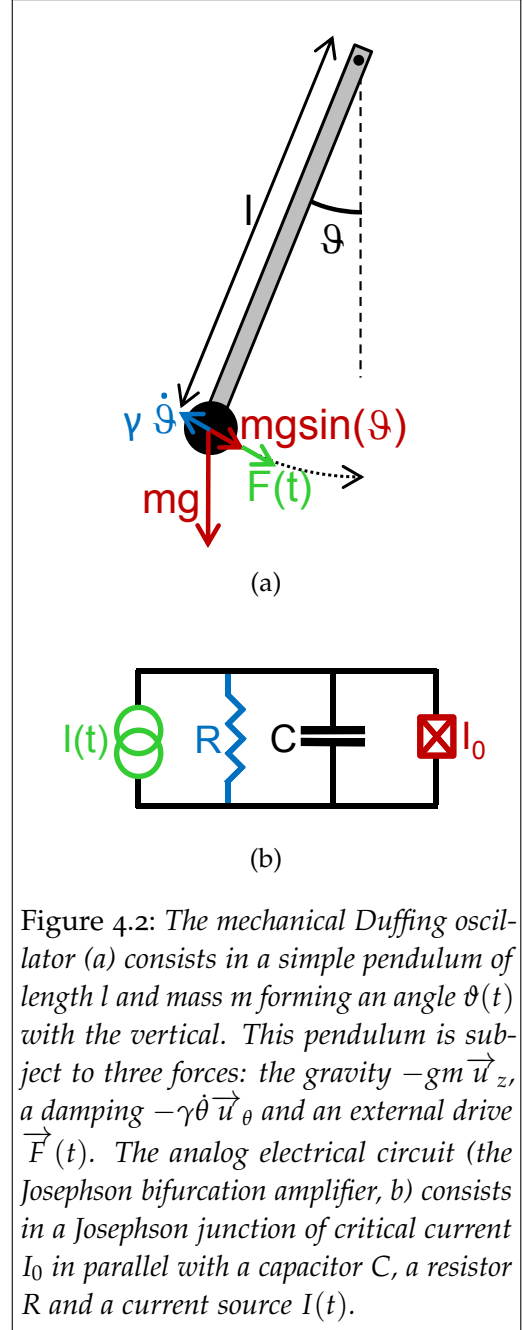


Figure 4.2: The mechanical Duffing oscillator (a) consists in a simple pendulum of length  $l$  and mass  $m$  forming an angle  $\vartheta(t)$  with the vertical. This pendulum is subject to three forces: the gravity  $-gm \vec{u}_z$ , a damping  $-\gamma\dot{\vartheta} \vec{u}_\theta$  and an external drive  $\vec{F}(t)$ . The analog electrical circuit (the Josephson bifurcation amplifier, b) consists in a Josephson junction of critical current  $I_0$  in parallel with a capacitor  $C$ , a resistor  $R$  and a current source  $I(t)$ .

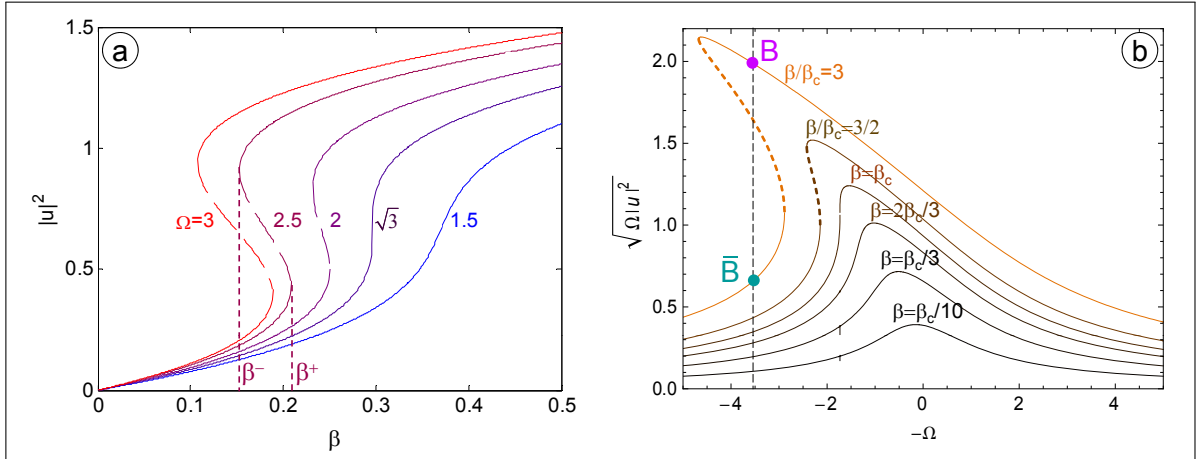


Figure 4.3: Steady-state solutions of Eq. 4.1 (a) As a function of the drive  $\beta$ , for several values of  $\Omega$ . For  $\Omega \geq \sqrt{3}$  there are three real-valued solutions, the central one (dashed lines) unstable, while for  $\Omega \leq \sqrt{3}$  there is only one. The bifurcation points  $\beta^\mp$  are respectively the maximum and minimum drive for which the lower and upper solutions exist. (b) As a function of the reduced frequency  $\Omega$ , for several values of  $\beta$ , with the two resonator states  $\bar{B}$  and  $B$  for  $\Omega = 3$  indicated.

Their square modulus  $|u|^2$  is solution of a 3rd degree equation

$$|u|^2/\Omega^2 + |u|^2 (|u|^2 - 1)^2 = \beta(\Omega)$$

and is plotted in Fig. 4.3 for various  $(\beta, \Omega)$  parameters. Depending on the  $(\beta, \Omega)$  parameter range, this equation has one or three solutions. More precisely, there are three solutions when  $\Omega > \sqrt{3}$  and  $\beta^-(\Omega) \leq \beta \leq \beta^+(\Omega)$  where  $\beta^\pm(\Omega)$  are the solution of  $d\beta/d(|u|^2) = 0$  i.e.

$$\beta^\pm(\Omega) = \frac{2}{27} \left[ 1 + \left( \frac{3}{\Omega} \right)^2 \pm \left( 1 - \frac{3}{\Omega^2} \right)^{3/2} \right].$$

In the rest of the  $(\Omega, \beta)$  plane, only one solution exists. When three solutions exist, it can easily be shown that the ones corresponding to the highest and lowest oscillations amplitude are stable, whereas the intermediate is unstable. The system can thus be in either one of two coexisting dynamical states for the same driving amplitude: it is therefore bistable, and as such well suited for implementing a sample-and-hold detector. We call  $\bar{B}$  (resp.  $B$ ) the low (resp. the high) oscillation amplitude state (see Fig. 4.3b). The points  $\beta^\pm(\Omega)$  at which the system can change state are called *bifurcation points*.

### Hysteresis

We have just seen that in the bistability region and under the same driving conditions the oscillator can be in one of two states of oscillations. But what determines the actual state of the oscillator?

Following the Fig. 4.4 we first consider the situation where we start with a very small driving amplitude. When increasing the drive, the amplitude  $u$  remains in the lower branch since it is stable, which corresponds to the state  $\bar{B}$ , until reaching  $\beta^+$ , where this solution suddenly disappears, and the amplitude grows to reach the upper branch. This switching process between the two dynamical states is called *bifurcation*.

In the reverse direction when starting with a large amplitude drive  $\beta > \beta^+$  and lowering it, the amplitude  $u$  stays in the upper branch  $B$  since it is also stable until reaching  $\beta^-$  where this solution disappears, and  $u$  suddenly decreases to reach the lower branch  $\bar{B}$ .

This process is therefore hysteretic, with a hysteresis cycle shown in Fig. 4.4. This hysteresis is crucial in our experiment, since we can hold the resonator state by keeping the drive between this two bifurcation points  $\beta^+ > \beta > \beta^-$ .

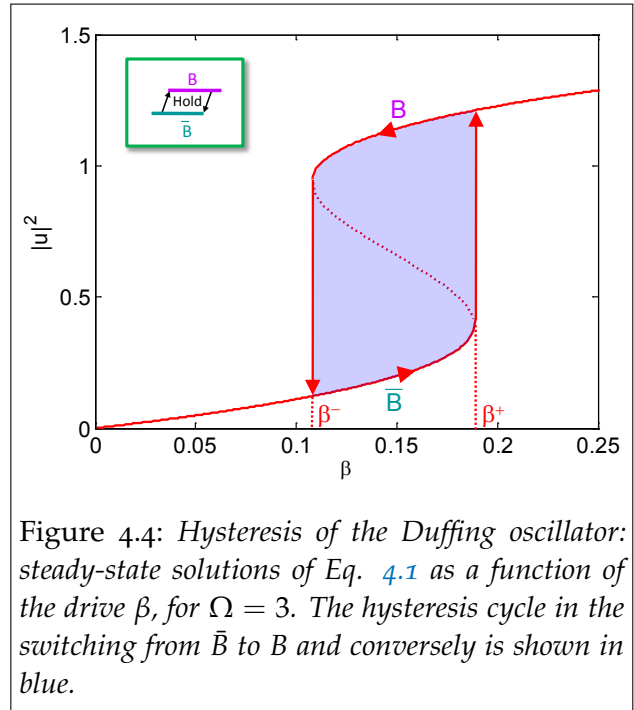


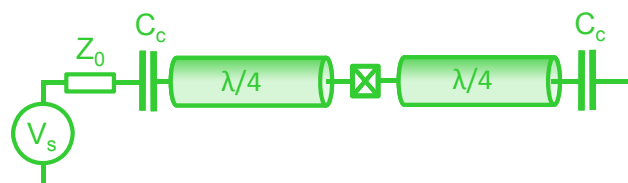
Figure 4.4: Hysteresis of the Duffing oscillator: steady-state solutions of Eq. 4.1 as a function of the drive  $\beta$ , for  $\Omega = 3$ . The hysteresis cycle in the switching from  $\bar{B}$  to  $B$  and conversely is shown in blue.

#### 4.2.2 THE CAVITY BIFURCATION AMPLIFIER

In our experiment the implementation of the Duffing oscillator is different from the JBA circuit shown in Fig. 4.2b. Instead of a lumped-element resonator, we used the coplanar transmission-line resonators that were described in earlier chapters and which form the building block of cQED, with a Josephson junction inserted in the middle. This implementation of Josephson Bifurcation Amplifier is called Cavity Bifurcation Amplifier (CBA) and was also invented in Michel Devoret’s group at Yale<sup>52</sup>. In this section we analyze the CBA circuit and its mapping to an RLC series non-linear resonator (in 4.2.2.1), which is itself described in 4.2.2.2. Finally we present the fabrication process and the setup used to perform the measurements.

##### 4.2.2.1 A non-linear transmission-line resonator

A Cavity Bifurcation Amplifier (CBA) consists in a  $\lambda/2$  transmission-line resonator (inductance per unit length  $\ell$ , total length  $\Lambda$ ), which is made non-linear by inserting in its middle a Josephson junction of critical current  $I_0$ . This junction is equivalent to a non-linear inductance whose value de-





depends on the current  $i$  through it:

$$L_J(i) = \frac{\varphi_0}{I_0} \sqrt{1 - \frac{i}{I_0}} \approx L_{J0} \left[ 1 + \frac{1}{2} \left( \frac{i}{I_0} \right)^2 \right] \quad (4.2)$$

### Resonance frequency

Due to the presence of the Josephson inductance  $L_J(i)$  in the center of the resonator, the CBA resonance frequency  $\omega_r$  is shifted compared to the frequency of the same resonator in the absence of the Josephson junction –the bare resonator frequency  $\omega_1$ –, even in the low power regime when  $L_J(i) \approx L_{J0}$ . In Chapter 5, which deals with tunable resonators, we calculate in detail the resonance frequency of a  $\lambda/2$  resonator containing in its center a SQUID (see 5.2.2). We use here the result of this calculation, which yields the implicit expression for the resonance frequency:

$$Z_0 \tan \left( \frac{\pi \omega_r - \omega_1}{2} \frac{\omega_1}{\omega_1} \right) = -\frac{L_{J0} \omega_r}{2}$$

### Lumped-element equivalent circuit

To allow the derivation of simple equations of motion for the CBA, we need the lumped-element equivalent circuit which reproduces the behaviour of CBA in the area of interest, that is around the resonance frequency  $\omega_r$ .

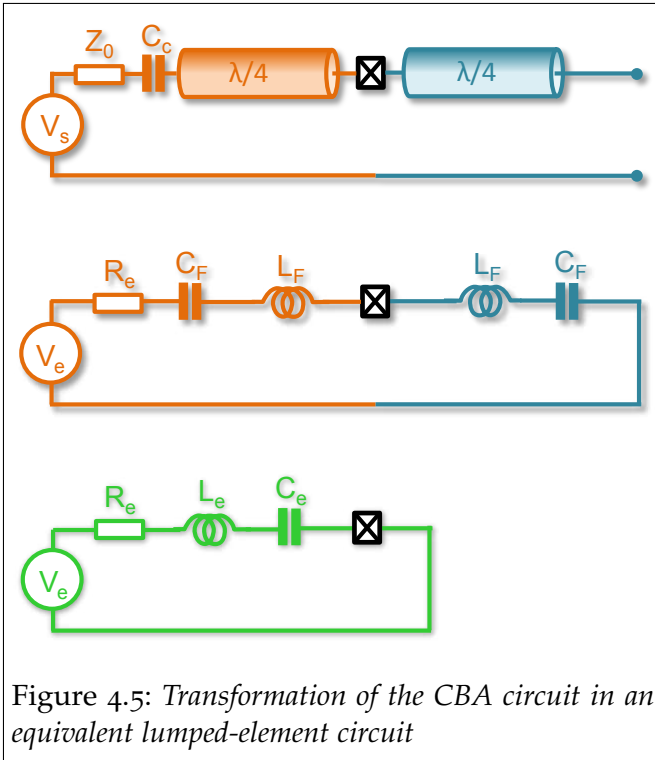


Figure 4.5: Transformation of the CBA circuit in an equivalent lumped-element circuit

This is the Thévenin equivalent circuit seen from the junction. Indeed, this equivalent circuit keeps:

- The current flowing through the junction, so that the junction non-linearity is preserved by this transformation.
- The impedance seen from the junction, so that the biasing circuit current-voltage relation is also preserved.

As shown in Fig. 4.5, the circuit seen from the junction is:

- to the right: a  $\lambda/4$  transmission-line ended in open circuit, equivalent to a series LC resonator with  $L_F = (\pi Z_0)/(4\omega_1)$  and  $C_F = 4/(\pi\omega_1 Z_0)$ .
- to the left of the junction, a  $\lambda/4$  transmission-line loaded by a small coupling capacitor  $C_c \ll 1/(\omega_r Z_0)$  in series with a microwave source  $V_s$  with  $Z_0 = 50 \Omega$  output impedance.

The impedance seen from the junction is the series impedance of these two circuits, which results as shown in Fig. 4.5 in a lumped non-linear RLC series resonator with elements:

$$\begin{aligned} L_e &= \frac{\pi Z_0}{2 \omega_1} \\ C_e &= \frac{2}{\pi Z_0 \omega_1} \\ R_e &= Z_0^3 \omega_r^2 C_c^2 \\ V_e &= C_c Z_0 \omega_r V_m \end{aligned}$$

These analytical expressions are the results of series of approximations valid in the limit where the quality factor is high, and where  $\Lambda \ell / L_{J0} \gg 1$ . To obtain more exact expressions, one needs to solve numerically the problem of finding the  $(R_e, L_e, C_e, V_e)$  circuit that approximates best the impedance and voltage seen from the junction. Note that in the rest of this chapter all equivalent circuits are found numerically and not using the formulas above.

#### 4.2.2.2 The RLC-series Duffing resonator

##### Equations of motion

The CBA is equivalent to the RLC-series non-linear resonator shown in Fig. 4.5. We will now show that once again, this circuit behaves as a Duffing oscillator and can thus be used as a JBA. The dynamics of this circuit can be described in terms of the charge  $q(t)$  stored in the capacitor plates with the following equation of motion:

$$[L_e + L_J(\iota)] \ddot{q} + R_e \dot{q} + \frac{q}{C_e} = V_e \cos(\omega_m t). \quad (4.3)$$

With the to second order expansion of the junction inductance (Eq. 4.2) and since  $\iota = \dot{q}$ , this equation of motion becomes

$$\left( L_e + L_J + L_J \frac{\dot{q}^2}{2I_0^2} \right) \ddot{q} + R_e \dot{q} + \frac{q}{C_e} = V_e \cos(\omega_m t).$$

We now define the total inductance  $L_t = L_e + L_J$  the participation ratio  $p = L_J / L_t$ , the linear resonance frequency  $\omega_r = 1 / \sqrt{L_t C_e}$  and the quality factor  $Q = \omega_r L_t / R_e$ . This leads to:

$$\ddot{q} + \frac{\omega_r}{Q} \dot{q} + \omega_r^2 q + \frac{p \dot{q}^2 \ddot{q}}{2I_0^2} = \frac{V_e}{L_t} \cos(\omega_m t).$$

We then write  $q(t) = \text{Re}(A(t)e^{i\omega_m t})$ , in which  $A(t)$  is a slowly varying function. so that  $\dot{A} \ll i\omega_m A$ . The equation of motion for such  $A(t)$  is then

$$\dot{A} + \Gamma A - i\Delta_m + i \frac{p\omega_m^3 |A|^2}{4I_0^2} A = -i \frac{V_e}{4\omega_m L_t}$$

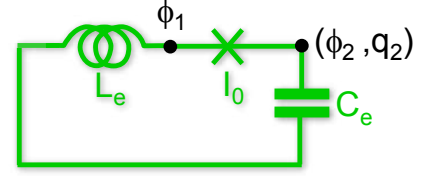
which, with the definitions of the dimensionless parameters  $\Omega$ ,  $\beta$  and  $u$  found in Table 4.1, becomes

$$\frac{du}{d\tau} = -\frac{u}{\Omega} - iu(|u|^2 - 1) - i\sqrt{\beta}.$$

This is equivalent to the general equation of Duffing oscillators (Eq. 4.1). So, despite their different configuration, the series and parallel RLC non-linear resonators behave in a very similar way.

### Hamiltonian

We will now derive the Hamiltonian for this circuit, neglecting dissipation which can be treated as for a linear resonator by introducing a coupling to the electromagnetic environment. We thus simply consider the circuit consisting of the series combination of the inductance  $L_e$ , capacitance  $C_e$ , and Josephson junction of critical current  $I_0$  (whose capacitance is included inside the other circuit elements). We will write the Hamiltonian as a function of the conjugate node variables  $(q_2, \phi_2)$  shown on the right. Denoting  $\phi_1$  the generalized flux across the inductance  $L_e$ , we have



$$H_{CBA} = \frac{\phi_1^2}{2L_e} - E_J \cos\left(\frac{\phi_2 - \phi_1}{\varphi_0}\right) + \frac{q_2^2}{2C_e}.$$

Since the current  $i$  flowing through the inductance and through the junction are identical, we also have

$$i = \frac{\phi_1}{L} = I_0 \sin\left(\frac{\phi_2 - \phi_1}{\varphi_0}\right)$$

yielding an implicit relation  $\phi_1 = g(\phi_2)$  between the two phases. The Hamiltonian thus writes

$$H_{CBA} = \frac{[g(\phi_2)]^2}{2L_e} - E_J \cos\left(\frac{\phi_2 - g(\phi_2)}{\varphi_0}\right) + \frac{q_2^2}{2C_e}.$$

By developing  $g(\phi_2)$  in powers of  $\phi_2$  we can obtain the CBA Hamiltonian to any order of Josephson junction non-linearity. For instance, to fourth order we obtain after some rewriting

$$H_{CBA} = \frac{\phi_2^2}{2L_t} + \frac{q_2^2}{2C_e} - \frac{1}{24} p^3 \frac{\phi_2^4}{L_t \varphi_0^2}.$$

To clarify this Hamiltonian, we will now write it in terms of the creation and annihilation operators, using  $\hat{\phi}_2 = \delta\varphi_0(\hat{a} - \hat{a}^\dagger)$  with  $\delta\varphi_0 = i\sqrt{\hbar Z_e/2}$  and  $Z_e = \sqrt{L/C_e}$

We see that the non-linear term  $\phi_2^4$  once developed will yield products of creation and annihilation operators to various powers. In the rotating wave approximation, we will keep only those with equal annihilation and creation operators; all the others will oscillate at frequencies  $2\omega_r$  or higher. Re-arranging the terms in the Hamiltonian yields finally

$$\hat{H}_{CBA} = \hbar\omega_r\hat{a}^\dagger\hat{a} + \hbar\frac{K}{2}(\hat{a}^\dagger)^2\hat{a}^2 \quad (4.4)$$

where

$$K = -\frac{\pi p^3 \omega_r Z_e}{R_K}$$

is called the Kerr constant. In fact we will even need in the following the Hamiltonian developed to the next order of junction non-linearity

$$\hat{H}_{CBA} = \hbar\omega_r\hat{a}^\dagger\hat{a} + \hbar\frac{K}{2}(\hat{a}^\dagger)^2\hat{a}^2 + \hbar\frac{K'}{3}(\hat{a}^\dagger)^3\hat{a}^3 \quad (4.5)$$

with

$$K' = 2\pi^2 \left( \frac{10p}{3} - 3 \right) p^5 \omega_r \left( \frac{Z_{eq}}{R_K} \right)^2.$$

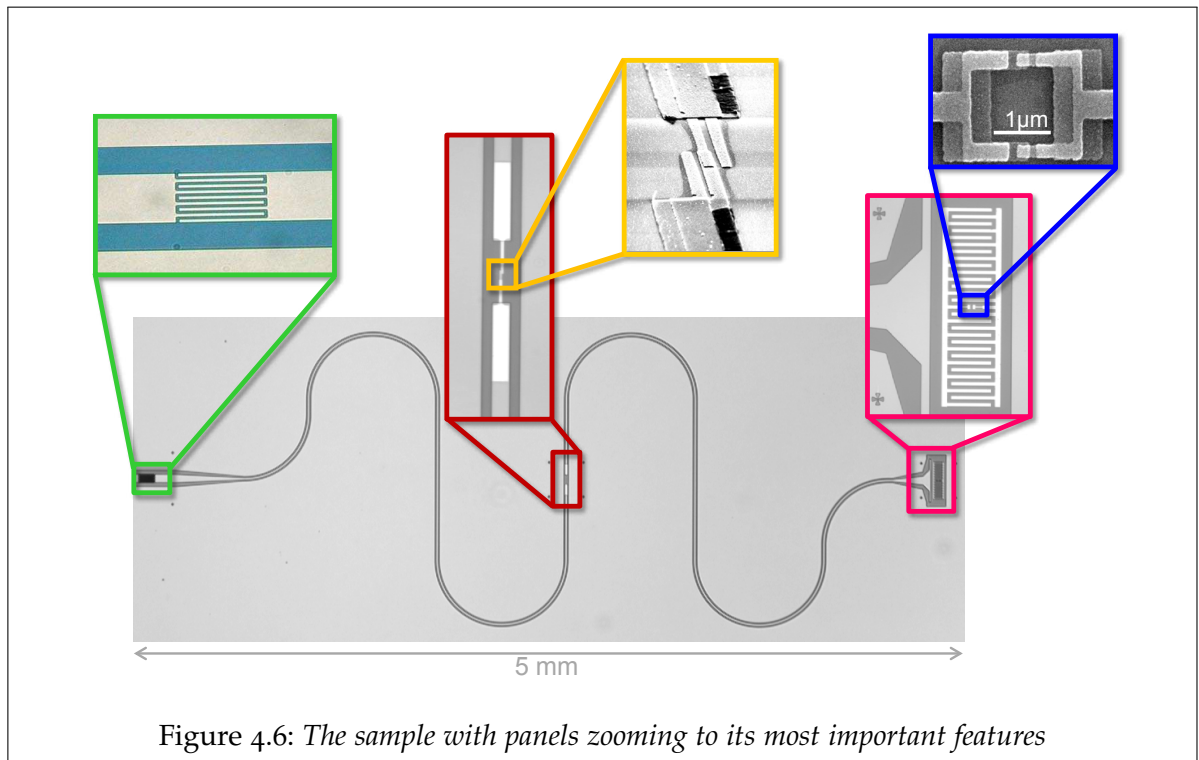
## 4.3 EXPERIMENTAL IMPLEMENTATION

### 4.3.1 THE SAMPLE

As shown in Fig. 4.6 the sample consists in a  $\lambda/2$  CPW resonator with a Josephson junction inserted in its middle to make it non-linear. The resonance frequency is  $\omega_r/2\pi \approx 6.45$  GHz, In the same way as in the former chapter, on one side of the resonator we fabricated a transmon (green rectangle), consisting in a split Cooper-pair box (orange rectangle) and a large shunt capacitor (blue rectangle). The other side of the resonator is connected to the input line through a coupling capacitor (red rectangle), which sets the quality factor  $Q = Q_c \approx 700$  which corresponds to a moderately large  $\kappa/2\pi \approx 9.2$  MHz bandwidth, a good compromise between the degradation of the relaxation time  $T_1$  due to the Purcell effect (2.3.1) and a readout fast enough compared to  $T_1$ .

The resonator is fabricated on a 120 nm-thick niobium film with the same process described in 2.1.4.1. The transmon and the Josephson junction of the CBA are patterned at the same time by e-beam lithography and double-angle evaporation of two aluminum thin-films, the first one being oxidized to form the junction tunnel barrier.

The sample is then glued on a microwave printed-circuit board made out of TMM10 ceramics. The whole is enclosed in a copper box and thermally anchored to the mixing chamber of a dilution refrigerator at typically 20 mK.



#### 4.3.2 MEASUREMENT SETUP

The measurement setup is shown in Fig. 4.7. As in the former chapter, two kinds of microwave signals are sent to the sample through the same input line:

- measurement pulses with voltage  $V_m$  (in green). The powers  $P_m$  given in this chapter are arbitrarily referred to 0 dBm at the input of the dilution refrigerator. The power of these pulses is controlled by a tunable attenuator which is a key element to acquire the so-called S-curves which will be discussed below.
- pulses to resonantly control the TLS state with voltage  $V_d$  (in pink).

Both of them are shaped in a DC-coupled mixer: a microwave tone generated by an Anritsu MG3692 microwave generator is mixed with the DC pulses generated by an arbitrary waveform generator Tektronix AWG5004A. These two microwave signals are combined and sent to the input line of the refrigerator which contains several filters and attenuators (77 dB in total), thermalized at the successive temperature stages.

The signal reflected on the sample is separated from the input signal by a cryogenic circulator. It is then routed through several isolators and a 4–8 GHz bandpass filter, to a cryogenic amplifier (CITCRYO1-12 from Caltech) with 38 dB gain and noise temperature  $T_N = 4$  K. The output signals are then amplified at room temperature with a total gain of 56 dB, and finally mixed down using a I/Q mixer with a local oscillator synchronous with the microwave tone used for generating the measurement microwave pulses. The resulting  $I_D$  and  $Q_D$  quadratures are filtered, amplified, sampled by an Acqiris DC282 fast digitizer and transferred to a computer that processes them.

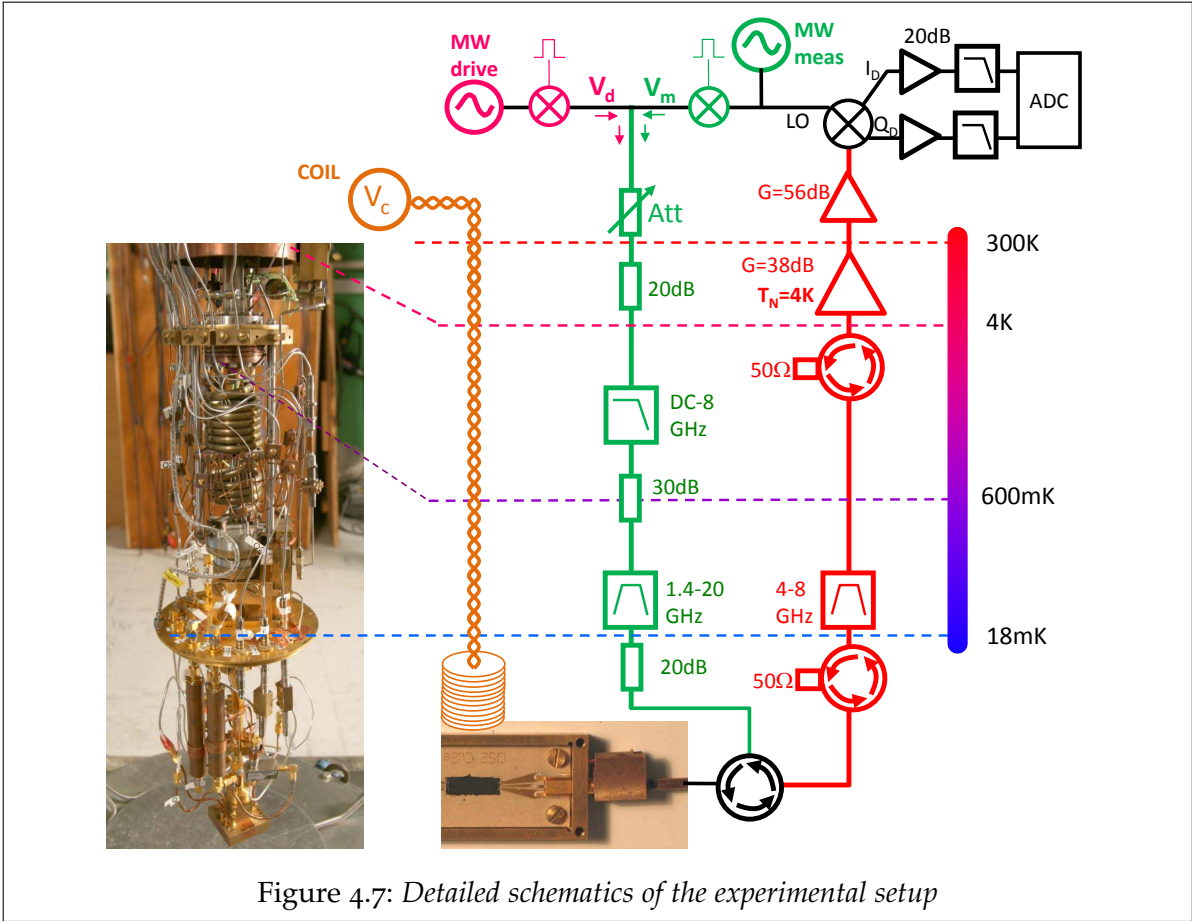


Figure 4.7: Detailed schematics of the experimental setup

A superconducting coil is screwed on the copper box containing the sample to vary the flux. A very-low cutoff RL filter formed by the coil itself and a 50  $\Omega$  resistor filters this line to reduce the thermal noise coming from room-temperature.

#### 4.4 EXPERIMENTAL CHARACTERIZATION OF THE CBA

Before operating the non-linear resonator as a single-shot detector for the qubit, we characterize its behaviour alone, by detuning the qubit far away from it. We first study its bistability and hysteresis as a function of the detuning  $\Omega$  and amplitude  $\beta$ .

In the vicinity of the bifurcation point  $\beta^+$  the transition  $\bar{B} \rightarrow B$  can occur with a finite probability. Indeed, the resonator acts as a semi-classical oscillator which may be excited by thermal or quantum fluctuations and jump to the  $B$  state. We discuss in this section how to measure the probability  $p_B$  of switching to the  $B$  state in this region, and so-called S-curves  $p_B(\beta)$ , which determine the sensitivity of the CBA.

##### 4.4.1 FREQUENCY RESPONSE

At very low measurement power  $P_m$  the resonator's response (blue curve in Fig. 4.8) is the one of an over-coupled linear resonator: a constant amplitude, and a phase shift of  $2\pi$  symmetric around the resonance frequency. This low power measurement

allows to determine the resonator linear resonance frequency  $\omega_r/2\pi = 6.4535$  GHz and its quality factor  $Q = Q_c = 670$ . Comparing this resonance frequency with the one of the bare resonator, we determine the junction critical current  $I_0 = 750$  nA, in good agreement with the  $I_0$  of other junctions fabricated with the same process.

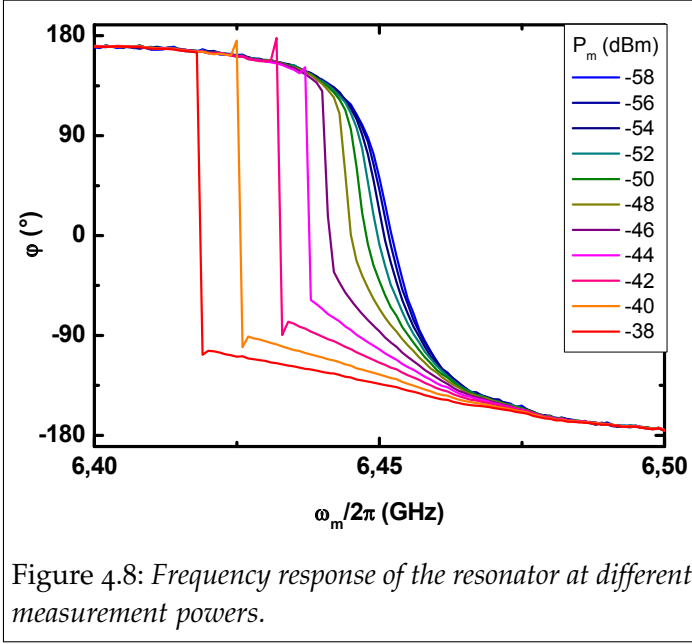


Figure 4.8: Frequency response of the resonator at different measurement powers.

When raising the power  $P_m$  the phase of the reflected signal starts to show some asymmetry and a higher slope (dark blue to purple curves in Fig. 4.8). For even higher powers a sudden jump happens signalling the bifurcation from  $\bar{B}$  to  $B$  state. This jump constitutes the first signature of the resonator bistability. The lowest power at which this jump happens corresponds to the bifurcation point  $\beta^+$ , and the higher the power is raised, the lower is the frequency at which this jump appears, as predicted by theory.

#### 4.4.2 BISTABILITY AND HYSTERESIS: THE $(\Omega, \beta)$ DIAGRAM

According to JBA theory, there is a region  $\Omega > \sqrt{3}$  and  $\beta^-(\Omega) < \beta < \beta^+(\Omega)$  in the  $(\Omega, \beta)$  plane where the transitions  $\bar{B} \leftrightarrow B$  are hysteretic. To find this region we perform the experiment shown in Fig. 4.9, which consists in sending a microwave pulse with a slow triangular envelope of 1 ms duration and measuring the phase of the reflected signal. The first part of the triangle corresponds to a growing signal: when the power reaches the bifurcation point  $\beta^+$ , the transition  $\bar{B} \rightarrow B$  occurs and a jump in the phase is observed. The second part of triangle corresponds to a decreasing signal: when the power reaches  $\beta^-$ , the transition  $B \rightarrow \bar{B}$  occurs and the phase shows a jump. The difference between the reflected phases measured while the signal is growing and decreasing –the hysteretic region– is shown in the bottom panel of Fig. 4.9. In this panel the frequency dependence of the jumps in phase corresponding to the bifurcation is compared with the theoretical curves  $\beta^+(\Omega)$  and  $\beta^-(\Omega)$ . To rescale these curves in the signal units  $s(\sqrt{mW})$  at the input of the dilution refrigerator, we have used

- the Kerr constant  $K/2\pi = 625$  kHz, whose value was experimentally determined using the procedure explained in 4.7.1.3
- the total attenuation from the input of the dilution refrigerator to the input of the CBA. We used for this attenuation the value 79.3 dB compatible with the known attenuation of our setup.

The slight reduction of the hysteretic region in the experiment, as compared to the theory, is likely to be due to the activation of the  $\bar{B} \leftrightarrow B$  transitions by thermal or



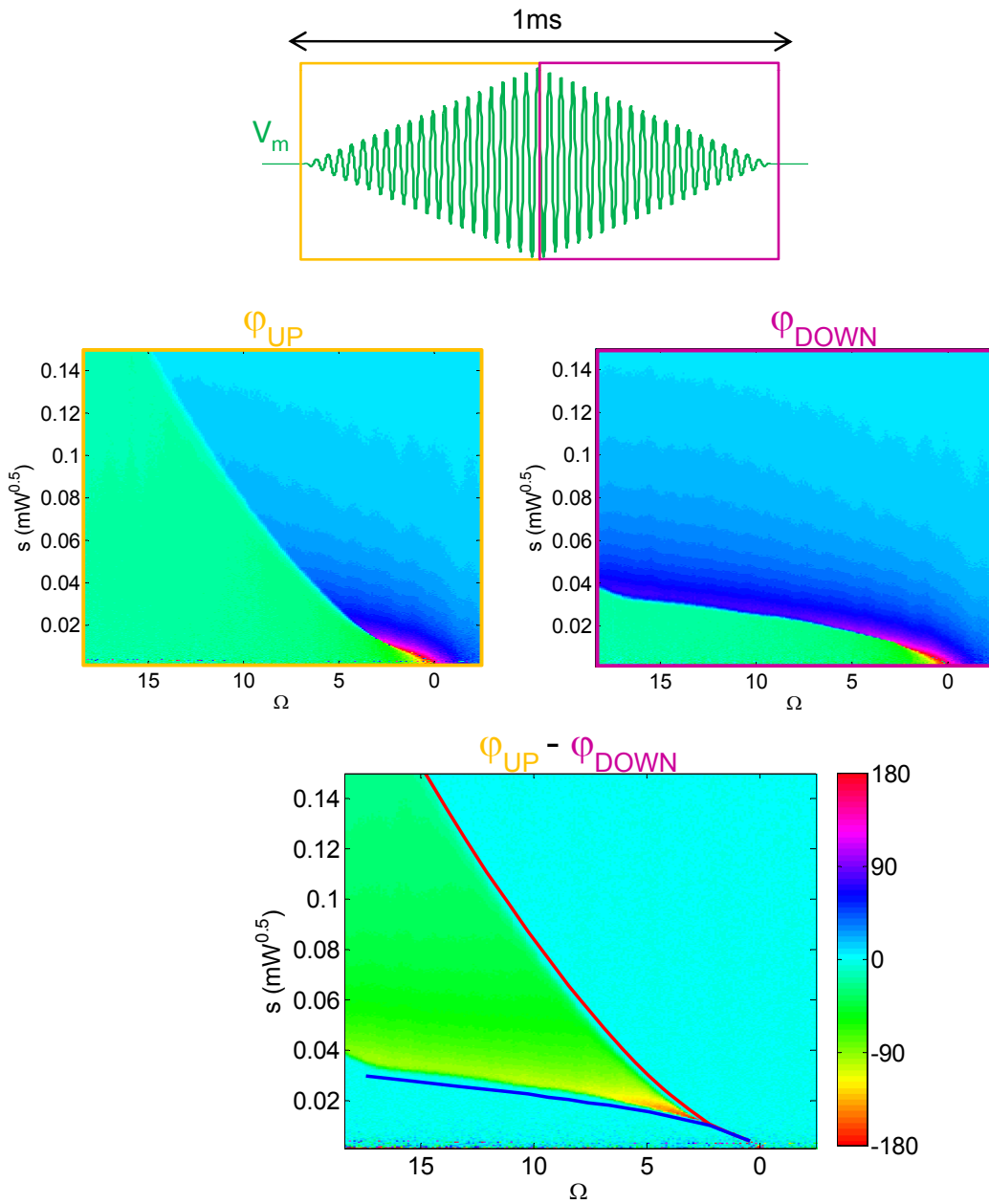


Figure 4.9: Experimental characterization of CBA hysteresis. A microwave pulse with a slow triangular envelope of 1 ms is sent to the CBA and we measure the phase of the reflected signal. The first part of the triangle (orange rectangle) corresponds to a growing signal: when the power reaches the bifurcation point  $\beta^+$ , the transition  $\bar{B} \rightarrow B$  occurs and a jump in the phase is observed. The second part of triangle (purple rectangle) corresponds to a decreasing signal: when the power reaches  $\beta^-$ , the transition  $B \rightarrow \bar{B}$  occurs and the phase shows a jump. The difference between the phases observed in these two experiments (bottom panel) shows the hysteretic region. The agreement of the theoretical bifurcation curves  $\beta^+(\Omega)$  and  $\beta^-(\Omega)$  (in red and blue respectively) with the experimental data is rather good.

quantum fluctuations as explained below.

#### 4.4.3 TRANSITIONS BETWEEN $\bar{B}$ AND $B$ : THE S-CURVES

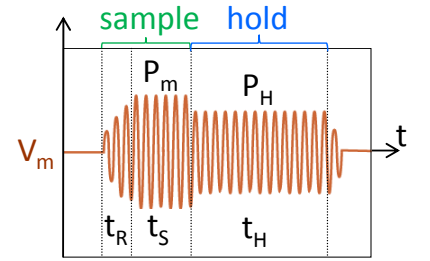
The CBA behaves as a semi-classical oscillator which may be excited by the thermal noise or by the quantum fluctuations which become dominant at very low temperatures. Due to these fluctuations, the switching from  $\bar{B}$  to  $B$  is a stochastic phenomenon occurring in a narrow region just below  $\beta^+$ . Since it determines the sensitivity of the CBA to the changes in parameters a good understanding of this narrow region is of critical importance for operating our resonator as qubit readout.

In this section we first explain how we measure the probability  $p_B$  of being in the  $B$  state and how the pulses are shaped to make profit of the resonator hysteresis. We then present the experimental data of  $p_B$  as a function of the measurement power –the so-called *S-curves*– and we analyze their width comparing them to simulations.

##### 4.4.3.1 The shape of the measurement pulse

To operate the resonator as a sample-and-hold detector, a microwave pulse with an appropriate shape is used :

- The pulse rises linearly in a time  $t_R$  similar to the resonator rise-time  $\kappa^{-1}$ .
- A short plateau of duration  $t_S$  during which the power reaches its maximum value  $P_m$ , which is typically in the vicinity of the bifurcation point, yielding –or not– a transition  $\bar{B} \rightarrow B$ .
- A long hold plateau of duration  $t_H$ , with a power slightly lower (typically  $P_H = .85P_m$ ) corresponding to  $\beta^- < \beta < \beta^+$  such that the resonator state does not change. The measurement is performed in a time window during this part of the pulse.



##### 4.4.3.2 Measuring $p_B$ : the probability of $B$ state

The transition from  $\bar{B}$  to  $B$  is not infinitely sharp: we therefore need to measure the probability  $p_B$  of finding the resonator in its  $B$  state during the hold plateau –more rigorously, the frequency of occurrence of  $B$ . Depending on which state ( $\bar{B}$  or  $B$ ) the resonator is, the demodulated the field components  $\bar{I}_D$  and  $\bar{Q}_D$  averaged over a time-window in the hold plateau are different. Therefore, two decision regions in the  $(\bar{I}_D, \bar{Q}_D)$  plane corresponding to the  $\bar{B}$  and  $B$  states can be defined. A simplification consists in digitally transforming the  $(\bar{I}_D, \bar{Q}_D)$  plane so that the region  $\bar{I}_D < 0$  corresponds to  $\bar{B}$  and  $\bar{I}_D > 0$  corresponds to  $B$ . The automated calibration procedure to do so proceeds in three steps:

- First,  $P_m$  is ramped to find the specific value  $P_{50}$  at which  $p_B = 1/2$ . A simple algorithm for finding this point consists in measuring the total variance of

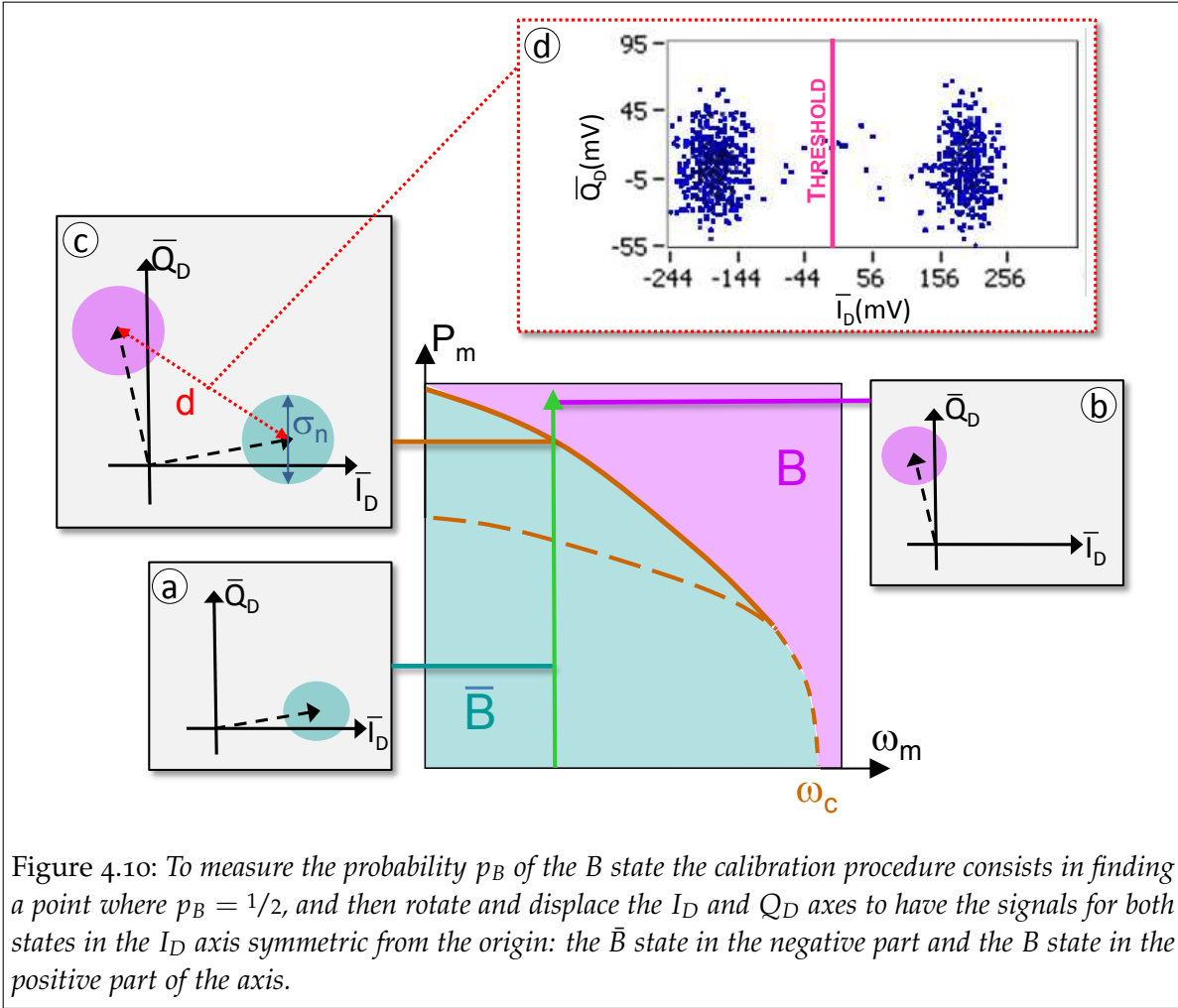


Figure 4.10: To measure the probability  $p_B$  of the  $B$  state the calibration procedure consists in finding a point where  $p_B = 1/2$ , and then rotate and displace the  $I_D$  and  $Q_D$  axes to have the signals for both states in the  $I_D$  axis symmetric from the origin: the  $\bar{B}$  state in the negative part and the  $B$  state in the positive part of the axis.

the signal  $\sigma^2 = \sigma_I^2 + \sigma_Q^2$  where  $\sigma_I^2$  and  $\sigma_Q^2$  are the variances of the  $\bar{I}_D$  and  $\bar{Q}_D$  components. The total variance is maximum at  $P_{50}$ , indeed: when the resonator is always in the  $\bar{B}$  state or in the  $B$  state (Fig. 4.10a and b), the variance  $\sigma = \sigma_n$  is related to the noise, but when both states are present (Fig. 4.10c), the variance includes the same component  $\sigma_n$ , plus a component  $d$  due to the separation between the states  $d$ . If the states are well separated,  $d \gg \sigma_n$  leading to a clear maximum in the variance at  $P_{50}$ .

- Then,  $P_m$  is set to  $P_{50}$ , and the signal is digitally displaced and rotated in the IQ plane to place the regions corresponding to the  $\bar{B}$  and  $B$  states aligned along the  $\bar{I}_D$  axis and symmetric around zero (Fig. 4.10d).
- To determine which of the regions corresponds to  $\bar{B}$  and which to  $B$ , the power is slightly increased: if the average  $\bar{I}_D$  grows, a rotation of  $\pi$  is performed, to place  $B$  on the positive part of the  $\bar{I}_D$  axis.

After this calibration with  $P_m$  set to  $P_{50}$ , the 2D histogram of the  $\bar{I}_D$  and  $\bar{Q}_D$  is similar to the one shown in Fig. 4.10d, where the measurements are grouped in two families corresponding to the  $\bar{B}$  and  $B$  states.  $p_B$  is measured by counting the number of traces with  $\bar{I}_D$  larger or smaller than the threshold  $\bar{I}_D = 0$ .

#### 4.4.3.3 S-curves: experimental data

In order to determine the width of the  $\bar{B} \rightarrow B$  transition we measure  $p_B(P_m)$  by varying the attenuation of the tunable attenuator. At very low  $P_m$ , we start by observing  $p_B \simeq 0$ . In the vicinity of the bifurcation point the probability starts growing (Fig. 4.11). Once the power corresponding to  $\beta^+$  is reached,  $p_B \simeq 1$ . The resulting curve has the characteristic shape of an S and is thus nicknamed S-curve.

To confirm that this S-curve corresponds indeed to an evolution of the probability of two well separated states, and not to some single-valued signal crossing the threshold of detection, we acquire some time traces (Fig. 4.11 heavily filtered with a 10 MHz low-pass filter), which show two clearly different families of trajectories. Correspondingly, the histograms of the  $I$  component of the signal show two distinct peaks corresponding to the states  $\bar{B}$  and  $B$  and nothing in between.

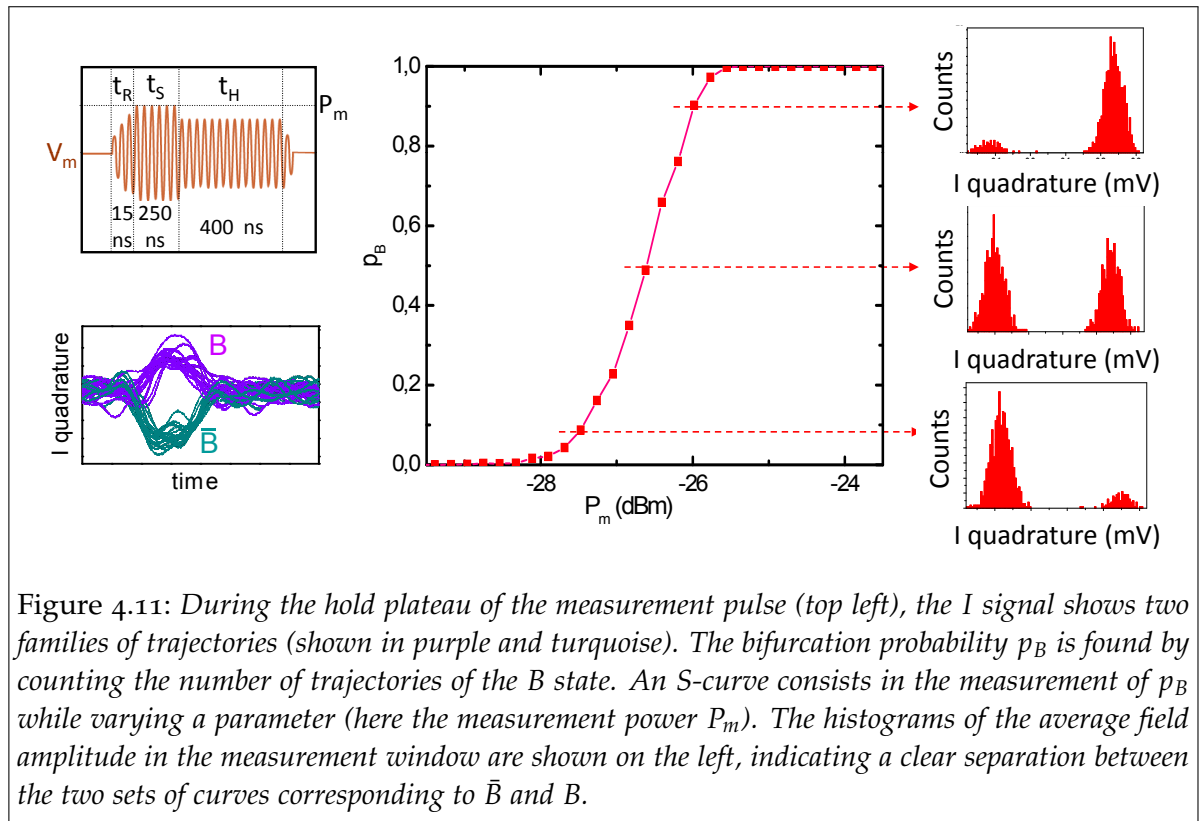


Figure 4.11: During the hold plateau of the measurement pulse (top left), the  $I$  signal shows two families of trajectories (shown in purple and turquoise). The bifurcation probability  $p_B$  is found by counting the number of trajectories of the  $B$  state. An S-curve consists in the measurement of  $p_B$  while varying a parameter (here the measurement power  $P_m$ ). The histograms of the average field amplitude in the measurement window are shown on the left, indicating a clear separation between the two sets of curves corresponding to  $\bar{B}$  and  $B$ .

#### 4.4.3.4 Theoretical results on the escape process

The transition from  $\bar{B}$  to  $B$  in the vicinity of the bifurcation point  $\beta^+$  may be activated by thermal noise and quantum fluctuations, yielding some probability to escape from the attractor corresponding to the  $\bar{B}$  solutions and to reach the  $B$  state. Several authors have studied theoretically the dynamics of these escape processes for the Duffing oscillator in the adiabatic limit<sup>135,136</sup>. Unfortunately to our knowledge no theory deals with the actual situation in our experiment, which is far from being adiabatic because the measurement pulse raises very quickly. Therefore we performed numerical simulations of the escape process to compare them with experimental data.

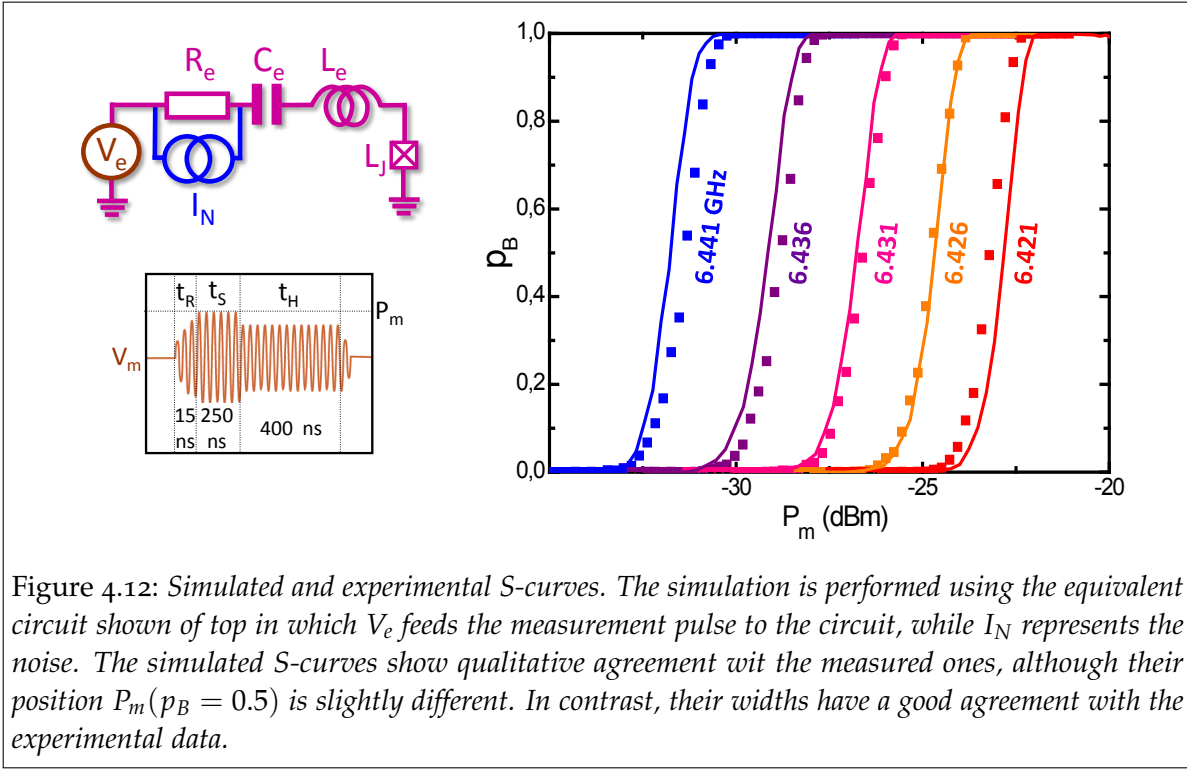


Figure 4.12: Simulated and experimental  $S$ -curves. The simulation is performed using the equivalent circuit shown of top in which  $V_e$  feeds the measurement pulse to the circuit, while  $I_N$  represents the noise. The simulated  $S$ -curves show qualitative agreement with the measured ones, although their position  $P_m(p_B = 0.5)$  is slightly different. In contrast, their widths have a good agreement with the experimental data.

However for shedding some light on the switching process we present the theory of adiabatic escape for CBA in Appendix A.

#### 4.4.3.5 $S$ -curves: numerical simulations

Since the analytical expressions are only valid for the adiabatic limit, the only way to have a prediction for the non-adiabatic measurement pulses which are used in the experiment is to perform a numerical simulation of the switching process.

The circuit we simulate is sketched in Fig. 4.12. The equation of motion of the charge stored in the capacitor plates is (Eq. 4.3):

$$(L_e + L_J(\dot{q})) \ddot{q} + R_e \dot{q} + \frac{q}{C_e} = V_e(t) \cos(\omega_m t) + R_e I_N(t).$$

where  $V_m(t)$  is the envelope of the measurement pulse, which is slow compared to  $\omega_m$ . Moving to dimensionless units for the time and the charge:

$$\begin{aligned} \tau &= \omega_r t \\ \zeta &= \omega_r q / I_0, \end{aligned}$$

we obtain

$$\left(1 - p + \frac{p}{\sqrt{1 - \zeta^2}}\right) \partial_\tau^2 \zeta + \frac{\partial_\tau \zeta}{Q} + \zeta = \tilde{V}_e(\tau) \cos\left(\left(1 - \frac{\Omega}{2Q}\right) \tau\right) + \tilde{V}_N(\tau)$$

with  $\tilde{V}_N(\tau) = R_e I_N(\tau / \omega_r) / I_0 \omega_r L_t$  and  $\tilde{V}_e(\tau) = V_e(\tau / \omega_r) / I_0 \omega_r L_t$ . This second-order differential equation can be written as a system of two first-order differential equations

tions:

$$\begin{aligned}\partial_\tau \zeta &= \eta \\ \partial_\tau \eta &= \frac{1}{1-p+p/\sqrt{1-\eta^2}} \left[ -\frac{\eta}{Q} - \zeta + \tilde{V}_N(\tau) + \tilde{V}_e(\tau) \cos \left( \left(1 - \frac{\Omega}{2Q}\right) \tau \right) \right]\end{aligned}$$

These equations are simulated numerically. The realizations of the Gaussian noise  $\tilde{V}_N(n\Delta\tau)$  are generated for each step  $n$  using the Box-Muller method<sup>137</sup>. This method allows to generate two Gaussian random variables by transforming two computer-generated pseudo-random variables with a uniform distribution. The differential equations are then numerically solved in discrete time steps  $\Delta\tau = 2\pi/501$  using the simple Euler method, which yields the following recursive relations:

$$\begin{aligned}\zeta_{n+1} &= \zeta_n + \eta_n \Delta\tau \\ \eta_{n+1} &= \eta_n + \frac{\Delta\tau}{1-p+p/\sqrt{1-\eta_n^2}} \left[ -\frac{\eta_n}{Q} - \zeta_{n+1} + \underbrace{\tilde{V}_e(n\Delta\tau) \cos \left( \left(1 - \frac{\Omega}{2Q}\right) \tau \right)}_{\text{measurement pulse}} + \underbrace{\tilde{V}_N(n\Delta\tau)}_{\text{noise}} \right]\end{aligned}$$

In Fig. 4.12 the S-curves simulated with the parameters of the sample are compared to the actual experimental curves. The main difference is the position of the curves, which for a yet unknown reason is not well reproduced in the simulation. However, their widths, which play a critical role since they determine the sensitivity of the bifurcation amplifier, are in good agreement with the experimental data.

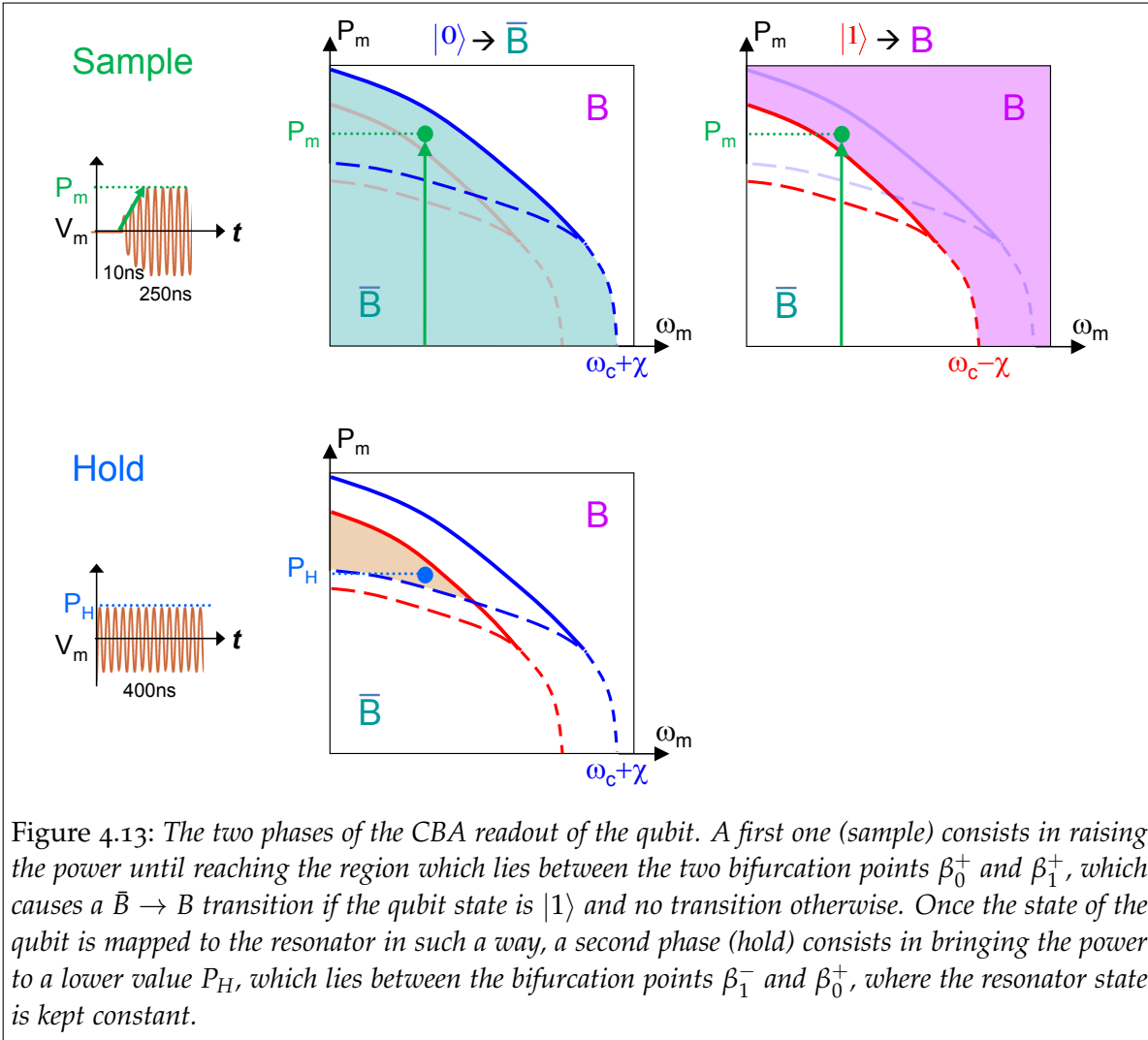
## 4.5 OPERATING THE CBA FOR QUBIT READOUT

### 4.5.1 MAPPING THE QUBIT STATE TO THE RESONATOR

To use the CBA as a detector for the qubit a last ingredient is needed: a procedure to quickly map the qubit states  $|0\rangle$  or  $|1\rangle$  to the resonator states  $\bar{B}$  or  $B$  respectively. To do so we use the cavity pull, which shifts the bifurcation curves  $\beta^\pm(\omega_m)$  by  $+\chi$  or  $-\chi$ , yielding the bifurcation curves  $\beta_0^\pm(\omega_m)$  and  $\beta_1^\pm(\omega_m)$  for qubit states  $|0\rangle$  or  $|1\rangle$  respectively, as shown in Fig. 4.13. To exploit this shift in frequency to map the qubit state on the resonator, we follow these steps:

- A value of  $\Omega$  which is high enough to produce bifurcation is selected. The power of the measuring pulse is first quickly raised to a value  $P_m$  which lies below  $\beta_0^+$  and above  $\beta_1^+$ , and kept at this value for some time to allow the CBA dynamics to develop. If the qubit state is  $|1\rangle$ , the power is above  $\beta_1^+$ , and thus the resonator ends in the  $B$  state. Conversely, if the qubit state is  $|0\rangle$ , the power is below  $\beta_0^-$ , and thus the resonator stays in the  $\bar{B}$  state.

- The power is lowered to a value  $P_H$  which lies below  $\beta_1^+$  but above  $\beta_0^-$ , so that the resonator undergoes no transition. This power is hold as long as needed to average the resonator signal and discriminate with accuracy its state.



#### 4.5.2 CHARACTERIZATION OF THE QUBIT PARAMETERS

Using this technique, we perform the spectroscopy of the transmon with the sequence of pulses sketched in Fig. 4.14: a first long pulse whose frequency  $\omega_d$  is scanned saturates the  $|0\rangle \rightarrow |1\rangle$  transition. Then, a CBA measurement pulse detects the transmon state. When  $\omega_d \simeq \omega_{01}$ , the population of  $|1\rangle$  raises, which translates to a higher  $p_B$  as shown in Fig. 4.14. Using this protocol, we performed a spectroscopy while varying the flux threading the transmon. With a similar protocol, but with an auxiliary pulse which saturates the  $|0\rangle \rightarrow |1\rangle$  transition, we perform a spectroscopy of the second energy level of the transmon. The lower left panel of Fig. 4.14 shows the position of these two spectral lines as a function of the flux. By fitting them with the expected dependence, we obtain the characteristic energies of the system, namely the Josephson energy  $E_J = 24.9$  GHz and the charging energy  $E_C = 1.05$  GHz.



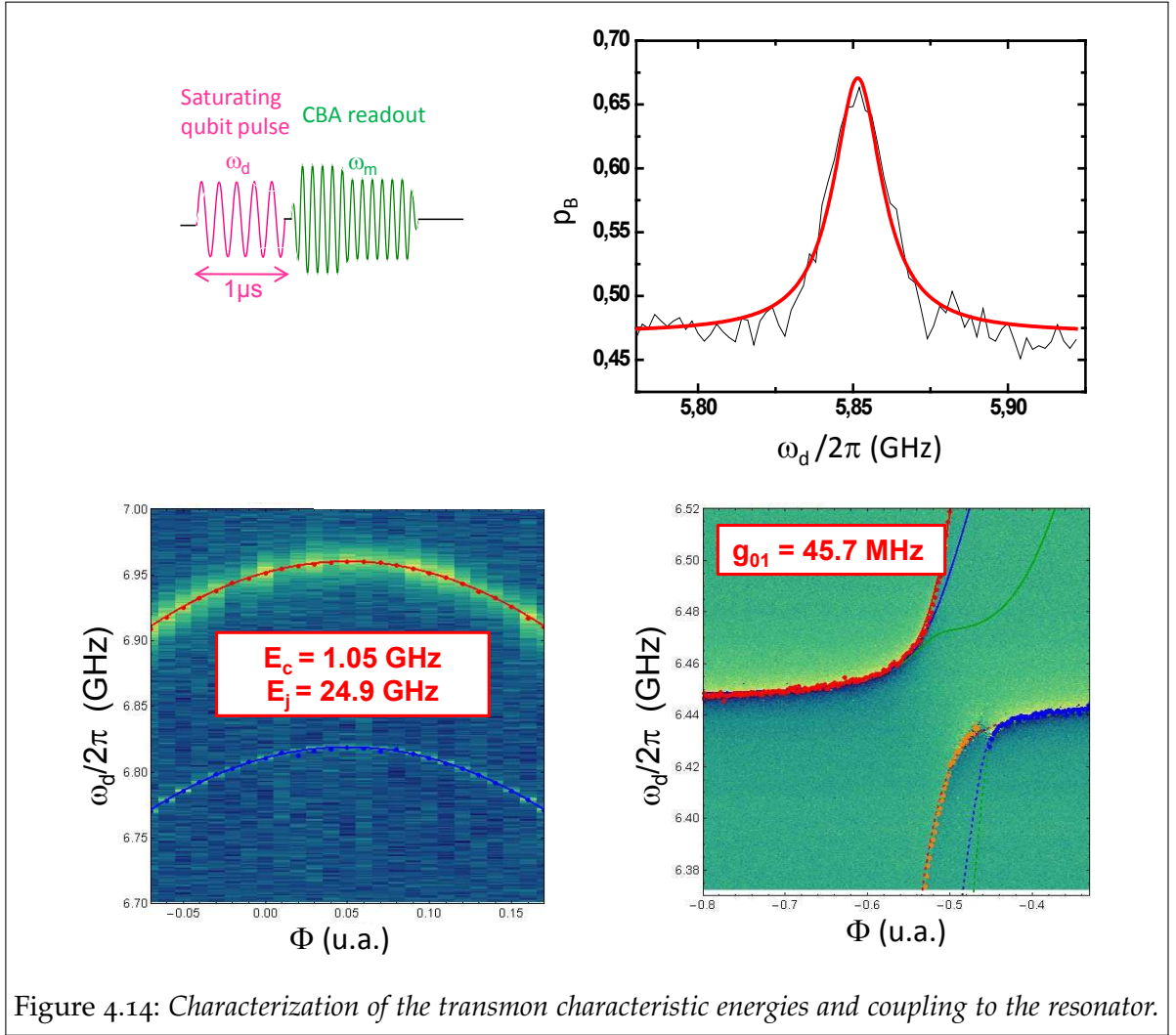


Figure 4.14: Characterization of the transmon characteristic energies and coupling to the resonator.

To characterize the qubit-resonator coupling constant, we characterize the phase of the reflected signal as a function of the frequency and the flux through the transmon, in the area of the anti-crossing. This yields the data of the lower-right panel of Fig. 4.14, which is fitted yielding  $g/2\pi = 45.7 \pm 3$  MHz.

#### 4.5.3 HIGH FIDELITY READOUT

In this section we present the highest fidelity we observed. We start by presenting the S-curves for the  $|0\rangle$  and  $|1\rangle$  qubit states, which show a maximum fidelity of 88%. We then analyze the remaining 12% which is mainly due to relaxation and we extract an *effective measurement time* which gives some insight on the CBA measurement dynamics. We finally present a further trick which allows to improve the fidelity up to 94% by shelving the  $|1\rangle$  state to  $|2\rangle$ , and present the variation of the fidelities and lifetimes of the qubit with detuning, which show that CBA allows to have >80% fidelity in a large span of qubit frequencies.

#### 4.5.3.1 Maximum fidelity and contrast

Fig. 4.15 shows the S curves  $S_{\omega_m}^0$  and  $S_{\omega_m}^1$  acquired when the qubit is in its  $|0\rangle$  and  $|1\rangle$  states respectively for  $\Delta/2\pi = 380$  MHz and  $\Delta_m/2\pi = 17$  MHz. For the  $S_{\omega_m}^1$  the qubit is excited to  $|1\rangle$  by a resonant  $\pi$  pulse of length  $t_\pi \simeq 15$  ns. The contrast, defined as the maximum difference between both curves, reaches 87% for a measurement frequency  $\omega_m = \omega_c - 2\pi \times 17$  MHz.

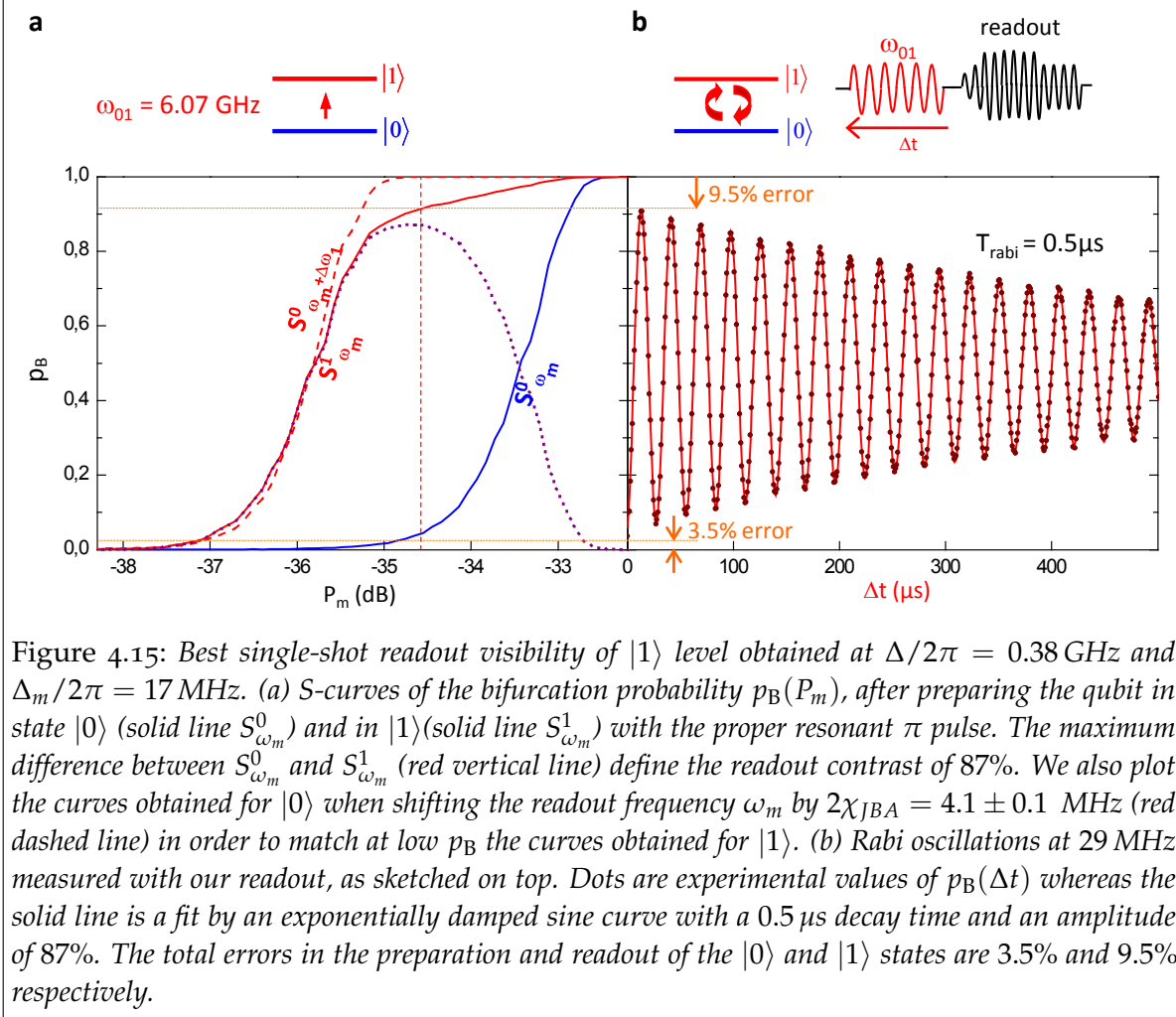


Figure 4.15: Best single-shot readout visibility of  $|1\rangle$  level obtained at  $\Delta/2\pi = 0.38$  GHz and  $\Delta_m/2\pi = 17$  MHz. (a) S-curves of the bifurcation probability  $p_B(P_m)$ , after preparing the qubit in state  $|0\rangle$  (solid line  $S_{\omega_m}^0$ ) and in  $|1\rangle$  (solid line  $S_{\omega_m}^1$ ) with the proper resonant  $\pi$  pulse. The maximum difference between  $S_{\omega_m}^0$  and  $S_{\omega_m}^1$  (red vertical line) define the readout contrast of 87%. We also plot the curves obtained for  $|0\rangle$  when shifting the readout frequency  $\omega_m$  by  $2\chi_{JBA} = 4.1 \pm 0.1$  MHz (red dashed line) in order to match at low  $p_B$  the curves obtained for  $|1\rangle$ . (b) Rabi oscillations at 29 MHz measured with our readout, as sketched on top. Dots are experimental values of  $p_B(\Delta t)$  whereas the solid line is a fit by an exponentially damped sine curve with a  $0.5 \mu s$  decay time and an amplitude of 87%. The total errors in the preparation and readout of the  $|0\rangle$  and  $|1\rangle$  states are 3.5% and 9.5% respectively.

To interpret the power separation between the S-curves, we search the measurement frequency  $\omega_m + \Delta\omega_1$  that makes  $S_{\omega_m+2\chi_{JBA}}^0$  coincide with  $S_{\omega_m}^1$  at low bifurcation probability. Since the difference between  $S_{\omega_m}^0$  and  $S_{\omega_m}^1$  comes from the qubit cavity pull,  $2\chi_{JBA}$  is an indirect determination of the cavity pull  $2\chi$ . And indeed  $2\chi_{JBA}/2\pi = 4.1$  MHz, in good agreement with the value  $2\chi/2\pi = 4.35$  MHz calculated from the experimental parameters. At high  $p_B$  however the two S-curves do not coincide, but  $S_{\omega_m}^1$  has some slope while  $S_{\omega_m+2\chi_{JBA}}^0$  has reached  $p_B = 1$ . This can be explained taking into account that the qubit is subject to relaxation during the readout, and therefore  $S_{\omega_m}^1$  is a linear combination of  $S_{\omega_m+2\chi_{JBA}}^0$  and  $S_{\omega_m}^0$ , the latter weighted by the population which has relaxed before the resonator reaches its final state and the readout is finished. Actually, this factor is the dominant source of errors of this

readout method.

### *Qubit relaxation during the measurement*

We used a measurement pulse with  $t_R = 15$  ns,  $t_S = 250$  ns and  $t_H = 700$  ns, these values being experimentally optimized for maximum contrast. Although  $t_S$  is of the same order of magnitude as  $\Gamma_1^{-1}$ , the observed relaxation-induced loss of contrast is rather low, which may seem surprising.

To study further the qubit relaxation during the measurement we acquired a set of  $S_{\omega_m}^{\rho_{ee}}$  where  $\rho_{ee}$  is the population of the excited state  $|1\rangle$  at the beginning of the readout pulse. We start exciting the qubit to  $|1\rangle$  with a  $\pi$  pulse resonant to its transition frequency. We then wait for a time  $\Delta t$  during which the population of the excited state decreases as  $\rho_{ee}(\Delta t) = \exp(-\Gamma_1 \Delta t)$  before the readout pulse is applied. The resulting S-curves can be fitted with a linear combination

$$S_{\mathbf{f}}^{\rho_{ee}} \equiv \rho'_{ee}(\Delta t) S_{\omega_m + 2\chi_{JBA}}^0 + [1 - \rho'_{ee}(\Delta t)] S_{\omega_m}^0$$

where  $\rho'_{ee}(\Delta t)$  is the *effective population* of the excited state seen by the readout. Comparing the population *before* the readout  $\rho_{ee}$  and the population seen by the readout  $\rho'_{ee}$  we can define an *effective readout time*  $t_M$  so that the population seen by the readout after  $\Delta t$  is the same than the bare population after  $t_M + \Delta t$ . As shown in Fig. 4.16 this process yields  $t_M = 53$  ns for  $\Delta = 360$  MHz. This same result was found for a much larger detuning of 700 MHz, while for  $\Delta = 200$  MHz the readout time was of only  $t_M = 38$  ns.

This reveals an interesting property of our readout: when the qubit is in state  $|1\rangle$ , the JBA bifurcates with a high probability, implying that all bifurcation events occur at the very beginning of the readout pulse (instead of being distributed exponentially during  $t_S$ ). We nevertheless keep  $t_S = 250$  ns because the bifurcation process itself needs such a duration to develop properly.

#### 4.5.3.2 *Improving fidelity with $|1\rangle \rightarrow |2\rangle$ shelving*

Since the qubit relaxation during readout account for a large part of readout errors, we implemented a technique that protects the qubit against relaxation in order to further increase the readout contrast. This technique consists in transferring all the population of state  $|1\rangle$  into the next excited state of the transmon  $|2\rangle$  making profit of the very low decay rate from  $|2\rangle$  to  $|0\rangle$ , which comes from the vanishingly-small matrix element  $\langle 0 | \hat{n} | 2 \rangle$  of the transmon (see 2.2.4). With this technique, the relaxation to  $|0\rangle$  can only happen in two ways: during the short time during which the  $1 \rightarrow 2$  excitation takes place, or afterwards, relaxing first from  $|2\rangle$  to  $|1\rangle$  and then to  $|0\rangle$ , a double relaxation process which takes more time. Therefore, this technique, analogous to electron shelving in atomic physics, and which has been already used with other Josephson qubits<sup>5</sup>, leads to a decrease in the overall relaxation during the readout.

To implement this technique a  $\pi$  pulse resonant to the  $1 \rightarrow 2$  transition and with a length of typically 15 ns is sent just before the readout pulse. This yields the S-curve

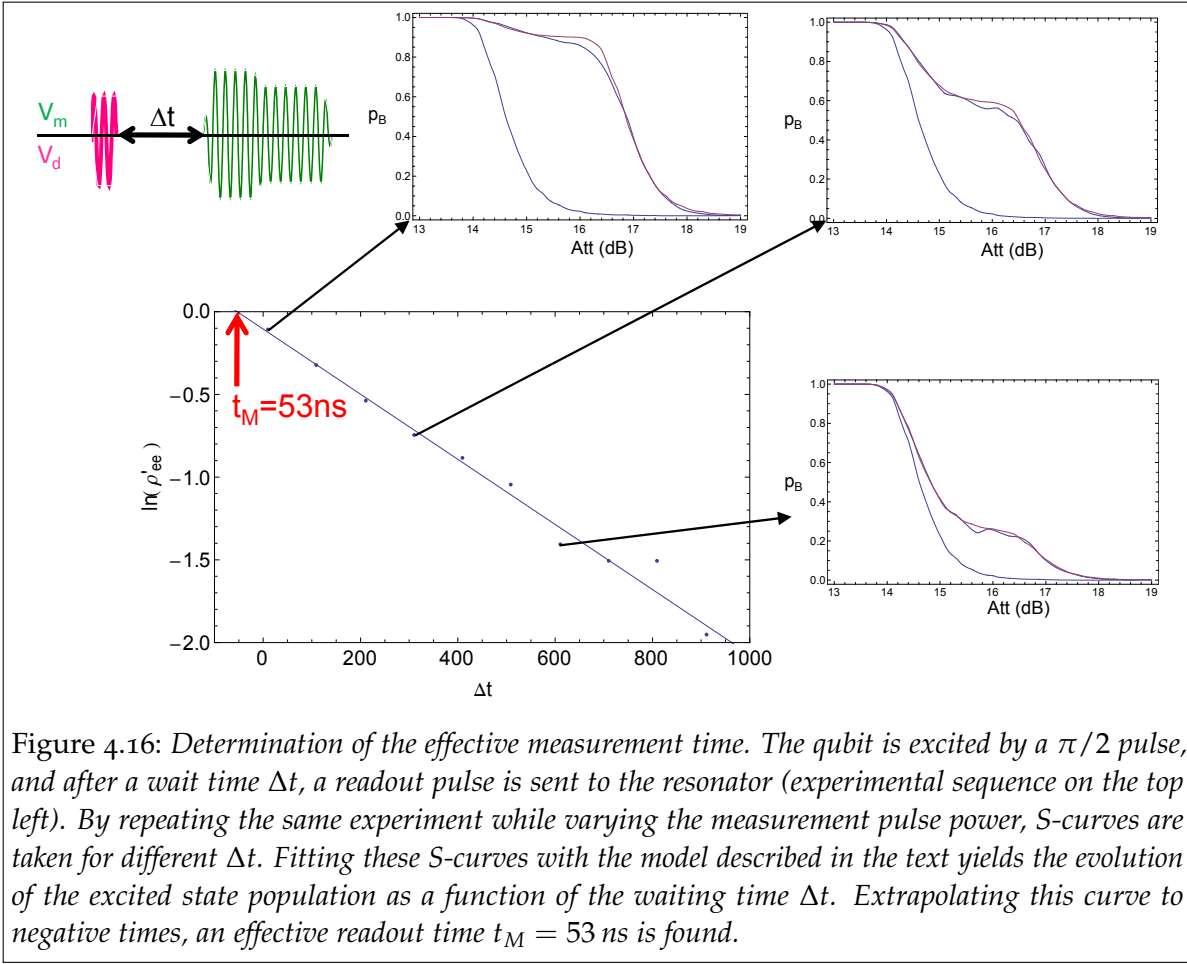


Figure 4.16: Determination of the effective measurement time. The qubit is excited by a  $\pi/2$  pulse, and after a wait time  $\Delta t$ , a readout pulse is sent to the resonator (experimental sequence on the top left). By repeating the same experiment while varying the measurement pulse power, S-curves are taken for different  $\Delta t$ . Fitting these S-curves with the model described in the text yields the evolution of the excited state population as a function of the waiting time  $\Delta t$ . Extrapolating this curve to negative times, an effective readout time  $t_M = 53$  ns is found.

$S_{r,m}^2$  shown in Fig. 4.17a with a 92% contrast. Figure 4.17b shows Rabi oscillations between  $|0\rangle$  and  $|1\rangle$  obtained with a composite readout pulse comprising the  $1 \rightarrow 2$  pulse for the qubit plus the standard readout pulse. The visibility, defined as the fitted amplitude of the oscillations, is 94%, and the Rabi decay time is  $0.5 \mu\text{s}$ . Of the remaining 6% loss of visibility we estimate that about 4% is due to relaxation before bifurcation and 2% to residual out-of-equilibrium population of  $|1\rangle$  and to control pulse imperfections.

To ensure that the  $1 \rightarrow 2$  pulse hardly affects the  $|0\rangle$  state, we record an S-curve starting in  $|0\rangle$  and applying a  $\pi$  pulse at  $\omega_{12}$  (dotted blue S-curve of Fig. 4.17): it reveals that this pulse induces a spurious population of the  $|1\rangle$  state of order 1%. We checked that this effect is corrected by using quality factor of the CBA resonator  $Q = Q_c$  and the non-linearity quantified by the critical current of the junction  $I_0$  affect the performance of the CBA readout, we measured several other samples with different  $Q_c$ , and a sample with a SQUID, instead of a Josephson junction in its middle, which allowed to in-situ tune  $I_0$ .

#### 4.5.3.3 Trade-off between qubit coherence and readout fidelity

Is the high-fidelity described above effective in a large span of qubit-resonator detunings  $\Delta = \omega_c - \omega_{01}$ ? Indeed, besides acting as a qubit state detector the resonator also

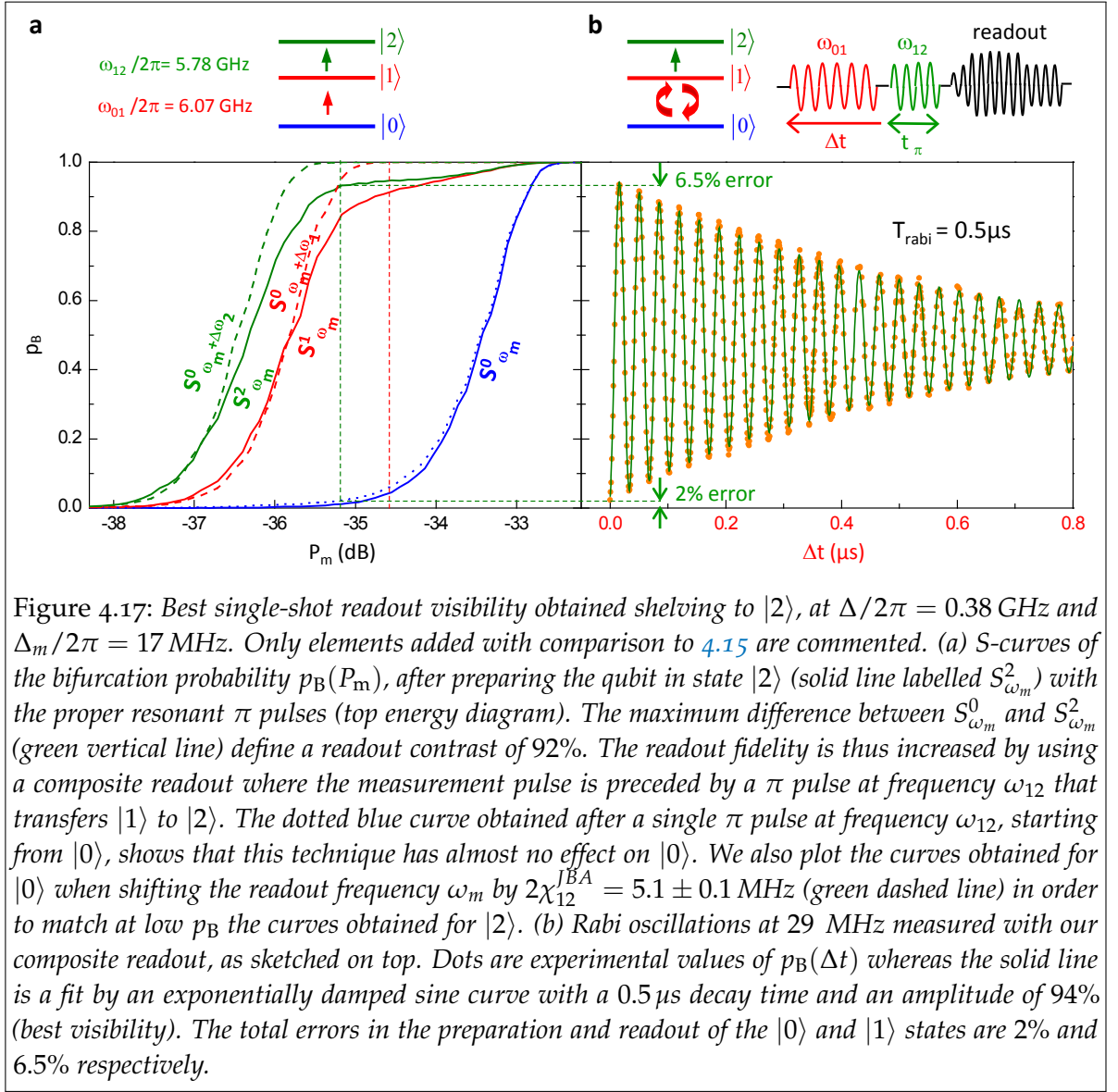


Figure 4.17: Best single-shot readout visibility obtained shelving to  $|2\rangle$ , at  $\Delta/2\pi = 0.38$  GHz and  $\Delta_m/2\pi = 17$  MHz. Only elements added with comparison to 4.15 are commented. (a) S-curves of the bifurcation probability  $p_B(P_m)$ , after preparing the qubit in state  $|2\rangle$  (solid line labelled  $S^2_{\omega_m}$ ) with the proper resonant  $\pi$  pulses (top energy diagram). The maximum difference between  $S^0_{\omega_m}$  and  $S^2_{\omega_m}$  (green vertical line) define a readout contrast of 92%. The readout fidelity is thus increased by using a composite readout where the measurement pulse is preceded by a  $\pi$  pulse at frequency  $\omega_{12}$  that transfers  $|1\rangle$  to  $|2\rangle$ . The dotted blue curve obtained after a single  $\pi$  pulse at frequency  $\omega_{12}$ , starting from  $|0\rangle$ , shows that this technique has almost no effect on  $|0\rangle$ . We also plot the curves obtained for  $|0\rangle$  when shifting the readout frequency  $\omega_m$  by  $2\chi_{12}^{JBA} = 5.1 \pm 0.1$  MHz (green dashed line) in order to match at low  $p_B$  the curves obtained for  $|2\rangle$ . (b) Rabi oscillations at 29 MHz measured with our composite readout, as sketched on top. Dots are experimental values of  $p_B(\Delta t)$  whereas the solid line is a fit by an exponentially damped sine curve with a  $0.5 \mu s$  decay time and an amplitude of 94% (best visibility). The total errors in the preparation and readout of the  $|0\rangle$  and  $|1\rangle$  states are 2% and 6.5% respectively.

serves as a filter protecting the qubit against spontaneous emission on the environment. When the resonator and the qubit are nearby, the cavity pull is large and thus also separation between  $S^0_{\omega_m}$  and  $S^1_{\omega_m}$  curves. This would improve the contrast but the relaxation is also faster, as explained in 2.3.1, and leads to a reduction in  $\rho'_{ee}(\Delta t)$ . Conversely, when the resonator and the qubit are far detuned the relaxation becomes lower, until reaching a saturation at  $\Gamma_1 \approx 700$  ns, but the cavity pull is also reduced.

Fig. 4.18 presents a summary of our measurements of contrast and coherence times. The qubit coherence times are measured using standard experimental sequences<sup>6</sup>. For the relaxation time  $\Gamma_1^{-1}$ , we apply a  $\pi$  pulse and measure the qubit state after a variable delay, yielding an exponentially decaying curve whose time constant is  $\Gamma_1^{-1}$ . At small detuning  $\Delta$ ,  $\Gamma_1^{-1}$  is in quantitative agreement with calculations of the spontaneous emission through the resonator. However it presents a saturation, similarly as observed in previous experiments<sup>85</sup>, but at a smaller value around  $0.7 \mu s$ .



The effective cavity pull  $2\chi_{JBA}$  determined from the S-curves shifts is in quantitative agreement with the value of  $2\chi$  calculated from the sample parameters. The contrast varies with  $\Delta$  as anticipated and shows a maximum of 92% at  $\Delta/2\pi = 0.38$  GHz, where  $\Gamma_1^{-1} = 0.5 \mu\text{s}$ . Larger  $\Gamma_1^{-1}$  can be obtained at the expense of a lower contrast and reciprocally.

Another important figure of merit is the pure dephasing time<sup>17</sup>  $\Gamma_\phi^{-1}$  which controls the lifetime of a superposition of qubit states.  $\Gamma_\phi^{-1}$  is extracted from Ramsey fringes experiments: two  $\pi/2$  pulses are applied at a frequency slightly off-resonance with the qubit and with a variable delay; this yields an exponentially damped oscillation whose time constant is  $\Gamma_2^{-1}$ . We then extract the pure dephasing contribution  $\Gamma_\phi = \Gamma_2 - 1/2\Gamma_1$ . Such pure dephasing  $\Gamma_\phi$  shows a smooth dependence on the qubit frequency, in qualitative agreement with the dephasing time deduced from a  $1/f$  flux noise of spectral density set to  $20 \mu\phi_0/\sqrt{\text{Hz}}$  at 1 Hz, a value similar to those reported elsewhere<sup>91,92</sup>. Note that  $\Gamma_\phi^{-1} \approx 2.5 \pm 0.5 \mu\text{s}$  at the flux optimal point ( $\Delta/2\pi \approx -0.75$  GHz, data not shown in 4.18).

To summarize our circuit performances, we obtained a 400 MHz frequency range (pink area on Fig. 4.18) where the readout contrast is higher than 85%,  $\Gamma_1^{-1}$  is between  $0.7 \mu\text{s}$  and  $0.3 \mu\text{s}$ , and  $\Gamma_\phi^{-1}$  between  $0.7 \mu\text{s}$  and  $1.5 \mu\text{s}$ .

#### 4.5.4 IS THE CBA A QUANTUM NON DESTRUCTIVE (QND) DETECTOR?

The readout unavoidably perturbs the qubit by collapsing its state  $\alpha|0\rangle + \beta|1\rangle$  to  $|0\rangle$  if 0 is read and conversely. A desirable feature is that no other perturbation in addition to this projection affects the qubit state. Specifically, the measurement

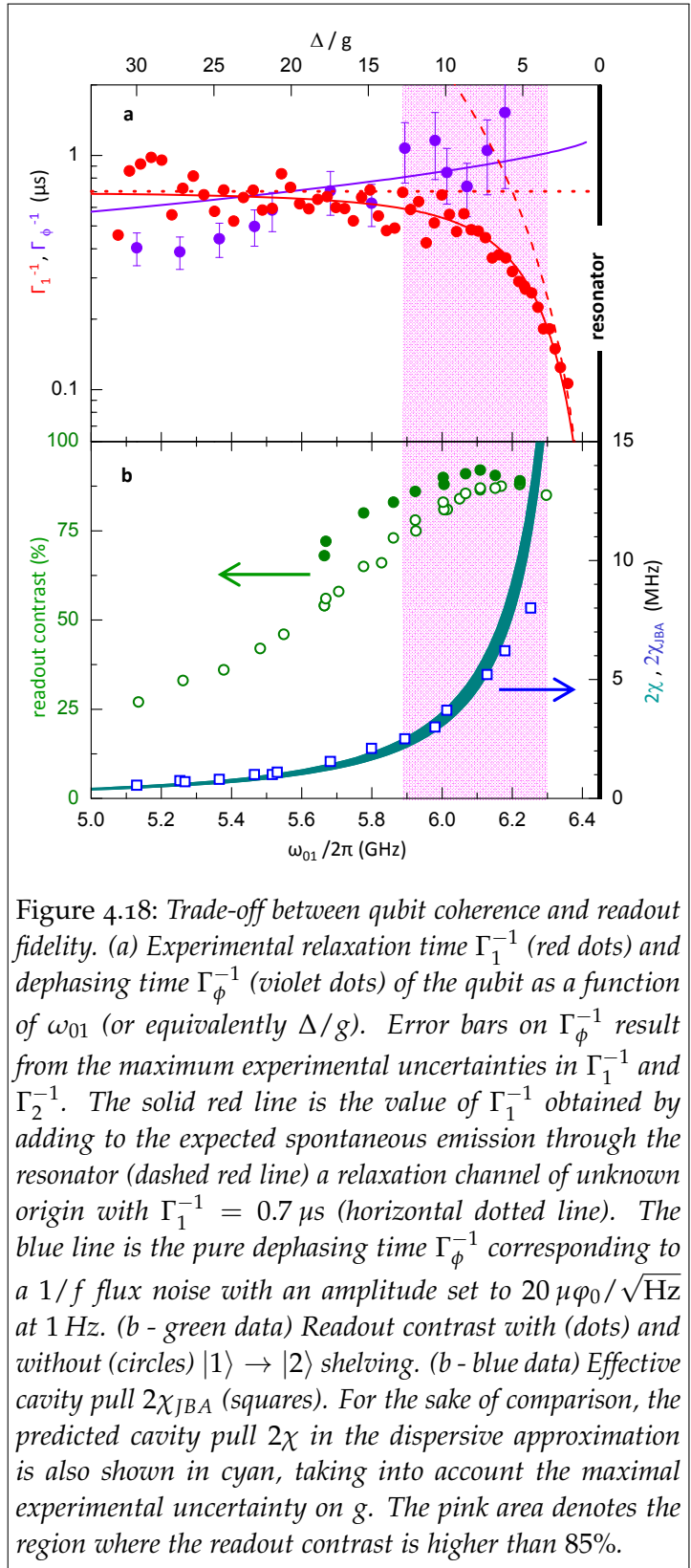


Figure 4.18: Trade-off between qubit coherence and readout fidelity. (a) Experimental relaxation time  $\Gamma_1^{-1}$  (red dots) and dephasing time  $\Gamma_\phi^{-1}$  (violet dots) of the qubit as a function of  $\omega_{01}$  (or equivalently  $\Delta/g$ ). Error bars on  $\Gamma_\phi^{-1}$  result from the maximum experimental uncertainties in  $\Gamma_1^{-1}$  and  $\Gamma_2^{-1}$ . The solid red line is the value of  $\Gamma_1^{-1}$  obtained by adding to the expected spontaneous emission through the resonator (dashed red line) a relaxation channel of unknown origin with  $\Gamma_1^{-1} = 0.7 \mu\text{s}$  (horizontal dotted line). The blue line is the pure dephasing time  $\Gamma_\phi^{-1}$  corresponding to a  $1/f$  flux noise with an amplitude set to  $20 \mu\phi_0/\sqrt{\text{Hz}}$  at 1 Hz. (b - green data) Readout contrast with (dots) and without (circles)  $|1\rangle \rightarrow |2\rangle$  shelving. (b - blue data) Effective cavity pull  $2\chi_{JBA}$  (squares). For the sake of comparison, the predicted cavity pull  $2\chi$  in the dispersive approximation is also shown in cyan, taking into account the maximal experimental uncertainty on  $g$ . The pink area denotes the region where the readout contrast is higher than 85%.

process should not induce extra relaxation of the qubit, or spurious excitations<sup>49</sup>. Indeed, former implementations of JBA readout on superconducting qubits show a strong increase in relaxation when the resonator switches from the  $\bar{B}$  state to the high-amplitude  $B$  state<sup>138,139</sup>.

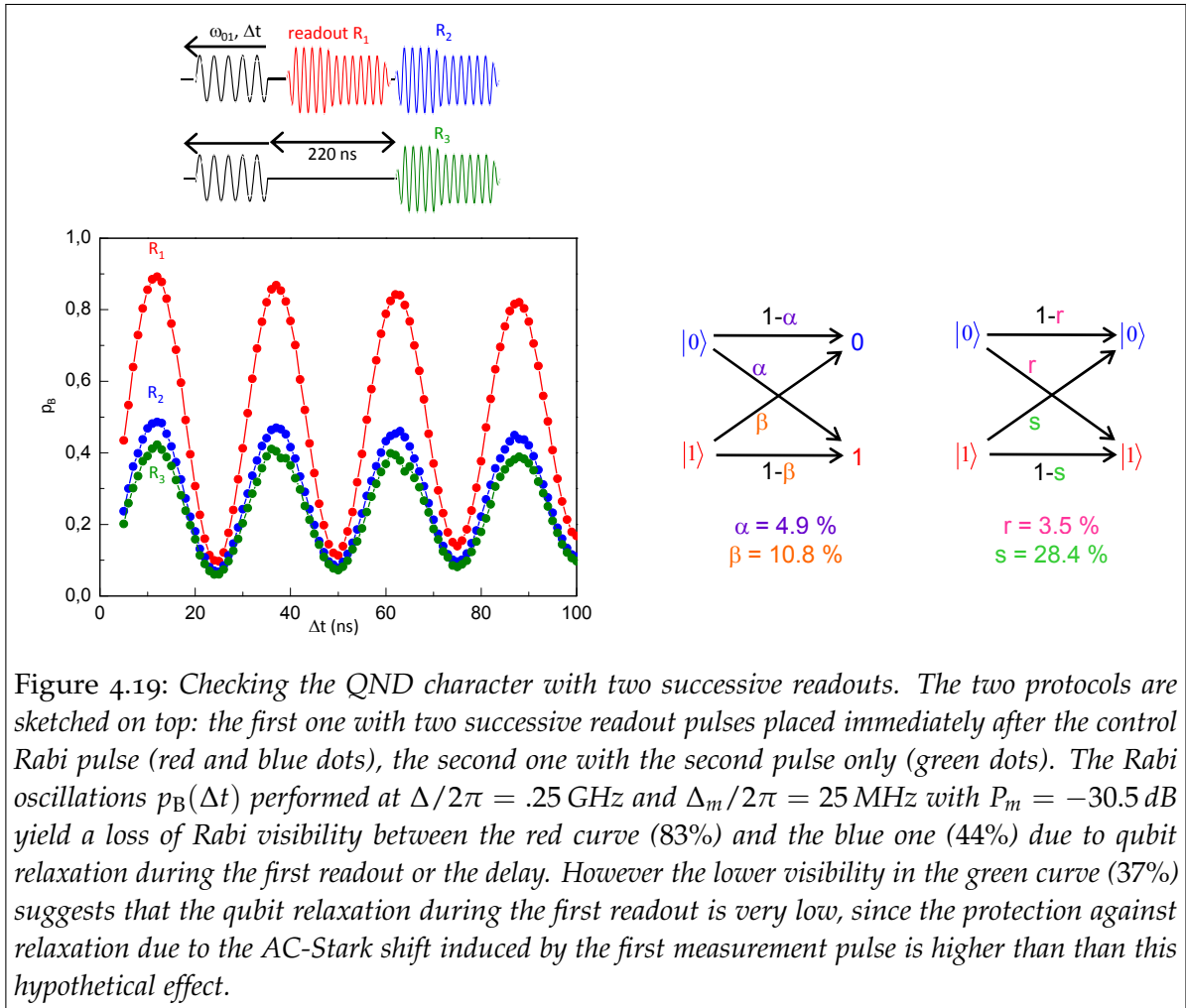


Figure 4.19: Checking the QND character with two successive readouts. The two protocols are sketched on top: the first one with two successive readout pulses placed immediately after the control Rabi pulse (red and blue dots), the second one with the second pulse only (green dots). The Rabi oscillations  $p_B(\Delta t)$  performed at  $\Delta/2\pi = .25$  GHz and  $\Delta_m/2\pi = 25$  MHz with  $P_m = -30.5$  dB yield a loss of Rabi visibility between the red curve (83%) and the blue one (44%) due to qubit relaxation during the first readout or the delay. However the lower visibility in the green curve (37%) suggests that the qubit relaxation during the first readout is very low, since the protection against relaxation due to the AC-Stark shift induced by the first measurement pulse is higher than this hypothetical effect.

A strong criterion for testing the back-action of the readout consists in performing a set of successive readouts and checking if they yield the same result. If they indeed do, the readout is said to be *Quantum Non-Demolition* (QND). For that purpose we compare (at  $\Delta = 0.25$  GHz) Rabi oscillations obtained with two different protocols: the control pulse is either followed by two successive readout pulses yielding curves  $R_1$  and  $R_2$ , or by only the second readout pulse yielding curve  $R_3$  (see Fig. 4.19).  $R_2$  and  $R_3$  exhibit almost the same loss of visibility compared to  $R_1$ , indicating that relaxation in the presence of the first readout pulse is the same as (and even slightly lower than) in its absence.

In this experiment the readout is performed with a large detuning  $\Delta_m/2\pi = 25$  MHz, to reduce the total measurement duration. Indeed, as a larger readout detuning implies a higher driving power and thus a higher reflected power, the signal to noise ratio is increased which allows to shorten  $t_H$  to 50 ns. We also used for these data  $t_R = 10$  ns and  $t_S = 40$  ns to shorten the overall measurement time, which also



decreases the maximal contrast to approx 83%. Finally, a delay time of 120 ns between the two readout pulses has been optimized experimentally to empty the resonator of all photons due to the first measurement, and thus avoid any spurious correlations between the two outcomes of the sequence.

#### 4.5.4.1 Modifications in qubit relaxation $\Gamma_1$ due to the readout

In order to investigate further the influence of a readout pulse on the qubit relaxation, we measure  $\Gamma_1$  in presence of a perturbing microwave field at the same frequency  $\omega_m$  as readout and with a power  $P_P$  (see Fig. 4.20). We first roughly estimate the intra-cavity mean photon number  $\bar{n}(P_P)$  by measuring the AC-Stark shifted qubit frequency  $\omega_{01}(P_P)$  as explained in 3.3.2.2. However the correspondence between  $\omega_{01}(\bar{n})$  and  $\bar{n}$  is linear only for the low photon numbers  $\bar{n} \ll n_{crit}$ , above  $n_{crit}$  the dispersive approximation breaks down, so we obtained the exact dependence by numerically diagonalizing the full Hamiltonian of the transmon coupled to a field mode with  $n$  photons (as detailed below in 4.7.1.2).

Bifurcation is clearly revealed by a sudden jump of  $\bar{n}$  from about 5-10 to 50-100 photons. Meanwhile  $\Gamma_1^{-1}$  does not show any decrease up to about 5 dB above bifurcation. It even slightly increases because the qubit frequency is pushed away from the cavity, slowing down spontaneous emission. This is in strong contrast with all previous experiments using a JBA readout<sup>138,139</sup>. These results prove that our design achieves very low back-action on the qubit. A similar behavior was observed for most qubit frequencies, except at certain values of  $P_P$  and  $\omega_{01}$  where dips in  $T_1(P_P)$  were occasionally observed above bifurcation (see 4.7.3 for more information on these dips).

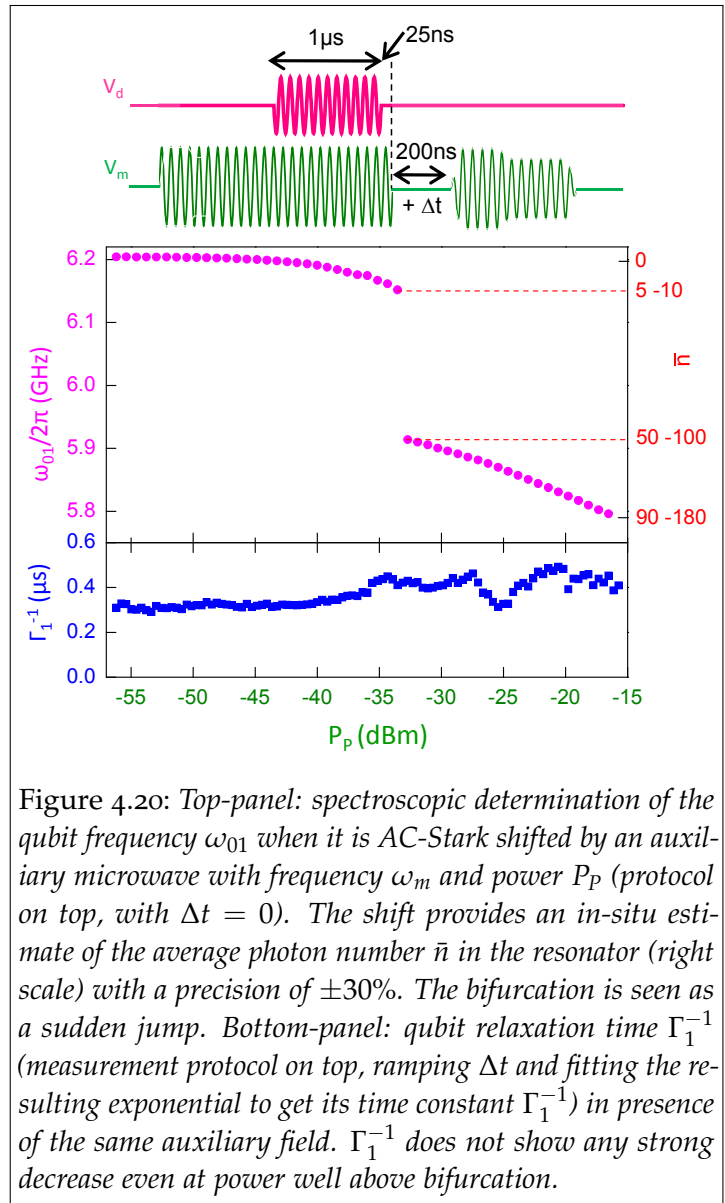


Figure 4.20: Top-panel: spectroscopic determination of the qubit frequency  $\omega_{01}$  when it is AC-Stark shifted by an auxiliary microwave with frequency  $\omega_m$  and power  $P_P$  (protocol on top, with  $\Delta t = 0$ ). The shift provides an in-situ estimate of the average photon number  $\bar{n}$  in the resonator (right scale) with a precision of  $\pm 30\%$ . The bifurcation is seen as a sudden jump. Bottom-panel: qubit relaxation time  $\Gamma_1^{-1}$  (measurement protocol on top, ramping  $\Delta t$  and fitting the resulting exponential to get its time constant  $\Gamma_1^{-1}$ ) in presence of the same auxiliary field.  $\Gamma_1^{-1}$  does not show any strong decrease even at power well above bifurcation.

#### 4.5.5 CONCLUSIONS ABOUT THE CBA QUBIT READOUT

Using the CBA to readout a qubit allowed to reach a high fidelity while keeping the good coherence properties of the cQED qubits and the QND character of the readout. A crucial characteristic of this new design is its very low back-action during readout compared to previous JBA designs- This is probably due to the fact that the qubit frequency depends only on the slowly-varying photon number inside the resonator , yielding less relaxation than in previous experiments where the qubit was coupled to a rapidly varying variable of the JBA (the intra-resonator current). Furthermore the resonator was designed to make it bifurcate at a low photon number, thus avoiding spurious qubit state transitions during readout.

These good characteristic of our readout circuit were reproduced in another sample which was used to study further the optimal parameters for CBA (see the next section). The high fidelities achieved should allow a test of Bell's inequalities using two coupled transmons, each one with its own CBA single-shot readout. Moreover, our method could be used in a scalable quantum processor architecture, in which several transmon-CBAs with staggered frequencies are read by frequency multiplexing.

#### 4.6 OPTIMIZATION OF THE CBA PARAMETERS

Is it possible to enhance further the fidelity of the readout by finely tuning the sample parameters? The readout visibility depends from the separation and the slope of the S-curves. The former is controlled by the cavity pull  $\chi$ , however, as explained above, this  $\chi$  cannot be indefinitely increased, since this would yield also a larger relaxation due to the Purcell effect.

Regarding the slope, four parameters play a role:

- The resonator quality factor  $Q$
- The resonator anharmonicity controlled by the critical current of the junction  $I_0$
- The detuning  $\Delta_m$  between the resonator drive and its resonance frequency (expressed as  $\Omega$ )
- The pulse shape

The influence of the pulse shape in the S-curve width is an interesting problem of optimization which remains unexplored up to now. However, with the standard CBA pulse shape, we studied in several conditions the dependence of the S-curves with the times  $t_R$ ,  $t_S$  and  $t_H$ , yielding only slight gains in visibility  $\sim 1\%$ .

In order to study the influence of the three other parameters in the visibility, we designed two new samples after the one which has been used before that we call sample A. This new samples (that we call sample B and sample C) have a larger  $Q$  than the sample A to check the influence of  $Q$  in the visibility. In addition, in order to study the influence of  $I_0$ , in samples B and C the resonator contains a SQUID in its center instead on a single Josephson junction, allowing to tune in-situ  $I_0$  by varying

the flux  $\Phi$ :

$$I_0(\Phi) = 2I_0 |\cos(\pi\Phi/\Phi_0)|$$

where  $I_0$  is the critical current of each of the junctions in the SQUID.

#### 4.6.1 STUDY WITH FIXED QUBIT FREQUENCY (SAMPLE B)

Sample B has tunable critical current with  $I_0(\Phi = 0) = 1.2 \mu\text{A}$  and very large quality factor  $Q(\Phi = 0) = 1750 \pm 50$ . Due to an unwanted cut in one of the arms of the transmon, the transition frequency of the qubit  $\omega_{ge} = 5.65 \text{ GHz}$  is not tunable. The dependence of the resonance frequency is as expected (see Section 5.2)

$$\omega'_r(\Phi) = \frac{\omega_r}{1 + 2\epsilon(\Phi)}.$$

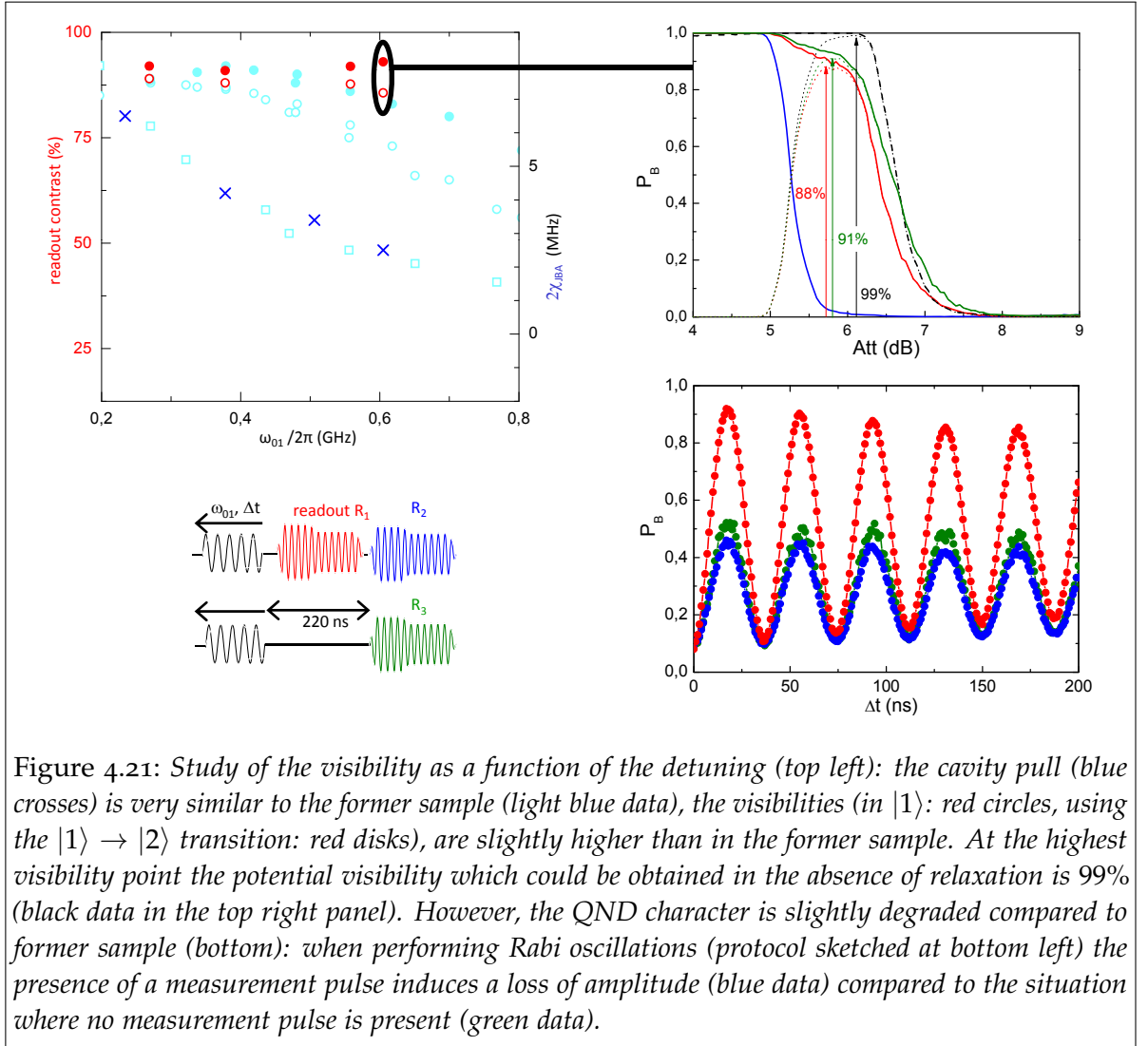
To study the visibility without tuning the qubit we define a new parameter, the *potential visibility* which is obtained as follows:

1. We measure the cavity pull  $\chi$  for the different qubit-resonator detunings  $\Delta(\Phi) = \omega_{ge} - \omega'_r(\Phi)$ ,
2. We measure S-curves for different values of  $I_0(\Phi)$  and  $\Omega$  with the qubit in its ground state  $|0\rangle$ .
3. We obtain the S-curves for the excited state  $|1\rangle$  by displacing  $2\chi$  in frequency the S-curve for measured for  $|0\rangle$ . We stress that this procedure completely neglects the effect of relaxation.
4. We calculate the potential visibility as the maximum difference between the two S-curves.

The results on the potential visibility of this sample are that  $\Omega$  has only a marginal importance for maximizing the visibility. Conversely the anharmonicity plays an important role: larger potential visibilities were obtained for the smaller anharmonicities. Therefore it may be interesting to increase the critical current  $I_0$  of the resonator junction. However, if we do so, the critical intra-resonator field at which the resonator bifurcates becomes also larger. Could this constitute a problem for the good QND properties of the readout by increasing the qubit relaxation during the readout procedure?

#### 4.6.2 STUDY WITH VARIABLE QUBIT FREQUENCY (SAMPLE C)

In sample C the resonator  $\omega_r(\Phi = 0) = 6.92 \text{ GHz}$  is tunable with  $I_0(\Phi = 0) = 1.3 \mu\text{A}$  very similar to sample B. The quality factor  $Q(\Phi = 0) = 1106 \pm 20 \text{ GHz}$  is between the one of sample A and of sample B. The qubit was tunable, but the on-chip flux line which controlled its flux independently from the flux of the resonator SQUID had a very reduced coupling. Therefore we could not perform a systematic study of the



best readout conditions both in  $\Delta$  and in  $I_0$ . However, because of the very different periodicity of the variation of  $\omega_{ge}(\Phi)$  and  $I_0(\Phi)$ , we were able to study a discrete number of points which are representative of the full behaviour of the system.

The results of such a study are sketched in Fig. 4.21. We observed slightly higher values of the raw visibility than those measured in the former samples. The potential visibilities defined in 4.6.1 are at some working points over 99%, showing that the only parameter which could allow to improve substantially the visibility is  $T_1$ .

We also performed a study on two successive readouts to check the QND character, and this is actually worse than the one observed in the previous sample. Specifically, the Rabi oscillations measured with a second readout pulse lose 16% of their amplitude compared to the ones performed without a previous measurement pulse. We have checked that the  $T_1$  in the range where the qubit is AC-Stark shifted by the measurement pulse cannot account for such a loss, like it could happen if for instance a two-level fluctuator was at the vicinity of this frequency. This loss in visibility could therefore be the first sign of a compromise between the readout fidelity and the QND character.

As a conclusion of this study, the main parameter which could allow further

increases in the readout visibility is the qubit  $T_1$ . The optimization of the other parameters could bring small increases of the order of the percent, but some unwanted compromises, like the one between the visibility and the QND character may arise.

#### 4.7 NON-LINEAR JAYNES-CUMMINGS PHYSICS : STRONG COUPLING OF A NON-LINEAR RESONATOR AND A QUBIT

As we discussed in Section 3.3, when the resonator is linear the interaction between its microwave field and the qubit is well understood theoretically<sup>22</sup> and was first studied experimentally at Yale<sup>21</sup>. Our results completely agree with these former studies: the qubit spectroscopic line is shifted in frequency (AC-Stark shift) and broadened due to the measurement back-action.

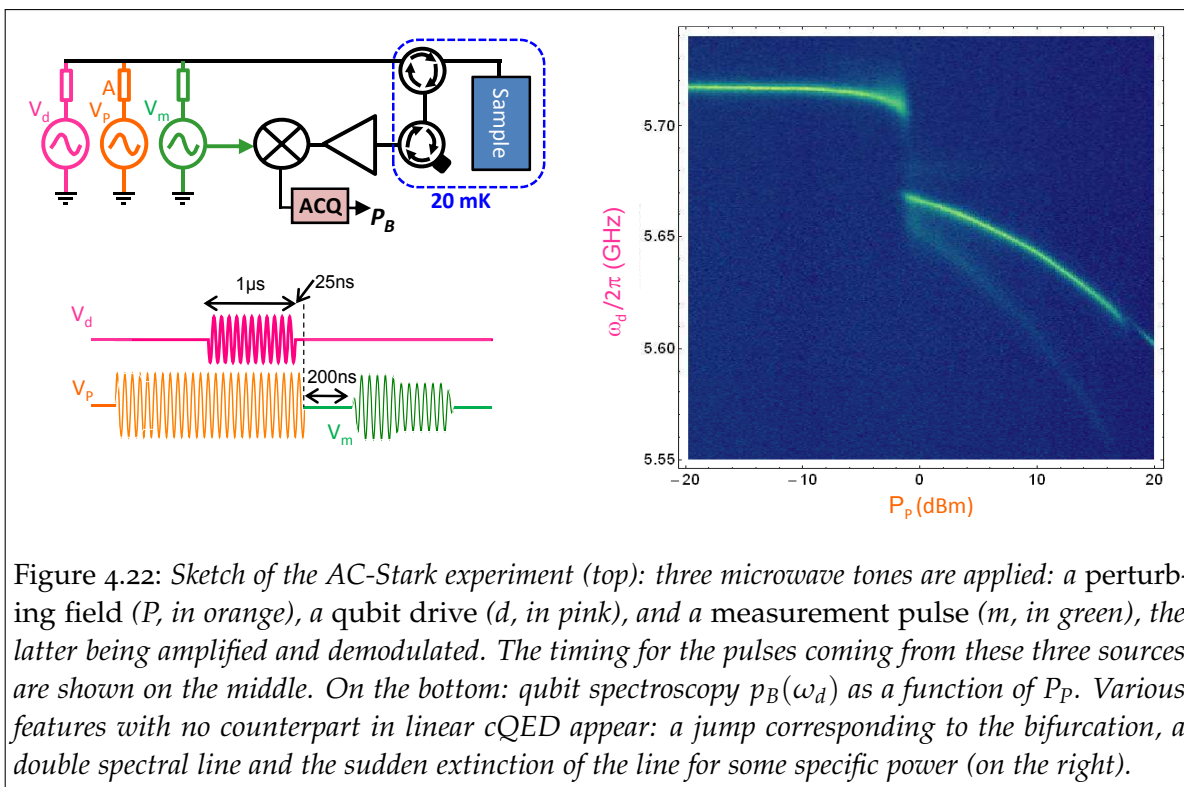


Figure 4.22: Sketch of the AC-Stark experiment (top): three microwave tones are applied: a perturbing field ( $P$ , in orange), a qubit drive ( $d$ , in pink), and a measurement pulse ( $m$ , in green), the latter being amplified and demodulated. The timing for the pulses coming from these three sources are shown on the middle. On the bottom: qubit spectroscopy  $p_B(\omega_d)$  as a function of  $P_p$ . Various features with no counterpart in linear cQED appear: a jump corresponding to the bifurcation, a double spectral line and the sudden extinction of the line for some specific power (on the right).

However, in the new circuit we use in this chapter for achieving high-fidelity readout the resonator is not anymore linear. The understanding of the qubit-field interaction in the case of a non-linear resonator is still largely lacking. Besides its practical interest for quantum information processing, a better knowledge of this interaction is of high fundamental interest: indeed it is the same as that of an atom strongly coupled to a Kerr medium, a physical system yielding e.g. parametric amplification and squeezed states of light. Such a situation, up to now out of reach with real atoms and lasers, can easily be investigated using superconducting circuits since they provide nonlinearities orders of magnitude larger than those available in atomic physics.

Our main goal here is to present first experimental investigations of this non-linear cQED system, and to give an idea of the physical processes coming into play, without

presenting a detailed and comprehensive theoretical explanation. We study the absorption spectrum of the qubit while the resonator is driven by a microwave source  $V_P$  that establishes an intra-resonator field of  $\bar{n}$  photons in average (Fig. 4.22). As in the linear resonator case studied in detail in Chapter 3, the qubit line is frequency-shifted and broadened by the interaction with the field; however the dependence of the qubit line frequency and width on the power and frequency of  $V_P$  is found to be strikingly modified by the resonator non-linearity. We show that we can quantitatively understand the position of the lines, and use these measurements to obtain the non-linear resonator parameters with high accuracy. The width of the lines is well reproduced with a simple extension of the model for measurement-induced dephasing of Chapter 3, showing that the link between measurement and dephasing pertains even for non-linear resonators. Finally we show that at larger spectroscopy power, additional lines appear in the spectrum. We identify the higher order physical processes relevant for these lines.

#### 4.7.1 AC-STARK SHIFT WITH A NON-LINEAR RESONATOR

In this paragraph we discuss the frequency shift and broadening of the qubit resonance line in presence of a field in the non-linear resonator to which it is dispersively coupled.

##### 4.7.1.1 *Experimental results*

We start by presenting the experimental results that we will discuss in this section. They were obtained with sample A, but similar effects were observed with all three samples that have been measured. The experimental setup is the same as throughout this chapter, but for the microwave pulse sequence, which is depicted in Fig. 4.22. Qubit spectroscopy is performed with a microwave pulse from a source  $V_d$  at frequency  $\omega_d$ , using a microwave power low enough not to saturate the qubit transition. During this pulse, the resonator is driven close to its resonance frequency by a “pump” microwave source  $V_P$  of frequency  $\omega_P$  (corresponding to a reduced detuning  $\Omega$ ) and power  $P_P$ . To make sure that the resonator field has reached its steady-state during the qubit spectroscopy, this pump pulse starts one microsecond before  $V_d$  is switched on. Both pulses end up at the same time, so that the spectroscopy pulse lasts  $1 \mu s$  and the pump pulse  $2 \mu s$ . The qubit state at the end of this experimental sequence is finally measured with a third microwave pulse applied by a source  $V_m$  with fixed frequency  $\omega_m$ , amplitude and temporal shape optimized for qubit readout as described in the previous paragraphs. Moreover the readout pulse is applied 200 ns after switching off the two other pulses, a time long enough to let the intra-resonator field relax before readout, but shorter than the qubit relaxation time  $T_1 = 700$  ns. In this way, the switching probability  $p_B$  depends only on the qubit state and not at all on the pump pulse amplitude. In all the experiments discussed in this section the qubit frequency in absence of resonator field  $\omega_{01}$  is fixed at  $\Delta/2\pi = 725$  MHz, much larger than  $g/2\pi = 45$  MHz so that the qubit-resonator coupling is far in the dispersive regime, with  $\chi/2\pi \simeq 0.8$  MHz.



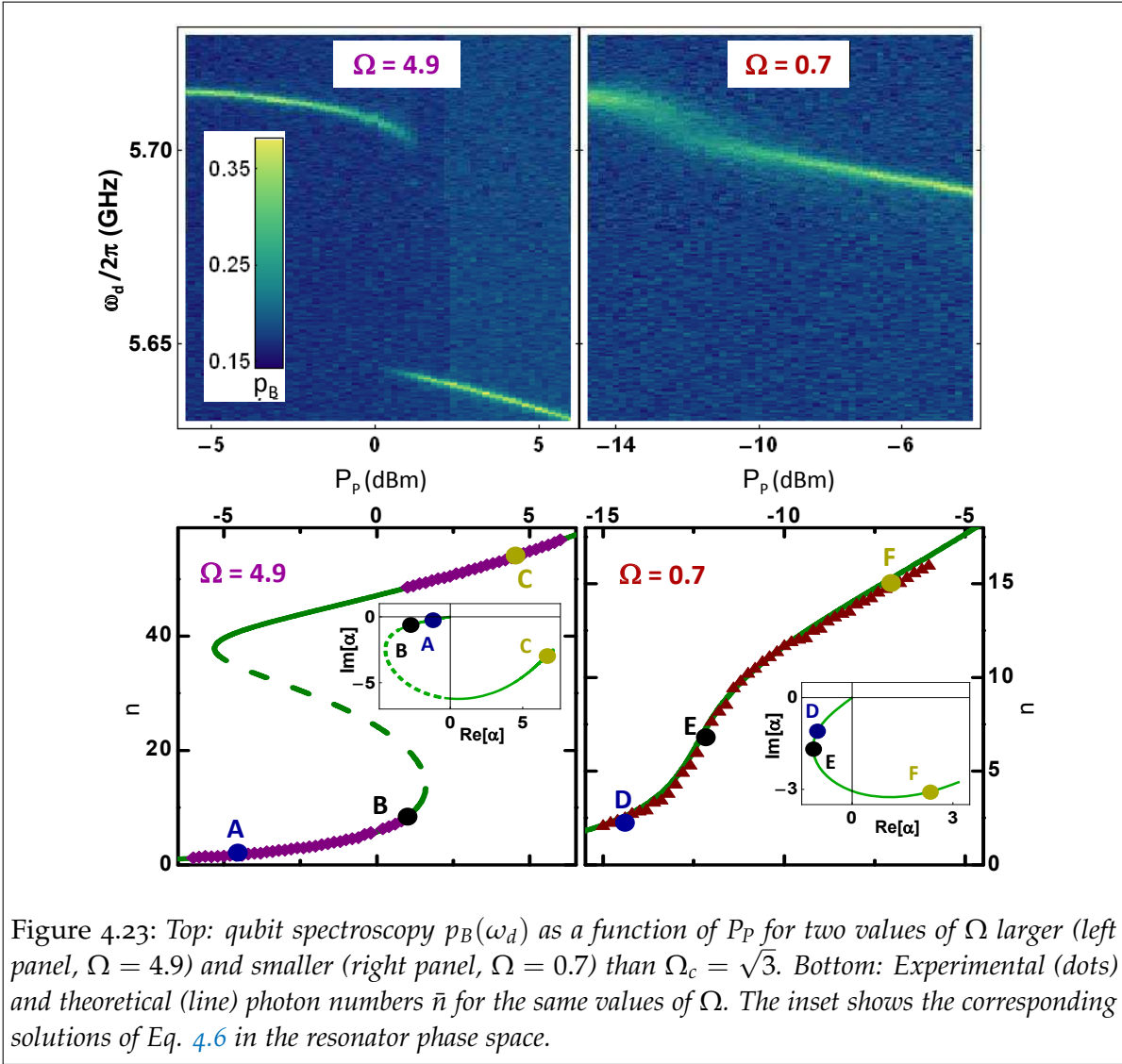


Figure 4.23: Top: qubit spectroscopy  $p_B(\omega_d)$  as a function of  $P_p$  for two values of  $\Omega$  larger (left panel,  $\Omega = 4.9$ ) and smaller (right panel,  $\Omega = 0.7$ ) than  $\Omega_c = \sqrt{3}$ . Bottom: Experimental (dots) and theoretical (line) photon numbers  $\bar{n}$  for the same values of  $\Omega$ . The inset shows the corresponding solutions of Eq. 4.6 in the resonator phase space.

Typical results are shown in Fig. Fig. 4.22. The two-dimensional graph shows  $p_B$  as a function of the qubit drive frequency  $\omega_d$  for various pump field input powers  $P_p$ . For each  $P_p$  value  $p_B$  shows a peak when  $\omega_d$  coincides with the qubit frequency  $\omega_{01}(P_p)$ . This peak is AC-Stark shifted towards low frequencies, as expected for increasing mean photon number  $\bar{n}$  in the resonator. However it is not at all linear in input power, as was the case for a linear resonator. The quantitative understanding of the position and width of these peaks as a function of  $P_p$  and  $\Omega$  is the object of this section. In addition to the qubit line, two additional weaker lines can be seen around the qubits for certain driving conditions; these sidebands will be qualitatively discussed in the next section.

#### 4.7.1.2 Converting the qubit frequency into photon number

From now on, we will focus on two datasets, obtained for  $\Omega = 4.9$  and  $\Omega = 0.7$ , shown in Fig. 4.23. The qubit resonance frequency is shifted down when increasing  $P_p$ . For  $\Omega = 4.9$ , an abrupt discontinuity in this AC-Stark shift strikingly evidences a



sudden increase in the intra-cavity field as the resonator switches from  $\bar{B}$  to  $B$ . For  $\Omega = 0.7$  the shift is continuous revealing that in these conditions the intra-resonator field evolves smoothly from  $\bar{B}$  to  $B$ . In both cases, the line is broadened only in the vicinity of  $\bar{B}$  to  $B$  transition.

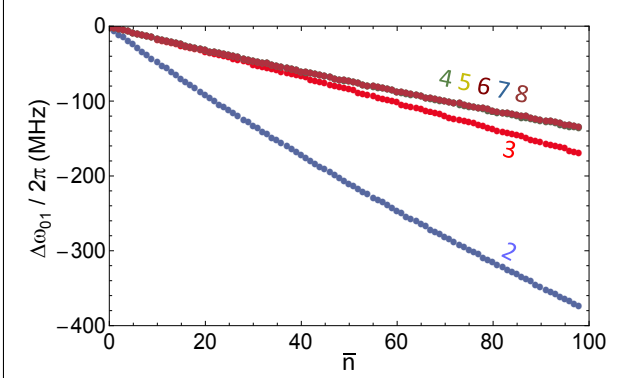


Figure 4.24: Conversion of the qubit line shift  $\Delta\omega_{01}$  to the average photon number  $\bar{n}$  in the resonator. The different colors correspond to the number  $M$  of transmon levels used in the Hamiltonian which is diagonalized (colored numbers). From  $M = 5$  the solutions show almost no differences,

To analyze the data, we fit each peak with a Lorentzian yielding the qubit frequency shift  $\Delta\omega_{01}(P_p) = \omega_{01}(P_p) - \omega_{01}(0)$ . According to the AC-Stark shift theory discussed in chapter 2 and 3, the shift should be very simply related to  $\bar{n}$  by the relation  $\Delta\omega_{01}(P_p) = 2\chi\bar{n}(P_p)$ . However this relation is only true as long as  $\bar{n} \ll n_{crit}$ . Here  $n_{crit} = 65$  and we measure frequency shifts of the same order as  $2\chi n_{crit}$ . In order to extract an accurate value for  $\bar{n}(P_p)$ , we therefore diagonalized numerically for the parameters of our experiment the full “transmon-resonator” Hamiltonian

$$\hat{H} = \hbar \sum_{i=0}^{M-1} \sum_{n=0}^{n_{max}} (n\omega_p + \omega_i) |i, n\rangle \langle i, n| + (g_i \sqrt{n} |i, n+1\rangle \langle i+1, n| + \text{h.c.})$$

where  $M$  is the total number of transmon states and  $n_{Max}$  the maximal number of Fock states considered. We also stress that we had to consider a resonator at the frequency  $\omega_p$  of the pump field instead of its resonance frequency  $\omega_r$ ; the validity of this procedure is confirmed by a detailed analysis performed by M. Boissonneault.

The resulting calculated frequency shift  $\Delta\omega_{01}(\bar{n})$  is shown in Fig. Fig. 4.24, taking into account various numbers of transmon levels. We see that taking into account only 2 levels yields completely wrong results, as already explained in Chapter 2. With three levels, the frequency shifts are well predicted at low photon numbers but are wrong by  $\sim 10\%$  around  $\bar{n} = 50$ . Taking into account one more level solves the problem. Using this numerical diagonalization we are thus able to numerically convert the measured  $\Delta\omega_{01}(P_p)$  in the corresponding  $\bar{n}(P_p)$ , yielding the graphs shown in the lower part of Fig. Fig. 4.23.

#### 4.7.1.3 Comparison with the theoretical non-linear resonator photon number

From the measured qubit frequency shift  $\Delta\omega_{01}(P_p)$  we therefore have obtained a measurement of the intra-resonator photon number  $\bar{n}(P_p)$ . We now wish to compare it to the theoretical  $\bar{n}(P_p)$  dependence for the CBA alone. This is conveniently obtained from the input-output theory using the CBA Hamiltonian Eq. 4.5. It yields the steady-state intra-resonator field amplitude  $\alpha$  as a function of the drive  $\epsilon_p$

$$i \left( \Omega \frac{\kappa}{2} \alpha + K |\alpha|^2 \alpha + K' |\alpha|^4 \alpha \right) + \frac{\kappa}{2} \alpha = -i \epsilon_p. \quad (4.6)$$

where the drive is related to  $P_P$  by the relation  $\epsilon_P = \sqrt{P_P/(A\hbar\omega_P)}$  with  $A$  the total line attenuation. The mean photon number is then simply  $n = |\alpha|^2$ . We have numerically adjusted the values of the two unknown parameters  $A$  and  $K$  to fit  $\bar{n}(P_P)$ . As can be seen in Fig. 4.23 we obtain a remarkable agreement with the data for  $K^{fit}/2\pi = -(625 \pm 15)$  kHz and  $A^{fit} = (110.8 \pm 0.2)$  dB over the whole  $(\Omega, P_P)$  parameter range, consistent with the design value  $K/2\pi = -750 \pm 250$  kHz and with independent measurements of the line attenuation  $A = 111 \pm 2$  dB<sup>40</sup>. This demonstrates that measuring the AC-Stark shift of a qubit is an accurate method for characterizing its Kerr non linearity, yielding much higher precision than usual methods based on parametric effects<sup>40</sup>, which are generally hindered by a poor knowledge of the power at the resonator input.

#### 4.7.1.4 Measurement-induced dephasing

We now investigate the qubit dephasing induced by the perturbing field. The qubit linewidth  $\Delta\omega$  (FWHM) is directly related to the decoherence rate  $\Gamma_2$  by  $\Delta\omega = 2\Gamma_2 + 2\Gamma_\phi^{ph}$ , where  $\Gamma_\phi^{ph}$  is the perturbing field contribution and  $\Gamma_2$  accounts for all other decoherence processes. As illustrated in Fig. 4.25a for  $\Omega = 4.9$ , the linewidth  $\Delta\omega$  shows a sharp increase when the resonator is driven near bifurcation. On the other hand an abrupt narrowing of the line occurs right above the bifurcation threshold, the line staying narrow even at large photon numbers  $\bar{n} = 50$ . For  $\Omega = 0.7$ ,  $\Delta\omega$  shows a smooth peak around the transition from  $\bar{B}$  to  $B$  as illustrated in Fig. 4.25b. In both cases the intra-resonator field induces qubit dephasing mostly around the  $\bar{B}$  to  $B$  transition, which is also the region where the JBA can be used as a qubit state detector most effectively. This non-monotonic behavior is strikingly different from the case of a linear resonator, where in all envisioned limits the dephasing rate increases with the photon number.

This new dependence of the dephasing rate with the intra-resonator photon number can nevertheless be described by a model very similar to the one described in Chapter 3 (see 3.3.1.3). There we had introduced the resonator pointer states  $|\alpha_g\rangle$  or  $|\alpha_e\rangle$  as the qubit-dependent stationary states of the resonator field. The qubit dephasing rate was then shown to be

$$\Gamma_\phi^{ph} = \kappa D^2/2, \quad (4.7)$$

with  $D = |\alpha_g - \alpha_e|$ , the distinguishability.

We will now investigate whether this simple formula could hold for our non-linear resonator. Due to the non-linearity, the pointer states  $|\alpha_i\rangle$  are expected to have a much more complex dependence on the drive parameters, and exhibit some degree of squeezing. Nevertheless we approximate them roughly by coherent states, with an amplitude  $\alpha_i$  given by the stationary solutions of Eq. 4.6 with  $\omega_r$  replaced by the qubit state dependent resonator frequency  $\omega_i$ . The predictions of Eq. 4.7, calculated without any adjustable parameter, are shown in Fig. 4.25a and 4.25b. The agreement with the experimental data is very good for  $\Omega = 4.9$ , and semi-quantitative for  $\Omega = 0.7$ , possibly due to the neglect of squeezing, which becomes more important when

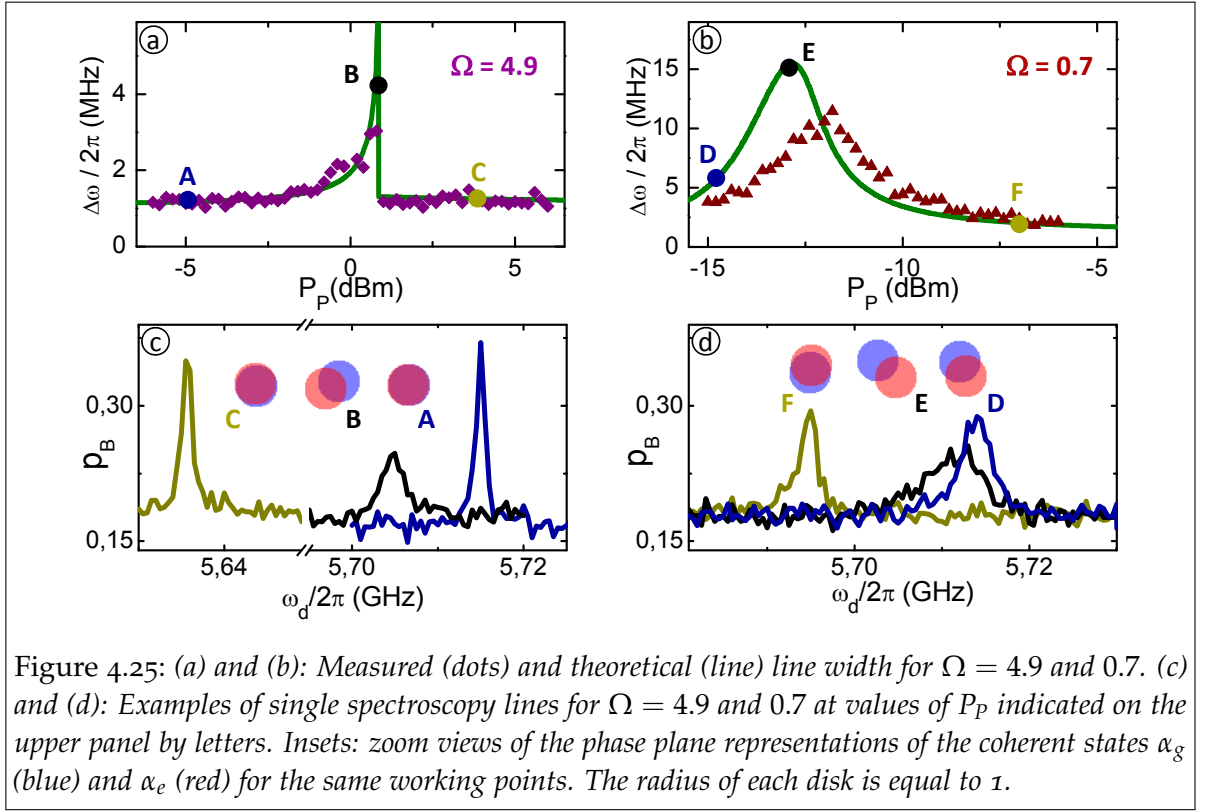


Figure 4.25: (a) and (b): Measured (dots) and theoretical (line) line width for  $\Omega = 4.9$  and  $0.7$ . (c) and (d): Examples of single spectroscopy lines for  $\Omega = 4.9$  and  $0.7$  at values of  $P_p$  indicated on the upper panel by letters. Insets: zoom views of the phase plane representations of the coherent states  $\alpha_g$  (blue) and  $\alpha_e$  (red) for the same working points. The radius of each disk is equal to 1.

closer to  $\Omega_c$ . Overall, the agreement is remarkable owing to the model simplicity, reproducing very well the non-trivial dependence of the qubit linewidth on the drive power over a large parameter range. Typical experimental spectra are shown in Fig. 4.25c and 4.25d, together with the graphical representation of the two pointer states, confirming that the direct link between qubit line broadening and distinguishability pertains even when the resonator is non-linear.

Despite the interest of our simple model, we can not expect this model to be valid in certain regions of the resonator phase diagram:

- In the bistable region  $\Omega_{g,e} > \sqrt{3}$  there is a small drive power range very close to the bifurcation threshold where the two pointer states  $\alpha_i$  correspond to different oscillator states; Eq. 4.7 then predicts dephasing rates much larger than observed.
- Around the critical point  $\Omega_i \simeq \sqrt{3}$ , where the pointer states are expected to be strongly squeezed.

A rigorous derivation of Eq. 4.7 and its limits will be provided in a future article by Boissonneault *et al.*

#### 4.7.2 BLUE AND RED SIDEBANDS

After having discussed the frequency and width of the qubit resonance line in presence of a field inside the non-linear resonator, we now turn to the study of the satellite lines that appear at high spectroscopy powers around the qubit main line. This effect is evident in Fig. 4.26 where two-dimensional plots of  $p_B$  showing the qubit

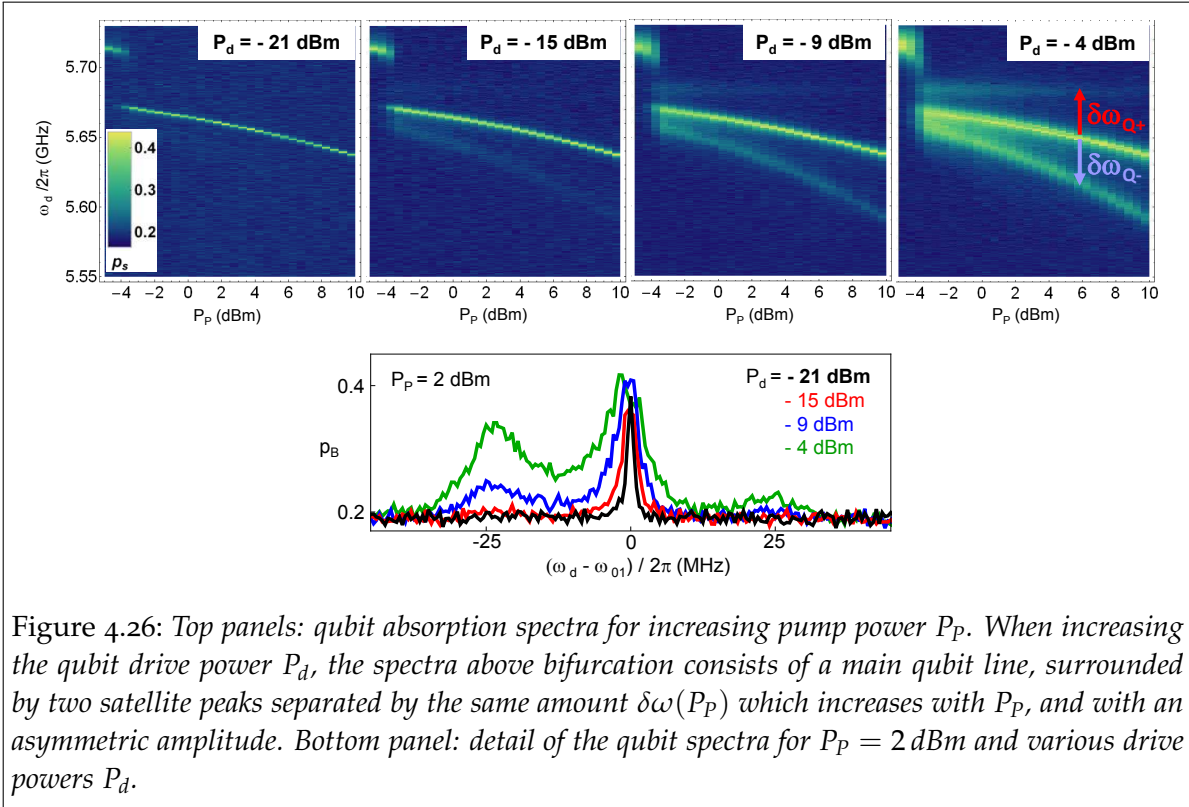


Figure 4.26: Top panels: qubit absorption spectra for increasing pump power  $P_p$ . When increasing the qubit drive power  $P_d$ , the spectra above bifurcation consists of a main qubit line, surrounded by two satellite peaks separated by the same amount  $\delta\omega(P_p)$  which increases with  $P_p$ , and with an asymmetric amplitude. Bottom panel: detail of the qubit spectra for  $P_p = 2$  dBm and various drive powers  $P_d$ .

absorption spectrum for increasing pump power  $P_p$  are shown for increasing qubit drive power  $P_d$ . Above bifurcation, the spectrum is observed to consist of one main qubit line, surrounded by two satellite peaks separated by the same amount  $\delta\omega(P_p)$  which increases with  $P_p$ , and with an asymmetric amplitude. Namely, the peak at lower frequency has a larger amplitude and area than the peak at higher frequency. In the following we will present in more detail this interesting phenomenon and provide a qualitative theoretical description in terms of two-photon absorption and emission processes between the qubit and the quasi-energy levels of the non-linear resonator.

#### Rabi oscillations in presence of a field

In order to obtain more insight into the peculiar shape of the qubit resonance line shown in Fig. 4.26, we have investigated the qubit coherent dynamics in the presence of the field in the resonator, at a given pump power  $P_p = +2$  dBm. Rabi oscillations obtained by driving the qubit at

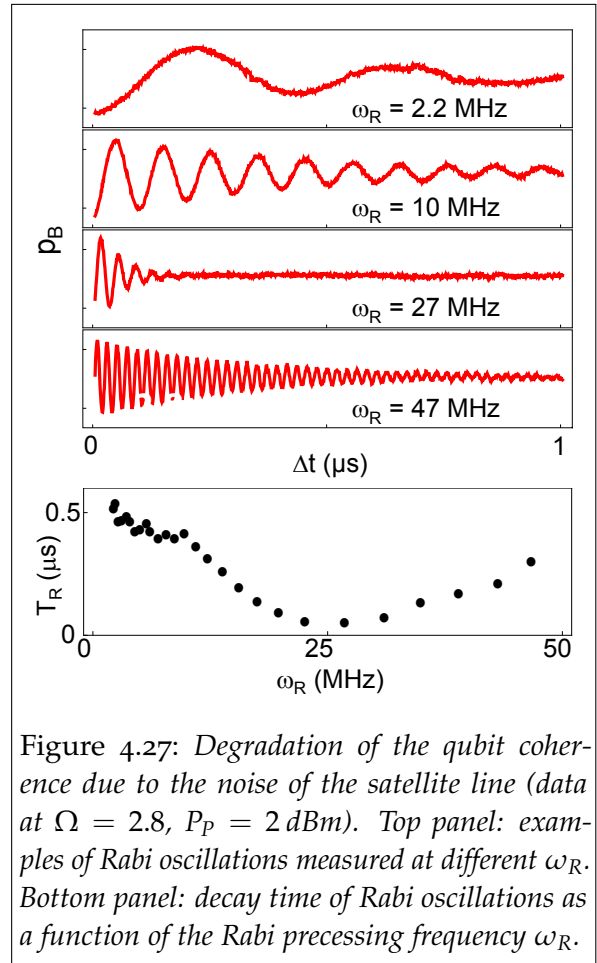


Figure 4.27: Degradation of the qubit coherence due to the noise of the satellite line (data at  $\Omega = 2.8$ ,  $P_p = 2$  dBm). Top panel: examples of Rabi oscillations measured at different  $\omega_R$ . Bottom panel: decay time of Rabi oscillations as a function of the Rabi precessing frequency  $\omega_R$ .

resonance with the AC-Stark shifted qubit line are shown in Fig. 4.27 for various Rabi frequencies. The most striking feature is a sudden drop of the Rabi oscillations decay time  $T_R$  when the Rabi frequency reaches a certain value that turns out to be exactly the frequency  $\delta\omega$  of the separation between the lines for this specific pump power. Since the decay of Rabi oscillations is essentially governed by the noise power spectrum at its frequency as discussed in Chapters 2 and 3, it is natural to investigate whether the resonator itself does not generate noise at this particular frequency  $\delta\omega$ .

#### *Quasi-energy levels of the driven non-linear oscillator*

We thus need to have a better understanding of the driven non-linear resonator dynamics. This can be obtained by linearizing the CBA Hamiltonian around its steady-state solution<sup>141</sup>. The driven CBA Hamiltonian in the Rotating Wave Approximation writes

$$\hat{H}_{CBA d} = \hbar\Delta_P \hat{a}^\dagger \hat{a} + \hbar \frac{K}{2} (\hat{a}^\dagger)^2 \hat{a}^2 + \hbar (iE_P \hat{a}^\dagger - iE_P^* \hat{a})$$

where  $\Delta_P = \omega_r - \omega_P$  is the pump field detuning from the resonator frequency, and  $E_P = \epsilon_P / \sqrt{\kappa}$  is the pump field amplitude. We then write  $\hat{a} = \alpha + \hat{b}$ , where  $\alpha$  is the solution of 4.6, and we linearize the resulting Hamiltonian yielding

$$\hat{H}_{CBA l} = \hbar\Delta_P \hat{b}^\dagger \hat{b} + 1/2 \hbar K (\alpha^{*2} \hat{b}^2 + \alpha^2 \hat{b}^{\dagger 2} + 4|\alpha|^2 \hat{b}^\dagger \hat{b}).$$

This Hamiltonian can be diagonalized with a transformation of the Bogoliubov type

$$\begin{aligned} \tilde{b} &= \mu \hat{b} + \nu \hat{b}^\dagger \\ \tilde{b}^\dagger &= \mu^* \hat{b}^\dagger + \nu^* \hat{b}. \end{aligned}$$

Choosing

$$\begin{aligned} \mu &= \cosh r \\ \nu &= e^{2i\theta} \sinh r \end{aligned}$$

we can see that the Hamiltonian can be rewritten

$$\tilde{H}_{CBA l} = \hbar\Delta'_P \tilde{b}^\dagger \tilde{b}. \tag{4.8}$$

provided we take  $(\Delta'_P, r, \theta)$  as solutions of

$$\begin{aligned} \Delta'_P \cosh 2r &= \Delta_P + 2K|\alpha|^2 \\ \Delta'_P \sinh 2r e^{-2i\theta} &= K\alpha^{*2}. \end{aligned}$$

This yields in particular the modulus of  $\Delta'_p$

$$\Delta'^2_p = \left(\Delta_p + 2K|\alpha|^2\right)^2 - K^2|\alpha|^2 \quad (4.9)$$

while its sign can be found from the equations above. We stress that this analysis is valid only provided  $\left(\Delta_p + 2K|\alpha|^2\right)^2 - K^2|\alpha|^2 > 0$ , which will be the case in the experiments discussed here.

To sum up, the driven non-linear resonator is equivalent around its stationary solution to an effective harmonic oscillator of frequency  $\omega'_c = \omega_p + \Delta'_p$ . The levels of this effective oscillator are called the quasi-energies. The frequency  $\Delta'_p$  also corresponds to the attempt frequency used in annex A to derive the switching rates of the bifurcation process. Note also that this analysis applies both in the situation where only one stable solution exists for the oscillator and in the case where the system is bistable, in which case two families of quasi-energy levels exist depending on the oscillator state.

It is very interesting to see how dissipation is transformed in the new  $\tilde{b}$  basis. It is possible to show<sup>141</sup> that the new master equation, in the frame rotating at  $\omega'_c$ , writes

$$\partial_t \hat{\rho} = \kappa \left(|\nu|^2 + 1\right) \mathcal{D} [\tilde{b}] \hat{\rho} + \kappa |\nu|^2 \mathcal{D} [\tilde{b}^\dagger] \hat{\rho}$$

describing this mode as being damped at the resonator rate  $\kappa$  but with an effective temperature that leads to a thermal population of the quasi-energy levels with an average number  $|\nu|^2$ . This emergence of an effective temperature whereas the physical temperature of the sample is taken to be 0 K in this analysis is typical for parametric processes and can be understood in terms of spontaneous parametric down-conversion. Pairs of photons from the pump at frequency  $\omega_p$  are converted into pairs of *quasi-photons* at frequencies  $\omega_p + \Delta'_p$  and  $\omega_p - \Delta'_p$ . Considering only one of these frequencies and neglecting the correlations with the photons emitted at the other frequency yields an effective thermal state.

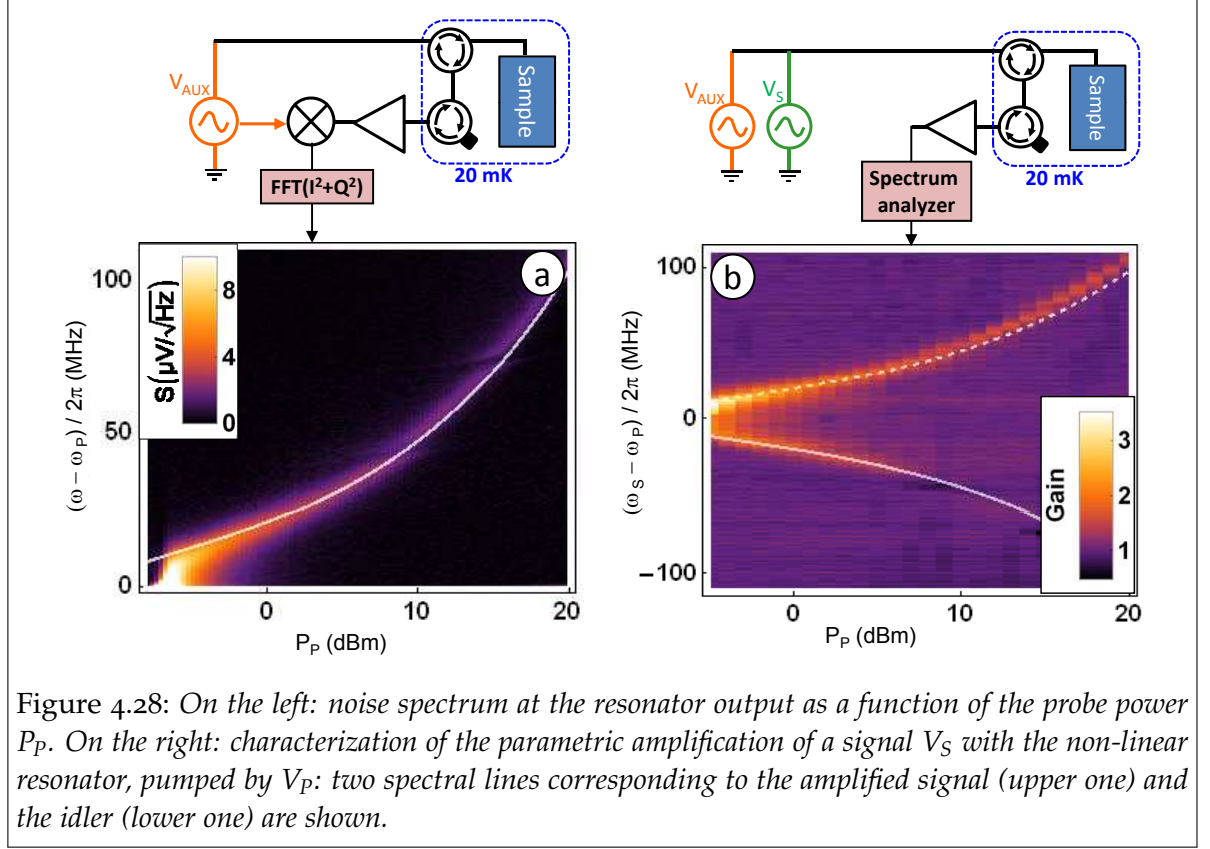
#### *Driven non-linear oscillator: noise spectrum and parametric gain*

Because of these parametric effects, photons should permanently be emitted from the resonator at frequencies  $\omega_p + \Delta'_p$  and  $\omega_p - \Delta'_p$  when it is driven at  $\omega_p$ , which should be measurable in the resonator noise spectrum. In order to do this we have used the very same setup as described in chapter 3 for continuously measuring the Rabi oscillations. The resonator is driven at pump frequency  $\omega_p$  for various powers  $P_p$ , and its total noise spectrum is recorded after demodulation at  $\omega_p$ . Typical results are shown in Fig. 4.28. They clearly show emission of photons at a frequency that depends on the pump power, in good agreement with the expected  $\Delta'_p(P_p)$  dependence without any adjustable parameter. We have also verified that this emission is phase-sensitive as expected, and squeezing was observed on one of the quadratures (data not shown).

Besides amplifying and squeezing vacuum fluctuations, the driven non-linear oscillator can also amplify a small input signal and be operated as a parametric



amplifier. We have measured this gain in various pumping conditions, and obtained a good agreement over the whole parameter range. In Fig. 4.28 we show only one typical curve, showing that the amplifier has gain around  $\omega_P + \Delta'_P$  and  $\omega_P - \Delta'_P$ .



### Stokes and anti-stokes transitions

We now use our understanding of the non-linear dynamics to give a qualitative account of the physical processes governing the appearance of the satellite peaks in the qubit absorption spectrum. The coupling of the qubit to the driven CBA can thus be envisioned as the dispersive coupling of the qubit to an effective harmonic oscillator, with a pump-power-dependent frequency  $\omega'_c = \omega_P + \Delta'_P$ , and an effective temperature characterized by its mean photon number  $|\nu|^2$ . This is reminiscent of the simpler situation of a qubit at frequency  $\omega_{ge}$  dispersively coupled to a linear resonator of frequency  $\omega_r$ , which has been shown in<sup>142</sup> to give rise to the appearance of sideband transitions at the sum and difference frequency of the qubit and resonator frequencies. The transition in absorption at  $\omega_S = \omega_{ge} + \omega_r$  correspond to a so-called “Stokes process” in which both the qubit and the resonator absorb one energy quantum simultaneously, while those at  $\omega_{AS} = \omega_{ge} - \omega_r$  correspond to an “anti-Stokes” process in which the qubit is excited from ground to excited state while a photon is emitted into the resonator mode. With a transmon qubit, these sidebands can not be excited by directly sending microwaves at  $\omega_S$  or  $\omega_A$  for symmetry reasons, however the Stokes (anti-Stokes) transition can be excited using two-photon transitions with two microwave sources of frequencies such that their sum (difference) is equal



to  $\omega_S$  ( $\omega_A$ )<sup>143</sup>. This has been used to generate entanglement between two transmon qubits<sup>144,145</sup>.

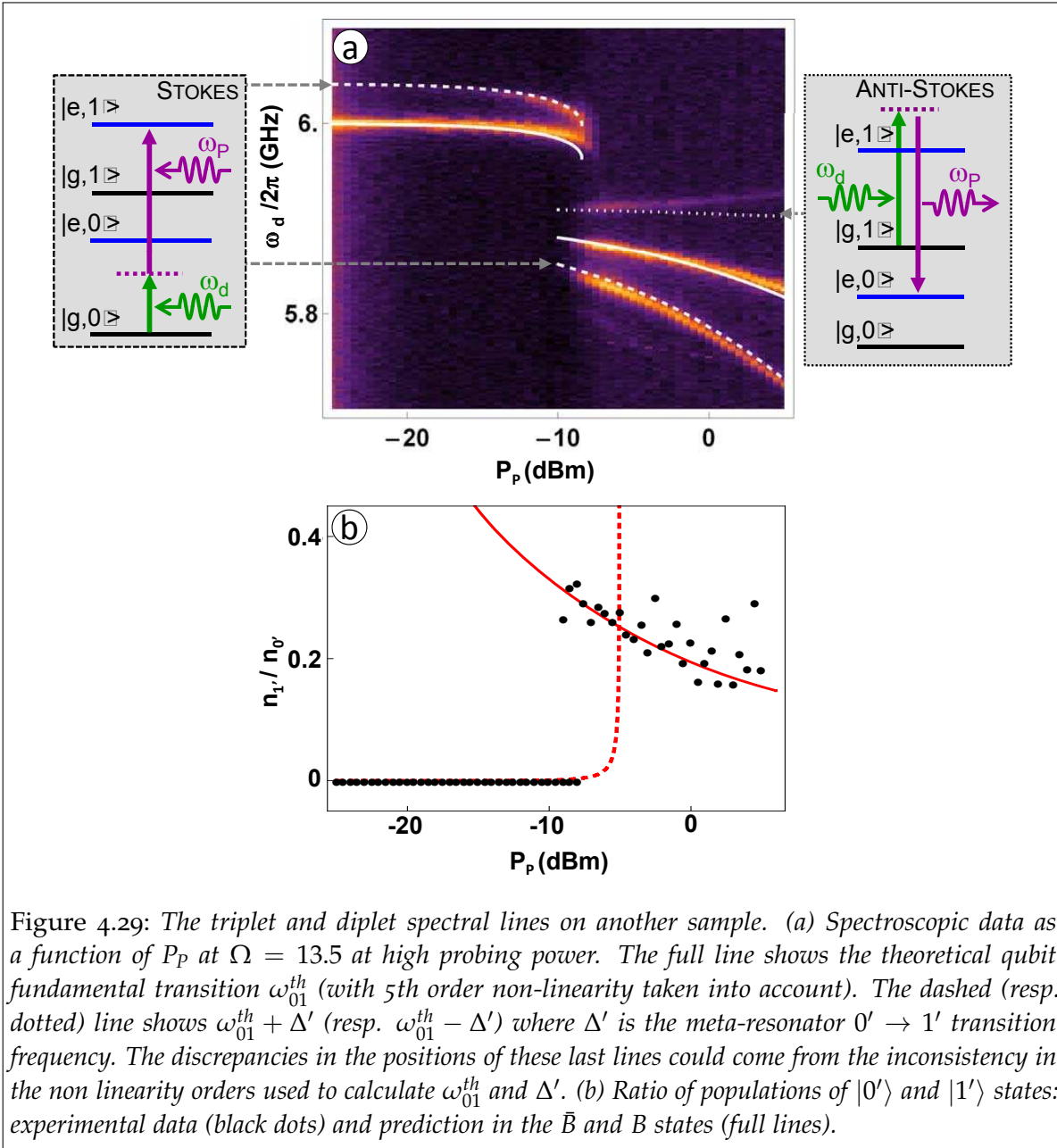


Figure 4.29: The triplet and diplet spectral lines on another sample. (a) Spectroscopic data as a function of  $P_p$  at  $\Omega = 13.5$  at high probing power. The full line shows the theoretical qubit fundamental transition  $\omega_{01}^{th}$  (with 5th order non-linearity taken into account). The dashed (resp. dotted) line shows  $\omega_{01}^{th} + \Delta'$  (resp.  $\omega_{01}^{th} - \Delta'$ ) where  $\Delta'$  is the meta-resonator  $0' \rightarrow 1'$  transition frequency. The discrepancies in the positions of these last lines could come from the inconsistency in the non linearity orders used to calculate  $\omega_{01}^{th}$  and  $\Delta'$ . (b) Ratio of populations of  $|0'\rangle$  and  $|1'\rangle$  states: experimental data (black dots) and prediction in the  $\bar{B}$  and  $B$  states (full lines).

In our situation, Stokes transitions from  $|g,0'\rangle$  to  $|e,1'\rangle$  (where  $|0'\rangle, |1'\rangle$  refer to the ground and first excited quasi-energy state of the driven CBA) can be similarly excited using the cavity pump and the qubit drive sources to perform the two-photon transition, under the resonance condition  $\omega_d + \omega_p = \omega_{ge} + \omega'_c$ , and anti-Stokes processes from  $|g,1'\rangle$  to  $|e,0'\rangle$  can be excited when  $-\omega_d + \omega_p = -\omega_{ge} + \omega'_c$ . To verify our understanding of these processes, we show in Fig. 4.29 a more detailed spectrum of the qubit absorption around bifurcation, together with the predictions for the qubit main resonance line and Stokes and anti-Stokes processes. The agreement is good.

The sidebands observed in the qubit spectrum give us another interesting test of the non-linear resonator theory described above. They allow a direct estimation of the

average photon number  $n_{th}$  inside the “effective resonator”, by simply comparing the areas of the Stokes and anti-Stokes sidebands. Indeed, it is well known from trapped ions experiments that the ratio of the heights of Stokes and anti-Stokes sidebands directly yields the ratio  $n_{th}/(1+n_{th})$ <sup>146</sup>. Here we can thus compare this ratio to the expected mean photon number  $|\nu|^2$ , which can be calculated without adjustable parameter. This comparison is done in Fig. 4.29 and shows a quantitative agreement, demonstrating in particular that the temperature of the mode observed here is not due to a simple heating effect but truly to spontaneous parametric down-conversion.

This provides a full validation of our interpretation of the satellite peaks observed in 4.29 as two-photon Stokes and anti-Stokes processes between the qubit and the non-linear resonator quasi-energy states. More generally, it illustrates the richness of phenomenon expected from the interplay between strong coupling and non-linear and parametric effects found in non-linear circuit QED, and which are here only starting to be unveiled.

#### 4.7.3 OTHER FEATURES LINKED TO THE SPECIFIC DYNAMICS OF NON-LINEAR OSCILLATIONS

The study of the qubit spectrum in the presence of a field in the non-linear resonator has also yielded other phenomena that we have not been able to understand but which are undoubtedly linked to the interaction of the qubit and the resonator. Already in 4.22, one can see that the qubit line vanishes for a certain pump drive power  $P_p$ , and reappears at larger power. We have studied the qubit energy relaxation time  $T_1$  for various pump powers in the same conditions, and found that  $T_1$  is reduced by one order of magnitude at the same point as the qubit line vanishes as can be seen in Fig. 4.30b. One might think that this reduction in  $T_1$  is due to a resonance in the environment at the specific frequency reached by the AC-Stark shifted qubit resonance frequency. However, this *extinction* of the qubit line occurs at different frequencies depending on the pump frequency  $\omega_p$  as can be seen in 4.22a. In addition, this behaviour is perfectly reproducible even after one thermal cycling to room-temperature of the sample, contrary to the usual two-level systems which unavoidably change from one cool-down to another. All this seems to indicate that the dynamics of the non-linear resonator in these specific resonant conditions cools down the qubit; unfortunately we have not been able to provide a detailed explanation of the mechanism by which this dynamical cooling operates.

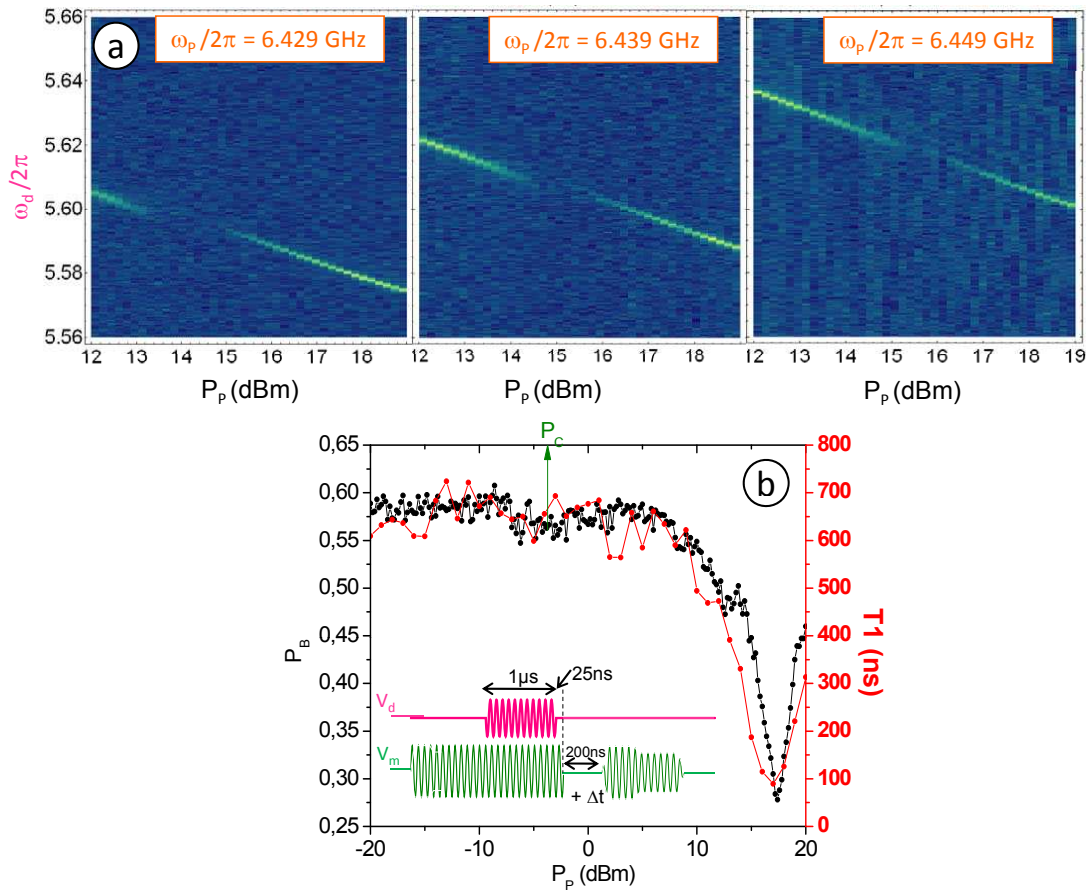


Figure 4.30: Extinction of the qubit spectral line. (a) Qubit spectra  $p_B(\omega_d)$  as a function of the perturbing field amplitude  $P_p$  for three values of  $\omega_p$ , showing the dependence the presence of an extinction which moves when  $\omega_p$  is varied. (b) Measurement of the bifurcation probability  $p_B$  after exciting the qubit and populating the resonator with a perturbing field (pulses shown in the inset), showing a large dip which corresponds to the extinction. The qubit relaxation times  $T_1$  measured in the presence of a perturbing field show the same behaviour. This extinction is not linked to bifurcation phenomena, which happen for much lower powers: the critical power  $P_C$  which correspond to the bifurcation is shown by a green arrow.



## Part III

# TOWARDS A MULTI-QUBIT ARCHITECTURE



## TUNABLE RESONATORS FOR COUPLING QUBITS

### 5.1 QUBIT INTERACTIONS MEDIATED BY A TUNABLE RESONATOR

The coherent coupling of two superconducting qubits through a capacitor<sup>147,148,149,150</sup>, an inductor<sup>151</sup> or a resonator<sup>152,153,54</sup> has been demonstrated by several groups worldwide. By violating the Bell's inequality with two coupled qubits<sup>118</sup>, the Yale group provided a strong proof of the coherent nature of the coupling. In all these experiments the coupling is fixed but it can be effectively switched on and off by tuning the qubit transition frequencies in and out of resonance. This scheme can in principle be extended to multi-qubit architectures<sup>154</sup>.

A more convenient scheme, however, might be to keep instead the qubits at fixed transition frequencies and to tune the coupling element –the resonator<sup>47</sup> or the ancilla qubit<sup>155</sup>– for bringing it in and out of resonance with each particular qubit. In this part of the thesis we describe the operation of a tunable resonator which could be used as a tunable coupling element for cQED qubits, in an architecture (Fig. 5.1) very similar to the one analyzed by Wallquist *et al.*<sup>47</sup>.

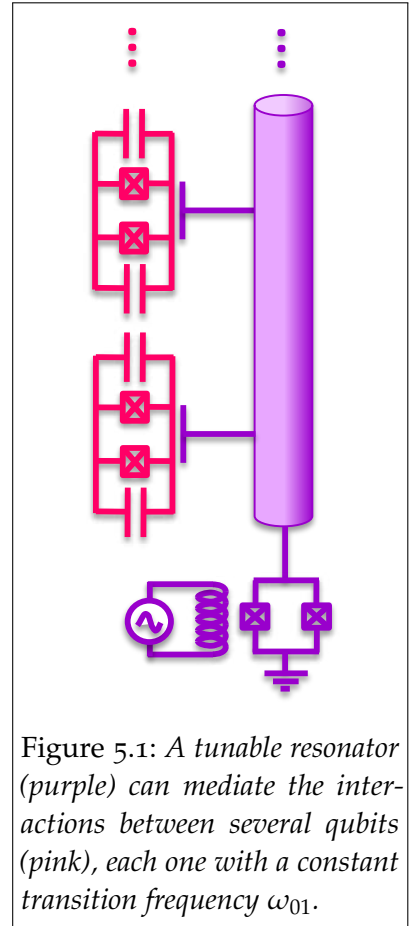


Figure 5.1: A tunable resonator (purple) can mediate the interactions between several qubits (pink), each one with a constant transition frequency  $\omega_{01}$ .

*Example of operation: creation of a Bell's state*

To create a Bell state with two qubits coupled to a tunable resonator as shown in Fig. 5.1, the following sequence of operations is performed<sup>47</sup>:

1. All three elements are set to be far detuned. The initial state  $|e0g\rangle_{1,r,2}$  is prepared by applying a  $\pi$  resonant control pulse to the first qubit.
2. The resonator is brought into resonance with the first qubit during a time corresponding to  $\pi/2$  or  $3\pi/2$  of a vacuum Rabi oscillation. This brings the system to the  $\left(|e0\rangle_{1,r} \pm |g1\rangle_{1,r}\right) |g\rangle_2$  state.
3. The resonator is brought into resonance with the second qubit during a time corresponding to  $\pi$  of a vacuum Rabi oscillation, so that it transfers its excitation to the qubit. The resonator ends up being empty and can be factorized, yielding the Bell state  $|\Psi_{\pm}\rangle_{1,2} |0\rangle_r = \left(|eg\rangle_{1,2} \pm |ge\rangle_{1,2}\right) |0\rangle_r$ .

With a more complex protocol it is possible to implement a two-qubit control-phase gate<sup>47</sup> which, combined with 1-qubit operations, provides a universal set of quantum



gates.

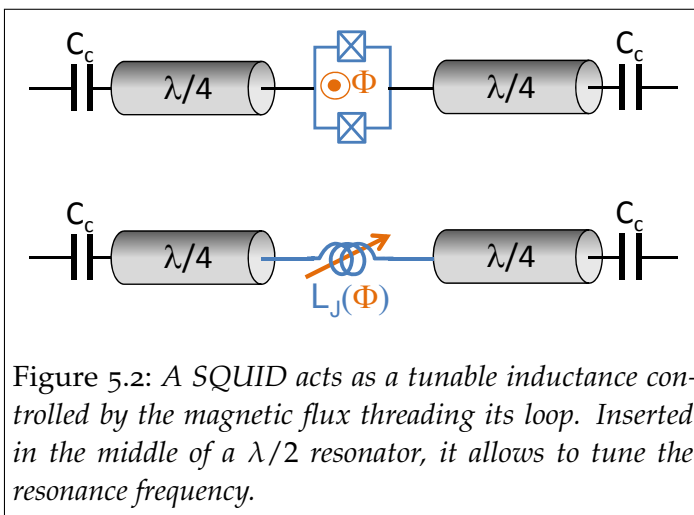
### Requirements for the coupling resonator

In order to be used as a coupling bus for a multi-qubit architecture, a tunable resonator should meet several requirements:

- In order to couple a large number of qubits, with different transition frequencies, the resonator frequency should be tunable in a large range.
- An important source of imperfections in two-qubit operations comes from the absorption of the energy in the coupling element. Therefore the resonator should have as little losses as possible.
- Since the qubit decoherence time limits the duration of quantum algorithms, two-qubit operations should be performed as fast as possible. The resonator should thus be tunable as fast as possible, although much slower than the resonance frequency to avoid parametric excitation.

In this chapter we present a circuit design which fulfills the first two criteria and potentially also the third one. Indeed, although our experimental setup did not allow to test fast tuning, this was demonstrated in Chalmers with a very similar design<sup>56</sup>.

### Studying the losses in Josephson circuits



An additional motivation for investigating tunable resonators with high quality factors is to obtain information on the losses in Josephson circuits. As explained in 2.2.3.7, the sources of relaxation in Josephson qubits are not yet well understood. Since tunable resonators also contain Josephson junctions, they are probably subject to the similar relaxation phenomena. Moreover, they constitute ideal systems to study these losses for two reasons: first because their high quality factors, which make them sensitive even to very small losses. Secondly, because the control on the parameters is

better than in qubits, which are too complex to perform such systematic study. Therefore studying the mechanisms which limit the quality factor of tunable resonators may provide important clues for understanding the limits of the qubit relaxation time  $T_1$ .

## 5.2 TUNING A RESONATOR WITH A SQUID

In order to build a resonator with tunable resonance frequency we need a tunable capacitor or a tunable inductance. Tunable capacitors are not easy to build, but conversely the SQUID, a basic superconducting circuit element, acts as a tunable inductor whose value  $L_J(\Phi)$  depends on the magnetic flux  $\Phi$  threading its loop. Inserting a SQUID in the center of a  $\lambda/2$  resonator (as shown in Fig. 5.2) makes its frequency tunable.

### 5.2.1 THE SQUID: A TUNABLE INDUCTOR

A SQUID consists in a superconducting loop interrupted by two Josephson junctions (Fig. 5.3). We derive here the variation of its inductance as a function of the magnetic flux  $\Phi$  threading its loop, neglecting for the moment the geometric inductance  $L_L$  of such a loop, which will be considered in the full treatment of 5.2.3.

We note  $\phi_1$  and  $\phi_2$  the superconducting phase difference across each of the junctions. Any magnetic flux going through the loop produces a difference between these phases:

$$\begin{aligned}\Phi &= \int \mathbf{B} \cdot d\mathbf{S} = \oint \mathbf{A} \cdot d\mathbf{r} = \\ &= \frac{\hbar}{2e} \oint (\nabla\theta) \cdot d\mathbf{r} = \varphi_0(\phi_1 - \phi_2)\end{aligned}$$

Introducing for the sake of simplicity the frustration  $f = \pi\Phi/\Phi_0$  and the auxiliary phases  $\phi_{ext} = 1/2(\phi_1 + \phi_2)$  and  $\phi_{int} = 1/2(\phi_1 - \phi_2)$ :

$$\begin{cases} \phi_1 = \phi_{ext} + \phi_{int} = \delta + f \\ \phi_2 = \phi_{ext} - \phi_{int} = \delta - f \end{cases}$$

In a balanced SQUID (in which the junctions have the same critical currents  $I_{c1} = I_{c2} = I_{c0}$ ) the Josephson equations yield

$$\begin{aligned}I_b &= I_1 + I_2 = I_{c1} \sin(\delta + f) + I_{c2} \sin(\delta - f) = 2I_{c0} \cos f \sin \delta \\ V &= \varphi_0 \dot{\delta}.\end{aligned}$$

These equations have the same form than the Josephson equations of a single junction of phase  $\delta$  and critical current  $I_c(\Phi) = 2I_{c0} |\cos f|$ .

In conclusion, as far as the self-inductance of the loop  $L_L$  remains negligible compared to  $L_J(\Phi)$  and the bias current  $I_b$  is low compared to the critical current of the SQUID  $I_c(\Phi)$ , a SQUID behaves as a **flux-tunable inductor** with an inductance

$$L_J(\Phi) = \frac{\varphi_0}{2I_{c0} |\cos f|}.$$

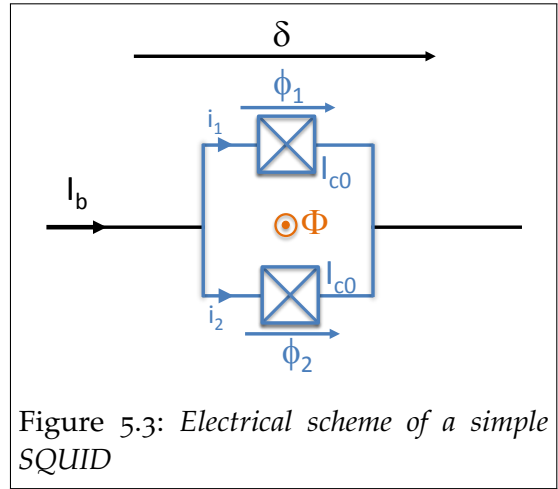


Figure 5.3: Electrical scheme of a simple SQUID

### 5.2.2 RESONANCE FREQUENCY OF A $\lambda/2$ RESONATOR CONTAINING A SQUID

Inserting the inductance  $L_J(\Phi)$  of a SQUID in the middle of a  $\lambda/2$  resonator changes its resonance frequency from  $\omega_1$  (without SQUID) to  $\omega_r(\Phi)$ . We will now calculate this new resonance frequency by calculating its input impedance. We will use a trick to simplify the calculation, and split by the thought the SQUID inductance in two series inductances  $L_J(\Phi)/2$ . By symmetry, the voltage at the middle point in-between the two inductances should be zero. The resonance frequency  $\omega_r$  thus has to be the same as that of a  $\lambda/4$  resonator shortcut to ground by an impedance  $Z_L = iL_J(\Phi)\omega/2$ . The input impedance of such a circuit at  $\omega$ , seen from the coupling capacitor, is

$$Z_{in} = Z_0 \frac{Z_L + iZ_0 \tan \beta\Lambda}{Z_0 + iZ_L \tan \beta\Lambda}$$

where  $\beta = \omega/\sqrt{\ell c}$  is the propagation constant. We now write  $\omega = \omega_1 + \delta\omega$  so that  $\tan \beta\Lambda = -1/\tan(\pi\delta\omega/2\omega_1)$ . This yields an input impedance

$$Z_{in} = Z_0 \frac{i\frac{L_J(\Phi)\omega}{2} - i\frac{Z_0}{\tan(\pi\delta\omega/2\omega_1)}}{Z_0 + \frac{L_J(\Phi)\omega}{2} \frac{1}{\tan(\pi\delta\omega/2\omega_1)}}$$

The resonance frequency is a pole of this input impedance given by the equation

$$Z_0 \tan \frac{\pi(\omega_r(\Phi) - \omega_1)}{2\omega_1} + \frac{L_J(\Phi)\omega_r(\Phi)}{2} = 0. \quad (5.1)$$

Expanding to the first order the tangent and using that  $l\Lambda = \pi Z_0/\omega_1$ , one can obtain the explicit expression

$$\omega_r(\Phi) \approx \omega_1 \frac{\ell\Lambda}{\ell\Lambda + L_J(\Phi)} = \frac{\omega_1}{1 + \epsilon(\Phi)} \quad (5.2)$$

where  $\epsilon(\Phi) = L_J(\Phi)/\ell\Lambda$ .

This variation of the resonance frequency also affects the coupling quality factor  $Q_c$ . By computing the equivalent RLC parallel circuit, one can also find its first order correction in  $\epsilon(\Phi)$ :

$$Q_c(\Phi) \approx Q_{c1} [1 + 4\epsilon(\Phi)], \quad (5.3)$$

where  $Q_{c1}$  is the bare coupling quality factor.

### 5.2.3 FULL ANALYSIS OF THE SQUID INDUCTANCE

In this paragraph we go further in the analysis of 5.2.1, considering the case of a symmetrical DC SQUID with a geometric inductance  $L_L$  as shown in Fig. 5.4 and

computing the first order corrections due to  $L_L$ , which were necessary to account for our experimental data.

We start from the Josephson equations, which give the currents in each branch  $I_i = I_{c0} \sin \phi_i$  ( $i = 1, 2$ ). The bias current  $I_b = I_1 + I_2$  as shown in Fig. 5.4. On the other hand, the presence of a circulating current  $J = (I_1 - I_2)/2$  yields a difference between the internal phase and the frustration:

$$\phi_{int} = 1/2(\phi_1 - \phi_2) = f - \pi L_L J / \Phi_0 = f - \pi \beta_0 \cos \phi_{int} \sin \phi_{ext},$$

where we have introduced  $\beta_0 = L_L I_{c0} / \Phi_0$ . Therefore the SQUID behaviour is controlled by the two relations:

$$\begin{cases} I_b = 2I_{c0} \cos \phi_{int} \sin \phi_{ext} \\ \phi_{int} = f - \pi \beta_0 \cos \phi_{ext} \sin \phi_{int} \end{cases} \quad (5.4)$$

Our goal is to obtain the equivalent inductance of the SQUID  $L_J = \varphi_0 \delta / \dot{I}_b$ . We first remark that  $\delta$  is obtained simply from  $\phi_{ext}$ , indeed

$$\delta = \frac{1}{2} \left[ \phi_1 + \phi_2 + \frac{L_L}{2\varphi_0} (I_1 + I_2) \right] = \frac{\pi}{2} \beta_0 \frac{I_b}{I_{c0}} + \phi_{ext}$$

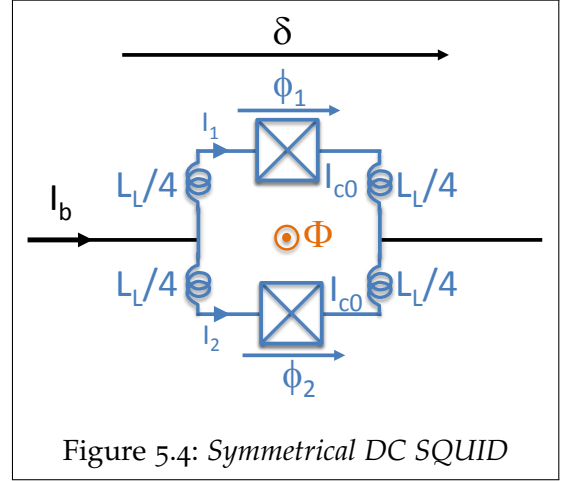


Figure 5.4: Symmetrical DC SQUID

and thus

$$L_J = \frac{\varphi_0 \pi \beta_0}{2I_{c0}} + \varphi_0 \frac{d\phi_{ext}}{dI_b}.$$

Therefore we only need to differentiate the relations 5.4 that give  $\phi_{int}$  and  $\phi_{ext}$  as a function of  $I_b$  and  $\Phi$ :

$$\begin{aligned} \frac{d\phi_{ext}}{dI_b} &= \frac{1}{2I_{c0}} \left[ \cos \phi_{ext} \cos \phi_{int} - \pi \beta_0 \frac{\sin^2 \phi_{ext} \sin^2 \phi_{int0}}{1 + \pi \beta_0 \cos \phi_{ext0} \cos \phi_{int0}} \right]^{-1} \approx \\ &\approx \frac{1}{2I_{c0}} \left[ \cos \phi_{ext0} \cos \phi_{int0} - \pi \beta_0 \sin^2 \phi_{ext0} \sin^2 \phi_{int0} \right]^{-1}. \end{aligned} \quad (5.5)$$

Now we need to develop  $\phi_{int}$  and  $\phi_{ext}$  to second order in  $I_b^2$  and to first order in  $\beta_0$  –still keeping the  $\beta_0 I_b^2$  terms. From Eq. 5.4 we obtain

$$\begin{aligned} \sin \phi_{ext} &\approx I_b / (2I_{c0} \cos \phi_{int}) \\ \phi_{int} &\approx f - \pi \beta_0 \sin f \sqrt{1 - [I_b / (2I_{c0} \cos f)]^2} \end{aligned}$$

which substituted in Eq. 5.5 and defining  $s(\Phi) = I_b / I_c(\Phi)$  yields

$$\frac{d\phi_{ext}}{dI_b} \approx \frac{1}{2I_{c0}} \frac{1}{\cos f + \pi \beta_0 \sin^2 f} \left[ 1 + \frac{s^2(\Phi)}{2} (1 + \pi \beta_0 \sin f \tan f) \right].$$

Therefore we get an inductance consisting in a linear term plus a non-linear term:

$$L_J(\Phi, I_b) = L_{J0}(\Phi) + A(\Phi)I_b^2 \quad (5.6)$$

with

$$L_{J0}(\Phi) = \frac{\varphi_0}{I_c(\Phi)} \left( 1 + \pi\beta_0 \frac{\cos^2 f - \sin^2 f}{\cos f} \right) \quad (5.7)$$

$$A(\Phi) = \frac{\varphi_0}{2I_c^3(\Phi)}. \quad (5.8)$$

#### 5.2.4 THE LINEAR REGIME

A SQUID behaves as a tunable inductance. This inductance, however, contains a non-linear  $A(\Phi)I_b^2$  term. This unwanted non-linear term is hardly an issue for using a SQUID-tuned resonator as coupling bus for qubits since the operation of such a device involves only one photon stored in the resonator. However, when characterizing the resonator, a large non-linearity  $A(\Phi)$  require to probe the resonator with a power  $P_{in}$  low enough to yield a  $\iota(\Lambda/2) \ll I_c(\Phi)$ . Specifically, when probing an over-coupled resonator ( $\gamma_L \ll \gamma$ ) with an input power  $P_{in}$  the average intra-resonator field (Eq. 2.17) is:

$$\bar{n} \approx \frac{Q_c}{\hbar\omega_r^2} P_{in}.$$

Thus, the higher the coupling quality factor  $Q_c$ , the more  $P_{in}$  has to be reduced to remain in the linear regime. As a consequence the bare  $\text{SNR} = P_{in}/(k_B T_N)$  is degraded, and longer averaging times are needed to characterize the resonator.

In all the data presented below, we have checked that  $P_{in}$  corresponds to the linear regime by repeating the measurements with half the power and checking that the transmission  $S_{21}$  remains constant.

The issues caused by the non-linearity becomes more significant as  $\Phi$  approaches  $\Phi_0/2$  where the critical current  $I_c(\Phi)$  vanishes. We analyze below the interesting situation which occurs when  $I_c(\Phi)$  becomes of the same order than the thermal current fluctuations.

### 5.3 IMPLEMENTATION

#### 5.3.1 FABRICATION OF TUNABLE RESONATORS

The tunable resonators are fabricated in the same way described in 2.1.4.3, but with an additional gap in the center of the resonator for inserting the SQUID as shown in Fig. 5.5.

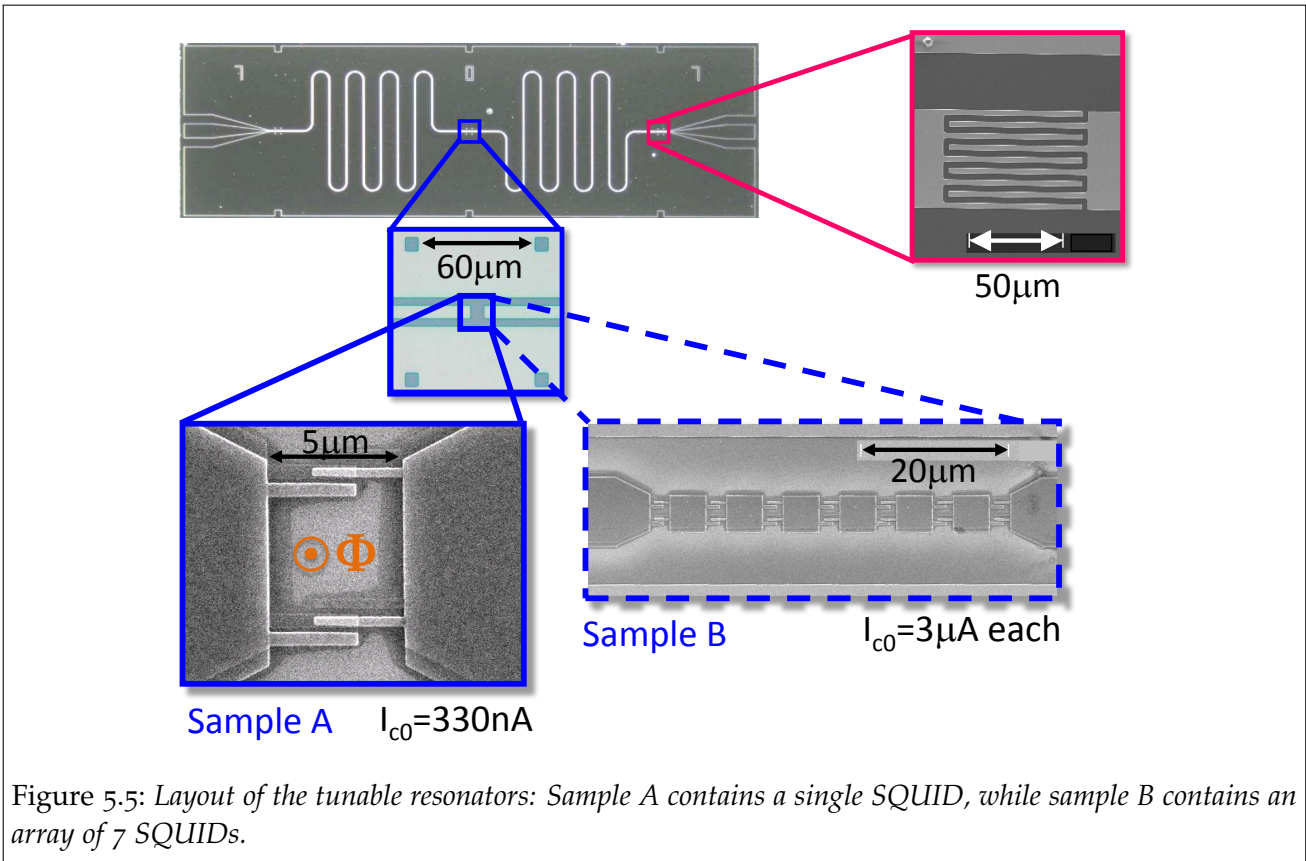


Figure 5.5: Layout of the tunable resonators: Sample A contains a single SQUID, while sample B contains an array of 7 SQUIDs.

The SQUIDs are fabricated by e-beam lithography and double angle deposition (see 3.2.1). In order to have a good aluminum-niobium contact, before depositing the aluminium SQUID, the niobium surface is cleaned by argon ion-milling ( $\lesssim 10^{18}$  neutralized 500 eV ions per  $\text{cm}^2$ ). The contact resistance has been found in the ohm range, yielding large tunnel junctions with negligible inductance.

### 5.3.2 MEASUREMENT SETUP

The experimental setup shown in Fig. 5.6 allows to measure the resonator transmission for intra-resonator energies of a few photons, which correspond to typical powers of  $-140$  dBm at resonator input. In this setup the resonators are thermalized to the lowest temperature stage of a dilution refrigerator operated at 40–60 mK. The measurements are performed with a room-temperature VNA which characterizes the transmission  $S_{21}$  in amplitude and phase as a function of the frequency. The input line is strongly attenuated (120 to 160 dB in total) with cold attenuators to protect the sample from external and thermal noise, and filtered above 2 GHz. The output line contains three cryogenic isolators, a cryogenic amplifier from Berkshire

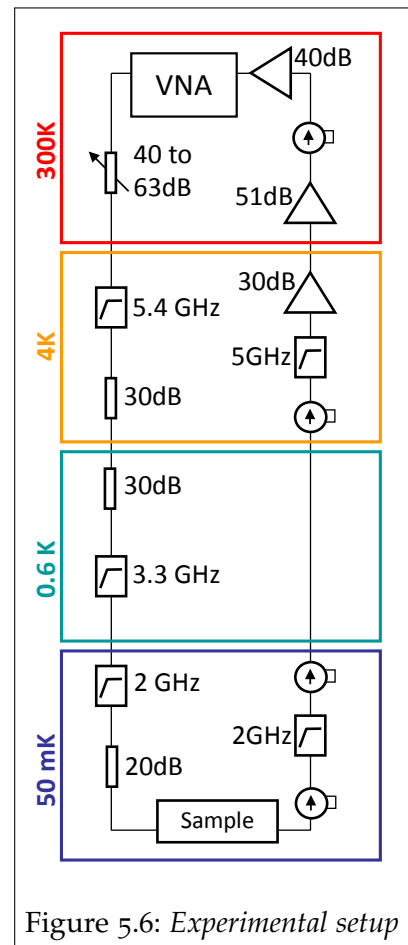


Figure 5.6: Experimental setup

operated at 4 K (with  $T_N = 3$  K) and several room-temperature amplifiers. Several filters are also used to reduce the average noise power to avoid amplifier saturation due to the noise.

#### 5.4 A FIRST TUNABLE RESONATOR (SAMPLE A)

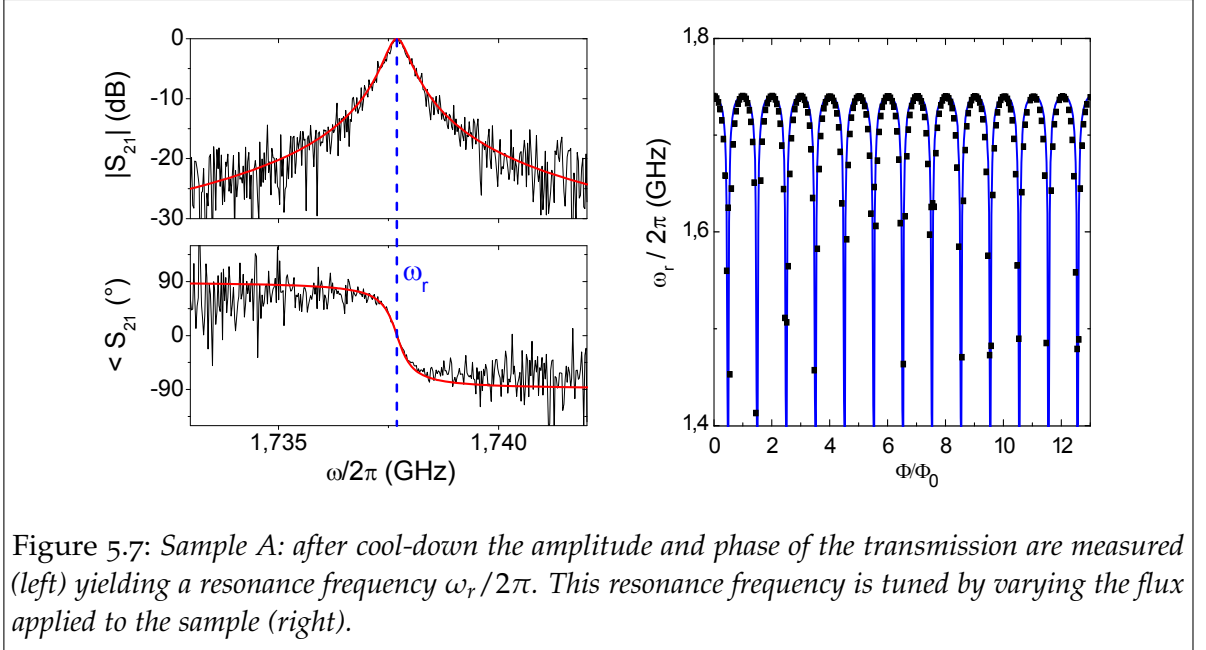


Figure 5.7: Sample A: after cool-down the amplitude and phase of the transmission are measured (left) yielding a resonance frequency  $\omega_r/2\pi$ . This resonance frequency is tuned by varying the flux applied to the sample (right).

A first experiment was performed with a tunable resonator containing a single SQUID with  $I_c = 330$  nA and large coupling capacitors  $C_c = 27$  fF, so that the quality factor is determined by  $Q_c = 3.4 \times 10^3$ .

After cooling down the sample we measured it with a VNA, yielding the  $S_{21}$  amplitude and phase curves shown on the left of Fig. 5.7. By fitting both the amplitude and the phase of this transmission, we obtained the resonance frequency  $\omega_r$  and the quality factor  $Q$ . When the flux through the SQUID loop is varied, the resonance frequency shifts periodically, as shown on the right of Fig. 5.7.

Parameter	Design	Fitted
Quality factor $Q$ ( $\Phi = 0$ )	$3.4 \times 10^3$	$3.5 \times 10^3$
Critical current $I_0$	375 nA	330 nA
Loop inductance $L_L$	$40 \pm 10$ pH	-
Bare resonance frequency $\omega_1/2\pi$	1.8 GHz	1.805 GHz

Table 5.1: Parameters of the sample A

To characterize the tunability range, we measured the resonance frequency for different values of the flux corresponding to the main flux period  $0 < \Phi/\Phi_0 < 1$  as



shown on the top of Fig. 5.8. This variation is fitted with Eq. 5.2 yielding a good agreement over the full period. The fit parameters which are found are very similar to the design values as shown in Table 5.1.

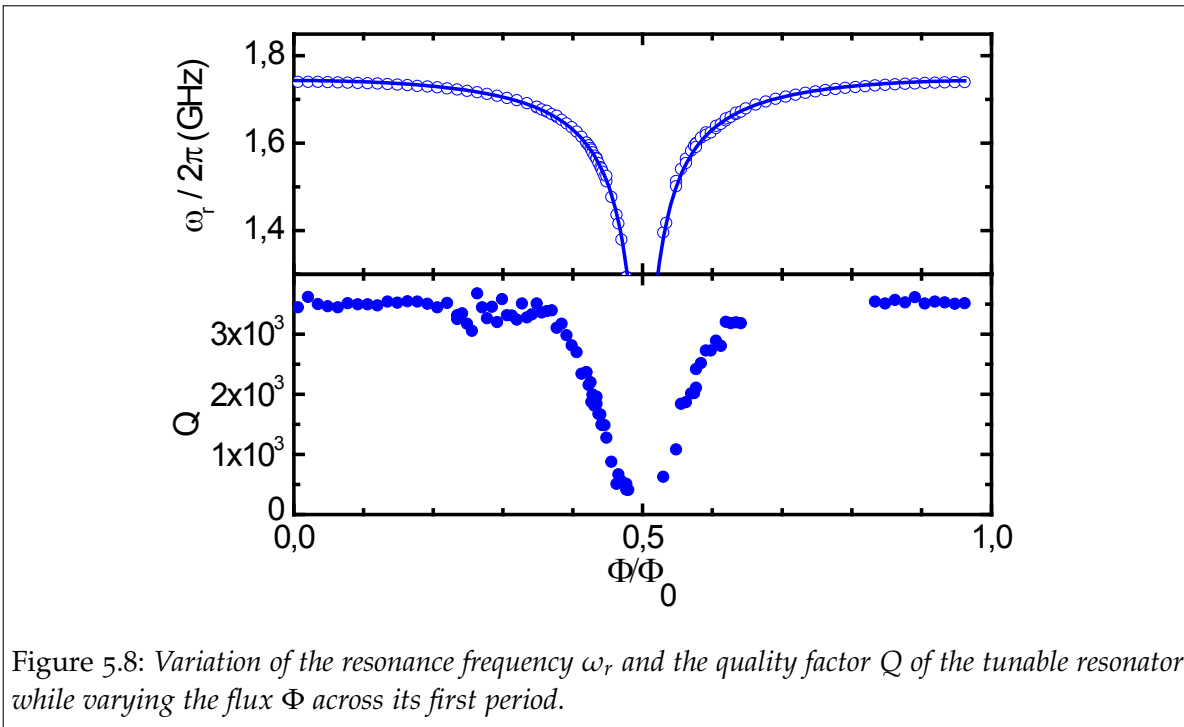


Figure 5.8: Variation of the resonance frequency  $\omega_r$  and the quality factor  $Q$  of the tunable resonator while varying the flux  $\Phi$  across its first period.

The quality factor is in Fig. 5.8 bottom panel: it shows a plateau around integer values of  $\Phi/\Phi_0$  where it is almost constant and equal to the coupling quality factor  $Q_c$ , whereas at  $\Phi/\Phi_0 = 1/2$  it shows a pronounced dip. This dip corresponds to a broadening which is not expected according to Eq. 5.3. In the next section we analyze a mechanism which may account for this unexpected effect: the thermal activation of non-linear effects in the SQUID.

#### 5.4.1 EXPLAINING THE DROP OF $Q$ AROUND $\Phi_0/2$

On the vicinity of  $\Phi_0/2$  the critical current  $I_c$  becomes very low, and it is precisely in this area that the quality factor drops down as shown in Fig. 5.8. This drop may thus be linked to the dependence of the resonator frequency  $\omega_r$  with the current  $I_b$  through the SQUID: since  $L_J(\Phi, I_b) = L_{J0}(\Phi) + A(\Phi)I_b^2$ , when  $I_b$  becomes comparable to  $I_c$ , the non-linear component of  $L_J$  cannot be neglected and induces an  $I_b$ -dependent shift of the resonance frequency. Now if  $I_c$  becomes so small that it is of the same order than the thermal fluctuations of the current inside of the resonator, these fluctuations induce an inhomogeneous broadening of the resonance  $\delta\omega_r(\Phi)$  which can be represented by the equivalent quality factor

$$Q_{inh} = \frac{\omega_r(\Phi)}{\delta\omega_r(\Phi)}$$

## Non-linear resonance shift

In order to calculate the fluctuations  $\delta\omega_r(\Phi)$  of the resonance frequency we write the equations of motion of the anharmonic oscillator. With this purpose we start by building the equivalent circuit seen from the junction. As sketched in Fig. 5.9, we first split the SQUID in a linear inductor  $L_{J0}(\Phi)$  and a non-linear one  $L_{NL}(\Phi) = A(\Phi) I_b^2$ . Then the biasing circuit is divided in two symmetric sub-circuits biased with a voltage  $V/2$ . The Thévenin equivalent for the sub-circuit between points A and B is

$$\begin{aligned} V_T &= V/a \\ Z_T &= 2R_0(1 - 2\varepsilon)/a^2 + j\pi R_0(1 + 2\varepsilon)(y - 1), \end{aligned}$$

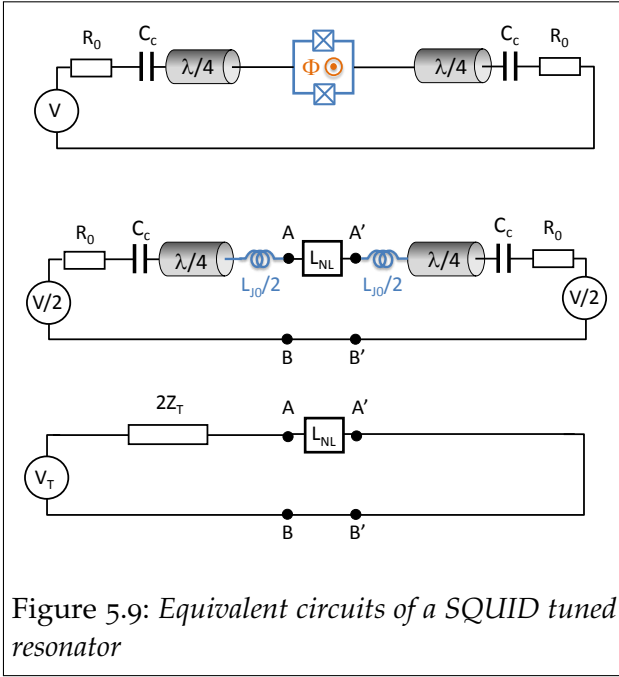


Figure 5.9: Equivalent circuits of a SQUID tuned resonator

with  $a = (C_c R_0 \omega_r)^{-1} = \sqrt{4Q/\pi}$ ,  $y = \omega/\omega_r(\Phi)$ ,  $\varepsilon = L_{J0}(\Phi)/L_{reson}$ , and keeping only the highest order terms in  $a$  –an approximation valid in the limit  $Q \gg 1$ . Finally, we find a mapping of  $Z_T$  with a series  $R'L'C'$  circuit by identifying the impedances:

$$\begin{aligned} 1/\sqrt{L'C'} &= \omega_r(\Phi) \\ \sqrt{L'/C'} &= \pi Z_0(1 + 2\varepsilon)/2 \\ R' &= 2R_0(1 - 2\varepsilon)/a^2. \end{aligned}$$

The equation of motion for this oscillator is, in the absence of drive,

$$0 = \frac{q}{C'} + R'\dot{q} + L'\ddot{q} \left[ 1 + \frac{L_{NL}}{2L'I_c^2(\Phi)} \left( \frac{dq}{dt} \right)^2 \right],$$

which can be written in a dimensionless form by introducing a dimensionless time  $\tau = \omega_r(\Phi)t$  and  $x = q\sqrt{L_{NL}\omega_r^2(\Phi)/2L'I_c^2(\Phi)}$ , yielding

$$\ddot{x} (1 + \dot{x}^2) + Q^{-1}\dot{x} + x = 0.$$

Now to find the resonance frequency of this dimensionless oscillator we follow the same treatment than Landau uses in his mechanics textbook<sup>156</sup> for the Duffing oscillator. In the absence of non-linearity, the resonance frequency would be 1. Now because of the cubic term, it is shifted to  $w = 1 + w^{(1)}$  for an amplitude of drive  $a$ . To determine the new  $w$  value one has to ensure that all higher order terms do not contain any contribution at  $w$  but only at  $nw$ . Let us first rewrite the equation as

$$\frac{1}{w^2}\ddot{x} + x = -\ddot{x}\dot{x}^2 - \left( 1 - \frac{1}{w^2} \right) \ddot{x},$$

with  $x = x^{(1)} + x^{(2)}$ ,  $x^{(1)}(\tau) = a \cos w\tau$  being the linear solution  $x^{(2)}$  the next order term, we get:

$$\ddot{x}^{(2)} + x^{(2)} = w^4 a^3 (\cos w\tau - \cos 3w\tau)/4 + 2w^{(1)} a \cos w\tau$$

where the term in  $\cos w\tau$  cancels if

$$w^{(1)} = -\frac{a^2}{4(2+a^2)} \approx -\frac{a^2}{8}.$$

And since the energy of the oscillator is  $e = (1/2)(x^2 + \dot{x}^2) = a^2/2$ , we obtain that  $w = 1 - e/4$ . and thus

$$\delta\omega_r = -\omega_r(\Phi) \left[ \frac{2\omega_r(\Phi)}{\pi R_0(1+2\varepsilon)} \right]^2 \frac{\varphi_0}{8I_c^3(\Phi)} E.$$

*Thermal fluctuations of the resonance frequency*

The fluctuations of the number of photons stored in the resonator are

$$\delta\bar{n}^2 = \bar{n}^2 - \bar{n}^2 = \bar{n}(\bar{n} + 1),$$

yielding the fluctuation of the energy

$$\sqrt{\delta\bar{E}^2} = \sqrt{\bar{E}^2 + \bar{E}\hbar\omega_r(\Phi)},$$

where the average thermal energy is

$$\bar{E} = \frac{\hbar\omega_r(\Phi)}{\exp(\hbar\omega_r(\Phi)/k_B T) - 1}.$$

The characteristic time of these fluctuations being the resonator damping time  $Q/\omega_r$  with  $Q \gg 1$ , a simple quasi-static analysis leads to an inhomogeneous broadening with an equivalent quality factor

$$Q_{inh}^{-1}(\Phi) = \frac{\delta\omega_r(\Phi, \sqrt{\delta\bar{E}^2})}{\omega_r(\Phi)} = - \left( \frac{2\omega_r(\Phi)}{\pi Z_0 [1 + 2\varepsilon(\Phi)]} \right)^2 \frac{\varphi_0}{8I_c^3(\Phi)} \sqrt{\delta\bar{E}^2}. \quad (5.9)$$

*Comparison with experimental data*

Since the resonator is over-coupled, the effect of the quality factor  $Q_L$  coming from the losses in the total quality factor is negligible. Therefore the total quality factor  $Q(\Phi)$  can be predicted to be  $Q(\Phi) = [Q_c^{-1}(\Phi) + Q_{inh}^{-1}(\Phi)]^{-1}$  where  $Q_c(\Phi)$  is given by 5.3, and  $Q_{inh}^{-1}$  by Eq. 5.9, with the sample temperature 60 mK. This prediction is compared to the experimental data in Fig. 5.10, showing rather good agreement.

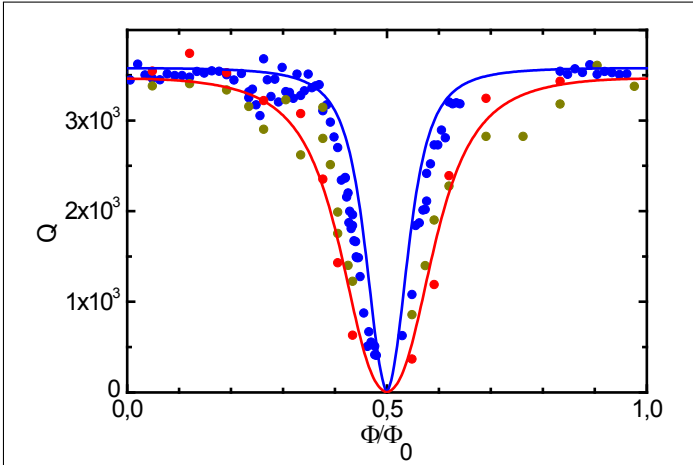


Figure 5.10: Quality factors measured in the experiment 1 as a function of the flux : the blue disks correspond to the lowest  $50 \pm 10\text{mK}$  temperature, golden disks correspond to a hotter value and red disks to the hottest one. In these two latter cases the sample temperature could not be determined due to a dysfunction of the thermometer. Comparison with theoretical prediction: the blue line corresponds to  $60\text{mK}$  and the red one to  $200\text{mK}$ .

To check that the broadening by thermal noise is the dominant mechanism causing the dip in  $Q$ , we increased the temperature of the sample and measured the variation of  $Q$  in flux. The maximum  $Q$  remains unchanged, whereas the dip broadens. The data taken at the highest temperature (red circles) are best fitted by taking a temperature of  $200\text{mK}$  in the model. However, for this specific set of data, no quantitative comparison with the sample temperature was possible, since the thermometers were out of order during this part of the experiment.

#### Other sources of broadening

Although the mechanism described above gives a satisfactory explanation for the broadening, other mechanisms

could also yield a degradation of the quality factor at  $\Phi/\Phi_0 = 1/2$ :

- the SQUID is highly sensitive to flux noise around  $\Phi/\Phi_0 = 1/2$ . The universal  $1/f$  flux noise is therefore expected to cause a broadening of the resonance in this region. However, the typical amplitude of the  $1/f$  flux noise which is measured in other experiments<sup>91</sup> ( $A = 10^{-5}\Phi_0$ ) would result in a broadening several orders of magnitude smaller than the one observed, and the sensitivity of the broadening to the temperature is difficult to explain with such mechanism.
- if there is a dissipative channel in the SQUID, an increase in the inductance  $L_J(\Phi)$  results in a higher voltage  $V$  across the SQUID and a higher dissipated power  $V^2/R$ . The Chalmers group suggested<sup>56</sup> that a dissipative channel l—with  $R_s$  of some  $\text{k}\Omega$ — could exist due to sub-gap resonances of the junction. The variation of these sub-gap resonances with the temperature of the sample could in this case account for the variation in temperature of the broadening.

## 5.5 A HIGH-Q TUNABLE RESONATOR (SAMPLE B)

The sample A was over-coupled with  $Q \simeq Q_c = 3500$  to ensure that it was easy to measure it in the linear regime. To study the internal losses we designed another sample with a higher  $Q_c = 6 \times 10^5$ . In order to avoid the non-linear effects which could arise when measuring a resonator with much larger  $Q_c$  in the same conditions of the former experiment, we reduced the amount of non-linearity by increasing the critical current  $I_{c0}$  of the SQUID junctions. To keep the same tunability range we compensated the reduction of  $L_J(\Phi) \propto I_0^{-1}$  by fabricating a chain of several SQUIDs

in series, as shown in Fig. 5.5. Specifically we built a chain of 7 SQUIDs in series, each one with a critical current  $I_{c0} = 7I_{c0}^{(sample\ A)} \simeq 2.1\ \mu\text{A}$ . To fabricate SQUIDs with such a high critical current while keeping the same junctions geometry, we the insulator oxide layer was fabricated with a much lower pressure of oxygen (0.1 mbar instead of 18.1 mbar in sample A).

### 5.5.1 RESONANCE PARAMETERS VERSUS FLUX

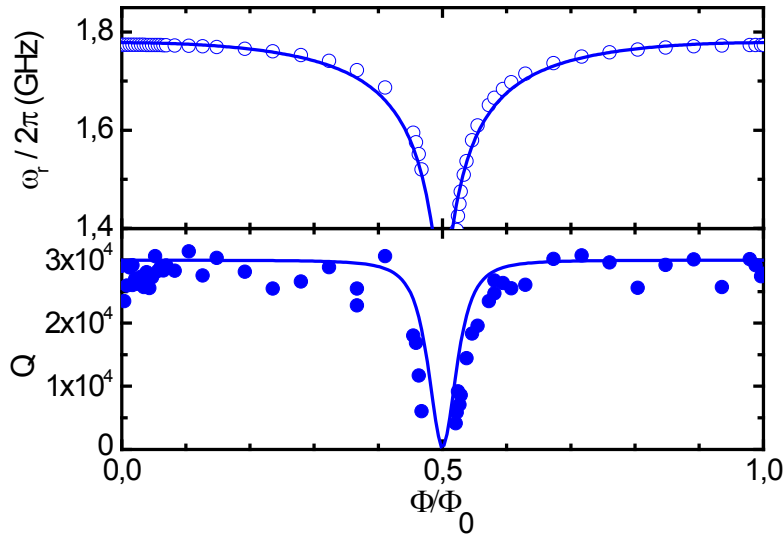


Figure 5.11: Resonance frequency (top panel, the blue disks are experimental data, the blue line the fit) and quality factor (bottom panel: the blue circles are experimental data, the blue line the thermal noise model prediction) of the high- $Q$  tunable resonator (sample B) for the first flux period.

We characterized the resonance frequency and quality factor while scanning the flux over the first period  $0 < \Phi < \Phi_0/2$  as shown in the Fig. 5.11. The frequencies range from 1.38 GHz to 1.78 GHz, that is, a tunability range of 400 MHz, 22% of  $\omega_r(0)$ .

The fit of the resonance frequency is performed using the same expressions above but with  $\epsilon(\Phi) = 7L_J(\Phi)/(\Lambda\ell)$  where  $L_J(\Phi)$  is the inductance of a single SQUID. The agreement is good, although slightly worse than for the sample A, probably due to some dispersion of the loop areas of the different SQUIDs in the array. The fitted value of the critical current  $I_c = 2.2\ \mu\text{A}$  is close to the design value.

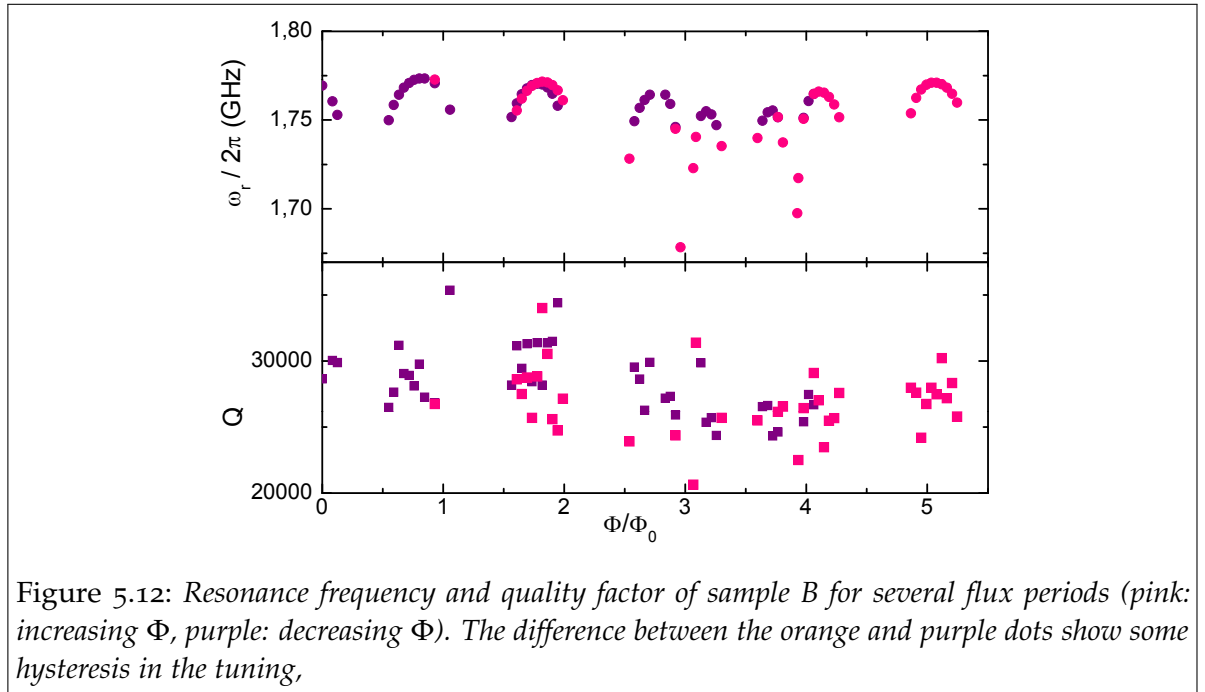
The maximum quality factor  $Q \approx 3 \cdot 10^4$  is one order of magnitude larger than the one of sample A, and it is lower than  $Q_c = 6 \times 10^5$ , which shows that it is limited by the internal losses  $Q \simeq Q_L$ .

The variation of  $Q$  with the flux is similar to the sample A: it shows a stable a plateau around integer flux quanta and a dip in the vicinity of half flux quanta. The continuous line in the Fig. 5.11 represents the prediction of the model described above for the sample temperature of 50 mK, and is in good overall agreement with the experimental data, although slightly worse than for sample A. This is probably due to the presence of several SQUIDs which parameters may have some dispersion.

Parameter	Design	Fitted
Quality factor $Q$ ( $\Phi = 0$ )	$Q_c = 6 \times 10^5$	$3 \times 10^4$
Critical current $I_0$	$2.5 \mu\text{A}$	$2.2 \mu\text{A}$
Loop inductance $L_L$	$20 \pm 10 \text{ pH}$	-
Bare resonance frequency $\omega_1/2\pi$	1.85 GHz	1.85 GHz

Table 5.2: Parameters of the sample B

### 5.5.2 PERIODICITY IN FLUX



To investigate the dependence of the maximum quality factor across different periods of flux, a scan over several periods of flux was performed yielding the results shown in Fig. 5.12.

The quality factor plateau remains at the same value across the different periods, showing that the maximum  $Q$  does not depend on the flux. On the other hand, the resonance frequencies for integer flux quanta vary from one flux period to another. This is probably due to some dispersion in the parameters of the different SQUIDs in the array: a dispersion in the loop areas of the different SQUIDs would indeed lead to different fluxes threading them and an aperiodic response. The highest resonance frequencies are attained in the period around  $\Phi = 0$ , showing that this period correspond to the minimum flux, since for zero flux the frequency is the highest whatever the areas of the SQUIDs.

### 5.5.3 MAXIMUM QUALITY FACTOR AND TEMPERATURE DEPENDENCE

In the sample B we have access to the quality factor  $Q_L$  due to the intra-resonator losses. This quality factor  $Q_L \simeq 3 \times 10^4$  is one order of magnitude lower than the quality factors  $Q_L$  observed in resonators without SQUIDs. Other groups also have observed quality factors  $Q_L \sim 10^4$  in tunable resonators containing SQUIDs with  $Q_c \simeq 2 \times 10^4$ . It seems therefore that the introduction of a SQUID brings some additional losses to the resonator. To obtain more information on these losses, we measured the quality factor while varying the temperature of the sample.

On Fig. 5.13 the maximum quality factors of the resonator ( $\Phi = 0$ ) are plotted as a function of the temperature. At the floor temperature  $-50$  mK– the quality factors are around  $3 \times 10^4$ , but when the temperature is raised to  $150$  mK, they surprisingly rise to  $\sim 5 \times 10^4$ . To check a possible effect of the vortices trapped in the aluminium film, we thermally cycled the sample several times in zero magnetic field, but the behaviour was perfectly reproducible.

This effect, which remembers what happens with bare resonators (see 2.1.5.2), may be caused by microscopic two-level systems present in the junction's barrier with transition frequency  $\sim 1.8$  GHz. With such an hypothesis the variation of  $Q$  with temperature can be easily explained: at  $150$  mK, the thermal fluctuations saturate those TLSs, inhibiting their absorption, whereas at lower temperatures, more TLSs are in their ground state and contribute to the intra-resonator field relaxation. Another possible explanation would be the absorption of the resonator energy by non-equilibrium quasi-particles<sup>89</sup>.

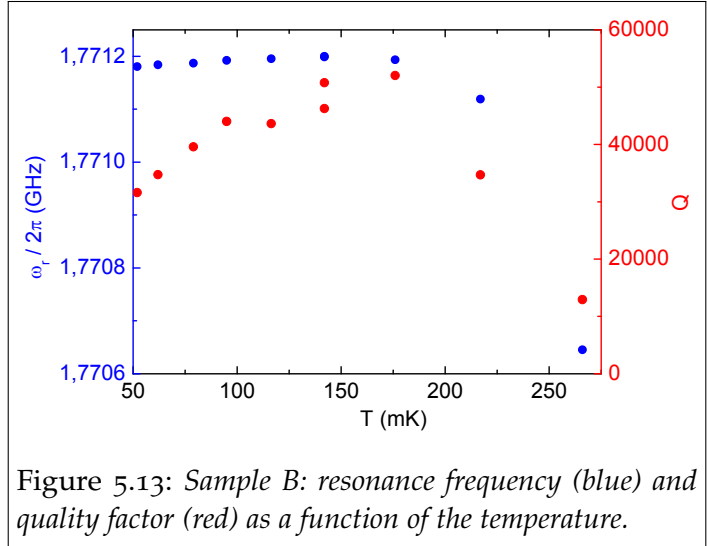


Figure 5.13: Sample B: resonance frequency (blue) and quality factor (red) as a function of the temperature.





## FUTURE DIRECTIONS

---

At the time of writing this thesis, the combined research efforts of all the groups developing superconducting qubits worldwide have made them the most serious candidates for implementing solid-state quantum processors. Over the last years, substantial improvements have been achieved for the coherence times<sup>19,9</sup>, for the fidelity of single-qubit<sup>125</sup> and two-qubit gates, for the fidelity of the readout methods<sup>53,150</sup>. The progress made is evidenced by the demonstration of entanglement of several superconducting qubits<sup>150,118</sup> and, recently, by the operation of simple quantum algorithms –Grover and Deutsch-Josza– with a superconducting circuit<sup>157</sup>. This first demonstration of solid-state quantum computation on a very elementary two-qubit processor qubits was nevertheless jeopardized by the need to repeat the experiment due to the lack of a high fidelity and single shot readout of the qubits. To go further beyond, i.e. to develop an operational quantum processor with a few qubits, will request significant progress.

Fundamental quantum physics experiments have also been successfully performed with superconducting quantum circuits in several groups using transmon qubits<sup>158,57</sup>, but also phase qubits. Using a cQED setup with a superconducting phase qubit coupled to a microwave resonator, the generation of arbitrary Fock states in the resonator<sup>159,160</sup> with photon number even higher than achieved in cavity QED, the monitoring of their decoherence<sup>161</sup>, and the generation and probing of NOON states<sup>1</sup> were successively demonstrated at UCSB.

We would like to finish this thesis by discussing about some of the future directions of the domain that seem particularly important to us, and about the experiments that, we believe, could bring a substantial progress to the field.

## CONTROLLING THE RELAXATION OF SUPERCONDUCTING QUBITS

One of the most critical limitations for superconducting qubits is their comparatively low coherence times compared to truly microscopic entities like ions, atoms or spins. The relaxation channel through photon emission in the electromagnetic environment of the qubits is understood, and its rate can be reduced by improving the microwave design of the circuits. However, other limiting relaxation channels with unknown origin are presently limiting the relaxation time of superconducting qubits in the few microseconds range. The lack of understanding and control of these relaxation channels is a serious threat for the development of superconducting processors. Two mechanisms have been proposed to explain their origin, namely the presence of impurities at the surface of the superconducting electrodes, and the presence of out-of-

---

<sup>1</sup>A NOON state is a superposition  $|n\rangle_a |0\rangle_b + |0\rangle_a |n\rangle_b$  of  $n$  photons in the electromagnetic mode  $a$  and 0 in the mode  $b$  and vice versa.

equilibrium quasi-particles in the superconductor. An important obstacle in probing relaxation mechanisms and test possible counter-measures is the low reproducibility of the qubit fabrication process: indeed, samples produced using the same recipe show a large dispersion in their relaxation times.

In order to perform a systematic study of relaxation, it would be therefore highly desirable to build qubits with different parameters but on the same chip. Frequency multiplexing techniques like the ones described in Section 1.4, which have already been successfully tested in Yale’s Qlab<sup>46</sup>, would allow to measure all the qubits through a single microwave line. In this way, accurate statistics on the influence of a given parameter on the lifetime could be obtained. This systematic study should allow to conclude on the incidence of the surface impurities on  $\Gamma_1$  by varying the surfaces and parameters of the qubit electrodes, and also on the incidence on the quasi-particles by making gap engineering in the superconducting electrodes.

Another much simpler way to obtain valuable information on the losses in superconducting qubit circuits would be to investigate more in depth simpler superconducting circuits such as microwave resonators and, in particular, tunable microwave resonators incorporating Josephson junctions. For instance, the fact that tunable resonators seem to have a lower quality factor than bare resonators indicates that Josephson junctions may contribute to losses. A systematic study of the influence of the tuning SQUID parameters on the magnitude of the losses could bring some clues on the dissipation mechanisms in Josephson circuits. Even more interestingly, the quality factor of these tunable resonators which is heavily degraded when tuning them far away from their maximum resonance frequency, informs us on the flux noise in the SQUID. In this case, introducing an asymmetry in the SQUID would reduce the influence of the flux noise. An experiment probing a few tunable resonators built in the same chip but with different asymmetries could tell if the flux noise is indeed the limiting mechanism for the quality factor in tunable resonators. Once this issue solved, design variations could clarify the influence of the different experimental parameters involving the junctions –junction critical current, junction current density, contacts, etc.

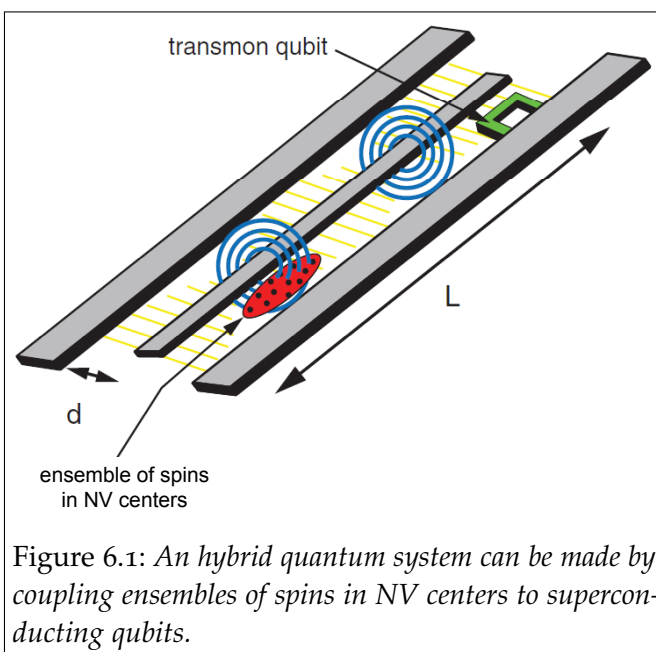


Figure 6.1: An hybrid quantum system can be made by coupling ensembles of spins in NV centers to superconducting qubits.

## HYBRID SYSTEMS: COUPLING CIRCUITS TO MICROSCOPIC SPINS

We have seen that superconducting artificial atoms couple strongly to electromagnetic fields, allowing fast single- and two-qubit gates, and benefit from a large flexibility in the design of their parameters, although their coherence times constitute an important limiting factor. On the other hand, natural microscopic quantum systems –atoms, photons, electron or nuclear spins– often benefit from a natural decoupling from environmental noise, which re-

sults in much longer coherence times<sup>162</sup>.

It is thus appealing to take the best of both worlds by combining artificial and natural quantum systems in hybrid quantum circuits that would exhibit long coherence times while allowing rapid quantum state manipulation. For instance, an hybrid architecture could be envisioned by combining a superconducting quantum processor where operations would be performed and a large set of microscopic elements acting as quantum memories for storing the intermediate results of the computation.

Among the systems proposed to make such hybrid structures, paramagnetic electron spins of nitrogen-vacancy (NV) centers<sup>163,164</sup> in diamond are particularly appealing. Indeed, coherent manipulation of these spins has attracted great interest in recent years because of the possibility to monitor optically a single spin at room temperature, and of their long coherence time, up to ms<sup>165</sup>. Recently, the strong coupling between a superconducting resonator and an ensemble of NV spins, which behave as a single effective spin, was demonstrated in the Quantronics group<sup>166</sup>, and similar results were obtained for other spin systems<sup>167</sup>. These experiments open the way to coherent transfer of energy mediated by a resonator between an effective spin and superconducting qubits<sup>168,169</sup>, which would constitute the basic building block of an hybrid architecture. Finally, in addition to the electron spin resonance, note that NV centers have two very interesting internal degrees of freedom: their narrow optical resonance, which might be used for converting coherently microwave into optical quantum states of the field<sup>170</sup>, and their coupling to the nitrogen atom nuclear spin could give access to coherence times much longer than with electron spins<sup>171</sup>.

## TOWARDS A SCALABLE SUPERCONDUCTING QUBIT ARCHITECTURE

The superconducting circuit in which a quantum algorithm was operated for the first time<sup>157</sup> contains only two qubits coupled and readout through the same resonator. Although the same scheme was used to couple three qubits<sup>172</sup>, it seems difficult to keep the same architecture while scaling up the number of qubits much further. Furthermore, this architecture does not provide single shot qubit readout.

The architecture overseen in this thesis, where a set of superconducting qubits are individually readout by a dedicated non-linear resonator and coupled together by a tunable resonator, might be a better starting point to build a processor with 5-10 qubits able to demonstrate more sophisticated algorithms<sup>44</sup>, and possibly to implement error correction on a single qubit. Scaling up this architecture would however not be simple since the qubits have to be detuned enough in order to avoid spurious interactions between them, and have readout resonators with staggered frequencies.

To go further in the direction of a scalable architecture, we propose a cascaded architecture (see Fig. 6.2) in which a tunable resonator mediates the interactions between several clusters of 5-10 qubits connected to a tunable resonator. The interaction between qubits in different clusters would be performed through intermediate steps in which the excitation of the qubit of one cluster is swapped (possibly partially) to its coupling bus, then to the general coupling bus and finally to the coupling bus of the cluster containing the target qubit. The overhead brought by this procedure increases

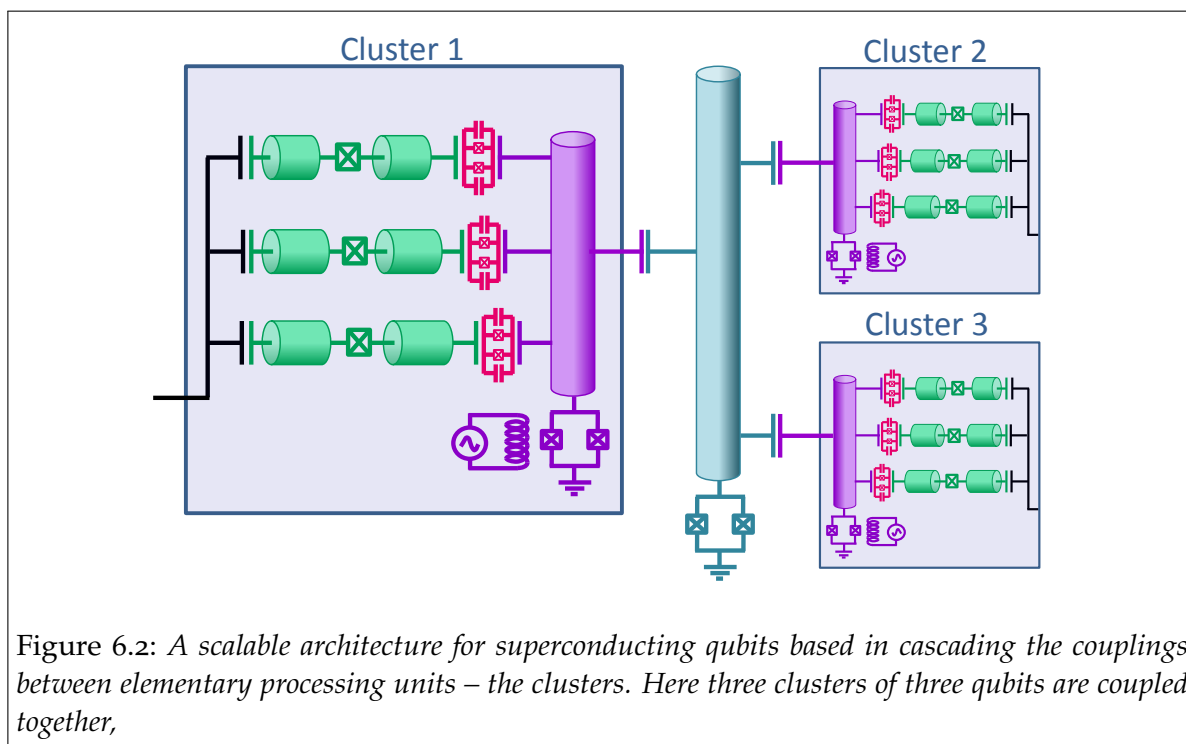


Figure 6.2: A scalable architecture for superconducting qubits based in cascading the couplings between elementary processing units – the clusters. Here three clusters of three qubits are coupled together,

the time needed for performing two qubit gates, but only logarithmically with the total number of qubits.

## QUANTUM OPTICS WITH MICROWAVE PHOTONS

We discussed in this thesis the first experimental results on a TLS coupled to a non-linear resonator. The physical effects found arise from the interplay between two phenomena already thoroughly investigated in quantum optics, but independently: non-linearity, which yields parametric amplification, optical bistability and squeezing, and, on the other hand, strong coupling of an atom to an electromagnetic field. Circuit QED thus allows to investigate interesting situations that combine these phenomena. Investigating their interplay opens a broad variety of new experiments, for instance, the study of the qubit dephasing when it interacts with squeezed resonator fields. This type of experiment performed in electrical microwave circuits in which concepts and phenomena well known in quantum optics play a central role is not an exception. Combined with other recent ones, they tend to form a new field of quantum optics in which microwave photons propagating along 1D transmission lines interact with electrical circuits. Let us mention here a few recent results that contribute to enlarge the tool-box available for quantum optics experiments in the microwave domain.

First, single photon sources have been operated by letting an excited TLS to emit single photons in a transmission line<sup>173</sup>, and non-classical first and second order coherence functions of the microwave field were characterized in ETH<sup>114</sup> using efficient digital signal processing. Indeed, mixing signals and digitizing mixed-down signals is far easier than in optics, which allows to perform sophisticated signal analysis. Note that photon counting has not been achieved yet, but is thought to be

possible.

A very different kind of photon source has also been recently demonstrated in the Quantronics group using a Josephson junction connected in series with a microwave resonator with resonance  $\omega_r$ , and voltage biased below the gap. In this Coulomb blockade regime of the Josephson junction, the transfer of a Cooper pair has to release an energy  $2eV$  in the junction environment, which yields one photon in the resonator per pair when  $2eV = \hbar\omega_r$ . A more sophisticated circuit with a junction in series with two resonators  $\omega_{r1}$  and  $\omega_{r2}$  could, in principle, produce pairs of entangled photons at these frequencies. Scattering experiments of photons propagating on a transmission line coupled to superconducting qubits has also been achieved recently, with the demonstration of a microwave single photon switch<sup>174</sup>. Superconducting quantum circuits are thus now opening the way to a *quantum microwave engineering* which a large variety of tools and resources able to reproduce for microwave fields functions well known in quantum optics, but also other impossible to difficult to achieve with optical fields.





## APPENDIX



## ADIABATIC ESCAPE THEORY FOR CBA

---

We introduce here some theoretical tools which allow to calculate analytically, in the adiabatic limit, the transition rates between  $\bar{B}$  and  $B$  due to thermal or quantum fluctuations. This development follows closely Vijay's thesis<sup>139</sup>, but is adapted to the CBA case. Note that this theory is only applicable to the adiabatic case which is far from our experiment in which the measurement pulse raises very fast. We did not performed a specific experiment with slowly raising pulses to check the agreement with this theory: such experiments have been previously performed by Vijay for JBA<sup>139</sup> and by Metcalfe for CBA<sup>46</sup> and are in good agreement with theory.

### A.1 NOISE AND CBA DYNAMICS

The thermal and quantum fluctuations can be considered as a perturbation which slightly changes the oscillation state of the CBA. In which conditions can this perturbation lead to a transition between the  $\bar{B}$  and  $B$  states?

Several authors have studied the dynamics of the Duffing oscillator<sup>135,136</sup> when moving apart from the stable steady-states  $\bar{B}$  and  $B$ . they have shown that the phase plane  $(q_{\parallel}, q_{\perp})$  is divided in *two basins of attraction* in each of which the resonator evolves towards the stable equilibrium point  $\bar{B}$  or  $B$  respectively. The frontier between these two basins, so-called *separatrix*, contains the third solution of Eq. 4.1, the saddle point through which it is easiest to escape from one basin of attraction to the other

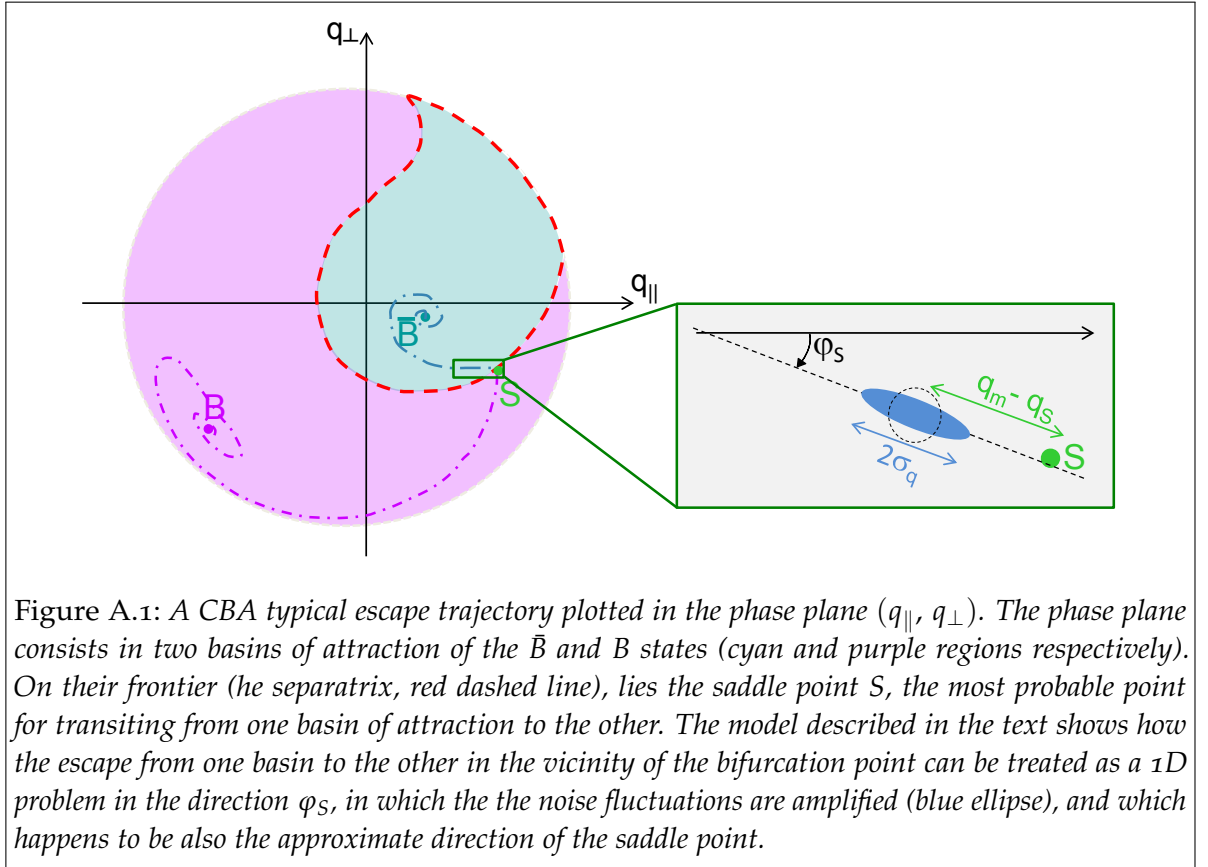
### A.2 THE EFFECT OF NOISE ON A DRIVEN CBA: PARAMETRIC EFFECTS

We study now, in the particular case of CBA, how the noise perturb the solution, and how this perturbation may allow to reach the saddle point and to transit to the bifurcated state  $B$ . For this purpose, we consider the CBA equation of motion (Eq. 4.3) with the drive term written as an arbitrary input field  $a_{in}(t)$ , which contains the usual drive, plus some noise:

$$\ddot{q} + 2\Gamma\dot{q} + \omega_r^2 q + \frac{p}{2I_{c0}^2} \dot{q}^2 \ddot{q} = \frac{2\sqrt{Z_0}}{L_t} a_{in}(t) \quad (\text{A.1})$$

Now to study the perturbation brought by the noise, which we represent as a perturbation  $q_N$ , we linearize the equation of motion around the steady-state driven solution  $q_m(t) = q_0 \sin(\omega_m t - \theta)$ . Replacing  $q(t) = q_m(t) + q_N(t)$  in the above equation yields:

$$\ddot{q}_N [1 + \alpha (1 + \cos(2\omega_m t - 2\theta))] + 2\dot{q}_N [\Gamma - \alpha\omega_m \sin(2\omega_m t - 2\theta)] + \omega_r^2 q_N = \frac{2\sqrt{R}a_{in}(t)}{L_t}$$



where  $\alpha = pq_0^2\omega_m^2 / (4I_{c0}^2)$ . With a Fourier transform, within the RWA and with the approximations  $\omega/\omega_m \approx 1$ ,  $\omega_m/\omega_r \approx 1$  we obtain

$$\left( \underbrace{\frac{\omega_r - \omega_m}{\Gamma}}_{\Omega} - \underbrace{\frac{\omega_m - \omega}{\Gamma}}_{-\Omega - f} - \underbrace{\frac{\alpha\omega_r}{2\Gamma}}_{2\epsilon} - i \right) q_N(\omega) - \frac{\omega\alpha e^{-i2\theta}}{4\Gamma} q_N^\dagger(2\omega_m - \omega) = \underbrace{\sqrt{\frac{2\hbar}{R\omega_0}}}_{\Xi} a_{in}(\omega)$$

Now with  $f = (\omega - \omega_r)/\Gamma$ , this yields

$$(\Omega \mp f - 2\epsilon - i) q_N(\pm f) - e^{-i2\theta} \epsilon q_N^\dagger(\mp f) = \Xi a_{in}(f)$$

which is formally equivalent to the expression for JBA<sup>139</sup>. These two equations plus their two conjugates have a solution

$$\frac{q_N(\pm f)}{\Xi} = A(\pm f) a_{in}(\pm f) + B(\pm f) a_{in}^\dagger(\mp f) \quad (\text{A.2})$$

where

$$A(f) = \frac{\Omega - 2\epsilon + f + i}{\epsilon^2 + (i + f)^2 - (\Omega - 2\epsilon)^2}$$

$$B(f) = \frac{\epsilon e^{i2\theta}}{\epsilon^2 + (i + f)^2 - (\Omega - 2\epsilon)^2}.$$

Eq. A.2 links creation and annihilation operators at frequencies which are symmetric around  $\omega_r$ , a typical feature of parametric amplification.

Now, when the system is very close to the bifurcation point, it can be shown that the fluctuations are maximally amplified in a direction  $\varphi_M$  which is almost the one of the saddle point, and maximally de-amplified in the orthogonal direction. This allows to neglect the effect of the fluctuations in this later direction, and to address only the 1D problem along the direction  $\varphi_M$ . The variance of the noise along this axis of maximal and minimal amplification can be calculated very similarly to JBA<sup>139</sup>, yielding respectively:

$$\langle q_N^2 \rangle_{\pm} = C_e k_B T_{eff} \sqrt{\frac{(\Omega - 2\epsilon)^2 + 1}{(\Omega - 2\epsilon)^2 + 1 \pm \epsilon}}.$$

At the bifurcation points ( $\epsilon = 1/3 (2\Omega \mp \sqrt{\Omega^2 - 3})$ ) the maximal fluctuation diverges, while the minimal one becomes  $k_B T_{eff} / 2E_c$ , i.e. it becomes squeezed by 3 dB compared to the undriven resonator, the maximum squeezing which may be obtained in the intra-resonator field<sup>175</sup>,

Expanding to the lowest order in  $\Omega$  the fluctuation around the bifurcation point yields:

$$\langle q_N^2 \rangle_{+} = C_e k_B T_{eff} \frac{1}{2\sqrt{3} \sqrt{1 - \frac{V_m}{V_{bif}^{+}}}}$$

whereas the same expansion yields for the distance to the saddle point

$$(q_m - q_s)^2 = \frac{32e^2}{9} \frac{\Omega}{Q} \left( 1 - \frac{V_m}{V_{bif}^{+}} \right).$$

Now the probability of escape from  $\bar{B}$  to  $B$  is reduced to a 1D escape through a barrier, which is the standard Kramer's problem<sup>176</sup>. The escape probability has an Arrhenius form

$$\Gamma_{esc} = \frac{\omega_a}{2\pi} \exp\left(\frac{1}{3} \frac{(q_m - q_s)^2}{\langle q_N^2 \rangle_{+}}\right) = \frac{\omega_a}{2\pi} \exp\left(\frac{32e^2}{9\sqrt{3}} \frac{\Omega}{Q} \frac{1}{C_e k_B T_{eff}} \left(1 - \frac{V_m}{V_{bif}^{+}}\right)^{3/2}\right) \quad (\text{A.3})$$

where the factor  $1/3$  is due to the overestimation of the barrier in the harmonic approximation<sup>177</sup>.

### A.3 1D EQUIVALENT: THE CUBIC META-POTENTIAL

An analysis equivalent to the above one was performed in the early 1980s by Dykman and Krivoglaz<sup>177</sup>, who remarked that when the drive is near to the bifurcation point  $\beta \sim \beta^+$ , the system dynamics becomes over-damped and one of the coordinates

becomes much slower than all the other time scales. Consequently Eq. 4.1 can be approximated<sup>1</sup> by a Langevin equation for an effective slow coordinate  $y(\tau)$ :

$$\frac{dy}{d\tau} = -\frac{dV}{d\tau} + \beta_N(t) \quad (\text{A.4})$$

equivalent to a massless Brownian particle subject to a random force  $\beta_N(t)$  moving in a cubic potential  $V(y)$  (shown in Fig. A.2)

$$V(y) = -1/3by^3 + \xi y$$

where

$$b(\Omega) = \frac{p(\Omega)}{\sqrt{\beta^+}} \left[ 5p(\Omega) - 3 + 3(2p(\Omega) - 1)^2 (p(\Omega) - 1) \Omega^2 \right]$$

with  $p(\Omega) = 2/3 \pm 1/3\sqrt{1 - 3\Omega^{-2}}$  and

$$\xi(\Omega, \beta) = \frac{\beta^+(\Omega) - \beta}{2\sqrt{\beta^+(\Omega)}}$$

Approximating the harmonic oscillation of the particle at the bottom of the potential, the oscillation frequency is

$$\omega_{mp} = 2\sqrt{b\xi} \approx \frac{4Q}{3\sqrt{3}} \frac{\Delta_m^2}{\omega_r}$$

In order for the above Langevin equation to be valid the movements in the meta-potential should be slow compared to the resonator dynamics:  $\omega_{mp} \ll \Gamma$ . If it is the case, the switching from  $\bar{B}$  to  $B$  can be modelled as the escape of the particle above the barrier of the meta-potential well, and the probability of escape can be found to be equivalent than the one obtained above (Eq. A.3).

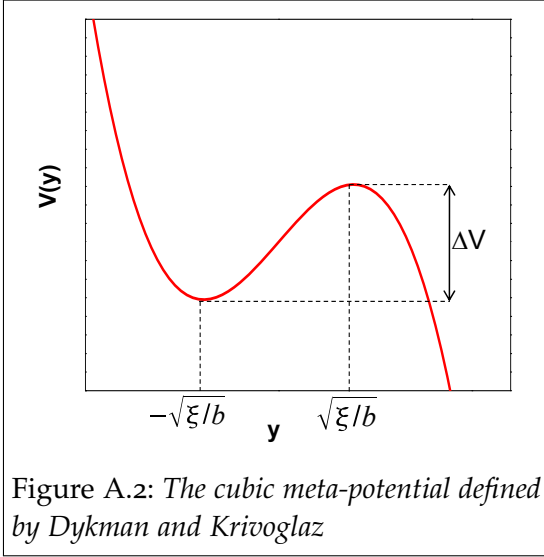


Figure A.2: The cubic meta-potential defined by Dykman and Krivoglaz

<sup>1</sup>A similar approach can be used for studying the re-trapping from  $B$  to  $\bar{B}$  state at  $\beta \sim \beta^-$

## TABLE OF SYMBOLS

---

### B.1 MATHEMATICAL SYMBOLS

$\mathcal{L}()$	Laplace transform
$\mathcal{F}()$	Fourier transform
$*$	Convolution
$u(t)$	Heaviside step function
$\dot{x}$ or $\partial_t x$	Time derivative of $x$
$E[\bullet]$ or $\langle \hat{\bullet} \rangle$	Ensemble average (classical or quantum signals, resp.)
$\bar{x}$	Time average of $x$

### B.2 QUANTUM FORMALISM

$\hat{\rho}$	Density matrix
$\mathcal{L}$	Lindblad super-operator
$\mathcal{D}[\hat{A}]$	Collapse super-operator
$\mathcal{M}[\hat{A}]$	Measurement super-operator
$ \bullet\rangle$	State $\bullet$
$ \alpha\rangle$	Coherent state of complex amplitude $\alpha$
$ g\rangle$	TLS ground state
$ e\rangle$	TLS excited state
$\hat{K}$	Operator $K$
$\hat{a}^\dagger$	Creation operator
$\hat{a}$	Annihilation operator



### B.3 CIRCUIT QED

$\omega_r$	Resonator's bare resonance frequency
$\kappa$	Resonator's bandwidth
$\kappa_L$	Resonator's internal losses
$Q$	Resonator's quality factor
$Q_c$	Resonator's coupling quality factor
$Z_c$	Resonator's characteristic impedance
$Z_0$	Transmission line's characteristic impedance
$\bar{c}$	Wave velocity in the transmission line
$\beta$	Propagation constant in a transmission line
$\Lambda$	Length of a transmission line resonator
$C_c$	Coupling capacitor
$\varphi_0 = \hbar/(2e)$	Reduced flux quantum
$\Phi_0 = h/(2e)$	Flux quantum
$I_c$	Critical current of a Josephson junction
$\omega_{01} = \omega_{ge}$	Transmon ground-to-excited transition frequency
$\omega_{i,j}$	Transmon $i \rightarrow j$ transition frequency
$C_g$	Gate capacitor
$g$	Transmon-resonator coupling constant
$T_N$	Equivalent noise temperature
$T_c$	Cryostat's lowest stage temperature
$V_m$	Microwave voltage used for measuring the resonator
$V_d$	Microwave voltage used for driving the TLS
$X = I, Q$	Intra-resonator field in-phase and quadrature components
$X_{out} = I_{out}, Q_{out}$	In-phase and quadrature components at resonator output
$X_D = I_D, Q_D$	Demodulated field in-phase and quadrature components
$\chi$	Dispersive cavity pull

$\Delta = \omega_c - \omega_{01}$	Resonator-TLS detuning
$\omega_R$	Rabi frequency
$\Gamma_1$	TLS relaxation rate
$\Gamma_2$	TLS decoherence rate
$\Gamma_\phi$	TLS pure dephasing rate
$f_{z,R}(t)$	Decay of the coherences due to pure dephasing
$\Gamma_{\omega_R}$	TLS driven decoherence rate at $\omega_R$
$\tilde{\Gamma}_1$	TLS driven relaxation rate
$\tilde{\Gamma}_2 = \Gamma_R$	TLS driven decoherence rate
$\tilde{\Gamma}_\phi$	TLS pure driven dephasing rate
$\Gamma_\phi^{ph}$	TLS measurement-induced dephasing
$\gamma_\phi^{ph}$	TLS measurement-induced dephasing per photon
$n_{crit}$	Critical number of photons for the dispersive approximation
$\delta = \Phi/\varphi_0$	Split-CPB frustration
$E_C$	CPB charging energy
$E_J$	CPB Josephson energy
$\bar{n}$	Average number of photons stored in the resonator
$\Delta_r = \omega_r - \omega_d$	Resonator-drive detuning
$\omega_d$	Resonator's drive frequency
$\pm\delta\phi_0$	Observed resonator's phase shift due to TLS
$\pm\delta\varphi_0$	Full resonator's phase shift due to TLS
$\hat{\rho}^{th}$	TLS steady-state density matrix at thermal equilibrium
$\hat{\rho}^{sat}$	TLS steady-state density matrix when saturated
$\tilde{\omega}_a$	Lamb-shifted resonator frequency
$\omega_a$	Lamb and AC-Stark shifted resonator frequency
$D$	State distinguishability

## B.4 NON-LINEAR CQED

$\Delta_r = \omega_r - \omega_m$	Resonator-drive detuning
$S_{\omega_m}^{\rho_{ee}}$	S-curve corresponding to $ e\rangle$ population $\rho_{ee}$ and $\omega_m$
$2\chi_{JBA}$	Frequency displacement of S-curves: effective cavity pull
$\bar{B}$	Low-amplitude state of a Duffing resonator
$B$	High-amplitude state of a Duffing resonator
$t_M$	CBA effective measurement time
$t_R$	CBA measuring pulse rise time
$t_S$	CBA measuring pulse switching plateau length
$t_H$	CBA measuring pulse hold plateau length
$P_H$	CBA measuring pulse hold plateau power

## B.5 OTHER PHYSICAL QUANTITIES

$\ell$	Inductance per unit length of a transmission line
$\ell_K$	Kinetic inductance per unit length
$c$	Capacitance per unit length of a transmission line
$T_c$	Critical temperature of a superconductor
$n_n$	Quasi-particle density
$T_F$	Cryostat lowest stage temperature
$\mathcal{L}$	Leggett's extensive difference
$\mathcal{D}$	Leggett's disconnectivity

## BIBLIOGRAPHY

---

- [1] J. M. Martinis, M. H. Devoret and J. Clarke. Experimental tests for the quantum behavior of a macroscopic degree of freedom: The phase difference across a Josephson junction. *Physical Review B* **35**, 4682–4698 (1987). (Cited on pages 9 and 27)
- [2] D. Deutsch. Quantum Theory, the Church-Turing Principle and the Universal Quantum Computer. *Proceedings of the Royal Society of London. A. Mathematical and Physical Sciences* **400**, 97–117 (1985). (Cited on pages 9, 18, 27, and 34)
- [3] M. A. Nielsen *et al.* Quantum Computation and Quantum Information. *American Journal of Physics* **70**, 558–559 (2002). (Cited on pages 9, 17, 27, 34, and 69)
- [4] Y. Nakamura, Y. A. Pashkin and J. S. Tsai. Coherent control of macroscopic quantum states in a single-Cooper-pair box. *Nature* **398**, 786–788 (1999). (Cited on pages 9, 11, 27, 28, and 66)
- [5] J. M. Martinis, S. Nam, J. Aumentado and C. Urbina. Rabi Oscillations in a Large Josephson-Junction Qubit. *Physical Review Letters* **89**, 117901 (2002). (Cited on pages 9, 27, and 172)
- [6] D. Vion *et al.* Manipulating the Quantum State of an Electrical Circuit. *Science* **296**, 886–889 (2002). (Cited on pages 9, 11, 27, 28, 69, 70, 71, 76, and 174)
- [7] I. Chiorescu, Y. Nakamura, C. J. P. M. Harmans and J. E. Mooij. Coherent Quantum Dynamics of a Superconducting Flux Qubit. *Science* **299**, 1869–1871 (2003). (Cited on pages 9 and 27)
- [8] P. Bertet *et al.* Dephasing of a Superconducting Qubit Induced by Photon Noise. *Physical Review Letters* **95**, 257002 (2005). (Cited on pages 9, 27, and 71)
- [9] J. A. Schreier *et al.* Suppressing charge noise decoherence in superconducting charge qubits. *Physical Review B* **77**, 180502 (2008). (Cited on pages 9, 11, 27, 29, 70, 75, and 213)
- [10] A. Blais, R. Huang, A. Wallraff, S. M. Girvin and R. J. Schoelkopf. Cavity quantum electrodynamics for superconducting electrical circuits: An architecture for quantum computation. *Physical Review A* **69**, 62320 (2004). (Cited on pages 9, 27, 107, and 124)
- [11] A. Wallraff *et al.* Strong coupling of a single photon to a superconducting qubit using circuit quantum electrodynamics. *Nature* **431**, 162–167 (2004). (Cited on pages 9, 27, and 80)
- [12] J. M. Raimond, M. Brune and S. Haroche. Manipulating quantum entanglement with atoms and photons in a cavity. *Reviews of Modern Physics* **73**, 565 (2001). (Cited on pages 9 and 27)

- [13] S. Haroche and J. Raimond. *Exploring the quantum* (Oxford University Press, 2006). (Cited on pages 9, 27, 41, 43, 80, and 84)
- [14] M. Brune *et al.* Quantum Rabi Oscillation: A Direct Test of Field Quantization in a Cavity. *Physical Review Letters* **76**, 1800 (1996). (Cited on pages 10 and 28)
- [15] V. Bouchiat, D. Vion, P. Joyez, D. Esteve and M. H. Devoret. Quantum Coherence with a Single Cooper Pair. *Physica Scripta* **T76**, 165 (1998). (Cited on pages 10, 28, and 66)
- [16] A. Cottet. *Implementation of a quantum bit in a superconducting circuit*. Ph.D. thesis, Universite Paris 6 (2002). (Cited on pages 11, 28, 66, 67, 68, 72, and 74)
- [17] G. Ithier *et al.* Decoherence in a superconducting quantum bit circuit. *Physical Review B* **72**, 134519 (2005). (Cited on pages 11, 29, 66, 71, 72, 73, and 175)
- [18] F. Nguyen. *Cooper pair box circuits : two-qubit gate, single-shot readout, and current to frequency conversion*. Ph.D. thesis, Universite Paris 6 (2008). (Cited on pages 11, 29, and 76)
- [19] J. Koch *et al.* Charge-insensitive qubit design derived from the Cooper pair box. *Physical Review A* **76**, 42319 (2007). (Cited on pages 11, 29, 66, 70, 71, 76, 77, 81, and 213)
- [20] M. H. Devoret, S. Girvin and R. Schoelkopf. Circuit-QED: How strong can the coupling between a Josephson junction atom and a transmission line resonator be? *Annalen der Physik* **16**, 767–779 (2007). (Cited on pages 11 and 29)
- [21] D. I. Schuster *et al.* ac Stark Shift and Dephasing of a Superconducting Qubit Strongly Coupled to a Cavity Field. *Physical Review Letters* **94**, 123602 (2005). (Cited on pages 12, 30, 100, 103, 109, 112, and 181)
- [22] J. Gambetta *et al.* Qubit-photon interactions in a cavity: Measurement-induced dephasing and number splitting. *Physical Review A* **74**, 042318 (2006). (Cited on pages 12, 30, 100, 103, 106, and 181)
- [23] J. Gambetta *et al.* Quantum trajectory approach to circuit QED: Quantum jumps and the Zeno effect. *Physical Review A* **77**, 012112 (2008). (Cited on pages 14, 30, 84, 108, 124, 129, and 130)
- [24] A. N. Korotkov and D. V. Averin. Continuous weak measurement of quantum coherent oscillations. *Physical Review B* **64**, 165310 (2001). (Cited on pages 14, 30, 32, 94, 115, 116, 118, and 128)
- [25] H. Goan and G. J. Milburn. Dynamics of a mesoscopic charge quantum bit under continuous quantum measurement. *Physical Review B* **64**, 235307 (2001). (Cited on pages 14, 30, and 116)
- [26] A. Shnirman, D. Mozyrsky and I. Martin. Output spectrum of a measuring device at arbitrary voltage and temperature. *Europhysics Letters* **67**, 840–846 (2004). (Cited on pages 14 and 30)
- [27] B. Misra and E. C. G. Sudarshan. The Zeno’s paradox in quantum theory. *Journal of Mathematical Physics* **18**, 756–763 (1977). (Cited on pages 14, 32, and 114)

- [28] J. Bernu *et al.* Freezing Coherent Field Growth in a Cavity by the Quantum Zeno Effect. *Physical Review Letters* **101**, 180402–4 (2008). (Cited on pages 14, 32, 114, 115, and 143)
- [29] A. J. Leggett and A. Garg. Quantum mechanics versus macroscopic realism: Is the flux there when nobody looks? *Physical Review Letters* **54**, 857 (1985). (Cited on pages 15, 33, 93, 94, 130, 132, and 138)
- [30] A. J. Leggett. Testing the limits of quantum mechanics: motivation, state of play, prospects. *Journal of Physics Condensed Matter* **14**, 415 (2002). (Cited on pages 15, 33, and 138)
- [31] S. F. Huelga, T. W. Marshall and E. Santos. Proposed test for realist theories using Rydberg atoms coupled to a high-Q resonator. *Physical Review A* **52**, R2497 (1995). (Cited on pages 15, 33, 132, and 141)
- [32] R. Ruskov, A. N. Korotkov and A. Mizel. Signatures of Quantum Behavior in Single-Qubit Weak Measurements. *Physical Review Letters* **96**, 200404 (2006). (Cited on pages 15, 16, 33, 94, and 133)
- [33] M. M. Wilde and A. Mizel. Addressing the clumsiness loophole in a Leggett-Garg test of macrorealism. *ArXiv* 1001.1777 (2010). (Cited on pages 15, 33, and 133)
- [34] J. F. Clauser, M. A. Horne, A. Shimony and R. A. Holt. Proposed Experiment to Test Local Hidden-Variable Theories. *Physical Review Letters* **23**, 880 (1969). (Cited on pages 15, 33, and 130)
- [35] M. E. Goggin *et al.* Violation of the Leggett-Garg inequality with weak measurements of photons. *ArXiv* 0907.1679 (2009). (Cited on pages 16 and 33)
- [36] J. Xu, C. Li, X. Zou and G. Guo. Experimentally identifying the transition from quantum to classical with Leggett-Garg inequalities. *ArXiv* 0907.0176 (2009). (Cited on pages 16 and 33)
- [37] R. Lapiedra. The fail of determinism and the limits of Bohm hidden variable theory. *ArXiv* 0903.4339 (2009). (Cited on pages 16, 33, and 141)
- [38] F. D. Zela. Single-qubit tests of Bell-like inequalities. *Physical Review A* **76**, 042119 (2007). (Cited on pages 16, 33, 139, and 140)
- [39] R. Ruskov and A. N. Korotkov. Quantum feedback control of a solid-state qubit. *Physical Review B* **66**, 041401 (2002). (Cited on pages 16, 33, and 142)
- [40] M. A. Castellanos-Beltran, K. D. Irwin, G. C. Hilton, L. R. Vale and K. W. Lehnert. Amplification and squeezing of quantum noise with a tunable Josephson metamaterial. *Nature Physics* **4**, 929–931 (2008). (Cited on pages 16, 33, 95, 142, and 185)
- [41] N. Bergeal *et al.* Analog information processing at the quantum limit with a Josephson ring modulator. *Nature Physics* **6**, 296–302 (2010). (Cited on pages 16, 33, 95, and 142)
- [42] A. Palacios-Laloy *et al.* Spectral measurement of the thermal excitation of a superconducting qubit. *Physica Scripta* **T137**, 014015 (2009). (Cited on pages 17 and 34)

- [43] A. K. Ekert. Quantum cryptography based on Bell's theorem. *Physical Review Letters* **67**, 661 (1991). (Cited on pages 17 and 34)
- [44] P. W. Shor. Polynomial-Time Algorithms for Prime Factorization and Discrete Logarithms on a Quantum Computer. *SIAM Journal on Computing* **26**, 1484–1509 (1997). (Cited on pages 18, 34, and 215)
- [45] P. K. Day, H. G. LeDuc, B. A. Mazin, A. Vayonakis and J. Zmuidzinas. A broadband superconducting detector suitable for use in large arrays. *Nature* **425**, 817–821 (2003). (Cited on pages 18 and 35)
- [46] M. Metcalfe. *A new microwave readout for superconducting qubits*. Ph.D. thesis, Yale University (2008). (Cited on pages 18, 35, 214, and 221)
- [47] M. Wallquist, V. S. Shumeiko and G. Wendin. Selective coupling of superconducting charge qubits mediated by a tunable stripline cavity. *Physical Review B* **74**, 224506 (2006). (Cited on pages 18, 22, 35, 39, and 197)
- [48] D. P. Divincenzo. The Physical Implementation of Quantum Computation. *Fortschritte der Physik* **48**, 771–783 (2000). (Cited on pages 18, 36, and 143)
- [49] M. Boissonneault, J. M. Gambetta and A. Blais. Nonlinear dispersive regime of cavity QED: The dressed dephasing model. *Physical Review A* **77**, 060305–4 (2008). (Cited on pages 19, 37, 82, 149, and 176)
- [50] M. D. Reed *et al.* High Fidelity Readout in Circuit Quantum Electrodynamics Using the Jaynes-Cummings Nonlinearity. *ArXiv* 1004.4323 (2010). (Cited on pages 20, 37, and 151)
- [51] I. Siddiqi *et al.* RF-Driven Josephson Bifurcation Amplifier for Quantum Measurement. *Physical Review Letters* **93**, 207002 (2004). (Cited on pages 21, 38, and 152)
- [52] E. Boaknin *et al.* Dispersive microwave bifurcation of a superconducting resonator cavity incorporating a Josephson junction. *ArXiv* 0702445 (2007). (Cited on pages 21, 38, and 155)
- [53] F. Mallet *et al.* Single-shot qubit readout in circuit quantum electrodynamics. *Nature Physics* **5**, 791–795 (2009). (Cited on pages 21, 38, and 213)
- [54] M. A. Sillanpaa, J. I. Park and R. W. Simmonds. Coherent quantum state storage and transfer between two phase qubits via a resonant cavity. *Nature* **449**, 438–442 (2007). (Cited on pages 22, 39, and 197)
- [55] A. Palacios-Laloy *et al.* Tunable Resonators for Quantum Circuits. *Journal of Low Temperature Physics* **151**, 1034–1042 (2008). (Cited on pages 23 and 39)
- [56] M. Sandberg *et al.* Tuning the field in a microwave resonator faster than the photon lifetime. *Applied Physics Letters* **92**, 203501–3 (2008). (Cited on pages 23, 40, 198, and 208)
- [57] A. Palacios-Laloy *et al.* Experimental violation of a Bell's inequality in time with weak measurement. *Nature Physics* **6**, 442–447 (2010). (Cited on pages 33 and 213)



- [58] C. Cohen-Tannoudji, J. Dupont-Roc and G. Grynberg. *Photons and Atoms - Introduction to Quantum Electrodynamics* (Wiley, 1997). (Cited on page 41)
- [59] B. Yurke and J. S. Denker. Quantum network theory. *Physical Review A* **29**, 1419 (1984). (Cited on page 41)
- [60] M. H. Devoret. Quantum Fluctuations. 351 (Elsevier, Amsterdam, Netherlands, 1997). (Cited on page 41)
- [61] C. Gerry and P. Knight. *Introductory Quantum Optics* (Cambridge University Press, 2004). (Cited on page 42)
- [62] D. F. Walls and G. J. Milburn. *Quantum Optics* (Springer, 2008). (Cited on pages 42, 48, 116, 117, and 127)
- [63] K. Kurokawa. Power Waves and the Scattering Matrix. *Microwave Theory and Techniques, IEEE Transactions on* **13**, 194–202 (1965). (Cited on page 47)
- [64] C. W. Gardiner and M. J. Collett. Input and output in damped quantum systems: Quantum stochastic differential equations and the master equation. *Physical Review A* **31**, 3761 (1985). (Cited on page 48)
- [65] C. W. Gardiner and P. Zoller. *Quantum noise* (Springer, 2004). (Cited on pages 48 and 127)
- [66] L. Frunzio, A. Wallraff, D. Schuster, J. Majer and R. Schoelkopf. Fabrication and characterization of superconducting circuit QED devices for quantum computation. *Applied Superconductivity, IEEE Transactions on* **15**, 860–863 (2005). (Cited on page 54)
- [67] M. Goppl *et al.* Coplanar waveguide resonators for circuit quantum electrodynamics. *Journal of Applied Physics* **104**, 113904 (2008). (Cited on page 54)
- [68] K. C. Gupta, R. Garg, I. Bahl and P. Bhartia. *Microstrip Lines and Slotlines* (Artech House, Norwood, 1996). (Cited on page 54)
- [69] D. M. Pozar. *Microwave engineering* (Wiley, New York), 2004 edn. (Cited on pages 58, 59, and 87)
- [70] R. Collin. *Foundations for microwave engineering* (McGraw-Hall, New York), 1993 edn. (Cited on page 59)
- [71] M. Tinkham. *Introduction to superconductivity* (Courier Dover Publications, 2004). (Cited on page 61)
- [72] D. C. Mattis and J. Bardeen. Theory of the Anomalous Skin Effect in Normal and Superconducting Metals. *Physical Review* **111**, 412 (1958). (Cited on page 61)
- [73] R. Barends. *Photon-detecting superconducting resonators*. Ph.D. thesis, TU Delft (2009). (Cited on pages 61 and 62)

- [74] D. Rutledge, D. Neikirk and D. Kasilingam. Integrated-circuit antennas. In *Infrared and Millimeter Waves*, vol. 10, 1–87 (K. J. Button, New York, 1983), academic edn. (Cited on page 64)
- [75] A. Vayonakis and J. Zmuidzinas. Radiative losses from 2-D apertures (2001). (Cited on page 64)
- [76] P. Macha *et al.* Losses in coplanar waveguide resonators at millikelvin temperatures. *Applied Physics Letters* **96**, 062503 (2010). (Cited on page 64)
- [77] S. Kumar *et al.* Temperature dependence of the frequency and noise of superconducting coplanar waveguide resonators. *Applied Physics Letters* **92**, 123503 (2008). (Cited on page 64)
- [78] T. Lindstrom, J. E. Healey, M. S. Colclough, C. M. Muirhead and A. Y. Tzalenchuk. Properties of superconducting planar resonators at millikelvin temperatures. *Physical Review B* **80**, 132501 (2009). (Cited on page 64)
- [79] J. Gao *et al.* A semiempirical model for two-level system noise in superconducting microresonators. *Applied Physics Letters* **92**, 212504 (2008). (Cited on page 64)
- [80] J. Gao, J. Zmuidzinas, B. A. Mazin, H. G. LeDuc and P. K. Day. Noise properties of superconducting coplanar waveguide microwave resonators. *Applied Physics Letters* **90**, 102507 (2007). (Cited on page 64)
- [81] J. Gao *et al.* Experimental evidence for a surface distribution of two-level systems in superconducting lithographed microwave resonators. *Applied Physics Letters* **92**, 152505 (2008). (Cited on page 64)
- [82] A. D. O’Connell *et al.* Microwave dielectric loss at single photon energies and millikelvin temperatures. *Applied Physics Letters* **92**, 112903 (2008). (Cited on page 64)
- [83] V. Bouchiat. *Quantum fluctuations of the charge in single electron and single Cooper pair devices*. Ph.D. thesis, Universite Paris 6 (1997). (Cited on page 66)
- [84] N. Boulant *et al.* Quantum nondemolition readout using a Josephson bifurcation amplifier. *Physical Review B* **76**, 014525 (2007). (Cited on pages 66 and 152)
- [85] A. A. Houck *et al.* Controlling the Spontaneous Emission of a Superconducting Transmon Qubit. *Physical Review Letters* **101**, 080502 (2008). (Cited on pages 71, 79, and 174)
- [86] D. J. V. Harlingen *et al.* Decoherence in Josephson-junction qubits due to critical-current fluctuations. *Physical Review B* **70**, 064517 (2004). (Cited on pages 71 and 75)
- [87] R. W. Simmonds *et al.* Decoherence in Josephson Phase Qubits from Junction Resonators. *Physical Review Letters* **93**, 077003 (2004). (Cited on page 71)
- [88] J. M. Martinis *et al.* Decoherence in Josephson Qubits from Dielectric Loss. *Physical Review Letters* **95**, 210503 (2005). (Cited on pages 71 and 76)

- [89] J. M. Martinis, M. Ansmann and J. Aumentado. Energy Decay in Josephson Qubits from Non-equilibrium Quasiparticles. *ArXiv* 0904.2171 (2009).  
(Cited on pages 75, 147, and 211)
- [90] D. Schuster. *Circuit Quantum Electrodynamics*. Ph.D. thesis, Yale University (2007).  
(Cited on page 75)
- [91] F. C. Wellstood, C. Urbina and J. Clarke. Low-frequency noise in dc superconducting quantum interference devices below 1 K. *Applied Physics Letters* **50**, 772–774 (1987).  
(Cited on pages 75, 175, and 208)
- [92] F. C. Wellstood, C. Urbina and J. Clarke. Flicker ( $1/f$ ) noise in the critical current of Josephson junctions at 0.09–4.2K. *Applied Physics Letters* **85**, 5296 (2004).  
(Cited on pages 75 and 175)
- [93] A. B. Zorin *et al.* Background charge noise in metallic single-electron tunneling devices. *Physical Review B* **53**, 13682 (1996).  
(Cited on page 76)
- [94] E. M. Purcell, H. C. Torrey and R. V. Pound. Resonance Absorption by Nuclear Magnetic Moments in a Solid. *Physical Review* **69**, 37 (1946).  
(Cited on page 79)
- [95] H. Carmichael. *An Open Systems Approach to Quantum Optics*. No. 18 in Lecture Notes in Physics Monographs (Springer, Berlin, Heidelberg, 1993). (Cited on page 84)
- [96] A. N. Korotkov. Noisy quantum measurement of solid-state qubits: Bayesian approach. *ArXiv* cond-mat/0209629 (2002).  
(Cited on page 84)
- [97] C. L. Hutchison, J. M. Gambetta, A. Blais and F. K. Wilhelm. Quantum trajectory equation for multiple qubits in circuit QED: Generating entanglement by measurement. *Canadian Journal of Physics* **87**, 225–231 (2009). (Cited on pages 84, 103, and 116)
- [98] H. M. Wiseman and G. J. Milburn. Squeezing via feedback. *Physical Review A* **49**, 1350 (1994).  
(Cited on page 85)
- [99] T. M. Stace and S. D. Barrett. Continuous Quantum Measurement: Inelastic Tunneling and Lack of Current Oscillations. *Physical Review Letters* **92**, 136802 (2004).  
(Cited on page 95)
- [100] D. V. Averin and A. N. Korotkov. Comment on "Continuous Quantum Measurement: Inelastic Tunneling and Lack of Current Oscillations". *Physical Review Letters* **94**, 069701 (2005).  
(Cited on page 95)
- [101] T. M. Stace and S. D. Barrett. Stace and Barrett Reply. *Physical Review Letters* **94**, 069702 (2005).  
(Cited on page 95)
- [102] E. Il'ichev *et al.* Continuous Monitoring of Rabi Oscillations in a Josephson Flux Qubit. *Physical Review Letters* **91**, 097906 (2003).  
(Cited on page 95)
- [103] R. Deblock, E. Onac, L. Gurevich and L. P. Kouwenhoven. Detection of Quantum Noise from an Electrically Driven Two-Level System. *Science* **301**, 203–206 (2003).  
(Cited on page 95)

- [104] M. Brune *et al.* Observing the Progressive Decoherence of the "Meter" in a Quantum Measurement. *Physical Review Letters* **77**, 4887 (1996). (Cited on pages 100 and 102)
- [105] D. I. Schuster *et al.* Resolving photon number states in a superconducting circuit. *Nature* **445**, 515–518 (2007). (Cited on page 103)
- [106] A. Wallraff *et al.* Approaching Unit Visibility for Control of a Superconducting Qubit with Dispersive Readout. *Physical Review Letters* **95**, 060501 (2005). (Cited on page 106)
- [107] H. C. Torrey. Transient Nutations in Nuclear Magnetic Resonance. *Physical Review* **76**, 1059 (1949). (Cited on pages 112 and 118)
- [108] W. M. Itano, D. J. Heinzen, J. J. Bollinger and D. J. Wineland. Quantum Zeno effect. *Physical Review A* **41**, 2295 (1990). (Cited on page 114)
- [109] A. N. Korotkov. Output spectrum of a detector measuring quantum oscillations. *Physical Review B* **63**, 085312 (2001). (Cited on pages 116 and 118)
- [110] R. Ruskov and A. N. Korotkov. Spectrum of qubit oscillations from generalized Bloch equations. *Physical Review B* **67**, 075303 (2003). (Cited on page 116)
- [111] A. V. Oppenheim, J. R. Buck and R. W. Schafer. *Discrete-Time Signal Processing* (Prentice-Hall, Upper Saddle River, NJ, 1999). (Cited on page 120)
- [112] M. Frigo and S. Johnson. The Design and Implementation of FFTW3. *Proceedings of the IEEE* **93**, 216–231 (2005). (Cited on page 120)
- [113] M. P. da Silva, D. Bozyigit, A. Wallraff and A. Blais. Schemes for the observation of photon correlation functions in circuit QED with linear detectors. *1004.3987* (2010). (Cited on page 124)
- [114] D. Bozyigit *et al.* Measurements of the Correlation Function of a Microwave Frequency Single Photon Source. *ArXiv* 1002.3738 (2010). (Cited on pages 124 and 216)
- [115] S. M. Tan. A computational toolbox for quantum and atomic optics. *Journal of Optics B: Quantum and Semiclassical Optics* **1**, 424–432 (1999). (Cited on page 126)
- [116] A. Aspect, P. Grangier and G. Roger. Experimental Realization of Einstein-Podolsky-Rosen-Bohm Gedankenexperiment: A New Violation of Bell's Inequalities. *Physical Review Letters* **49**, 91 (1982). (Cited on page 131)
- [117] M. Ansmann *et al.* Violation of Bell's inequality in Josephson phase qubits. *Nature* **461**, 504–506 (2009). (Cited on page 131)
- [118] J. M. Chow *et al.* Entanglement Metrology Using a Joint Readout of Superconducting Qubits. *ArXiv* 0908.1955 (2009). (Cited on pages 131, 197, and 213)
- [119] S. F. Huelga, T. W. Marshall and E. Santos. Temporal Bell-type inequalities for two-level Rydberg atoms coupled to a high-Q resonator. *Physical Review A* **54**, 1798 (1996). (Cited on page 132)

- [120] J. Kofler and C. Brukner. Conditions for Quantum Violation of Macroscopic Realism. *Physical Review Letters* **101**, 090403 (2008). (Cited on page 132)
- [121] A. J. Leggett. Macroscopic Quantum Systems and the Quantum Theory of Measurement. *Progress of Theoretical Physics Supp.* **69**, 80–100 (1980). (Cited on pages 138 and 139)
- [122] J. I. Korsbakken, F. K. Wilhelm and K. B. Whaley. Electronic structure of superposition states in flux qubits. *Physica Scripta* **T137**, 014022 (2009). (Cited on page 139)
- [123] A. N. Korotkov. Simple quantum feedback of a solid-state qubit. *Physical Review B* **71**, 201305 (2005). (Cited on page 142)
- [124] H. M. Wiseman and G. J. Milburn. *Quantum measurement and control* (Cambridge University Press, 2010). (Cited on page 142)
- [125] J. M. Chow *et al.* Randomized Benchmarking and Process Tomography for Gate Errors in a Solid-State Qubit. *Physical Review Letters* **102**, 090502–4 (2009). (Cited on pages 143 and 213)
- [126] M. Steffen *et al.* Measurement of the Entanglement of Two Superconducting Qubits via State Tomography. *Science* **313**, 1423–1425 (2006). (Cited on page 143)
- [127] T. Sleator, E. L. Hahn, C. Hilbert and J. Clarke. Nuclear-spin noise. *Physical Review Letters* **55**, 1742 (1985). (Cited on page 143)
- [128] C. Cohen-Tannoudji, J. Dupont-Roc and G. Grynberg. *Atom-Photon Interactions: Basic Processes and Applications* (Wiley, 1998). (Cited on page 144)
- [129] R. Vijay, M. H. Devoret and I. Siddiqi. Invited Review Article: The Josephson bifurcation amplifier. *Review of Scientific Instruments* **80**, 111101 (2009). (Cited on pages 149 and 152)
- [130] S. Filipp *et al.* Two-Qubit State Tomography Using a Joint Dispersive Readout. *Physical Review Letters* **102**, 200402 (2009). (Cited on page 151)
- [131] J. Gambetta, W. A. Braff, A. Wallraff, S. M. Girvin and R. J. Schoelkopf. Protocols for optimal readout of qubits using a continuous quantum nondemolition measurement. *Physical Review A* **76**, 012325 (2007). (Cited on page 151)
- [132] I. Siddiqi *et al.* Direct Observation of Dynamical Bifurcation between Two Driven Oscillation States of a Josephson Junction. *Physical Review Letters* **94**, 027005 (2005). (Cited on page 152)
- [133] I. Siddiqi *et al.* Dispersive measurements of superconducting qubit coherence with a fast latching readout. *Physical Review B* **73**, 054510 (2006). (Cited on page 152)
- [134] A. Lupascu *et al.* Quantum non-demolition measurement of a superconducting two-level system. *Nature Physics* **3**, 119–125 (2007). (Cited on page 152)



- [135] M. I. Dykman and M. A. Krivoglaz. Theory of fluctuational transitions between stable states of a nonlinear oscillator. *Soviet Journal of Experimental and Theoretical Physics* **50**, 30 (1979). (Cited on pages 166 and 221)
- [136] R. L. Kautz. Thermally induced escape: The principle of minimum available noise energy. *Physical Review A* **38**, 2066 (1988). (Cited on pages 166 and 221)
- [137] G. E. P. Box and M. E. Muller. A Note on the Generation of Random Normal Deviates. *The Annals of Mathematical Statistics* **29**, 610–611 (1958). (Cited on page 168)
- [138] T. Picot, A. Lupascu, S. Saito, C. J. P. M. Harmans and J. E. Mooij. Role of relaxation in the quantum measurement of a superconducting qubit using a nonlinear oscillator. *Physical Review B (Condensed Matter and Materials Physics)* **78**, 132508–4 (2008). (Cited on pages 176 and 177)
- [139] R. Vijayaraghavan. *Amplifying quantum signals using a dynamical bifurcation*. Ph.D. thesis, Yale University (2008). (Cited on pages 176, 177, 221, 222, and 223)
- [140] F. R. Ong *et al.* ac-Stark shift and dephasing of a qubit strongly coupled to a non-linear resonator. *in preparation* . (Cited on page 185)
- [141] D. A. unpublished notes. (Cited on pages 188 and 189)
- [142] I. Chiorescu *et al.* Coherent dynamics of a flux qubit coupled to a harmonic oscillator. *Nature* **431**, 159–162 (2004). (Cited on page 190)
- [143] A. Wallraff *et al.* Sideband Transitions and Two-Tone Spectroscopy of a Superconducting Qubit Strongly Coupled to an On-Chip Cavity. *Physical Review Letters* **99**, 050501 (2007). (Cited on page 191)
- [144] P. J. Leek *et al.* Using sideband transitions for two-qubit operations in superconducting circuits. *Physical Review B* **79**, 180511 (2009). (Cited on page 191)
- [145] P. J. Leek *et al.* Cavity Quantum Electrodynamics with Separate Photon Storage and Qubit Readout Modes. *Physical Review Letters* **104**, 100504 (2010). (Cited on page 191)
- [146] C. Monroe *et al.* Resolved-Sideband Raman Cooling of a Bound Atom to the 3D Zero-Point Energy. *Physical Review Letters* **75**, 4011 (1995). (Cited on page 192)
- [147] A. J. Berkley *et al.* Entangled Macroscopic Quantum States in Two Superconducting Qubits. *Science* **300**, 1548–1550 (2003). (Cited on page 197)
- [148] Y. A. Pashkin *et al.* Quantum oscillations in two coupled charge qubits. *Nature* **421**, 823–826 (2003). (Cited on page 197)
- [149] T. Yamamoto, Y. A. Pashkin, O. Astafiev, Y. Nakamura and J. S. Tsai. Demonstration of conditional gate operation using superconducting charge qubits. *Nature* **425**, 941–944 (2003). (Cited on page 197)

- [150] R. McDermott *et al.* Simultaneous State Measurement of Coupled Josephson Phase Qubits. *Science* **307**, 1299–1302 (2005). *(Cited on pages 197 and 213)*
- [151] J. B. Majer, F. G. Paauw, A. C. J. ter Haar, C. J. P. M. Harmans and J. E. Mooij. Spectroscopy on Two Coupled Superconducting Flux Qubits. *Physical Review Letters* **94**, 090501 (2005). *(Cited on page 197)*
- [152] T. Hime *et al.* Solid-State Qubits with Current-Controlled Coupling. *Science* **314**, 1427–1429 (2006). *(Cited on page 197)*
- [153] J. Majer *et al.* Coupling superconducting qubits via a cavity bus. *Nature* **449**, 443–447 (2007). *(Cited on page 197)*
- [154] F. Helmer *et al.* Cavity grid for scalable quantum computation with superconducting circuits. *EPL (Europhysics Letters)* **85**, 50007 (2009). *(Cited on page 197)*
- [155] A. O. Niskanen, K. Harrabi, F. Yoshihara, Y. Nakamura and J. S. Tsai. Spectroscopy of three strongly coupled flux qubits. *Physical Review B* **74**, 220503 (2006). *(Cited on page 197)*
- [156] L. Landau and E. Lifshitz. *Mechanics*. Course of theoretical physics (Pergamon Oxford), 1982 edn. *(Cited on page 206)*
- [157] L. DiCarlo *et al.* Demonstration of Two-Qubit Algorithms with a Superconducting Quantum Processor. *0903.2030* (2009). *(Cited on pages 213 and 215)*
- [158] P. J. Leek *et al.* Observation of Berry’s Phase in a Solid-State Qubit. *Science* **318**, 1889–1892 (2007). *(Cited on page 213)*
- [159] M. Hofheinz *et al.* Generation of Fock states in a superconducting quantum circuit. *Nature* **454**, 310–314 (2008). *(Cited on page 213)*
- [160] M. Hofheinz *et al.* Synthesizing arbitrary quantum states in a superconducting resonator. *Nature* **459**, 546–549 (2009). *(Cited on page 213)*
- [161] H. Wang *et al.* Measurement of the Decay of Fock States in a Superconducting Quantum Circuit. *Physical Review Letters* **101**, 240401–4 (2008). *(Cited on page 213)*
- [162] C. F. Roos *et al.* Bell States of Atoms with Ultralong Lifetimes and Their Tomographic State Analysis. *Physical Review Letters* **92**, 220402 (2004). *(Cited on page 215)*
- [163] A. Gruber *et al.* Scanning Confocal Optical Microscopy and Magnetic Resonance on Single Defect Centers. *Science* **276**, 2012–2014 (1997). *(Cited on page 215)*
- [164] F. Jelezko, T. Gaebel, I. Popa, A. Gruber and J. Wrachtrup. Observation of Coherent Oscillations in a Single Electron Spin. *Physical Review Letters* **92**, 076401 (2004). *(Cited on page 215)*
- [165] G. Balasubramanian *et al.* Ultralong spin coherence time in isotopically engineered diamond. *Nat Mater* **8**, 383–387 (2009). *(Cited on page 215)*



- [166] Y. Kubo *et al.* Strong Coupling of a Spin Ensemble to a Superconducting Resonator. *ArXiv* 1006.0251 (2010). *(Cited on page 215)*
- [167] D. I. Schuster *et al.* High cooperativity coupling of electron-spin ensembles to superconducting cavities. *ArXiv* 1006.0242 (2010). *(Cited on page 215)*
- [168] J. Twamley and S. D. Barrett. A superconducting cavity bus for single Nitrogen Vacancy defect centres in diamond. *ArXiv* 0912.3586 (2009). *(Cited on page 215)*
- [169] D. Marcos *et al.* Coupling Nitrogen Vacancy Centers in Diamond to Superconducting Flux Qubits. *ArXiv* 1001.4048 (2010). *(Cited on page 215)*
- [170] D. Englund *et al.* Deterministic coupling of a single nitrogen vacancy center to a photonic crystal cavity. *ArXiv* 1005.2204 (2010). *(Cited on page 215)*
- [171] M. V. G. Dutt *et al.* Quantum Register Based on Individual Electronic and Nuclear Spin Qubits in Diamond. *Science* **316**, 1312–1316 (2007). *(Cited on page 215)*
- [172] L. DiCarlo *et al.* Preparation and Measurement of Three-Qubit Entanglement in a Superconducting Circuit. *ArXiv* 1004.4324 (2010). *(Cited on page 215)*
- [173] A. A. Houck *et al.* Generating single microwave photons in a circuit. *Nature* **449**, 328–331 (2007). *(Cited on page 216)*
- [174] A. A. Abdumalikov *et al.* Electromagnetically induced transparency on a single artificial atom. *ArXiv* 1004.2306 (2010). *(Cited on page 217)*
- [175] G. Milburn and D. F. Walls. Production of squeezed states in a degenerate parametric amplifier. *Optics Communications* **39**, 401–404 (1981). *(Cited on page 223)*
- [176] H. A. Kramers. Brownian motion in a field of force and the diffusion model of chemical reactions. *Physica* **7**, 284–304 (1940). *(Cited on page 223)*
- [177] M. I. Dykman and M. A. Krivoglaz. Fluctuations in nonlinear systems near bifurcations corresponding to the appearance of new stable states. *Physica A Statistical Mechanics and its Applications* **104**, 480–494 (1980). *(Cited on page 223)*